JUSTUS-LIEBIG-
UNIVERSITÄT
GIESSEN

Aus dem Institut für Ernährungswissenschaft
Professur für Molekulare Ernährungsforschung
der Justus-Liebig-Universität Gießen

Effects of 4-Phenylbutyric Acid and Caprylic Acid on Proteostasis and Mitochondrial Homeostasis in an Alzheimer's Disease Model of the Nematode *Caenorhabditis elegans*

Inaugural-Dissertation
Zur Erlangung des Doktorgrades Dr. rer. nat.
im Fachbereich Agrarwissenschaften, Ökotrophologie und Umweltmanagement der Justus-Liebig-Universität Gießen

vorgelegt von
Stefan Baumanns
geboren in Moers

Gießen, 2022

Mit Genehmigung des Fachbereichs Agrarwissenschaften, Ökotrophologie und Umweltmanagement der Justus-Liebig-Universität Gießen

Prüfungskommission

1. Gutachter: Prof. Dr. Uwe Wenzel
2. Gutachter: Prof. Dr. Gunter P. Eckert
3. Gutachter: Prof. Dr. Mathias Fasshauer
Prüfer: Prof. Dr. Klaus K. Eder
Prüferin: Prof. Dr. Anika Wagner
Vorsitzender: Prof. Dr. Marc Schetelig

Tag der Disputation: 06.02.2023

„Die Wissenschaft fängt eigentlich erst da an interessant zu werden, wo sie aufhört.“

Justus Freiherr von Liebig (1803 - 1873)

Table of Content

List of Figures

List of Tables

List of Abbreviations

AA	ascorbic acid
ABAD	Aβ peptide alcohol dehydrogenase
ABU	activated in blocked UPR
Aβ	amyloid-β
ACAT	acetyl-CoA acetyltransferase
ACDH	acyl-CoA dehydrogenase
AD	Alzheimer's disease
ADAM; ADM	a disintegrin and metalloproteinase domain-containing protein
AICD	amyloid intracellular domain
AKG	alpha-ketoglutarate
AKG-DH	AKG dehydrogenase
ALA	α-lipoic acid
AMBRA1	activating molecule in beclin-1-regulated autophagy
APA	American Psychiatric Association
APH1	anterior pharynx-defective 1
APL-1	amyloid precursor-like
APP	amyloid precursor protein
ARE	antioxidant response element
ATF	activating transcription factor
ATG	autophagy-related
ATP	adenosine triphosphate
ATFS-1	activating transcription factor associated with stress 1
α7nAChR	α-7 nicotinic acetylcholine receptor
BACE1	β-site APP-cleaving enzyme 1
BAG3	BCL2-associated anthogene 3
BBB	blood-brain barrier
BCA	bicinchoninic acid
BCL2	B-cell lymphoma 2
BCL2L13	BCL2 like protein 13
BHB	β-hydroxybutyric acid
BHB-DH	BHB dehydrogenase
BIP	binding immunoglobulin protein
BLAST	Basic Local Alignment Search Tool
BNIP3	BCL2/adenovirus E1B 19 kDa protein-interacting protein 3
BSA	bovine serum albumin
CA	caprylic acid
CGC	Caenorhabditis Genetics Center

CHIP	carboxy terminus of HSP70-interacting protein
CHOP	C/EBP homologous protein
CK2	casein kinase 2
CLPP	caseinolytic protease proteolytic subunit
CMA	chaperone-mediated autophagy
CoA	coenzyme A
CSF	cerebrospinal fluid
CTF	C-terminal fragment
CYPD	cyclophilin D
C/EBP	CCAAT/enhancer-binding protein
DAF	abnormal dauer formation
DCT-1	DAF-16/FOXO controlled
DH	dehydrogenase
DHLA	dihydro lipoic acid
DMSO	dimethyl sulfoxide
DNC	dorsal nerve cord
DRP1	dynamin-related protein 1
DVE-1	defective proventriculus 1
dsRNA	double-stranded RNA
EAT-3	EATing: abnormal pharyngeal pumping
eIF2α	eukaryotic initiation factor-2α
ER	endoplasmic reticulum
ERAD	ER-associated protein degradation
ETC	electron transport chain
E1	ubiquitin-activating enzymes
E2	ubiquitin-conjugating enzymes
E3	ubiquitin ligases
FA	fatty acids
FACS	fluorescence-activated cell sorting
FAD	familial Alzheimer‘s disease
$FADH_2$	reduced flavin adenine dinucleotide
FAO	fatty acid oxidation; β-oxidation
FDG	^{18}F-fluorodeoxyglucose
FHRE	forkhead-responsive element
Fiji	Fiji is just ImageJ
FIS1	mitochondrial fission 1 protein
FKBP8	FK506-binding protein 8
FL	focal length
FOXO	forkhead box O

FPS	frames per second
FUDR	5-fluoro-2‘-deoxyuridine
FUNDC1	FUN14 domain containing 1
FZO-1	fuzzy onions
GABARAP	gamma-aminobutyric acid receptor-associated protein
GFP	green fluorescent protein
GOI	gene of interest
GPX	glutathione peroxidase
GRP	glucose-regulated protein
GTP	guanosine triphosphate
HAF-1	half transporter 1
HAT	histone acetyltransferases
HDAC/ HDA	histone deacetylase
HDACI	histone deacetylase-inhibitor
HMG	3-hydroxy-3-methyl-glutaryl
HMG-5	high mobility group 5
HOP	HSP70/HSP90 organizing protein
HOP-1	homolog of presenilin
Hsc70	heat shock cognate protein of 70 kDa
HSE	heat shock element
HSF	heat shock factor
HSP	heat shock protein
HSR	heat shock response
IC50	half maximal inhibitory concentrations
IDE	insulin-degrading enzyme
IMM	inner mitochondrial membrane
IPTG	isopropyl-β-D-thiogalactopyranoside
IRE1α	inositol-requiring enzyme 1α
ISR	integrated stress response
IWG	International Working Group
JNK	c-Jun N-terminal kinase
KEAP1	Kelch-like ECH associated protein 1
LAMP2A	lysosomal-associated membrane protein 2A
LCFA	long-chain fatty acid
LCT	long-chain triglycerides
LC3	microtubule-associated proteins 1A/1B light chain 3B
LIAS	lipoic acid synthetase
LIPT2	lipoyl(octanoyl) transferase 2
LIR	LC3-interacting region

LONP	lon protease
LRP1	low-density lipoprotein receptor-related protein 1
MAD	mitochondrial-associated degradation
MAM	mitochondria-associated ER membrane
MCI	mild cognitive impairment
MCS	multiple cloning site
MCT	medium-chain triglycerides
MDV	mitochondrial-derived vesicles
MFN	mitofusin
MID49	mitochondrial dynamics proteins of 49 kDa
MID51	mitochondrial dynamics proteins of 51 kDa
MIP	maximum intensity projection
MMP	mitochondrial membrane potential
MP	megapixel
MPTP	mitochondrial permeability-transition pore
mRNA	messenger RNA
mtDNA	mitochondrial DNA
MTR	MitoTracker™ Red
NA	numerical aperture
NADH + H^+	reduced nicotinamide adenine dinucleotide
NBR1	neighbor of BRCA1 gene 1
NCBI	National Center for Biotechnology Information
NDP52	nuclear dot protein 52 kDa
NEP	neprilysin
NGM	nematode growth medium
NIA-AA	National Institute on Aging and the Alzheimer's Association
NIX/BNIP3L	Nip3-like protein X
NMDAR	N-methyl-D-aspartate receptor
NRF1	nuclear respiratory factor 1
NRF2	nuclear factor erythroid-2-related factor 2
OAA	Oxalacetate; oxalacetic acid
OD_{600}	optical density at 600 nm
OMM	outer mitochondrial membrane
OPA1	optic atrophy 1
OPTN	optineurin
OXPHOS	oxidative phosphorylation
PAA	phenylacetic acid
PC	pyruvate-carboxylase
PDH	pyruvate dehydrogenase

PDR-1	Parkinson's disease related 1
PEK-1	PERK kinase homologue
PEN2	presenilin enhancer 2
PET	positron emission tomography
PGAM5	phosphoglycerate-mutase 5
PGC1α	PPARγ coactivator-1α
PINK1	PTEN-induced putative kinase 1
PI3K	phosphatidylinositol 3-kinase
PKB	protein kinase B
PPARγ	peroxisome proliferator-activated receptor-γ
PQCS	protein quality control system
PreP	presequence protease
PSEN	presenilin
PSF	point spread function
PTL-1	protein with tau-like repeats
PTM	post-translational modification
P62/SQSTM1	ubiquitin-binding protein P62; sequestosome-1
Q	ubiquinone
QH_2	ubiquinol (reduced ubiquinone)
qPCR	quantitative polymerase chain reaction
RAGE	receptor for advanced glycation end-products
RIDD	regulated IRE1α-dependent decay
RISC	RNA-induced silencing complex
RNAi	RNA interference
ROI	region of interest
rRNA	ribosomal RNA
SAHA	suberoylanilide hydroxamic acid
sAPP	soluble APP
SCFA	short-chain fatty acid
SCOT	Succinyl-CoA:3-oxoacyl-CoA-transferase
SEL-12	suppressor/enhancer of lin-12
SIAH1	seven in absentia homolog 1
SID-1	systemic RNAi defective 1
siRNA	small-interfering RNA
SKN-1	skinhead 1
SMURF1	SMAD ubiquitination regulatory factor 1
SNARE	Soluble N-ethylmaleimide-sensitive factor attachment protein receptor
SOD	superoxide dismutase
SSBP1	single-stranded DNA binding protein 1

STX17	Syntaxin 17
SUP-17	SUPpressor
S1P	membrane-bound transcription factor site-1 protease
TAX1BP1	tax1-binding protein 1
TBK1	TANK-binding kinase 1
TIM	translocase of the inner membrane
TCA	tricarboxylic acid
TFAM	mitochondrial transcription factor A
TMRE	tetramethylrhodamine ethylester perchlorat
TOM	translocase of the outer membrane
tRNA	transfer RNA
UBD	ubiquitin-binding-domain
UBL	ubiquitin-like domain
ULK1	unc-51 like autophagy activating kinase 1
UPR^{ER}	unfolded protein response of the endoplasmic reticulum
UPR^{mt}	unfolded protein response of mitochondria
UPS	ubiquitin–proteasome system
USP	ubiquitin-specific protease
VNC	ventral nerve cord
WDR-23	WD repeat protein 23
WF-NTP	wide field-of-view nematode tracking platform
XBP1	X-box binding protein 1
YME1L1	yme1-like 1 ATPase
YT	yeast extract tryptone
4-HNE	4-hydroxy-2-nonenal
4-PBA	4-phenylbutyric acid

1 Introduction

1.1 Alzheimer's Disease

Alzheimer's disease (AD), first described by Alois Alzheimer in 1906, is a neurodegenerative disease and the most common form of dementia. The neurodegeneration results in progressive memory loss as well as psychological changes and can ultimately lead to an almost complete loss of cognitive abilities [1]. In addition to the far-reaching consequences for the patients, AD places a great burden on family members and the health care system due to the need for intensive care. As an age-associated disease, AD is becoming increasingly prominent in a steadily aging population. The incidence of AD doubles approximately every five years after age 65. Worldwide, more than 45 million people are estimated to suffer from dementia. This prevalence is expected to triple by 2050 [2].

Histopathologically, AD is characterized by extensive degeneration of neurons in the hippocampus and cerebral cortex as well as deposition of misfolded protein aggregates. These protein deposits include the extracellular senile plaques, containing amyloid-β (Aβ) peptide as a major component, and the intracellular neurofibrillary tangles derived from hyperphosphorylated tau protein[1] [1]. Since pathological changes develop many years before the first symptoms emerge, the pathogenesis is defined by a long preclinical phase during which irreversible neurodegeneration progresses [3, 4].

Several clinical diagnostic criteria for AD were defined by the National Institute on Aging and the Alzheimer's Association (NIA-AA), the American Psychiatric Association (APA) and the International Working Group (IWG). In these criteria, the three disease stages of preclinical phase, mild cognitive impairment (MCI) and AD dementia are distinguished by assessment of symptoms and pathological markers. Cerebrospinal fluid (CSF) examinations commonly determine levels of Aβ and hyperphosphorylated tau. Furthermore, ^{18}F-fluorodeoxyglucose (FDG) positron emission tomography (PET) is used to detect cerebral glucose hypometabolism associated with AD (Chapter 1.4). In addition, PET provides visual assessment of Aβ aggregation following administration of specific tracers. However, several issues including a lack of standardization, insufficient clinical routine and vague interpretation of results, limit the diagnostic use, particularly in the early stages of the disease [3–5].

[1] Physiologically, tau is a microtubule-associated protein, promoting microtubule assembly and stabilization of the microtubule network.

Based on etiology, a distinction is made between the familial and the sporadic type of AD. The rare familial form affects about 5 to 10% of AD patients. It is characterized by an early-onset of symptoms before the age of 65, caused by mutations in the genes of the amyloid precursor protein (APP) or its metabolizing enzymes [6] (Chapter 1.1.1).
The more common sporadic form of AD has not yet been attributed to clear causes. It is based on complex interactions of influenceable and non-influenceable risk factors. Due to the strong age association of the disease, increasing age is consequently considered the greatest risk factor [1]. In addition, cardiovascular factors such as hypertension or elevated cholesterol levels, psychological factors such as depression or anxiety disorders, certain polymorphisms such as those of apolipoprotein E, and lifestyle factors such as diet or physical activity have a significant influence on the risk of developing AD [7].

Although intensive research has been conducted, current therapy is limited to purely symptomatic treatment of altered cholinergic and glutaminergic neurotransmission with acetylcholinesterase inhibitors and the N-methyl-D-aspartate receptor (NMDAR) antagonist memantine, respectively. This lack of treatment options is partly due to the complex pathogenesis of AD. Moreover, the long preclinical phase before the onset of symptoms and extensive irreversible neurodegeneration, during which treatment may be most effective, poses further challenges to research on AD therapy [8].

Given the central role of Aβ in this work, the formation of this peptide following processing of the APP is described in the following Chapter 1.1.1. Thereafter, potential mechanisms of Aβ proteotoxicity are presented (Chapter 1.1.2).

1.1.1 Processing of the Amyloid Precursor Protein

The APP is a ubiquitously expressed integral membrane protein that exists in several different isoforms generated by alternative splicing. It consists of a large N-terminal, a transmembrane and a short C-terminal domain. Of the three major forms, APP695, APP751 and APP770, primarily APP695 is expressed in the brain [9, 10].

The processing of the APP shown in Figure 1.1 involves sequential proteolytic cleavage by enzymes or enzyme complexes with α-, β- and γ-secretase activity. Depending on the enzymes involved and the sequence of proteolytic cleavage, a distinction is made between the amyloidogenic and the non-amyloidogenic pathway.

Processing of the APP physiologically occurs primarily via the non-amyloidogenic pathway. The first step is a proteolytic cleavage within the Aβ domain by enzymes with α-secretase activity, which excludes the formation of Aβ. Enzymes with α-secretase activity identified to date are a disintegrin and metalloproteinase domain-containing protein (ADAM) 9, ADAM10 and ADAM17. Cleavage results in generation of the soluble APP (sAPP)-α and the membrane-remaining C-terminal fragment (CTF) 83. CTF83 is subsequently split by the γ-secretase complex into the extracellular soluble P3 fragment and the amyloid intracellular domain (AICD). The active site of the γ-secretase complex is formed by presenilin (PSEN), of which the two homologs PSEN1 and PSEN2 are known. In addition, the proteins nicastrin, anterior pharynx-defective 1 (APH1) and presenilin enhancer-2 (PEN2) are involved in the assembly of the complex [11].

In the amyloidogenic pathway, the APP is first processed by the β-secretase β-site APP-cleaving enzyme 1 (BACE1) to the fragments sAPP-β and CTF99. Further cleavage of CTF99 by the γ-secretase complex leads to the formation of the AICD and Aβ, which is a major factor in AD pathogenesis. The Aβ formed can vary in length from 30 to 51 amino acids, although primarily $A\beta_{1\text{-}40}$ and $A\beta_{1\text{-}42}$ are produced in a ratio of about ten to one [11, 12]. Under physiological conditions, the generation of Aβ and its aggregation into proteotoxic aggregates is counterbalanced by action of the proteostasis network (Chapter 1.2), cell-mediated clearance, active export from the brain and deposition into less toxic insoluble aggregates. In AD, however, failure and overload of these control mechanisms lead to proteotoxic stress, which interferes with a multitude of biological functions and ultimately results in impaired neurotransmission and neurodegeneration (Chapter 1.1.2 & 1.4).

Whereas the APP plays a central role in the pathogenesis of AD as the precursor of Aβ, its physiological function is less understood. This is based on the existence of several different APP isoforms as well as their complex and partly imprecise processing by sequential proteolytic cleavage, which may also involve further proteases not described in this Chapter, resulting in a broad range of biologically active fragments [10, 12]. Thus, the APP seems to be involved in several biological processes including nervous system development, the formation and function of the neuromuscular junction, synaptogenesis, axonal growth and regulation of synaptic functions [10].

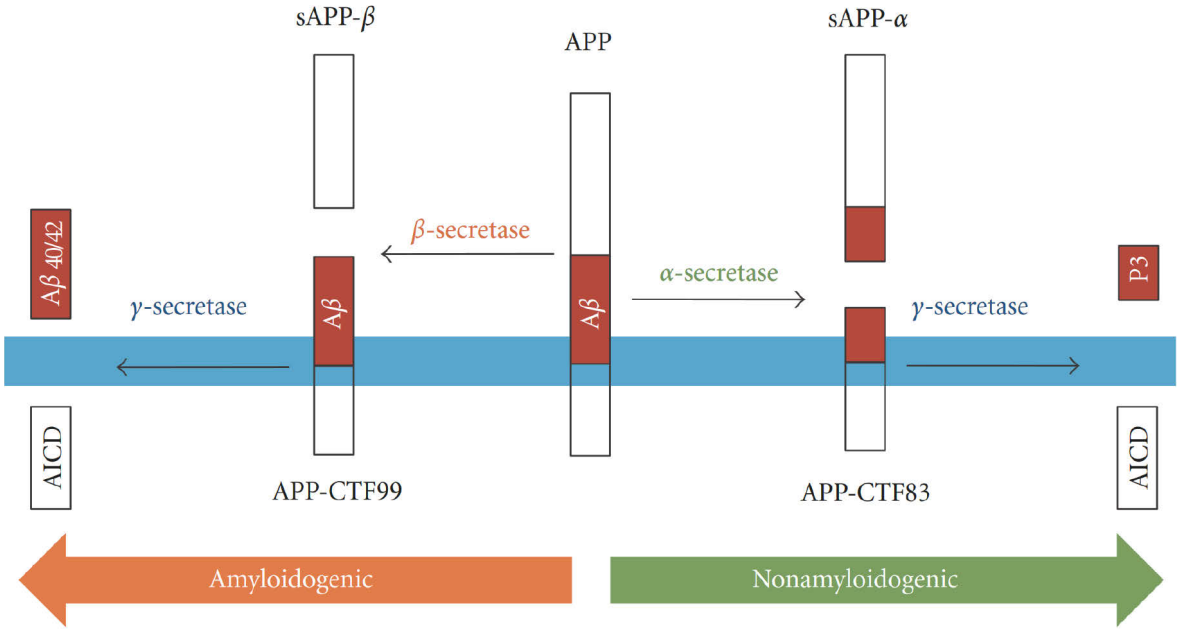

Figure 1.1 | Schematic illustration of APP processing

The transmembrane protein APP can be processed via the amyloidogenic and the non-amyloidogenic pathway. Physiologically, the APP is mainly processed via the non-amyloidogenic pathway. In this process, enzymes with α-secretase activity cleave the APP in the Aβ domain, excluding the formation of Aβ. The proteolytic cleavage results in generation of the fragments sAPP-α and APP-CTF83. During the second step, the γ-secretase complex cleaves the APP-CTF83 to form the AICD and the P3 fragment. In the amyloidogenic pathway, the APP is first processed by the β-secretase BACE1 into the fragments sAPP-β and APP-CTF99. Further cleavage of the APP-CTF99 by the γ-secretase complex leads to the formation of the AICD and Aβ [13]. AICD = amyloid intracellular domain, APP = amyloid precursor protein, Aβ = amyloid-β, BACE1 = β-site APP-cleaving enzyme 1, CTF = C-terminal fragment, sAPP = soluble APP.

1.1.2 Proteotoxicity of Amyloid-β

Based on the observation of senile plaques in the brains of AD patients (Chapter 1.1), the classical amyloid cascade hypothesis proposed that the pathogenesis is promoted by these extracellular Aβ deposits. The involvement of Aβ in the pathogenesis has been further reinforced by research on the early-onset familial form of AD (familial Alzheimer's disease, FAD) and the unraveling of its etiology, which is caused by mutations in the three autosomal dominant genes *APP*, *PSEN1* and *PSEN2*. These mutations affect the processing of APP, the metabolism of Aβ or its stability and thus promote increased Aβ deposition [11].

In the history of AD research, however, increasing evidence has led to several modifications of the classic amyloid cascade hypothesis. First, no clear correlation of senile plaques to the local extent of neuronal cell loss or cognitive dysfunction was found [14]. This lack of

correlation resulted in research on other forms of Aβ aggregation. Of the two major products of amyloidogenic APP processing (Chapter 1.1.1), aggregation of $A\beta_{1-42}$ occurs significantly faster due to the longer hydrophobic peptide chain [15]. The structures formed by aggregation range from dimers, to oligomers, to polymeric fibrils, which can eventually form β-sheets and constitute the insoluble fibers of senile plaques [11]. According to current research, oligomers exhibit the highest toxicity among the various forms of aggregation. They are characterized by a high complexity as well as dynamics of their conformation and consequently may interact with a wide range of biomolecules [16].
Moreover, intraneuronal accumulation of Aβ has been shown to be an early process in the pathogenesis of AD, prior to senile plaque formation. The primary source of intracellular Aβ is the uptake of secreted Aβ. Receptors involved include the α-7 nicotinic acetylcholine receptor (α7nAChR), the receptor for advanced glycation end-products (RAGE) and the low-density lipoprotein receptor-related protein 1 (LRP1) via receptor-mediated endocytosis. In addition, Aβ may also enter cells via diffusion [17–19] or can be generated intracellularly through APP processing at organelle membranes [11, 16]. Following its intracellular accumulation, Aβ can eventually be imported into different organelles. Accordingly, Aβ accumulation has been confirmed for mitochondria, the endoplasmic reticulum, the Golgi apparatus, endosomes and lysosomes [16]. Due to the accumulation in the aforementioned compartments, effects of Aβ on various intracellular processes beyond the potential proteotoxicity of extracellular senile plaques are explainable.

Indeed, a modified amyloid cascade hypothesis that is based on the proteotoxicity of lower molecular weight aggregates such as oligomers rather than senile plaques has been supported by a multitude of studies [1, 16].
At the extracellular level, interactions with a broad range of different receptors were identified. For instance, binding of Aβ to ionotropic glutamate receptors such as the NMDAR and metabotropic glutamate receptors has been demonstrated to result in excessive calcium influx and thus apoptosis through the process of excitotoxicity, substantiating the use of the NMDAR antagonist memantine as a therapeutic agent (Chapter 1.1). Complementarily, this breakdown of homeostasis of calcium and other ions is also possible through direct interaction of Aβ with membrane lipids, leading to the formation of ion channels or pores [1, 16].

On the intracellular level, Aβ can impair various biological processes, including organelle function. In this regard, particularly mitochondria were found to be a major target of Aβ

proteotoxicity, promoting the development of mitochondrial dysfunction (Chapter 1.4). Ultimately, the proteotoxicity of Aβ may result in disruption of neurotransmission and neuronal cell death. To counteract this detrimental proteotoxicity and to restore protein as well as mitochondrial homeostasis, cells have evolved complex networks of interacting stress response pathways, which are described in the Chapters 1.2 and 1.3.3.

1.2 Proteostasis

Proteins are a class of macromolecules with remarkable structural complexity and functional versatility that are involved in almost every biological process. They are synthesized as linear chains on ribosomes, which generally fold into specific three-dimensional conformations, also termed the native-state, to fulfil their physiological function [20]. However, correct protein folding is challenging, since a substantial fraction of proteins in eukaryotic cells adopt their native conformation only after interaction with binding partners or after import into specific organelles. Furthermore, the formation of oligomeric complexes requires precise stoichiometry of the individual polypeptides. Due to the thermodynamic variable cellular milieu, failure of correct protein folding and organelle mistargeting are common events that may lead to functional loss or proteotoxicity [21, 22].
According to the current model, polypeptides adopt several conformations as they progress downhill along a rugged funnel-shaped energy landscape towards the thermodynamically stable native state. During this process, however, non-native intra- and intermolecular interactions can occur that result in stable folding intermediates or misfolded states. Without assistance in overcoming the energetic barrier to adopt the native structure, these proteins may aggregate into oligomers, amorphous aggregates and amyloid fibrils [20, 22]. The formation of these potentially detrimental molecules is amplified by various factors, such as mutations, cellular stress, translation aberrations or post-translational modifications (PTMs) [20, 22, 23].

To restore the homeostasis of the proteome, also referred to as proteostasis, cells have evolved a protein quality control system (PQCS) of interconnected compartment-specific stress response pathways [20, 22]. It consists of the heat shock response (HSR) in the cytosol (Chapter 1.2.2), the unfolded protein response of the endoplasmic reticulum (UPR^{ER}) (Chapter 1.2.3) and the unfolded protein response of mitochondria (UPR^{mt}) (Chapter 1.2.4). This proteostasis network includes several hundred proteins, most prominently molecular chaperones and their regulators, which are described in the following Chapter 1.2.1. Moreover, the two major proteolytic pathways, the ubiquitin–proteasome system (UPS) and autophagy are presented in Chapter 1.2.5 and 1.2.6, respectively. Finally, the interconnection of the proteostasis network is outlined in Chapter 1.2.7.

1.2.1 Molecular Chaperones

Molecular chaperones are essential proteins of the proteostasis network that are expressed in almost every cellular compartment [24]. They are involved in a multitude of processes, including *de novo* folding of polypeptide chains, oligomeric assembly, refolding of misfolded proteins, suppression of aggregation, disaggregation of aggregates, protein transport and proteolytic degradation. Under physiological conditions, molecular chaperones are expressed at a constant level. However cellular stress that leads to formation of misfolded or aggregated proteins, such as heat, results in a substantial increase of their expression. Thus, molecular chaperones are also known as heat shock proteins (HSPs) [20, 22].

HSPs were originally categorized into functional protein families, such as small HSPs, HSP40, HSP60, HSP70, HSP90, HSP100 and HSP110, based on the molecular weight of their first-discovered members. However, due to variations in molecular weight and localisation in different cellular compartments as well as misleading trivial names, Kampinga et al. (2009) proposed a new nomenclature. Accordingly, molecular chaperone families should be referred to as HSPB [small HSP], DNAJ [HSP40], HSPD [HSP60], HSPA [HSP70], HSPC [HSP90] and HSPH [HSP100/ HSP110]. These basic identifiers are supplemented by additional numbers and letters, thereby uniquely classifying individual molecular chaperones. Par example, the cytosolic chaperone HSP70-1 is consequently termed HSPA1A, whereas a major ER resident chaperone of the HSP70 family called glucose-regulated protein (GRP) 78 or binding immunoglobulin protein (BIP) is specified as HSPA5 [25, 26]. Nevertheless, given the extensive use of the original nomenclature and trivial names in the literature, all common names are included in the following.

In general, molecular chaperones recognize hydrophobic amino acid side-chains and unfolded polypeptide backbones in their client proteins, which are usually not exposed in the native state [20, 22]. The major chaperone families involved in *de novo* protein folding and refolding are HSPA [HSP70], HSPC [HSP90] and the chaperonins HSPD [HSP60]. They directly participate in the folding process through ATP- and cofactor-regulated binding and release cycles, thereby providing the energy needed to overcome energetic barriers. Due to their active role in refolding, these chaperones are described as foldases. In contrast, ATP-independent chaperones, such as HSPBs [small HSPs], function as holdases by binding to unfolded or misfolded proteins and assisting their transport to foldases [20].

Molecular chaperones are further assisted by co-chaperones that modulate different aspects of chaperone function, such as binding of client proteins, ATPase activity or their capacity to form multiprotein complexes [20]. An important co-chaperone is the HSP70/HSP90 organizing protein (HOP), which facilitates the transfer of client proteins from HSPA [HSP70] to HSPC [HSP90] family members by connecting both chaperones [27]. Moreover, other molecular chaperones such as members of the DNAJ [HSP40] family can also operate as co-chaperones [20, 23]. In addition to their assistance in protein folding, specific co-chaperones also participate in protein degradation via the UPS and autophagy (Chapter 1.2.5 & 1.2.6). The targeting of client proteins for degradation is possibly based on random chance. Therefore, client proteins that are folding-incompetent and consequently exhibit a long chaperone residence time are more likely to interact with degradation mediating co-chaperones [28, 29].

In accordance with endogenous expressed molecular chaperones, the discovery of various substances that promote correct folding of proteins led to their classification as chemical or pharmacological chaperones (Chapter 1.5.1).

1.2.2 Heat Shock Response

To maintain proteostasis, the cytosol, ER and mitochondria have evolved distinct, yet interconnected stress response pathways. These pathways are generally triggered by the action of specific proteins that serve as stress sensors in reaction to accumulation of unfolded or misfolded proteins. This is typically followed by a stress response transduction, which leads to an arrest of translation to reduce the protein folding load and the expression of proteostasis effectors, such as molecular chaperones, co-chaperones or proteins involved in protein trafficking and degradation [30].

Based on its central function in coping with heat stress, the major cytosolic stress response is termed heat shock response (HSR). It is controlled by a group of transcription factors known as heat shock factors (HSFs), of which HSF1 is the best studied [22]. Although HSF1 has been the subject of extensive research, the conclusive picture of its activation is still unclear [31]. The common model depicted in Figure 1.2 proposes that under basal conditions, HSF1 is mainly localized in the cytosol in an inactive hetero-oligomeric complex. This complex may consist of cytosolic HSPA [HSP70] as well as HSPC [HSP90] chaperones and

other proteins such as histone deacetylase (HDAC) 6 that function as proteostasis detectors [22, 31–35]. Following an impairment of proteostasis due to accumulation of unfolded or misfolded proteins, the limited number of these proteostasis detectors dissociate from the complex to initiate the refolding of their client proteins [32, 35]. This dissociation leads to trimerization and transcriptional activation of HSF1, which binds heat shock elements (HSEs) located in target gene promoters to induce the expression of proteostasis effectors, most prominently of cytosolic HSPA [HSP70] and HSPC [HSP90] chaperones [32].

Together with a concurrent arrest of translation, the increased chaperone activity lowers the amount of client proteins. Depletion of client proteins increases the availability of free HSPA [HSP70] and HSPC [HSP90] chaperones, promoting reestablishment of the inactivated HSF1 complex. [22]. Thus, the activity of the HSR underlies a transcriptional negative feedback loop that serves to cope with stress induced accumulation of unfolded and misfolded proteins [36]. In addition to regulation by molecular chaperones, the activity of HSF1 is also modulated through several PTMs, such as acetylation, phosphorylation and sumoylation. Although these modifications are implicated in fine-tuning and attenuation of HSF1 activity, they appear to be dispensable for primary stress regulation [32, 36]. Moreover, HSF1 activity may be regulated through modifications of the repressor complex proteins (Chapter 1.5.2).

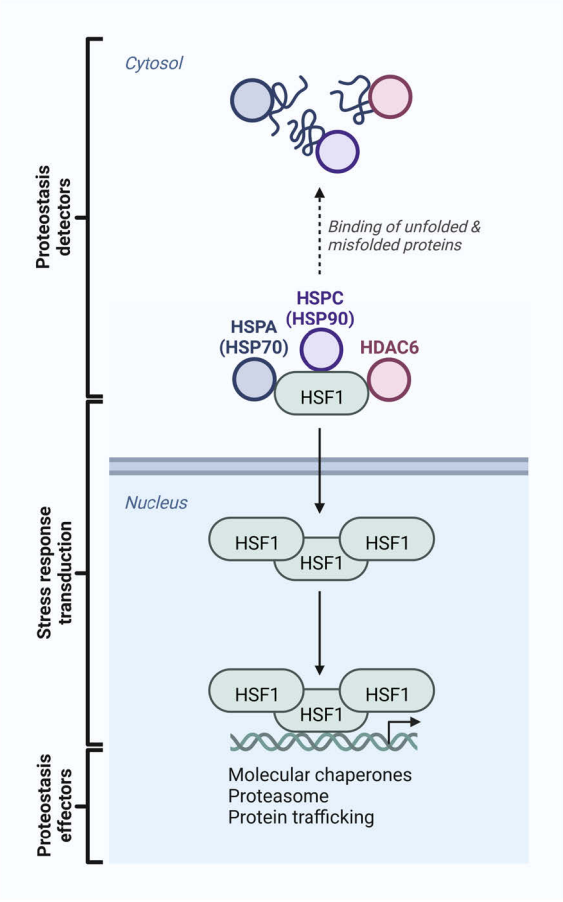

Figure 1.2 | HSR pathway

Under basal conditions, HSF1 is mainly localized in the cytosol in an inactive hetero-oligomeric complex, which may consist of cytosolic HSPA [HSP70] as well as HSPC [HSP90] chaperones and other proteins such as HDAC6 that function as proteostasis detectors. Accumulation of unfolded or misfolded proteins leads to dissociation of the repressive complex due to interaction of the proteostasis detectors with their client proteins. This results in HSF1 trimerization and transcriptional activation. Ultimately, the expression of proteostasis effectors, most prominently of cytosolic HSPA [HSP70] and HSPC [HSP90] chaperones, is induced. In turn, the activity of these molecular chaperones may result in a transcriptional negative feedback loop through depletion of client proteins and eventually reestablishment of the repressive HSF1 complex. Created with BioRender.com. HDAC = histone deacetylase, HSF = heat shock factor, HSP = heat shock protein.

1.2.3 Unfolded Protein Response of the Endoplasmic Reticulum

Since the endoplasmic reticulum (ER) is heavily involved in the synthesis, folding and structural maturation of proteins, it is evident that this organelle is also essential for maintaining proteostasis. In analogy to the HSR, accumulation of unfolded and misfolded proteins due to adverse endogenous and exogenous stimuli leads to a condition termed ER stress, which triggers a compartment-specific stress response pathway called the unfolded protein response of the ER (UPR^{ER}) (Figure 1.3) [37, 38].

Induction of the UPR^{ER} is based on activation of the three ER transmembrane stress sensors endoribonuclease inositol-requiring enzyme 1α (IRE1α), protein kinase RNA-like endoplasmic reticulum kinase (PERK) and activating transcription factor (ATF) 6, which are bound by the ER chaperone HSPA5 [GRP78; BIP] under basal conditions. Similar to the function of cytosolic HSPA [HSP70] and HSPC [HSP90] chaperones and HDAC6 in the HSR, accumulation of unfolded and misfolded proteins in the ER leads to increased interaction of HSPA5 [GRP78; BIP] with client proteins, thus promoting its dissociation from the stress sensors [37, 38].
This dissociation results in oligomerization and autophosphorylation of PERK as well as IRE1α [39]. Subsequently, PERK phosphorylates eukaryotic initiation factor-2α (eIF2α), leading to a decrease in global protein synthesis and increased expression of the transcription factor ATF4, which in turn regulates expression of genes involved in the proteostasis network [37, 38]. The activation of the RNase IRE1α on the other hand results in transcriptional as well as post-transcriptional regulation of gene expression. This is based on splicing of the transcription factor X-box binding protein 1 (XBP1) mRNA, which eventually promotes transcriptional activity, and the degradation of RNA in a process called regulated IRE1α-dependent decay (RIDD) that may serve to further reduce the protein folding load in the ER [37, 38]. The dissociation of HSPA5 [GRP78; BIP] also reveals an ER export motif of ATF6 [40], which leads to cleavage of the transcription factor by the membrane-bound transcription factor site-1 protease (S1P) and S2P in the Golgi apparatus. As a result, ATF6 becomes active and induces transcription of its target genes [37, 38].

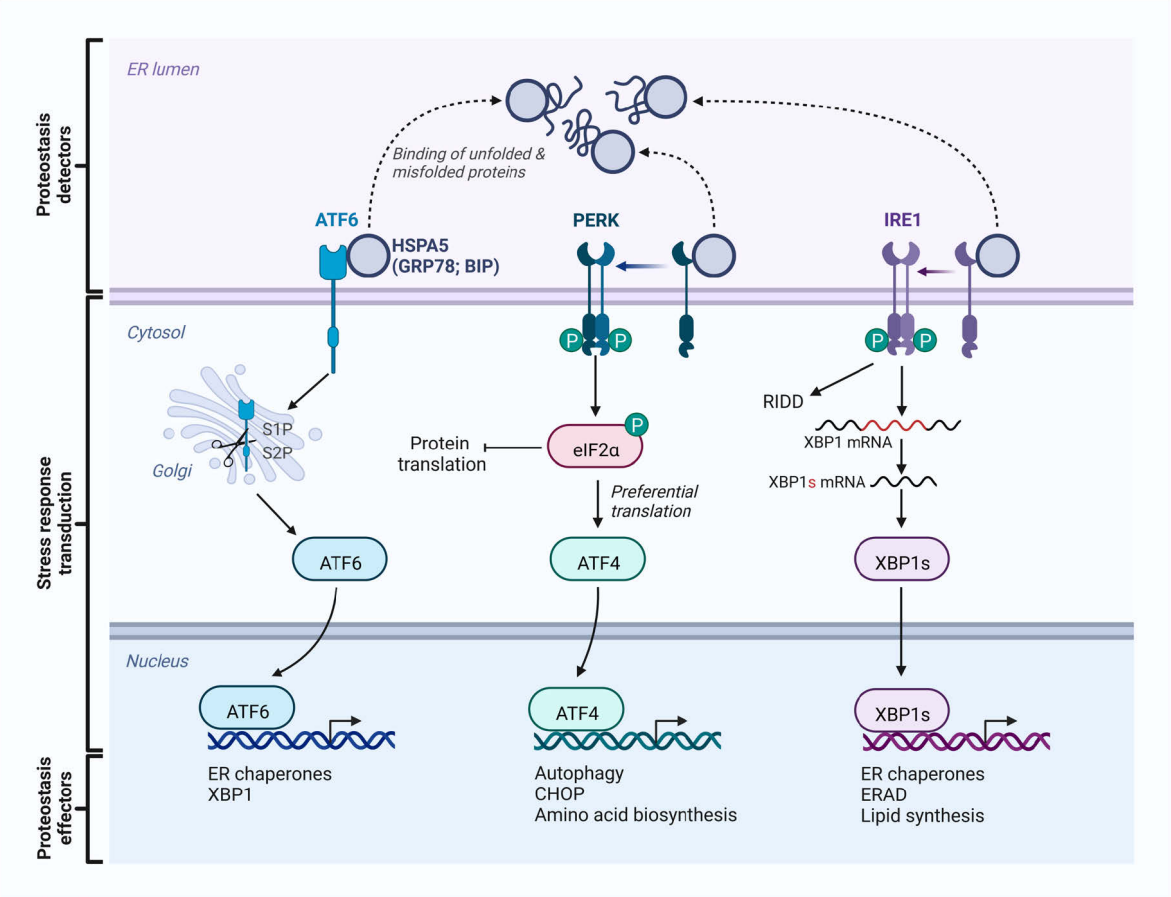

Figure 1.3 | UPR^{ER} pathway

Under basal conditions, the three ER transmembrane stress sensors IRE1α, PERK and ATF6 are bound by the ER chaperone HSPA5 [GRP78; BIP]. Accumulation of unfolded or misfolded proteins leads to interaction of HSPA5 [GRP78; BIP] with its client proteins. The dissociation reveals an ER export motif of ATF6, which results in cleavage of the transcription factor by the S1P and S2P in the Golgi apparatus. Furthermore, oligomerization and autophosphorylation of PERK as well as IRE1α is triggered. PERK decreases global protein synthesis by phosphorylation of eIF2α. Moreover, preferential translation of the transcription factor ATF4 is induced. Activation of the RNase IRE1α leads to splicing of the transcription factor XBP1 mRNA and promotes the degradation of RNA in a process called RIDD. ATF6, ATF4 and XBP1 ultimately determine cell fate by induction of gene expression to maintain ER homeostasis, such as molecular chaperones like HSPA5 [GRP78; BIP] or proteins involved in the ERAD. Termination of the UPR^{ER} is mainly mediated by PTMs of the involved transcription factors and renewed binding of the stress sensors by HSPA5 [GRP78; BIP] in a negative feedback loop. Adapted from "UPR Signaling (ATF6, PERK, IRE1)", by BioRender.com (2022). Retrieved from https://app.biorender.com/biorender-templates. ATF = activating transcription factor, eIF2α = eukaryotic initiation factor-2α, ER = endoplasmic reticulum, ERAD = ER-associated protein degradation, HSPA5 = heat shock protein A5, IRE1α = endoribonuclease inositol-requiring enzyme 1α, PERK = protein kinase RNA-like endoplasmic reticulum kinase, PTM = post-translational modification, RIDD = regulated IRE1α-dependent decay, S1P = membrane-bound transcription factor site-1 protease, UPR^{ER} = unfolded protein response of the endoplasmic reticulum, XBP1 = X-box binding protein 1.

Together, the activated transcription factors ATF6, ATF4 and XBP1 determine cell fate by induction of gene expression to maintain ER homeostasis, such as molecular chaperones like HSPA5 [GRP78; BIP] or proteins involved in the ER-associated protein degradation (ERAD), a process that transports misfolded proteins to the cytosol and mediates degradation by the UPS (Chapter 1.2.5).
Termination of the UPR^{ER} appears to occur similarly to the HSR through PTMs of the involved transcription factors and renewed binding of the stress sensors by HSPA5 [GRP78; BIP] in a negative feedback loop [41]. If ER homeostasis cannot be restored, however, the UPR^{ER} ultimately shifts signaling to the induction of apoptosis. This is partly mediated by a transcription factor downstream of ATF4, termed CCAAT/enhancer-binding protein (C/EBP) homologous protein (CHOP), which inhibits expression of the anti-apoptotic B-cell lymphoma 2 (BCL2). Moreover, additional mechanism that involve IRE1α and proapoptotic BCL2-related proteins may stimulate cell death under prolonged ER stress [30, 37, 41, 42].

1.2.4 Unfolded Protein Response of Mitochondria

The third organelle-specific stress response pathway of the proteostasis network is the unfolded protein response of mitochondria (UPR^{mt}) (Figure 1.4), which is trigged by mitochondrial accumulation of unfolded and misfolded proteins. Furthermore, several other stimuli that disrupt mitochondrial function, such as inhibition of the electron transport chain (ETC) or alterations in mitochondrial DNA (mtDNA), lead to activation of the UPR^{mt} [43, 44].

These stimuli generally result in impaired mitochondrial protein import [43, 44]. As a consequence, ATF5, a transcription factor that is normally imported into mitochondria and degraded by the mitochondrial lon protease (LONP), accumulates in the cytoplasm and subsequently becomes transcriptional active in the nucleus [43–45].
Ultimately, ATF5 induces the expression of proteins involved in mitochondrial proteostasis, such as the molecular chaperones HSPD1 [HSP60; GroEL] and HSPA9 [mtHSP70; mortalin], the mitochondrial proteases LONP, the caseinolytic protease proteolytic subunit (CLPP) or the yme1-like 1 ATPase (YME1L1) [44, 46, 47]. In addition to their function in degradation of unfolded or misfolded proteins, these proteases are further involved in maturation of proteins that regulate cellular processes like mitochondrial biogenesis [48].

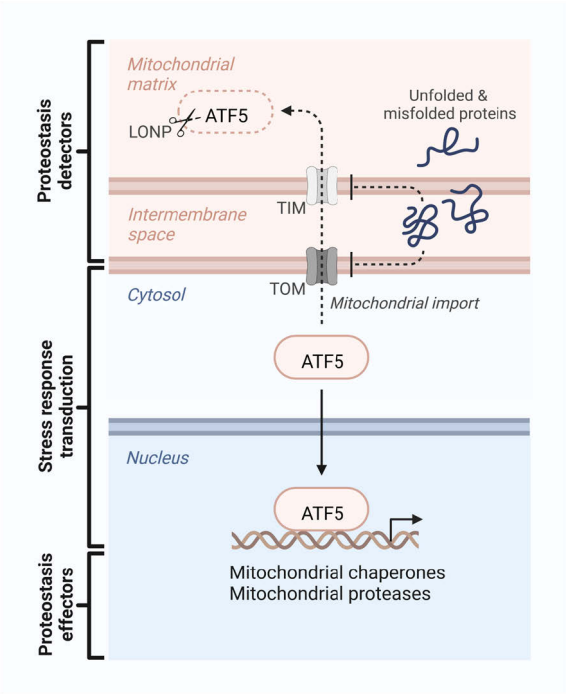

Figure 1.4 | UPR^{mt} pathway
Under basal conditions, the transcription factor ATF5 is imported into mitochondria and degraded by LONP. Accumulation of unfolded or misfolded proteins or disruption of mitochondrial function impairs mitochondrial uptake of ATF5, which consequently accumulates in the cytosol. Subsequently, the transcription factor becomes active in the nucleus, where it induces the expression of proteins involved in mitochondrial proteostasis, such as mitochondrial chaperones or mitochondrial proteases. Created with BioRender.com. ATF = activating transcription factor, LONP = lon protease, TIM = translocase of the inner membrane, TOM = translocase of the outer membrane, UPR^{mt} = unfolded protein response of mitochondria.

1.2.5 Ubiquitin-Proteasome System

Despite the contribution of molecular chaperones in assisting protein folding, proteins may fail to adopt their native state, which eventually leads to their degradation. At first, proteins can be degraded by a multitude of proteases with different substrate affinities and cleavage specificities (specific proteases for the degradation of Aβ are described in Chapter 1.4). In addition, cells evolved further pathways of protein degradation, termed the ubiquitin-proteasome system (UPS) and autophagy (Chapter 1.2.6), that involve molecular chaperones for recognition of unfolded and misfolded proteins or maintenance of a degradation-competent state [22].

The primary pathway for the degradation of individual non-aggregated substrate proteins is the cytosolic localized UPS (Figure 1.5). These substrate proteins are tagged by covalent attachment of multiple ubiquitin molecules, a highly conserved polypeptide of 76 amino acids, in a cascade involving three distinct classes of enzymes. First, ubiquitin is adenylated by ubiquitin-activating enzymes (E1). Subsequently, it is transferred to the active-site of ubiquitin-conjugating enzymes (E2). In the final step, enzymes of the ubiquitin ligases (E3) family identify the substrate proteins and catalyze the transfer of ubiquitin to an ε-NH_2 group of an internal lysine residue. Further addition of at least three ubiquitin moieties to internal lysine-48 residues on the previously conjugated ubiquitin molecules eventually serves as a degradation signal. Moreover, ubiquitination of distinct lysine residues participates in

several other cellular processes such as signal transduction [49]. Following the attachment of the polyubiquitin chain as a degradation signal, the substrate proteins are degraded by the 26S proteasome complex, composed of a 20S catalytic core particle that forms a barrel-shaped structure and two 19S regulatory particles. The proteasomal degradation is based on limited proteolysis by threonine proteases, which results in generation of free reusable ubiquitin and short peptide fragments that are further degraded by cytosolic proteases [49].

The UPS functions in concert with major cytosolic chaperones of the HSPA [HSP70] and HSPC [HSP90] families and several co-chaperones that are involved in initial recognition, tagging and docking of substrate proteins to the proteasome. Generally, a long chaperone residence time of unfolded or misfolded proteins promotes the interaction of HSPA [HSP70] and HSPC [HSP90] chaperones with co-chaperones that induce degradation, such as the carboxy terminus of HSP70-interacting protein (CHIP), which contains E3 activity and further mediates interaction with E2 [29].

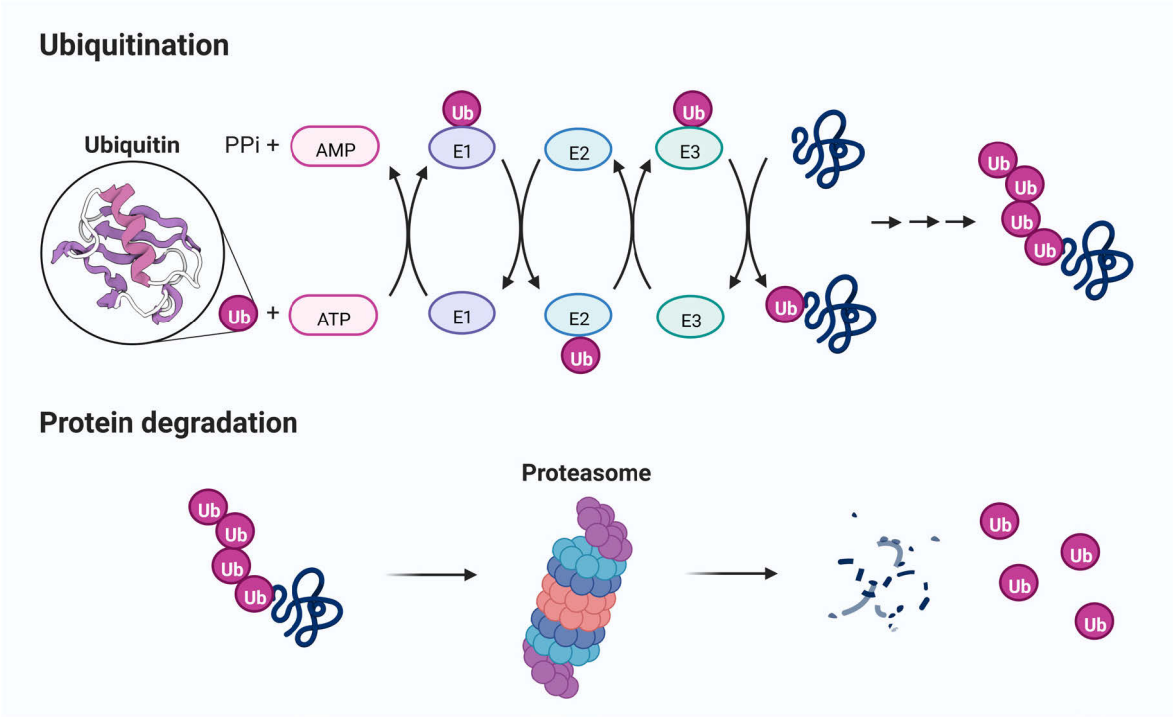

Figure 1.5 | UPS pathway

The UPS is the primary degradation pathway of individual non-aggregated substrate proteins. First, the substrate proteins are tagged by covalent attachment of at least four ubiquitin molecules through the sequential action of E1, E2 and E3. Tagged substrate proteins are subsequently degraded by the proteasome, which results in generation of free reusable ubiquitin and short peptide fragments that are further degraded by cytosolic proteases. Adapted from "Ubiquitin Proteasome System", by BioRender.com (2022). Retrieved from https://app.biorender.com/biorender-templates. AMP = adenosine monophosphate, ATP = adenosine triphosphate, E1 = ubiquitin-activating enzymes, E2 = ubiquitin-conjugating enzymes, E3 = ubiquitin ligases, PPi = pyrophosphate, Ub = ubiquitin, UPS = ubiquitin-proteasome system.

1.2.6 Autophagy

In contrast to the UPS, autophagy (from Greek: *autóphagos* - self-consuming) enables the degradation and recycling of diverse cellular material, including protein aggregates and whole organelles. It is a highly conserved and tightly regulated process involved in intracellular quality control, cellular homeostasis, cell differentiation and immunity via the removal of defective or excess cellular material. The basal activity under physiological conditions can be induced by several stress stimuli, such as starvation, dysfunctional organelles, infection or the accumulation of misfolded proteins [49–51]. Autophagy can be categorized in three major forms: macroautophagy, chaperone-mediated autophagy (CMA) and microautophagy (Figure 1.6). Although the recognition of cellular material and its lysosomal uptake differs substantially, each form ultimately leads to degradation of cellular material in lysosomes, acidic organelles that contain a large variety of cellular hydrolases, including proteases, lipases, nucleotidases and glycosidases [49, 51].

During macroautophagy, cellular material, such as protein aggregates or organelles, is enclosed by a double membrane that forms an autophagosome, which eventually undergoes fusion with a lysosome to constitute an autolysosome [49–51]. The formation, elongation and maturation of autophagosomes is mediated through orthologous proteins encoded by the autophagy-related (*ATG*) genes that were originally discovered in yeast and additional proteins that functionally interact with each other [49, 50, 52]. Furthermore, macroautophagy can function selectively or nonselectively. Nonselective macroautophagy is primarily a response to starvation that results in random engulfment of cytoplasm. In contrast, selective macroautophagy requires specific recognition of particular cargo, such as a protein complex, an organelle, or an invading microbe, in addition to the general autophagy machinery. This recognition is based on the interaction of receptor proteins resident on the cargo or adaptor proteins that contain a sequence termed microtubule-associated proteins 1A/1B light chain 3B (LC3)-interacting region (LIR) motif with proteins of the LC3 and gamma-aminobutyric acid receptor-associated protein (GABARAP) families in the autophagosomal membrane [51, 53]. Given the important role of mitophagy in AD, details on this selective autophagy of mitochondria are described in Chapter 1.3.3.2.

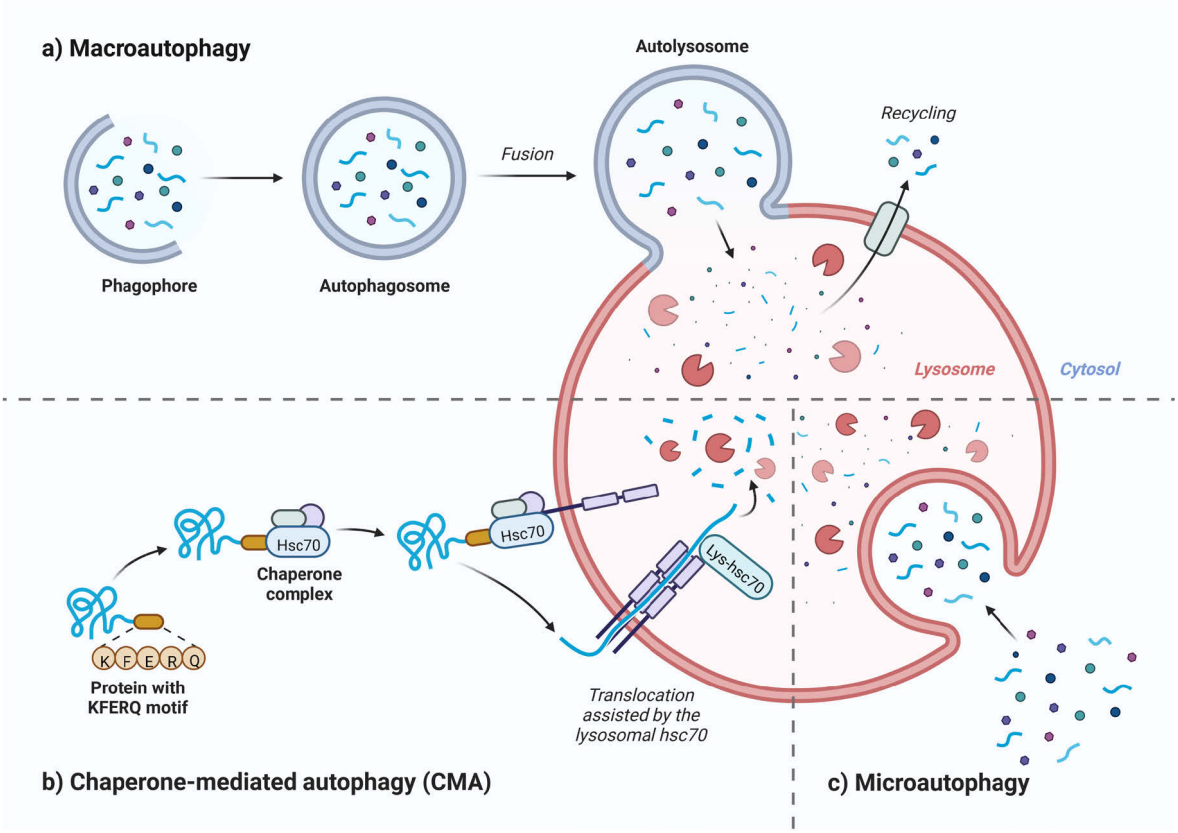

Figure 1.6 | Autophagy pathways

Autophagy can be categorized in three major forms: a) macroautophagy, b) CMA and c) microautophagy. Macroautophagy involves non-selective as well as selective enclosure of cellular material, such as protein aggregates or organelles, by a double membrane that forms an autophagosome, which eventually undergoes fusion with a lysosome to constitute an autolysosome. In contrast, CMA results in selective HSPA8 [Hsc70] mediated lysosomal uptake of individual cytosolic proteins with a KFERQ motif. Finally, microautophagy involves selective or nonselective uptake of cellular material into lysosomes, generally through an invagination or deformation of the lysosomal membrane. Adapted from "Three Main Types of Autophagy", by BioRender.com (2022). Retrieved from https://app.biorender.com/biorender-templates. CMA = chaperone-mediated autophagy, Hsc70 = heat shock cognate protein of 70 kDa.

Contrary to macroautophagy, CMA leads to selective direct uptake of individual cytosolic proteins with a consensus[2] KFERQ-like motif into lysosomes through the lysosomal-associated membrane protein 2A (LAMP2A), mediated by the molecular chaperone HSPA8 [heat shock cognate protein of 70 kDa (Hsc70)] and co-chaperones like proteins of the HSPC [HSP90] family or BCL2-associated anthogene 3 (BAG3) [51, 53, 54].

[2] A consensus sequence, also termed canonical sequence, is the calculated order of most frequent residues found at each position in a sequence alignment.

Finally, microautophagy involves selective or nonselective uptake of cellular material into lysosomes, generally through an invagination or deformation of the lysosomal membrane. Similar to macroautophagy, this process can enable degradation of protein aggregates or organelles [51, 53, 55].

1.2.7 Interconnection of the Proteostasis Network

Since pathologies associated with unfolded or misfolded proteins are rarely limited to a single cellular compartment, the stress response pathways of the proteostasis network are highly interconnected.

First, the UPR^{mt} is intimately linked to the UPR^{ER}. As described in Chapter 1.2.4, activation of the UPR^{mt} is based on impaired mitochondrial import of the transcription factor ATF5, leading to its transcriptional activity in the nucleus. A second layer of regulation, however, is based on the transcription of ATF5 itself. In response to adverse stimuli like ER stress, amino acid depletion, heme depletion or viral infection a common adaptive pathway, termed the integrated stress response (ISR), is activated. This results in phosphorylation of eIF2α and therefore a decrease in global protein synthesis as well as transcription of ATF4 and CHOP (Chapter 1.2.3), which eventually induce the expression of ATF5 [56].

Moreover, the UPR^{mt} shows a bidirectional interaction with the HSR. Mitochondrial stressors that impair the import of mitochondrial proteins lead to their cytosolic accumulation. As a consequence, these proteins may adopt non-native conformations that result in activation of the HSR [57]. Indeed, it has even been proposed that HSF1 is required for induction of mitochondrial chaperones during the UPR^{mt} [58]. On the other hand, cytosolic HSPA [HSP70] and HSPC [HSP90] chaperones are crucial for the import of mitochondrial proteins into mitochondria [59]. Cytosolic accumulation of unfolded or misfolded proteins could results in shortage of these chaperones, leading to mitochondrial dysfunction and hence induction of the UPR^{mt} due to an insufficient import of mitochondrial proteins. In addition, HSF1 activation in response to cytosolic accumulation of unfolded or misfolded proteins may induces expression of mitochondrial chaperones through interaction with the mitochondrial single-stranded DNA binding protein 1 (SSBP1) [60].

Besides its involvement in the UPR^{mt}, HSF1 further participates in the transcription of numerous other genes that are not related to the HSR, such as ER chaperones [61].

In addition to their propagation over multiple cellular compartments, pathologies associated with misfolded proteins are rarely limited to a single tissue. Recent evidence particularly derived from model organism such as *C. elegans* indicates that cellular stress response pathways may be activated cell non-autonomously by a systemic stress response through paracrine and endocrine signals that contribute to the maintenance of systemic homeostasis [30, 62]. Consequently, activation of the UPR^{mt} in neurons may leads to upregulation of mitochondrial stress responses in non-neuronal tissues. The relative importance of non-autonomous versus autonomous stress response activation and its role in mammals, however, needs to be further explored [30, 63].

1.3 Mitochondrial Homeostasis

Mitochondria are cell organelles of eukaryotes that are essential for energy metabolism and a multitude of other cellular processes, such as the production of ketone bodies (Chapter 1.6.2), the urea cycle, calcium homeostasis, apoptosis and various signal transduction pathways [64, 65]. Due to their bacterial origin, they are characterized by two functionally distinct membranes, termed the outer mitochondrial membrane (OMM) and the inner mitochondrial membrane (IMM), which are separated by an intermembrane space. This intermembrane space and the inner mitochondrial matrix form distinct aquatic compartments.

Every cell contains thousands of mitochondria, each carrying five to ten copies of circular maternally inherited mtDNA. The human mtDNA contains 16569 base pairs with 37 genes that code for 13 polypeptides of the electron transport chain (ETC), two ribosomal RNAs (rRNAs) and 22 transfer RNAs (tRNAs). In addition, mitochondrial function is dependent on over 1000 nuclear-encoded proteins. Despite this requirement for nuclear-encoded proteins, mtDNA replication is independent of the cell cycle [66].

In the following Chapter 1.3.1, the basic pathways of mitochondrial energy metabolism are described. Moreover, mitochondrial dysfunction is characterized (Chapter 1.3.2) and mitochondrial quality control pathways that counteract its detrimental effects to restore mitochondrial homeostasis are presented (Chapter 1.3.3).

1.3.1 Energy Metabolism

As the so-called “powerhouse of cells”, energy metabolism is the most defining function of mitochondria, in which their distinct membranes and compartments serve an essential role (Figure 1.7). In the cytosol, the metabolism of glucose via glycolysis results in generation of two reduction equivalents in form of reduced nicotinamide adenine dinucleotide (NADH + H^+), two ATP molecules and two pyruvate molecules. After import into the mitochondrial matrix, both pyruvate molecules can subsequently be converted into acetyl-coenzyme A (CoA), the central metabolite in energy metabolism, by oxidative decarboxylation via the pyruvate dehydrogenase (PDH) complex, generating two additional NADH + H^+ beyond those derived from glycolysis. In contrast, when oxygen is limited or within certain cell types, anaerobic glycolysis results in reduction of pyruvate to lactate by the enzymatic activity of lactate dehydrogenase, which consumes one of the reduction equivalents.

Another major source of acetyl-CoA is the fatty acid oxidation (FAO), also termed β-oxidation, which takes place primarily in the mitochondrial matrix. To this end, the majority of fatty acids (FAs) are activated through enzymatic conjugation with CoA and imported into mitochondria via the carnitine-shuttle system. During FAO, these activated FAs are progressively shortened by two-carbon atoms through a repeating sequence of four reactions that are catalyzed by the acyl-CoA dehydrogenase (ACDH), enoyl-CoA hydratase, hydroxyacyl-CoA dehydrogenase and ketoacyl-CoA thiolase. As a result, each cycle produces one molecule of reduced flavin adenine dinucleotide ($FADH_2$), NADH + H^+ and acetyl-CoA, until the carbon backbone of the FA itself is shortened to two-carbon atoms. Nevertheless, FAO might differ in some aspects based on the properties of the FAs. Complete FAO of FAs with an odd number of carbon atoms results in generation of propionyl-CoA as the final product, which is subsequently converted into succinyl-CoA, a substrate for gluconeogenesis[3] and energy metabolism. Moreover, branched-chain and very long-chain FA are initially oxidized in peroxisomes before FAO in mitochondria. Finally, the oxidation of unsaturated FA requires further enzymatic reactions to remove the double bonds [67].
In addition to glucose and FA, amino acids can enter the pathways of energy metabolism at different sites following their deamination. Due to the central function of proteins in the majority of cellular processes, however, their quantitative contribution to energy supply is particularly limited under most conditions [68].

Ultimately, the generated acetyl-CoA enters the tricarboxylic acid (TCA) cycle, also known as citric acid- and Krebs cycle, by reaction with oxalacetate (oxalacetic acid (OAA)) to the name-giving TCA citric acid. Citric acid is subsequently subjected to multiple enzymatic reactions including oxidation and partly decarboxylation through the isocitrate-, alpha-ketoglutarate (AKG)-, succinate- and malate dehydrogenase. The cycle ends with the generation of new OAA, three NADH + H^+, one $FADH_2$ and one guanosine triphosphate (GTP), which can be converted into ATP.
Furthermore, the TCA cycle generates important metabolites for the biosynthesis of nucleotides, heme, lipids, and amino acids. Since the required TCA intermediates such as OAA, citric acid and AKG leave the cycle via cataplerotic reactions, a balance with the anaplerotic

[3] Gluconeogenesis leads to the generation of glucose from non-carbohydrate carbon substrates that can be converted to pyruvate or intermediates of glycolysis. These substrates include glucogenic amino acids, glycerol, odd-chain FAs and lactate.

reactions that return carbons is essential [69]. A major anaplerotic enzyme that generates OAA from pyruvate in an ATP-dependent manner is the pyruvate carboxylase (PC) [70].

The generated reduction equivalents of glycolysis, FAO and TCA ultimately result in production of ATP via the process of oxidative phosphorylation (OXPHOS) in the ETC. The ETC involves a series of four large enzyme complexes and two mobile electron carriers that transfer electrons from electron donors to electron acceptors via redox reactions. With the exception of complex II (succinate dehydrogenase/succinate ubichinone oxidoreductase), which is attached to the inner surface of the IMM due to its function in the TCA cycle, all other complexes are located inside the membrane. Complex I (NADH ubiquinone oxidoreductase) transfers two electrons from $NADH + H^+$ to a lipid-soluble carrier called ubiquinone (Q). Additional reduced ubiquinone, also termed ubiquinol (QH_2), is generated by the action of complex II, which transfers electrons from $FADH_2$. Subsequently, the generated QH_2 freely diffuses within the IMM to complex III (cytochrome c reductase), where electrons are used to reduce cytochrome c, a water-soluble carrier located within the intermembrane space. Finally, electrons from cytochrome c are transferred to molecular oxygen by complex IV (cytochrome c oxidase), which results in the generation of water. Due to energy release during the transfer of electrons, an electrochemical proton gradient is established across the IMM. Ultimately, this proton gradient can be utilized by complex V, the ATP synthase, to generate ATP.

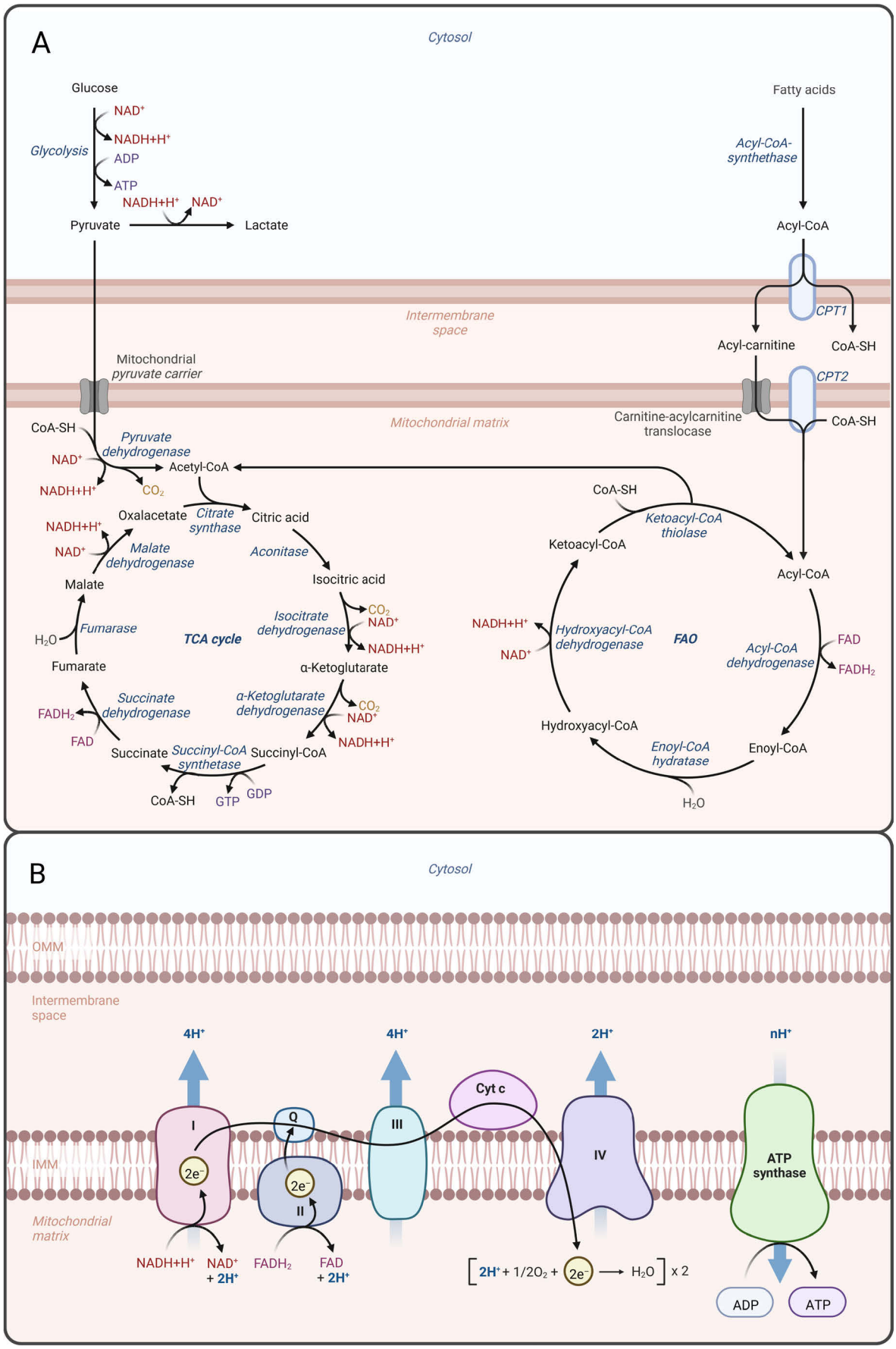
A
Cytosol
Glucose
NAD+
NADH+H+
Glycolysis
ADP
ATP
NADH+H+
NAD+
Pyruvate
Lactate
Fatty acids
Acyl-CoA-synthethase
Acyl-CoA
CPT1
Intermembrane space
Acyl-carnitine
CoA-SH
Mitochondrial pyruvate carrier
CPT2
Mitochondrial matrix
Carnitine-acylcarnitine translocase
CoA-SH
CoA-SH
Pyruvate dehydrogenase
NAD+
Acetyl-CoA
NADH+H+
CO2
Oxalacetate
Citrate synthase
Citric acid
CoA-SH
Ketoacyl-CoA thiolase
NADH+H+
NAD+
Malate dehydrogenase
Aconitase
Ketoacyl-CoA
Acyl-CoA
Malate
Isocitric acid
H2O
Fumarase
TCA cycle
Isocitrate dehydrogenase
CO2
NAD+
NADH+H+
NADH+H+
Hydroxyacyl-CoA dehydrogenase
FAO
NAD+
Acyl-CoA dehydrogenase
FAD
FADH2
Fumarate
α-Ketoglutarate
FADH2
Succinate dehydrogenase
α-Ketoglutarate dehydrogenase
CO2
NAD+
Hydroxyacyl-CoA
FAD
NADH+H+
Succinate
Succinyl-CoA synthetase
Succinyl-CoA
Enoyl-CoA hydratase
Enoyl-CoA
CoA-SH
GTP
GDP
H2O
B
Cytosol
OMM
Intermembrane space
4H+
4H+
2H+
nH+
Cyt c
I
Q
III
IV
ATP synthase
IMM
2e-
2e-
II
Mitochondrial matrix
NADH+H+
NAD+ + 2H+
FADH2
FAD + 2H+
[2H+ + 1/2O2 + 2e- → H2O] x 2
ADP
ATP

Figure 1.7 | Energy metabolism

The distinct membranes and compartments of mitochondria serve an essential role in energy metabolism. (A) Following aerobic glycolysis in the cytosol, pyruvate is transported into mitochondria, in which it is oxidative decarboxylated to acetyl-CoA, the central metabolite in energy metabolism. Another major source of acetyl-CoA is the FAO, which also takes place primarily in the mitochondrial matrix. During FAO, activated FAs are progressively shortened by two-carbon atoms through a repeating sequence of four enzymatic reactions, resulting in the generation of acetyl-CoA. Ultimately, acetyl-CoA enters the TCA cycle through reaction with OAA to the name-giving TCA citric acid. Citric acid is subsequently subjected to multiple enzymatic reactions including oxidation and partly decarboxylation, which finally restores OAA. Whereas some of these reactions involved in energy metabolism directly produce ATP, most generate reduction equivalents in the form of $NADH+H^+$ and $FADH_2$ (B) The reduction equivalents generated in energy metabolism ultimately result in production of ATP via the process of OXPHOS in the ETC. The ETC involves a series of four large enzyme complexes and two mobile electron carriers that transfer electrons from electron donors to electron acceptors via redox reactions. Finally, electrons are transferred to molecular oxygen, leading to the generation of water. Due to energy release during the transfer of electrons, an electrochemical proton gradient is established across the IMM. Ultimately, this proton gradient can be utilized to generate ATP. (A) Created with BioRender.com. (B) Adapted from "Electron Transport Chain", by BioRender.com (2022). Retrieved from https://app.biorender.com/biorender-templates. CPT = carnitine palmitoyltransferase, Cyt C = cytochrome C, ETC = electron transport chain, FAO = fatty acid oxidation; β-oxidation, IMM = inner mitochondrial membrane, OAA = oxalacetate/ oxalacetic acid, OXPHOS = oxidative phosphorylation, TCA = tricarboxylic acid, Q = ubiquinone, I = NADH ubiquinone oxidoreductase, II = succinate dehydrogenase/succinate ubichinone oxidoreductase, III = cytochrome c reductase, IV = cytochrome c oxidase.

Several factors such as the utilization of the reduction equivalents at different ETC complexes, energy costs for mitochondrial import of cytosolic $NADH + H^+$ generated by glycolysis, inefficiencies of the oxidative phosphorylation due to leakage of protons across the IMM and proton slippage of the ATP synthase determine the ATP generation in the ETC. Considering these factors, oxidation of 1 mol $NADH + H^+$ approximately leads to generation of approximately 2.5 mol ATP. In contrast, given the low difference of redox potential between complex II and Q and the consequent lack of proton transfer, 1 mol $FADH_2$ only provides around 1.5 mol ATP.

According to the description above, the oxidation of FAs generally produces substantially more energy than glucose. Based on the lower energy yield of $FADH_2$, however, energy metabolism of FAs consequently requires slightly more oxygen in relation to the generated ATP due to equal production of $NADH + H^+$ and $FADH_2$ by FAO.

The consumption of oxygen liberates a number of products termed reactive oxygen species (ROS). In fact, mitochondrial energy metabolism is the main source of endogenous ROS due to defective electron transfers that particularly occur at complex I and III of the ETC [69,

71]. Since mitochondrial dysfunction, characterized among other features by increased generation ROS, is a major pathological feature of AD, a brief description is provided in the next Chapter 1.3.2.

1.3.2 Mitochondrial Dysfunction

Due to their central role in a multitude of cellular processes, mitochondrial dysfunction is involved in the pathogenesis of numerous diseases (see Chapter 1.4 for the involvement in AD). Although mitochondrial dysfunction can manifest in different ways, the molecular basis is generally characterized by impaired ATP generation, a reduced mitochondrial membrane potential (MMP) and increased levels of ROS [72].

Under physiological conditions, ROS levels are counterbalanced by the cellular antioxidative system, composed of antioxidative enzymes and water- as well as lipid soluble antioxidants. Key determinants regulating antioxidant capacity include the transcription factor nuclear factor erythroid-2-related factor 2 (NRF2) and members of the forkhead box O (FOXO) transcription factor family.
The transcriptional activity of NRF2 is negatively regulated by its cytoplasmic repressor Kelch-like ECH associated protein 1 (KEAP1), which serves as an adaptor to mediate ubiquitination and degradation of NRF2. In the presence of electrophiles or ROS, NRF2 is released and translocated into the nucleus, where it binds to promoter sequences containing conserved antioxidant response elements (AREs). Subsequently, NRF2 induces the expression of antioxidative enzymes, such as superoxide dismutase (SOD), glutathione peroxidase (GPX) and catalase. NRF2 further regulates expression of proteins involved in xenobiotic metabolism and mitochondrial biogenesis (Chapter 1.3.3.3) [73, 74].
The family of FOXO transcription factors consists of four members, which regulate expression of genes that are involved in many cellular processes, including cell cycle regulation, metabolism and antioxidative defense. FOXO activity is negatively regulated by the insulin signaling pathway through phosphatidylinositol 3-kinase (PI3K) and protein kinase B (PKB), also known as AKT. Positive regulation is mediated by ROS via the c-Jun N-terminal kinase (JNK) signaling that eventually leads to nuclear translocation and transcriptional activity through binding to forkhead-responsive elements (FHREs) [75, 76].

However, the cellular antioxidative capacity can become overloaded as a result of excessive ROS generation, leading to a condition termed oxidative stress. Excessive ROS may induce extensive oxidation of macromolecules, which results in functional loss or toxicity. These potential harmful effects of ROS are especially prominent in mitochondria, substantiating the radical theory of aging, which states that increased ROS formation and damage to mitochondrial macromolecules, such as mtDNA or proteins, amplify each other in a vicious cycle [66].

1.3.3 Mitochondrial Quality Control

To maintain mitochondrial homeostasis, eukaryotes developed a complex system of mitochondrial quality control that also involves pathways of the proteostasis network (Chapter 1.2). At the molecular level, unfolded or misfolded mitochondrial proteins can be degraded by mitochondrial proteases or refolded by molecular chaperones. Moreover, the UPS may degrade damaged mitochondrial proteins of the OMM via mitochondrial-associated degradation (MAD). Mitochondrial proteins and oxidized lipids can further be enveloped by mitochondrial-derived vesicles (MDVs) and transported to lysosomes or peroxisomes for their breakdown [48, 59, 77].

At the organelle level, mitochondria form a morphologically dynamic network through the opposing processes of fission and fusion, which enables redistribution of functional and dysfunctional mitochondrial components. Finally, dysfunctional mitochondria can be degraded by selective autophagy, termed mitophagy [77]. In the following, the mechanisms of fission, fusion and mitophagy (Chapter 1.3.3.1 & 1.3.3.2) as well as their interconnectivity (Chapter 1.3.3.3) are explained in detail.

1.3.3.1 Mitochondrial Fission and Fusion

Through the opposing action of mitochondrial fission and fusion, which are also referred to as mitochondrial dynamics, mitochondrial components are constantly redistributed between organelles to maintain a functional population of mitochondria (Figure 1.8).

By segregating dysfunctional mitochondria, mitochondrial fission mediates the isolation of damaged components. This process is dependent on the cytosolic GTPase dynamin-related

protein 1 (DRP1), which can be recruited to the OMM and catalyze the constriction and subsequent fission of mitochondria into two daughter organelles [78]. Various proteins of the OMM are thought to be involved in the recruitment process. Accordingly, mitochondrial fission 1 protein (FIS1), mitochondrial fission factor (MFF) and mitochondrial dynamics proteins of 49 kDa (MID49) as well as 51 kDa (MID51) have previously been identified as receptors for DRP1 (Palmer et al., 2011; Losón et al., 2013). The activity and cellular localization of DRP1 is further regulated by various PTMs such as S-nitrosylation, phosphorylation, ubiquitination, and sumoylation [78].

In contrast, mitochondrial fusion enables dilution of damaged mitochondrial components by merging dysfunctional mitochondria with functional organelles [78]. This process is induced by the GTPases mitofusin (MFN) 1 and MFN2, which mediate fusion of the OMM of two mitochondria. Subsequently, the fusion of the IMM is accomplished by the GTPase optic atrophy 1 (OPA1) [78]. The regulation of mitochondrial fusion also occurs via PTMs. MFN1 and MFN2 are particularly regulated by phosphorylation and ubiquitination. In contrast, the modification of OPA1 is based on proteolytic cleavage [79].

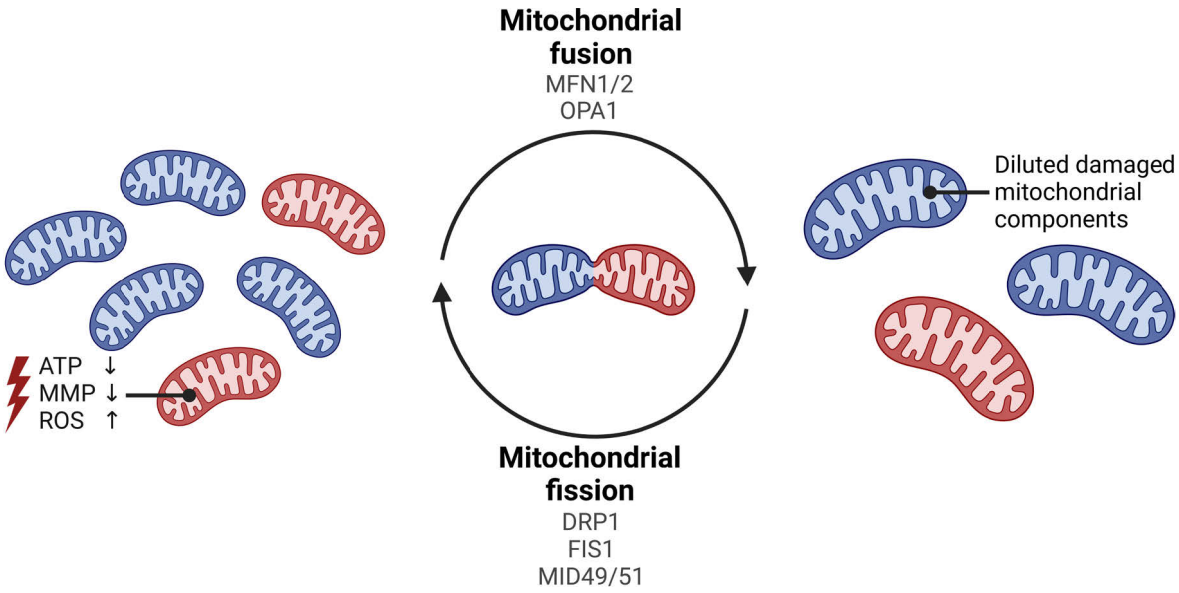

Figure 1.8 | Mitochondrial dynamics

The opposing processes of mitochondrial fission and fusion aid to maintain a functional population of mitochondria. Mitochondrial fission results in isolation of damaged mitochondrial components through segregation of dysfunctional mitochondria. In contrast, fusion of mitochondria enables dilution of damaged mitochondrial components by merging dysfunctional mitochondria with functional organelles. Created with BioRender.com. ATP = adenosine triphosphate, DRP1 = dynamin-related protein 1, FIS1 = mitochondrial fission 1 protein, MID49/51 = mitochondrial dynamics proteins of 49 and 51 kDA, MMP = mitochondrial membrane potential, OPA1 = optic atrophy 1, ROS = reactive oxygen species.

1.3.3.2 Mitophagy

Mitophagy is the selective degradation of dysfunctional or excess mitochondria via macroautophagy (Chapter 1.2.6). The recognition of mitochondria represents the decisive step of selectivity that is dependent on the action of specific factors. In contrast, the following steps of autophagosome formation, retrograde transport, fusion with lysosomes and lysosomal digestion require the general machinery of autophagy [80]. Since an impaired MMP is a characteristic of dysfunctional mitochondria, depolarization of mitochondria is a central driving force for mitophagy [81, 82]. Generally, two pathways termed receptor-mediated mitophagy and PTEN-induced putative kinase 1 (PINK1)/parkin-mediated mitophagy are distinguished due to different mechanisms of mitochondrial recognition by autophagosomes (Figure 1.9).

Receptor-mediated mitophagy is based on the activation of specific receptors that contain a LIR motif that interacts with LC3 or GABARAP family proteins in the autophagosomal membrane, leading to mitochondrial engulfment by autophagosomes [53, 80].
The receptors are mainly proteins of the OMM such as BCL2/adenovirus E1B 19 kDa protein-interacting protein 3 (BNIP3), Nip3-like protein X (NIX), also called BNIP3L, FUN14 domain containing 1 (FUNDC1) and BCL2 like protein 13 (BCL2L13). They are typically regulated by stress-dependent phosphorylation through kinases such as unc-51 like autophagy activating kinase 1 (ULK1), an enzyme also essential for autophagosome formation, which increases the affinity for interaction with LC3 or GABARAP family proteins [80]. FUNDC1 is additionally regulated by the casein kinase 2 (CK2) and the phosphatase phosphoglycerate-mutase 5 (PGAM5). Phosphorylation by CK2 leads to deactivation of FUNDC1, which is reversed via dephosphorylation by PGAM5 [83]. Contrary to the aforementioned mitophagy receptors, the OMM protein FK506-binding protein 8 (FKBP8) is thought to be regulated independent of interconversion due to the lack of phosphorylatable residues near the LIR [84].
In addition to OMM proteins, the IMM protein prohibitin 2 was found to act as a mitophagy receptors following OMM disruption [85]. Moreover, the phospholipids cardiolipin and ceramide may also function as mitophagy receptors, which likely involves specific binding sites of LC3 family proteins [86, 87]. Finally, additional mitophagy receptors such as SMAD ubiquitination regulatory factor 1 (SMURF1) and activating molecule in beclin-1-regulated autophagy (AMBRA1) were identified, but their physiological function needs to be further elucidated [80].

Compared with receptor-mediated mitophagy, the pathway of PINK1/Parkin-mediated mitophagy is considerably more complex. The induction of this pathway is dependent on the kinase PINK1, which is integrated into the IMM and subsequently degraded under physiological conditions. In the case of mitochondrial dysfunction with impaired MMP, the transport process is disrupted and PINK1 accumulates in the OMM. This accumulation results in the activation of PINK1 through dimerization followed by autophosphorylation [80]. As a consequence of PINK1 activation, the autoinhibitory state of the cytosolic E3 ubiquitin ligase Parkin is released by phosphorylation of serine 65 in its ubiquitin-like domain (UBL). Furthermore, PINK1 phosphorylates serine 65 of ubiquitinated OMM proteins, recruiting additional Parkin molecules to damaged mitochondria for their activation by PINK1. Parkin activation in turn leads to polyubiquitination of OMM proteins, which are subsequently phosphorylated by PINK1. Thus, PINK1 and Parkin interact in a feed-forward mechanism to generate phospho-polyubiquitinated OMM proteins that ultimately serve as recruitment sites for specific adapter proteins [80, 88].
These adaptor proteins act as mitophagy receptors and link polyubiquitinated OMM proteins to proteins of the LC3 or GABARAP families via their ubiquitin-binding-domain (UBD) as well as LIR motif and can thus lead to mitochondrial engulfment by autophagosomes [80]. Accordingly, this is in clear contrast to receptor-mediated mitophagy, in which mitochondrial receptors are directly linked to these autophagosomal membrane proteins. Among the known adaptor proteins that recognize polyubiquitinated proteins, nuclear dot protein 52 kDa (NDP52) and optineurin (OPTN) appear to be the primary receptors for PINK1/Parkin-mediated mitophagy [89]. The remaining receptors tax1-binding protein 1 (TAX1BP1), neighbor of BRCA1 gene 1 (NBR1) and ubiquitin-binding protein P62 (P62), also termed sequestosome-1 (SQSTM1) are thought to have redundant functions and could be recruited to distinct cell types under different physiological and pathophysiological conditions [90].

It was further shown that Parkin is dispensable for the recruitment of these adaptor proteins. The phosphorylation of polyubiquitin chains on OMM proteins by PINK1 may consequently be the essential signal for the induction of mitophagy, which is only amplified by Parkin [89]. However, polyubiquitination of OMM proteins may also occur through other E3 ubiquitin ligases, such as seven in absentia homolog 1 (SIAH1), in a PINK1-dependent manner [91, 92].
PINK1/Parkin-mediated mitophagy is regulated at multiple levels within the signaling pathway. Parkin, like other ubiquitin ligases, is subject to regulation through autoubiquitination.

The resulting inactivation of Parkin can be abrogated by ubiquitin-specific protease (USP) 8 [93]. In addition, USP15, USP30, and USP35 can counteract the feed-forward mechanism of PINK1 and Parkin via deubiquitination of OMM proteins [94, 95]. As another means of regulation, the affinity of adapter proteins for polyubiquitin can be increased via phosphorylation by TANK-binding kinase 1 (TBK1) [96].

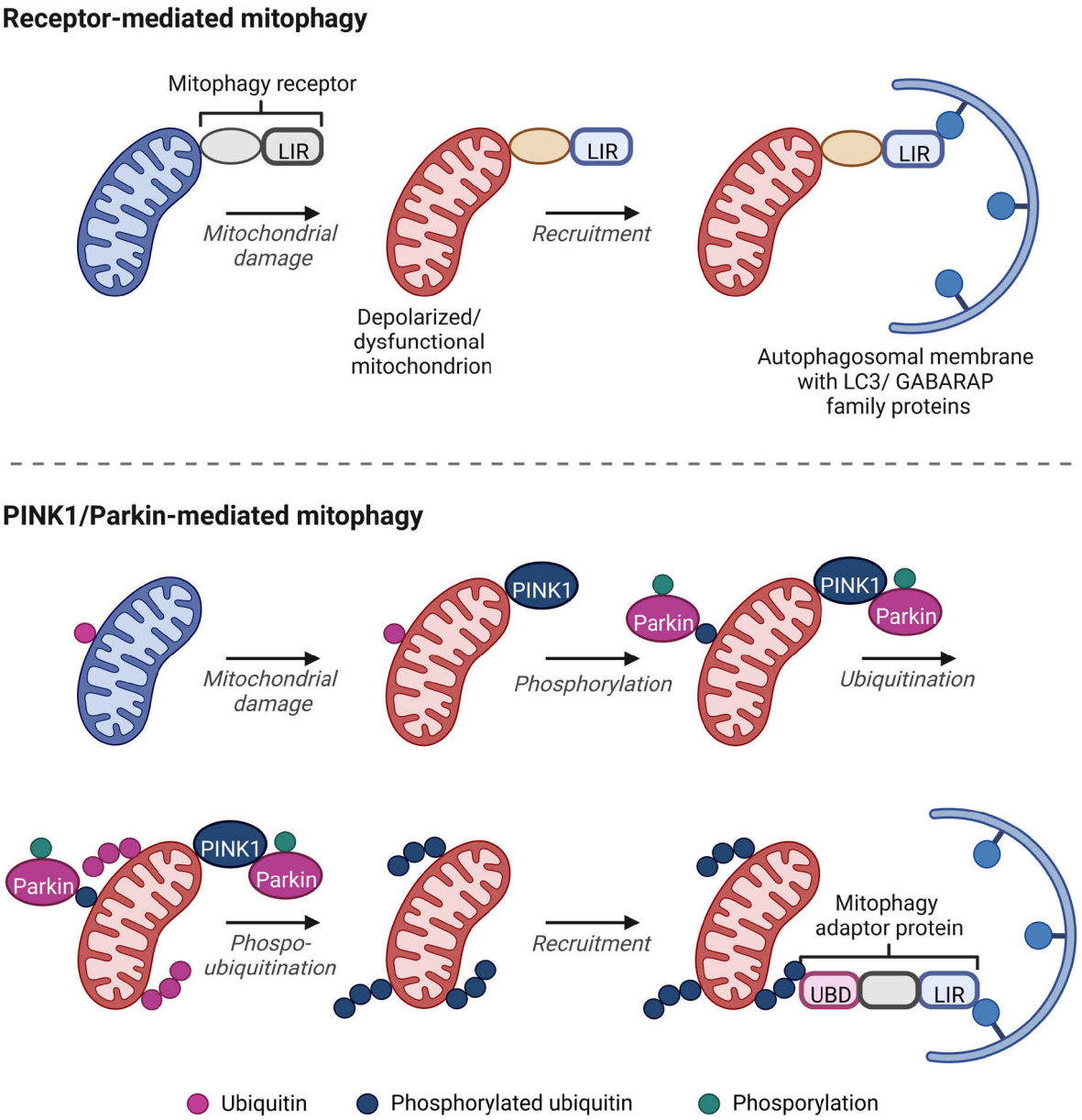

Figure 1.9 | Mitophagy pathways

Receptor-mediated mitophagy is based on the activation of specific receptors, which generally contain a LIR motif that interacts with LC3 or GABARAP family proteins in the autophagosomal membrane, leading to mitochondrial engulfment by autophagosomes. In contrast, PINK1/Parkin-mediated mitophagy is a multi-step process that is based on stabilisation and activation of the kinase PINK1, which phosphorylates ubiquitinated OMM proteins and the cytosolic E3 ubiquitin ligase Parkin. This results in Parkin recruitment as well as activation and eventually leads to polyubiquitination of OMM proteins, which are also phosphorylated by PINK1.

Thus, PINK1 and Parkin cooperate in a feed-forward mechanism to generate phospho-polyubiquitinated OMM proteins that ultimately serve as recruitment sites for specific adaptor proteins, which connect mitochondria to autophagosomes through their UBD and LIR-motif. Adapted from [52]. Created with BioRender.com. GABARAP = gamma-aminobutyric acid receptor-associated protein, LIR = LC3-interacting region, PINK1 = PTEN-induced putative kinase 1, UBD = ubiquitin-binding-domain.

Although a multitude of studies explored mitophagy, the stimuli that activate the different pathways and involved proteins are mostly unclear. Nevertheless, it appears that different mitophagy mechanisms are involved in the response to specific mitochondrial stresses such as hypoxia and uncoupling of the ETC or fulfill specific functions during processes like the maturation of reticulocytes or differentiation of retinal ganglion cells [97–99]. In response to acute mitochondrial stresses, particularly PINK1/Parkin-mediated mitophagy appears to be of great importance [98]. However, plenty of evidence is based on triggering mitophagy using harsh depolarizing agents like protonophores or OXPHOS inhibitors that poorly mimic physiological or even pathophysiological situations. Moreover, the relevant mitophagy pathways could vary in biological relevance depending on the cell type. Consequently, the importance of different mitophagy mechanisms *in vivo* needs to be further elucidated [48].

1.3.3.3 Interconnection of the Mitochondrial Quality Control

The mitochondrial quality control at the organelle level is subject to a complex interplay of the involved processes, which ultimately serves to maintain mitochondrial homeostasis.
First, several studies have suggested that different mitophagy pathways are potentially interdependent. Prohibitin 2, a protein resident in the IMM, was shown to function as a mitophagy receptor following the breakdown of the OMM by PINK1/Parkin-mediated mitophagy [85]. Moreover, BNIP3-induced mitophagy was reduced in parkin-deficient cells [100]. BNIP3 in turn may stabilizes PINK1 and thus reduces its degradation via the proteasome [101, 102]. In addition, the mitophagy receptor NIX was shown to participate in the translocation of parkin in reaction to mitochondrial depolarization [98].

Furthermore, mitophagy is essentially interconnected to mitochondrial dynamics. Since mitochondrial fission is coupled with a loss of MMP [81, 82] and may facilitate engulfment of mitochondrial fragments by autophagosomes of limited size [103], it has been proposed to promote mitophagy. Accordingly, inhibition of DRP1-mediated fission resulted in suppression of PINK1/Parkin- and receptor-mediated mitophagy [100, 104]. Conversely,

PINK1/Parkin-mediated mitophagy was found to promote the degradation of MFN1 as well as MFN2 that are essential for fusion of the OMM [104, 105]. Additionally, translocation of DRP1 to mitochondria may be promoted by receptor-mediated mitophagy via BNIP3 [100]. Mutual enhancement of fission and mitophagy with a concurrent suppression of mitochondrial fusion thus appears to be of importance for mitochondrial quality control. However, it has been suggested that fission is not essential for induction of mitophagy, since isolation of damaged mitochondrial part can also occur using the autophagy machinery independent of DRP1 [48, 82, 92, 106]. Moreover, whereas its physiological role is still unclear, a novel form of mitophagy that is initiated by Syntaxin 17 (STX17) following loss of FIS1 was described. This STX17-induced mitophagy was further independent of DRP1, thereby enabling even the degradation of hyperfused mitochondria [107].

In addition, mitochondrial quality control is linked to mitochondrial transport. This is necessary, on the one hand, for the distribution of mitochondria to positions with increased demand for energy as well as calcium buffer capacity and, on the other hand, for the degradation of dysfunctional mitochondria. Transport occurs via an ATP-dependent mechanism through motor proteins, some of which migrate along microtubules via interaction with adaptor proteins [78]. For example, PINK1/Parkin-mediated mitophagy was found to alter mitochondrial transport by promoting degradation of the motor protein Miro, which may ultimately serve to quarantine damaged mitochondria [108].

Finally, mitophagy was found to stimulate mitochondrial biogenesis. The coordination of these opposing processes aims to secure a quantitative functional population of mitochondria and allows adaptation to different metabolic states or stress stimuli [77]. As mitochondria cannot be generated *de novo*, mitochondrial biogenesis is based on growth and division of pre-existing mitochondria. The master regulator of mitochondrial biogenesis is the transcription factor peroxisome proliferator-activated receptor-γ (PPARγ) coactivator-1α (PGC1α), which further integrates and coordinates the activity of the transcription factors nuclear respiratory factor 1 (NRF1), NRF2 and the mitochondrial transcription factor A (TFAM). This coordinated transcriptional activity ultimately leads to replication of mtDNA, expression and correct mitochondrial integration of mtDNA- and nuclear DNA-encoded proteins as well as integration of phospholipids [109–111].

1.4 Proteostasis and Mitochondrial Homeostasis in Alzheimer's Disease

Since age is the major risk factor of sporadic AD, the pathogenesis is intimately linked to the functional decline of cellular processes during aging. These processes include cellular quality control systems like the proteostasis network and the mitochondrial quality control, which appear to be progressively disturbed on multiple levels, consequently promoting susceptibility to the accumulation of unfolded or misfolded proteins and dysfunctional mitochondria [25, 49, 112].

This functional decline of cellular processes is particularly detrimental for the brain. It requires a disproportionate 20% of the resting body's energy demand, despite accounting for only 2% of body mass [113–115]. In addition to its high demand for oxygen, the brain contains elevated amounts of peroxidizable polyunsaturated fatty acids, a high concentration of iron that may promote ROS formation and a relatively low antioxidative capacity, which renders it vulnerable to oxidative stress [116]. Furthermore, brain mitochondria fulfill essential functions in every step of neurotransmission, leaving this essential process prone to mitochondrial dysfunction [117].
Of the different cell types in the brain, neurons are considered the most vulnerable. They are post-mitotic cells, which prevents cellular waste, such as damaged proteins or organelles, from being diluted by cell division [118]. Neurons are further characterized by a highly polarized morphology with synapses generally located far away from the neuronal cell soma, requiring coordinated intracellular transport of molecules and organelles to their destined locations [119]. Moreover, neurons contribute up to 85% of the brain's energy demand due to their synaptic activity [114]. Finally, adult neurogenesis is limited and only occurs in the dentate gyrus of the hippocampus and subventricular zone of the lateral ventricle, hindering the replacement of degenerated neurons by new cells.

The vulnerability of neurons is further amplified in the pathogenesis of AD. Mechanistically, Aβ was shown to interfere with the proteostasis network on several levels. A fraction of Aβ is degraded by proteases termed Aβ degrading enzymes, such as neprilysin (NEP) or insulin-degrading enzyme (IDE), which differ in their localization and specificity towards aggregation states [120]. However, evidence suggests that these enzymes operate at or near their functional capacity in AD [121]. Furthermore, degradation of monomeric Aβ and low-molecular weight Aβ oligomers appears to be mediated predominantly by the UPS, whereas

autophagy enables the removal of higher molecular weight aggregates [122, 123]. Several studies, however, have shown that both degradation pathways are functionally impaired in AD, which may result as a consequence of Aβ proteotoxicity [49, 118]. Thus, protein degradation is progressively overloaded during AD pathogenesis, as evidenced by accumulation of Aβ aggregates as well as of autophagosomes and lysosomes with undegraded cellular material [49, 124]. The impairment of Aβ degradation by its own proteotoxicity therefore promotes a vicious cycle that further advances AD pathogenesis [49, 122].

In addition to its effects on the proteostasis network, a multitude of studies demonstrated that Aβ disrupts mitochondrial function. Aβ accumulates in mitochondria through different pathways. Following import or diffusion of secreted Aβ into cells or intracellular formation (Chapter 1.1.2), Aβ can accumulate in the OMM, the IMM and the mitochondrial matrix via translocase of the outer membrane (TOM)- and translocase of the inner membrane (TIM)-dependent transport [125]. Moreover, Aβ may also be taken up across the mitochondria-associated ER membrane (MAM) [126].
Within mitochondria, Aβ potentially disrupts the import of nuclear-encoded mitochondrial proteins. Aβ was further shown to impair the activity of the ETC complex IV as well as of several enzymes in the mitochondrial matrix, such as PDH and AKG dehydrogenase (AKG-DH) [125]. Additionally, binding of Aβ to cyclophilin D (CYPD) may promote the translocation of CYPD to the IMM, potentially leading to the formation of the mitochondrial permeability-transition pore (MPTP), an important trigger of apoptosis. As another factor, Aβ was demonstrated to inhibit the activity of Aβ peptide alcohol dehydrogenase (ABAD), which exhibits a cytoprotective role via detoxification of reactive aldehydes such as 4-hydroxy-2-nonenal (4-HNE) [127, 128].
Beyond direct impairment of mitochondrial function, disruption of mitochondrial quality control has been demonstrated by a growing body of evidence. It appears contradictory that Aβ was found to promote mitochondrial fission [90], which is generally associated with induction of mitophagy (Chapter 1.3.3.3). On the contrary, impaired mitophagy has been shown in cellular and animal AD models as well as in AD patients [129, 130]. This imbalance of excessive mitochondrial fission and inadequate mitophagy may finally promote the accumulation of fragmented dysfunctional mitochondria.
Accordingly, defective mitochondria with altered morphology, decreased energy metabolism, breakdown of the MMP and increased markers of oxidative stress have been demonstrated in the brains of AD patients [116, 127, 130, 131]. In terms of energy metabolism,

particularly metabolism of glucose, the major energy source of neurons, seems to be disrupted as a result of impaired glycolysis, PDH as well as complex I activity during aging and AD pathogenesis [72, 125, 132, 133]. In addition to the already described detrimental effects of excessive ROS on mitochondrial function (Chapter 1.3.2), they were further shown to promote the accumulation of Aβ [131, 134]. For instance, ROS have been reported to induce the expression and activity of BACE1, potentially promoting the formation of Aβ via the amyloidogenic pathway of APP processing [131] (Chapter 1.1.1). Furthermore, they can lead to decreased activity of the redox-sensitive presequence protease (PreP), which is localized in the mitochondrial matrix and functions as an Aβ degrading enzyme [134]. Although not evidenced, it is also plausible that impaired ATP generation and excessive ROS may exert additional stress on the proteostasis network, due to decreased function of ATP-dependent molecular chaperones and increased oxidative damage to proteins.

Although their temporal relationship is a matter of debate, the presented evidence clearly indicates that Aβ proteotoxicity and mitochondrial dysfunction reinforce each other in a vicious cycle that ultimately results in the impairment of neurotransmission and eventually neurodegeneration [135] (Figure 1.10). The failure of cellular quality control systems combined with irreversible neurodegeneration that generally widely progresses before diagnosis, substantiates the search for preventive therapies (Chapter 1.1). Consequently, timely intervention in Aβ proteotoxicity, mitochondrial dysfunction or cellular quality control systems could positively influence multiple facets of the complex pathomechanism and potentially delay or partially prevent irreversible damage.

As a prerequisite for their preventive use in AD, potential interventions are ideally bioavailable following oral administration, able to pass the blood-brain barrier (BBB) and safe for long term usage. Since the aromatic short-chain FA (SCFA) 4-phenylbutyric acid (4-PBA) and the saturated medium-chain FA (MCFA) caprylic acid (CA) both meet these requirements and may act on several levels to improve proteostasis as well as mitochondrial homeostasis (Chapter 1.5&1.6), this work investigated their molecular effects using an AD model of the nematode *Caenorhabditis elegans*.

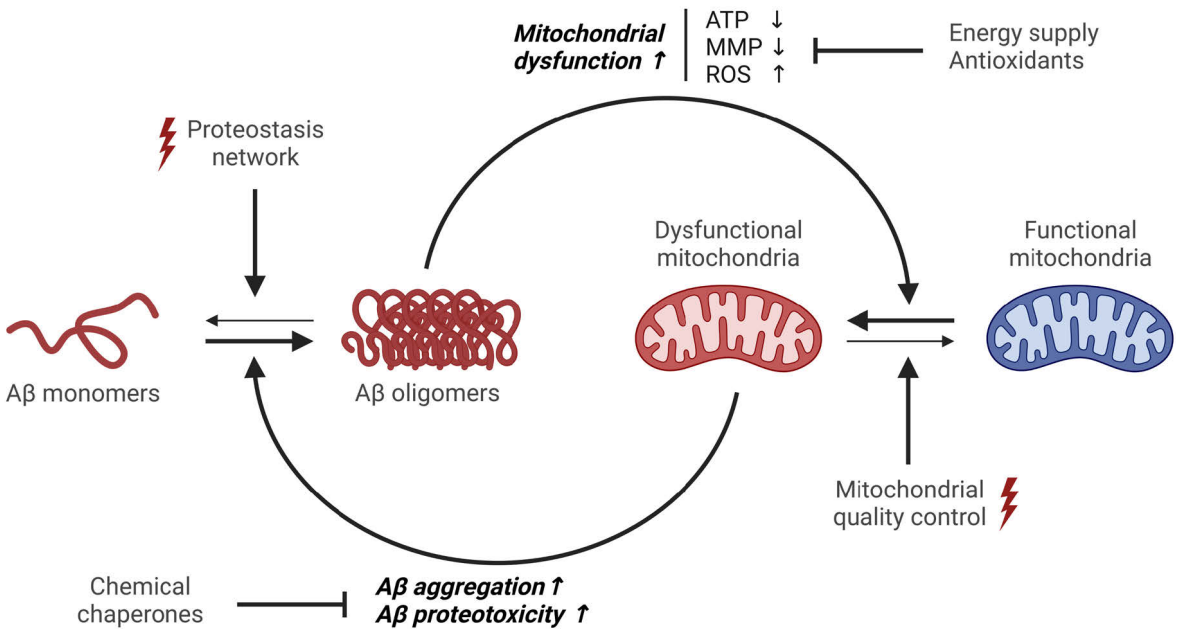

Figure 1.10 | Schematic illustration showing the vicious cycle of Aβ proteotoxicity and mitochondrial dysfunction in AD

AD pathogenesis is characterized by Aβ proteotoxicity and mitochondrial dysfunction, which mutually aggravate each other in a vicious cycle. Whereas the proteostasis network and the mitochondrial quality control evolved to maintain homeostasis, their function is disturbed in AD. The failure of cellular quality control systems combined with irreversible neurodegeneration that generally widely progresses before diagnosis, substantiates the search for preventive therapies. Timely intervention in Aβ proteotoxicity, mitochondrial dysfunction or cellular quality control systems could thus positively influence multiple facets of the complex pathomechanism and potentially delay or partially prevent irreversible damage. Created with BioRender.com. Aβ = amyloid-β, ATP = adenosine triphosphate, MMP = mitochondrial membrane potential, ROS = reactive oxygen species.

1.5 4-Phenylbutyric Acid

4-Phenylbutyric acid (4-PBA) (Figure 1.11) is an orally bioavailable aromatic short-chain fatty acid (SCFA) approved for the treatment of urea cycle disorders. Its mechanism of action as an ammonia scavenger is based on FAO to phenylacetic acid (PAA), which is subsequently conjugated with glutamine. The resulting water-soluble phenylacetylglutamine is finally excreted by the kidney to eliminate excess ammonia [136, 137].

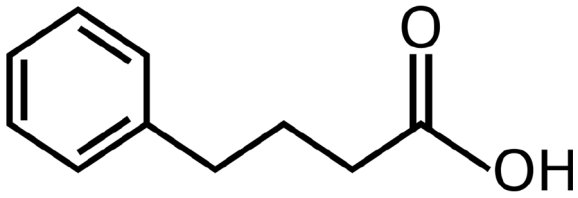

Figure 1.11 | Chemical structure of 4-PBA

In addition to its function as an ammonia scavenger, evidence suggests that 4-PBA further acts as a chemical chaperone (Chapter 1.5.1) and a weak inhibitor of histone deacetylases (HDACs) (Chapter 1.5.2), which may both have positive effects on AD pathogenesis [136, 137]. Moreover, energy supply through FAO of 4-PBA could partially compensate the energetic deficit in AD, consequently circumventing impaired glucose metabolism. Finally, as a prerequisite for its use in AD, 4-PBA and its metabolite PAA have been shown to readily cross the BBB [138].

1.5.1 Chemical Chaperones

In analogy to the function of molecular chaperones (Chapter 1.2.1), chemical chaperones non-selectively assist proteins to achieve or to maintain their native state. They generally have a low molecular weight and are categorized into osmolytes or hydrophobic compound based on their mechanism of action. Osmolytes, such as polyols or free amino acids and their derivatives, create a hydrophobic environment around proteins through sequestration of water, which thermodynamically promotes the native state. Moreover, they may regulate the function of molecular chaperones. In contrast to osmolytes, hydrophobic compounds prevent aggregation through direct interaction with surface-exposed hydrophobic segments of proteins [23, 139, 140]. In addition to chemical chaperones, the discovery of compounds that selectively bind specific proteins and promote proper folding led to their categorization as pharmacological chaperones [139].

Several studies showed that 4-PBA can reduce the aggregation of proteins that are involved in distinct diseases *in vitro* [141–143] and *in vivo* [144]. Moreover, 4-PBA was found to reduce Aβ aggregation in animal models of AD [145–147].

Whereas the reduction of protein aggregation could be based on a multitude of mechanisms, 4-PBA has been shown to prevent the aggregation of denatured lactalbumin as well as bovine serum albumin in a cell-free assay, directly evidencing that 4-PBA acts as a chemical chaperone [142, 148].

Furthermore, a multitude of studies have demonstrated that 4-PBA attenuates ER stress induced by different stressors, like tunicamycin or overexpression of disease associated proteins, *in vitro* [142, 149, 150] and *in vivo* [151]. Since the attenuation of ER stress was accompanied by reduced expression of molecular chaperones involved in the UPR^{ER}, such as HSPA5 [GRP78; BIP], the chemical chaperone properties of 4-PBA were further evidenced indirectly.

In addition to its properties as a chemical chaperone, evidence suggests that 4-PBA may also reduce protein aggregation and proteotoxicity through inhibition of HDACs, which is described in the following Chapter 1.5.2.

1.5.2 Histone Deacetylase Inhibitors

Histone acetyltransferases (HATs) and the opposing HDACs are enzymes with central function in the epigenetic regulation of gene expression. They affect the acetylation status of lysine residues of the basic histone proteins, which organize the genomic DNA of eukaryotes into a compact form, termed nucleosomes. Histone acetylation is generally associated with transcriptional activation due to neutralization of the positive charges of lysine residues, weakening the electrostatic interaction of histone proteins and the negatively charged DNA. This weakened interaction ultimately promotes the accessibility for the RNA polymerase, thus enabling transcription. In contrast, lysine residues regain their positive charge upon deacetylation by HDACs, resulting in reduced transcription. In addition to their effect on gene expression, the opposing action of HATs and HDACs on histone proteins further regulates processes like DNA replication, DNA repair or telomeric silencing. Moreover, the enzymes are involved in numerous other cellular processes, such as proteostasis and apoptosis, through PTM of non-histone proteins [152, 153].

Based on their homology to yeast, HDACs of mammals are categorized into four classes. The predominately nuclear localized class I consists of HDAC1, 2, 3 and 8. HDACs of class II are localized both in the nucleus as well as cytoplasm and are further categorized in two subclasses: Class IIa, which includes HDAC4, 5, 7 and 9 and class IIb, consisting of HDAC6 and 10. Enzymes of class III are called sirtuins and accordingly termed SIRT1-7. Finally, class IV contains HDAC11 [154]. Whereas the catalytic activity of class I, II and IV is dependent on Zn^{2+}, sirtuins require oxidized nicotinamide adenine dinucleotide (NAD^{+}) [153].

In aging and certain neurodegenerative diseases such as AD, the acetylation status of histone proteins shifts towards a state of hypoacetylation, which may promote further aging processes and disease progression [155, 156]. Consequently, HDAC-inhibitors (HDACIs) were proposed as potential therapeutic agents [154, 157].
However, due to the extensive involvement of HDACs in cellular processes on the transcriptional and the post-translational level, research on HDACIs is a complex field. They are structurally categorized into small molecular weight carboxylates, hydroxamic acids, benzamides, epoxyketones, cyclic peptides and hybrid molecules [152]. The majority of HDACIs functions non-selectively through a metal-binding moiety and a capping as well as a linker group that interact with the binding site of lysine and the active site of HDACs. In contrast, selective HDACIs act through specific protein-protein interactions [157]. Consequently, non-selective HDACIs affect a broader range of cellular processes than selective HDACIs, thereby potentially increasing the risk of adverse effects [154]. Another issue are off-target effects of non-selective as well as selective HDACIs [157, 158]. Finally, although the inhibition of specific HDACs was also modelled using knockdown experiments, the molecular effects may not be comparable to HDACI due to higher specificity and potency.
Given the heterogeneity of research studies, it is evident that HDAC inhibition in AD models was found to exhibit both neuroprotective and neurotoxic effects [157, 159]. Nevertheless, several potential mechanisms that may positively affect AD pathogenesis could be identified. Due to their relevance for this work, particularly molecular effects of class I and class IIb HDAC inhibition on proteostasis are described below.

At first, HDAC inhibition potentially reverts hypoacetylation of histone proteins during aging and disease pathogenesis, which may activate transcription of genes that promote health and longevity [158].
Furthermore, deacetylase-independent functions of HDACs that are connected to the proteostasis network could be affected by HDAC inhibition. HDAC1 was found to act as a

repressor of HSPA5 [GRP78; BIP] expression through promoter binding [160] and may sterically interfere with HSF1 DNA binding in a deacetylase-independent manner [161]. Additionally, HDAC6 is part of the repressive HSF1 complex (Chapter 1.2.2). Inhibition and consequently conformational change of HDAC1 or HDAC6 could therefore potentially induce the expression of HSPA5 [GRP78; BIP] and activate the HSR, respectively.
Moreover, HDACI may exert protective effects through hormesis [158]. Accordingly, inhibition of HDAC6 leads to acetylation of cytosolic HSPC [HSP90] chaperones, which results in loss of their chaperone function. As a consequence, misfolded proteins accumulate in the cytosol and may eventually induce the HSR [153, 162] (Chapter 1.2.2). Similarly, acetylation and thus functional loss of HSPA5 [GRP78; BIP] due to inhibition of HDAC1, 2, 3 or 6 may lead to activation of the UPR^{ER} [153, 163]. Consistent with these mechanisms, different HDACIs were shown to upregulate the expression of molecular chaperones, such as cytosolic HSPA [HSP70] family members or HSPA5 [GRP78; BIP] [164–166].
In addition to their effects on proteostasis, HDACIs have been found to exert further potential protective mechanisms, such as induction of neuritogenesis [157] and promotion of antioxidative defences [167].

Due to the progressive disruption of proteostasis in AD (Chapter 1.4), the described hormetic effect of HDACIs through accumulation of misfolded proteins substantiates a preventive rather than a therapeutic use and indicates that strong inhibition of HDAC could be detrimental. Accordingly, it may be advantageous that 4-PBA was found to act as a weak HDACI. Using a panel of *in vitro* assays that were based on trypsin cleavage of a fluorescent HDAC substrate, Fass et al. (2011) demonstrated an inhibitory effect of 4-PBA on class I and class IIb HDACs with half maximal inhibitory concentrations (IC_{50}) in the µM range, which were over 1000 times higher compared to the FDA-approved HDACI suberoylanilide hydroxamic acid (SAHA). They further showed that 4-PBA increased tubulin acetylation und thus inhibits HDAC6 in primary cultures of mouse forebrain neurons, whereas histone H3 acetylation and therefore class I HDAC activity was unaffected [168]. However, the authors used µM concentrations of 4-PBA, which were potentially insufficient to result in a meaningful inhibition of HDACs in cells. In contrast, mM concentrations of 4-PBA were shown to inhibit the activity of class I and class II HDACs as well as to increase the acetylation of histone H3 and H4 in different cellular models [142, 148, 166]. Moreover, the inhibitory effect of 4-PBA on HDAC was also evidenced *in vivo* by increased acetylation of histone H4 in the brains of mice [169].

In summary, 4-PBA may positively affect AD pathogenesis via its function as a weak HDACI that potentially promotes increased activity of the proteostasis network. First, this could directly induce the transcription of proteostasis effectors, such as molecular chaperones or proteins involved in protein degradation. Increased activity of the proteostasis network potentially also results from a hormetic response based on the functional loss of acetylated molecular chaperones. Since the proteostasis network is already progressively disturbed in AD (Chapter 1.4), however, this mechanism substantiates timely intervention with 4-PBA. Furthermore, both proposed mechanisms of HDAC inhibition by 4-PBA are consequently opposing to its properties as a chemical chaperone, which may lead to reduced expression of molecular chaperones through attenuation of cellular stress (Chapter 1.5.1). Nevertheless, it is important to note that all proposed mechanisms illustrated in Figure 1.12 ultimately promote proteostasis.

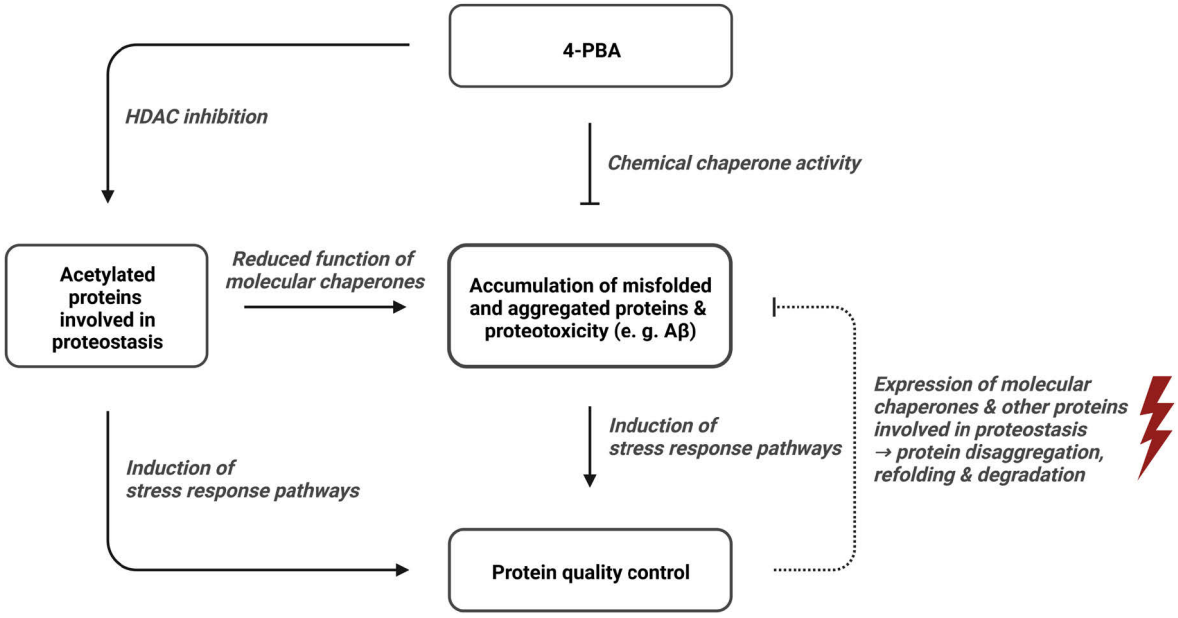

Figure 1.12 | Potential protective mechanisms of 4-PBA

4-PBA may promote proteostasis through several mechanisms. First, it has been shown that 4-PBA acts as a chemical chaperone and thus can attenuate the accumulation of misfolded or aggregated proteins through its chemical structure. Moreover, 4-PBA may positively affect AD pathogenesis via its function as a weak HDACI. This could directly induce the transcription of proteostasis effectors, such as molecular chaperones or proteins involved in protein degradation. Increased activity of the proteostasis network potentially also results from a hormetic response based on the functional loss of acetylated molecular chaperones. Since the proteostasis network is already progressively disturbed in AD, however, this mechanism substantiates timely intervention with 4-PBA. Aβ = amyloid-β, HDAC = histone deacetylase, HDACI = histone deacetylase inhibitor, 4-PBA = 4-phenylbutyric acid.

1.6 Caprylic Acid

Caprylic acid (CA) (Figure 1.13), also known as octanoic acid, is a saturated medium-chain fatty acid (MCFA) consisting of eight carbon atoms. Along with other MCFAs, CA is naturally found in the milk of various mammals as well as in palm kernel oil and coconut oil, primarily in the form of medium-chain triglycerides (MCTs). Moreover, CA and different MCTs, such as tricaprylin, are also available as supplements [170].

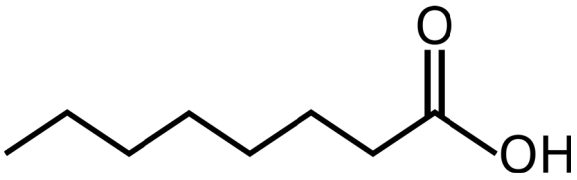

Figure 1.13 | Chemical structure of CA

In contrast to long-chain FAs (LCFAs) that are incorporated into chylomicrons and transported to the liver via the lymphatic system, MCTs are broken down in the gastrointestinal tract by lipases that preferentially hydrolyse medium-chain esters over long-chain esters and transferred via the portal bloodstream. Moreover, the transport of CA is independent of fatty acid transport proteins or fatty acid binding proteins and CA can permeate the inner mitochondrial membrane in the non-esterified form without the need for carnitine [170–172].

Since mitochondrial dysfunction is a major pathological hallmark of AD, exploration of mitoprotective interventions is of great importance (Chapter 1.4). At first, CA could compensate the energetic deficit in AD through energy supply via FAO, consequently circumventing impaired glucose metabolism. Moreover, CA is a precursor for the biogenesis of α-lipoic acid (ALA) (Chapter 1.6.1) and ketone bodies such as β-hydroxybutyric acid (BHB) (Chapter 1.6.2), which could further exert mitoprotective effects. Finally, CA is able to cross the BBB, which is evidently a prerequisite for its use in AD [173–175].

1.6.1 α-Lipoic Acid

ALA is a dithiol compound synthesized enzymatically in mitochondria from CA. During biogenesis, CA is first transferred to the H protein of the glycine cleavage system via the lipoyl(octanoyl) transferase 2 (LIPT2). Subsequently, the lipoic acid synthetase (LIAS) catalyzes the replacement of two hydrogens of CA with sulfur groups to generate ALA. After biogenesis or cellular uptake, ALA is partly enzymatically reduced to dihydro lipoic acid

(DHLA) or metabolized by FAO [176]. Together with ALA, DHLA and FAO metabolites function as antioxidants through different mechanisms including direct scavenging of radicals, donating electrons to oxidized molecules or reduction of other endogenous antioxidants. Moreover, ALA is a chiral molecule that exists as two enantiomers, of which (*R*)-ALA acts as an essential covalently bound coenzyme for 2-oxoacid (α-ketoacid) dehydrogenases, including the mitochondrial AKG-DH and PDH involved in energy metabolism (Chapter 1.3.1), whose activities are impaired in AD (Chapter 1.4) [176].

1.6.2 β-Hydroxybutyric Acid

Upon glycogen depletion during prolonged fasting or starvation, the human body particularly mobilizes FAs stored in adipose tissue for ketone body biosynthesis, also called ketogenesis, to meet the energy demand of primarily glucose-dependent cell types such as neurons.

Following generation of acetyl-CoA via FAO, ketogenesis starts with the connection of two acetyl-CoA to acetoacetyl-CoA via the acetyl-CoA acetyltransferase (ACAT), also described as thiolase. Subsequently, attachment of a third acetyl residue via the 3-hydroxy-3-methyl-glutaryl (HMG)-CoA synthase results in formation of HMG-CoA. Cleavage by the HMG-CoA lyase eventually results in generation of acetoacetate, the first of the three ketone bodies. The majority of acetoacetate is enzymatically reduced to (*R*)-BHB through the BHB dehydrogenase (BHB-DH). Moreover, acetoacetate undergoes spontaneous decarboxylation to acetone, which is mainly excreted by breath.

Whereas ketogenesis occurs almost exclusively in mitochondria of the liver and to some extend of astrocytes, the generated acetoacetate and BHB are only catabolized in extra-hepatic tissues or cells, including the brain. First, the reverted action of BHB-DH results in oxidation of BHB to acetoacetate. Then, the CoA of succinyl-CoA is transferred to acetoacetate via the Succinyl-CoA:3-oxoacyl-CoA-transferase (SCOT). Finally, ACAT cleaves acetoacetyl-CoA into two acetyl-CoA molecules that are further metabolized in the TCA cycle, eventually resulting in the generation of ATP.

Due to positive outcomes related to fasting, alternative ways to induce ketogenesis have been explored. Since ketogenesis is negatively regulated by insulin, which suppresses mobilization of FAs and their import into hepatic mitochondria, it can also be induced by restricted carbohydrate intake without the need of severe energy restriction. Diets that aim to induce

ketogenesis are consequently termed ketogenic diets and generally provide the majority of energy through long-chain triglycerides (LCTs), whereas carbohydrate intake is kept below 10%. Classical ketogenic diets, however, have substantial disadvantages due to the restriction of food choice that may leads to malnutrition [172, 177]. A simple alternative to induce ketogenesis, functioning without lowering insulin levels, is the consumption of MCTs or their constituent MCFAs, respectively. MCFAs, especially CA, are readily oxidized in the liver to generate an excess of acetyl-CoA, which promotes ketogenesis due to relative shortage of OAA [132]. Ultimately, both dietary interventions may lead to a state termed nutritional ketosis[4], characterized by plasma ketone concentrations of up to 8 mM [177].

Ketogenic MCT based diets were shown to improve cognitive functions of patients with MCI and AD [133, 178–180]. Mechanistically, energy metabolism of ketone bodies circumvents impaired glucose utilization associated with AD. As their brain uptake is generally directly proportional to their plasma concentration, ketone bodies can supply a substantial amount of energy demand [132, 133]. Moreover, their oxidation provides more energy per consumed oxygen compared to glucose and particularly FA metabolism [177].

[4] In contrast, ketoacidosis is a state of uncontrolled ketone body production mainly occurring in patients with untreated diabetes mellitus type I, resulting in plasma ketone concentrations of up to 25 mM that causes metabolic acidosis.

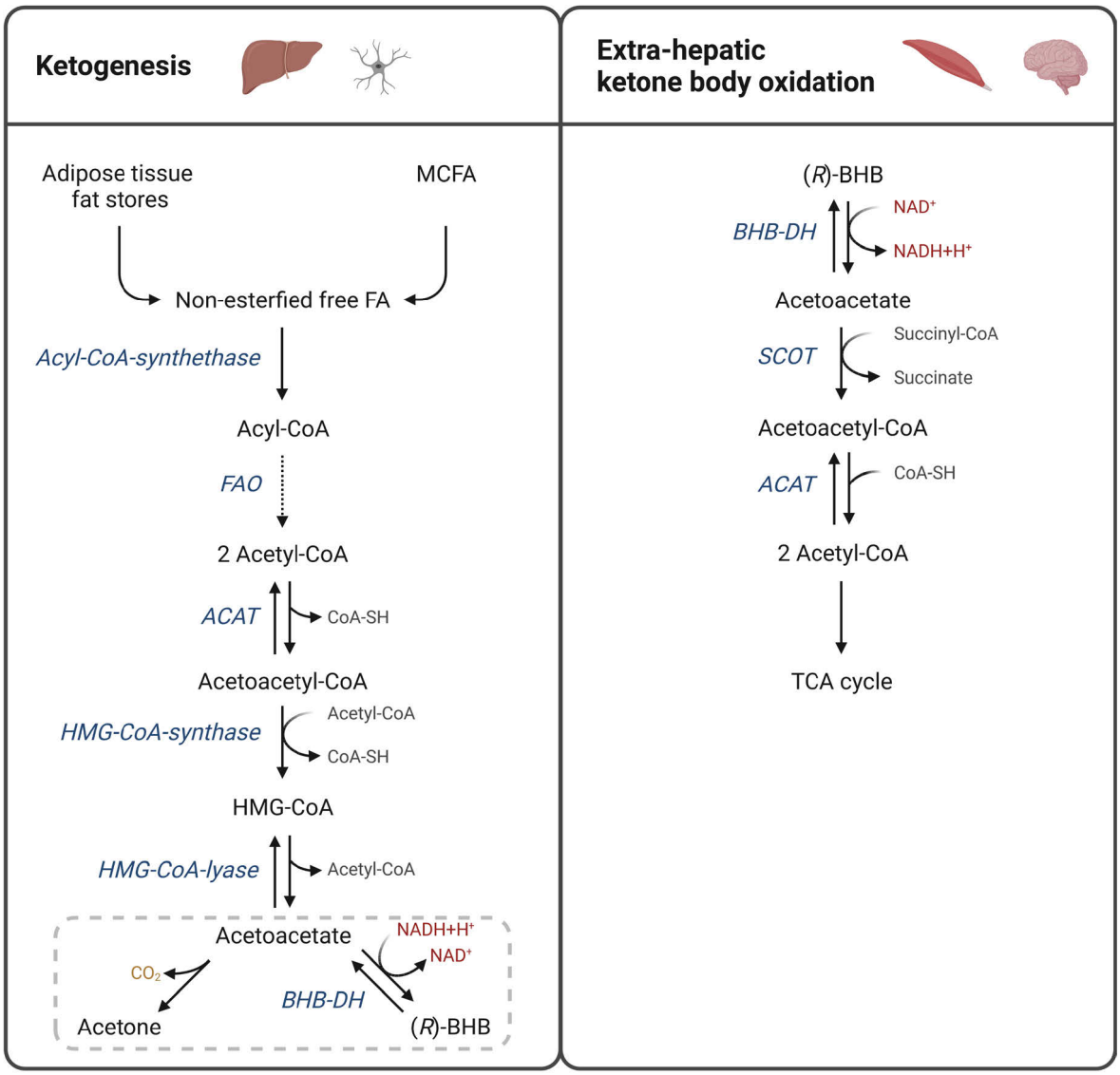

Figure 1.14 | Ketogenesis and ketone body oxidation

Glycogen depletion, prolonged fasting, starvation or a ketogenic diet with restricted carbohydrate intake result in the mobilization of FAs stored in adipose tissue for ketone body biosynthesis, also termed ketogenesis, to meet the energy demand of primarily glucose-dependent cell types such as neurons. A simple alternative to induce ketogenesis without the need of energy or carbohydrate restriction is the consumption of MCTs or their constituent MCFAs, respectively. Whereas ketogenesis occurs almost exclusively in mitochondria of the liver and to some extent of astrocytes, the generated acetoacetate and BHB are only catabolized in extra-hepatic tissues or cells, including the brain. Ketone body oxidation leads to the production of acetyl-CoA, which is further metabolized in the TCA cycle, eventually resulting in the generation of ATP. Adapted from [181]. Created with BioRender.com. ACAT = acetyl-CoA acetyltransferase, ATP = adenosine triphosphate, BHB = β-hydroxybutyric acid, BHB-DH = BHB dehydrogenase, CoA = coenzyme A, MCFA = medium-chain fatty acid, FA = fatty acid, FAO = fatty acid oxidation; β-oxidation, HMG = 3-hydroxy-3-methyl-glutaryl, TCA = tricarboxylic acid.

1.7 *Caenorhabditis elegans* as a Model Organism for Alzheimer's Disease

In the 1960s, the soil-living nematode *Caenorhabditis elegans* (*C. elegans*) was described by Sydney Brenner as a biological model organism for genetic studies [182]. The nematode feeds on bacteria and reaches a body length of about 1 mm. Of the two sexes of *C. elegan*s, the self-fertile hermaphrodites represent the vast majority of the population. In contrast, the slightly smaller male nematodes only develop at a frequency of approximately 0.1% due to rare spontaneous X chromosome nondisjunction[5] in the germline of hermaphrodites. With 959 somatic cells in hermaphrodites and 1031 somatic cells in males, both sexes exhibit a fixed number of somatic cells upon reaching adulthood, a phenomenon termed eutely [183].

A variety of beneficial properties have established *C. elegans* as a model organism for research in the fields of genetics, cell biology, neuroscience and aging [183]. First, the nematodes are easily cultivated on agar plates or in liquid medium containing *Escherichia coli* (*E. coli*) as the food source. Their development from eggs to adult nematodes is rapidly completed within three and a half days under proper conditions at room temperature. In addition to the short generation time, each adult hermaphrodite can produce approximately 300 offspring (Chapter 1.7.2). Furthermore, the *C. elegans* dauer stage (Chapter 1.7.2) resists freezing and thawing, which enables long-term storage [184].
C. elegans is characterized by a simple anatomy (Chapter 1.7.1.1) composed of various cell and tissue types, such as body wall muscle cells, neurons and an intestine, which makes the nematodes a suitable model for screening experiments based on phenotypic observations. Another beneficial property is their transparent cuticle across all developmental stages, which allows real-time observation of cellular processes in the living organism using microscopy. This is generally coupled with the use of fluorescent reporter genes or fluorescent probes to mark cells, organelles or specific molecules [184].
Finally, the *C. elegans* genome was completely sequenced by 1998, through which great similarities to the human genome were found. It was concluded that the nematode contains homologs for approximately 50% of human disease-associated genes [185]. The functions of these genes can be studied by different methods. Numerous mutants were generated using chemical reagents, UV light or ionizing radiation. Moreover, the nematodes are easily genetically modified through transgenesis or by crossing hermaphrodites with males of

[5] Nondisjunction is the failure of homologous chromosomes to separate properly during cell division.

different genotypes. These genetic changes remain conserved as a result of the sexual dimorphism of the hermaphrodites, which leads to the production of homozygous offspring [184]. In addition to genome manipulation, RNA interference (RNAi) can be used to inhibit the expression of specific genes on the post-transcriptional level (Chapter 1.7.3).

Due to the minor role of male nematodes in research, the following Chapters are mostly limited to the description of the anatomy (Chapter 1.7.1) and life cycle (Chapter 1.7.2) of hermaphrodites. Next, the principle of RNAi as a simple genetic tool for studying gene functions or molecular mechanisms of substances in *C. elegans* are described (Chapter 1.7.3) and considerations regarding orthologous genes are addressed (Chapter 1.7.4). Subsequently, the use of *C. elegans* as an AD model (Chapter 1.7.5) and evidence for the preservation of relevant cellular processes is presented (Chapters 1.7.6 - 1.7.9.).

1.7.1 Anatomy and Physiology of *Caenorhabditis elegans*

1.7.1.1 Body Shape

In analogy to other nematodes, *C. elegans* consists of an unsegmented cylindrical body that narrows distally with an inner and outer tube separated by a pseudocoelomic space. The outer tube includes the cuticle, hypodermis, excretory system, neurons and body wall muscles, while the inner tube includes the pharynx and intestine as well as the gonads in adult nematodes. To maintain body shape, the tissues are under internal hydrostatic pressure regulated by an osmoregulatory system [183]. The anatomy of adult *C. elegans* hermaphrodite and male nematodes is shown in Figure 1.15.

1.7.1.2 Cuticle and Hypodermis

C. elegans is surrounded by a collagenous cuticle formed by the underlying epithelium. The cuticle contains openings of various tissues. These openings include the excretory pore, which presumably functions in osmo- and ion-regulation and is located on the ventral side of the head, the vulva, located ventrally in the middle of the body, and the anus, emerging ventrally in front of the tail end. In addition, the cuticle contains sensilla that allow the nematode to interact with its environment [183].

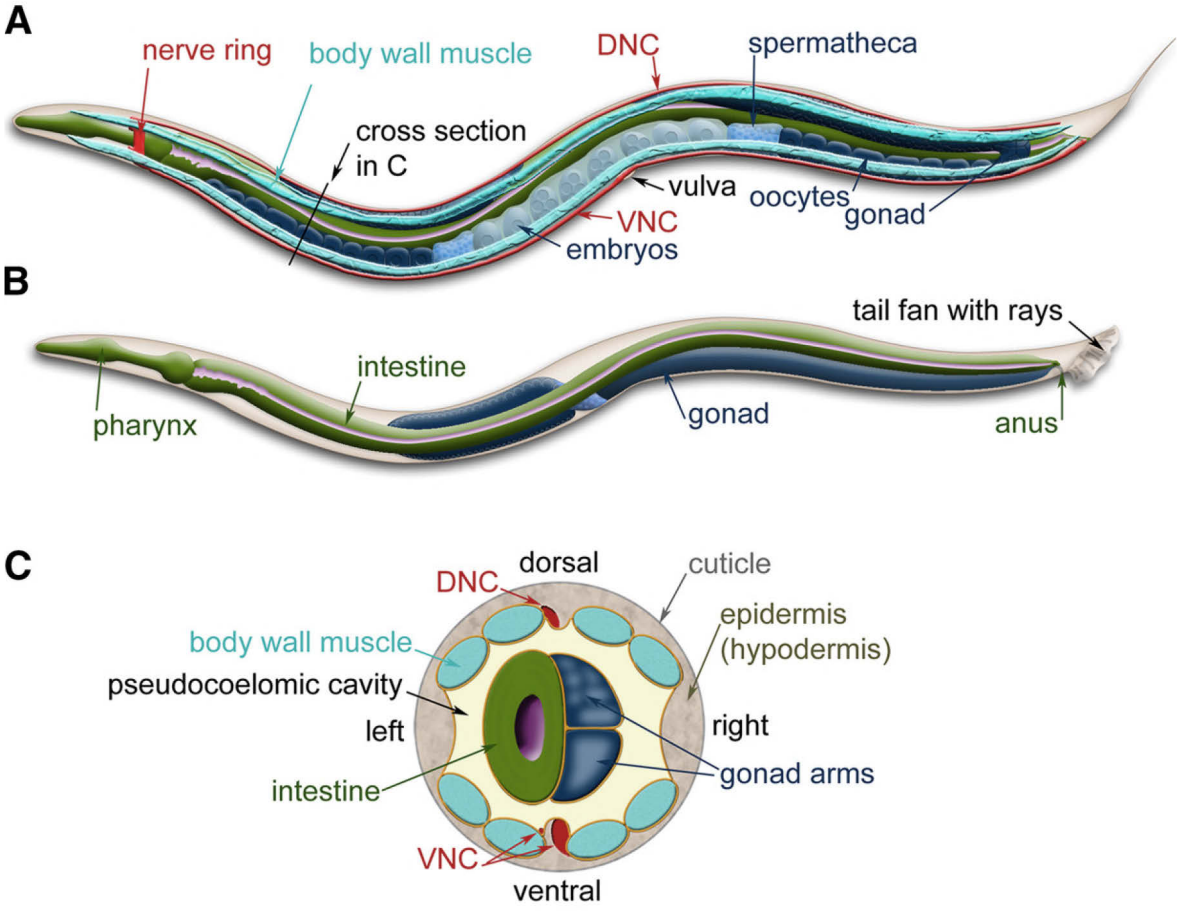

Figure 1.15 | Anatomy of adult *C. elegans* nematodes

The major anatomical features of adult *C. elegans* hermaphrodite and male nematodes are illustrated. (A) The DNC and VNC run along the entire length of the animal originating from the nerve ring, which contains the majority of neurons. Two of the four body wall muscle quadrants are shown. Additionally, the reproductive system of hermaphrodites is depicted. (B) The nervous system and body wall muscles are omitted to clearly reveal the pharynx and intestine. Moreover, the tail fan of male nematodes is shown. Furthermore, male nematodes naturally lack oocytes. (C) A cross-section through the anterior region of a hermaphrodite is shown [186]. DNC = dorsal nerve cord, VNC = ventral nerve cord

1.7.1.3 Nervous System

The cells of the nervous system are organized as ganglia in the head and tail region, with the majority of the 302 neurons composing the nerve ring located around the pharynx. In addition, neurons are continuously located along the body between the hypodermis and body wall muscles. Furthermore, two smaller ganglia as well as irregularly distributed neurons are located laterally. For most neurons, the transmission of impulses takes place via a dorsal nerve cord (DNC) and a ventral nerve cord (VNC), which project into the nerve ring. Moreover, the neurons are supported in their function by 56 glial cells. In contrast to vertebrates, in *C. elegans* the functions of several neurons are combined in one neuron. The neurons

serve to innervate the muscle cells of different tissues and process sensory inputs that contribute to a range of behavioral patterns, such as response to touch, movement toward food and aversion behavior [183, 187].

1.7.1.4 Muscle System

The muscle system of *C. elegans* consists of longitudinal striated muscle cells of the pharynx, intestine, anus, uterus, gonadal sheath and vulva as well as the obliquely striated body wall muscle cells. Functionally, the longitudinal striated muscle cells serve for pharyngeal pumping, defecation, ovulation, fertilization and oviposition [183, 188]. The 95 rhomboid-shaped mononuclear body wall muscle cells allow coordinated movement in dorsal and ventral directions in a sinusoidal pattern. They are separated from neurons as well as the hypodermis by a thin basal lamina and are organized into two dorsal and two ventral quadrants along the entire body length [183, 189].

1.7.1.5 Alimentary System

The alimentary system of *C. elegans* consists of the pharynx connected to the intestine, which is bordered posteriorly by the rectum. Food is ingested and grinded by the pharynx, which acts almost completely autonomously via its own nervous system, muscles, and epithelium [183]. The grinded food passes into the intestine, which consists of 20 epithelial cells that form a tube around the central lumen, where the food components are digested and absorbed. The apical surfaces of the intestinal cells form a brush border characterized by numerous microvilli. In addition to digestion and absorption of food components, the intestine performs functions in synthesis and storage of macromolecules, initiation of the innate immune response and nourishment of germ cells. Finally, excretion of the intestinal contents occurs via a rectal valve that connects the intestine to the rectum and anus [190].

1.7.1.6 Reproductive System

The reproductive system of *C. elegans* hermaphrodites is located in the pseudocoelom and consists of the somatic gonads, the germ line and the egg-laying apparatus. The two bilaterally symmetrical, U-shaped gonad arms are connected to the central uterus by the spermatheca, where the hermaphrodites produce and store spermatozoa. Generated oocytes are

fertilized in the spermatheca, mature in the uterus and are eventually deposited into the environment through the vulva [183, 191].

1.7.2 Life Cycle *Caenorhabditis elegans*

The life cycle of *C. elegans* hermaphrodites is illustrated in Figure 1.16. Through their life cycle, *C. elegans* nematodes undergo embryogenesis and four larval stages (L1 - L4) before reaching the adult stage. The larvae molt at the end of each larval stage, replacing the cuticle with a newly formed specific for the corresponding stage.

The embryogenesis of *C. elegans* is divided into the proliferation phase and the organogenesis phase. At the beginning of the proliferation phase is a single cell, which subsequently divides into about 550 undifferentiated cells. The first 150 minutes of proliferation occur intrauterine and end with oviposition after reaching the 30-cell stage. During the proliferation phase, embryos develop three germ layers, which give rise to the distinct tissues in the subsequent stage of organogenesis. Finally, larvae hatch approximately 800 minutes after the first cell division [183].

Further post-embryonic development of the larvae is influenced by the availability of food. In the event of food deprivation, the nematodes cease development and remain in the L1 stage to survive for up to ten days. If food supply is sufficient, further development continues three hours after hatching. Furthermore, in case of adverse environmental conditions, such as the presence of pheromones, shortage of food or space and high temperatures before entering the L2 stage, the larvae may enter the so-called dauer stage. In this stage, the nematodes completely halt their development and movement for up to four months. After environmental conditions improve, dauer larvae resume development and molt directly into L4 larvae within ten hours [183].

Without passing through the dauer stage, hermaphrodites reach the young-adult stage approximately 45 to 50 hours after hatching at a temperature of 22 to 25 °C and complete their reproductive cycle by oviposition. In the following four days, each adult hermaphrodite produces about 300 offspring. Following the reproductive phase, they live for up to 15 days under standardized laboratory conditions [183].

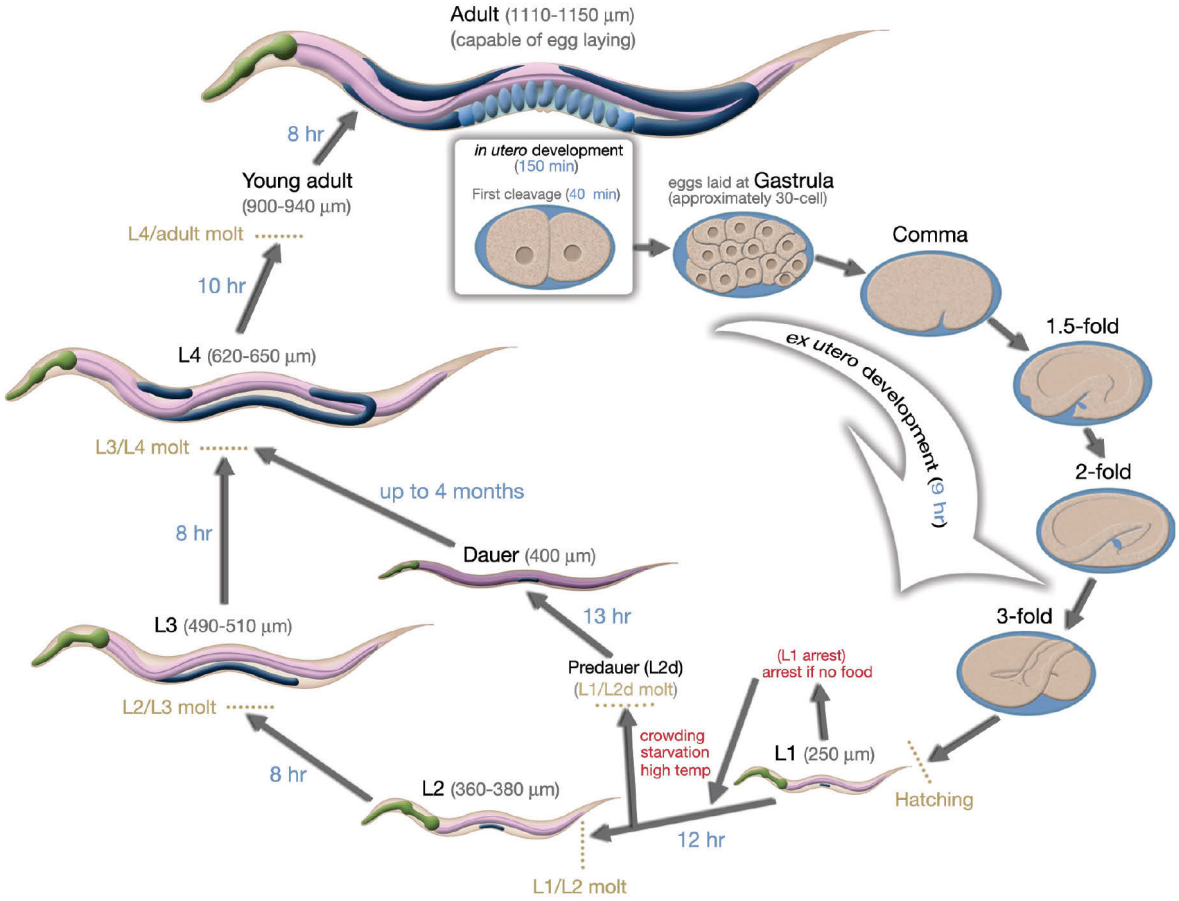

Figure 1.16 | Life cycle of *C. elegans* hermaphrodites at 22 °C

The life cycle of *C. elegans* is composed of the *in utero* and *ex utero* development of embryogenesis, the larval stages (L1-L4) and the adult stage. In the event of food deprivation in the L1 stage, *C. elegans* stops its development and resumes only if food is available. Furthermore, in the event of adverse environmental conditions prior to entering the L2 stage, the larvae may transition to the so-called dauer stage. The respective stages are indicated along with the approximate size of the nematodes. In addition, the duration of the individual developmental steps is shown next to the arrows. Adapted from [183].

1.7.3 RNA Interference in *Caenorhabditis elegans*

RNAi is a highly conserved cellular process of sequence-specific mainly post-transcriptional gene silencing. The pathway illustrated in Figure 1.17 is initiated by double-stranded RNA (dsRNA), which is processed in an ATP-dependent reaction to small-interfering RNAs (siRNAs) of around 25 nucleotides carrying phosphorylated 5’ ends and hydroxylated 3’ ends with two overhanging nucleotides by the endoribonuclease Dicer, a member of the RNase III family. Subsequently, the generated siRNA duplex molecules are incorporated into RNA-induced silencing complexes (RISCs) and ATP-dependently unwound to single-strands. After ejection of the passenger strand, the guide strand recruits the respective RISC to its

antisense complementary target messenger RNA (mRNA). Hybridization with the target mRNA eventually results in its endonucleolytic cleavage and consequently prevents translation [192].

In *C. elegans*, induction of RNAi has emerged as a potent, rapid and simple genetic tool to study loss-of-function phenotypes, genetic interactions and molecular mechanisms of substances based on knockdown of specific genes of interest (GOIs) [193]. Unlike in mammals, RNAi in *C. elegans* functions systemically and is heritable [194]. To induce RNAi, several methods to deliver exogenous dsRNA were developed. First, *in vitro* transcribed dsRNA can be injected directly into the nematodes. Another method is to soak the nematodes in a concentrated solution of dsRNA. Moreover, feeding of dsRNA expressing *E. coli* HT115(DE3) RNAi-clones is widely used (Chapter 3.1.2.1). In contrast to injection of dsRNA, the other two methods offer the advantage that nematodes of any stage can be exposed to RNAi. Thus, functions of gene products required for development, e.g., during embryogenesis, can be studied at later stages [184].

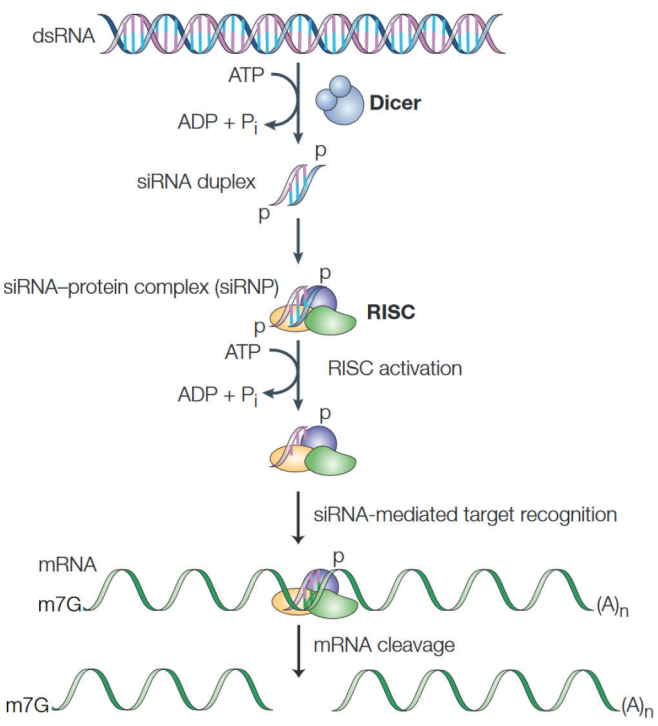

Figure 1.17 | Schematic illustration of RNAi
Long dsRNA is cleaved in an ATP-dependent reaction to siRNA by the RNase Dicer. The generated siRNA duplex molecules are integrated into RISC and ATP-dependently unwound. After ejection of the passenger strand, the guide strand can recruit the RISC to the antisense complementary target mRNA. Hybridization with the target mRNA eventually results in its endonucleolytic cleavage, thus preventing translation. Adapted from [192]. ADP = adenosine diphosphate, ATP = adenosine triphosphate, dsRNA = double-stranded RNA, mRNA = messenger RNA, RISC = RNA-induced silencing complex, siRNA = short-interfering RNA.

1.7.4 Orthologous Genes and Proteins in *Caenorhabditis elegans*

The knowledge of conserved genes between humans and *C. elegans* can facilitate reverse genetic[6] screens based on RNAi. Although *C. elegans* is evolutionarily distant from humans, its genome contains a substantial number of orthologous genes that were determined based on their sequence similarity [185, 195, 196].

Generally, it is assumed that orthologs retain similar biological functions [197]. The subject, however, becomes more complex once variables such as functional interactions, temporal gene expression and cellular as well as subcellular localization of orthologous proteins are included. To identify the spatiotemporal expression of orthologs proteins especially fusion proteins with fluorescent markers such as green fluorescent protein (GFP) or gene expression analysis of isolated cells following fluorescence-activated cell sorting (FACS) are used [198–201]. Nevertheless, despite the availability of a substantial amount of data, more research needs to be conducted in order to clearly characterize individual orthologs.

In the following, orthologs involved in cellular processes of interest to this work are described and important differences to humans are outlined. Furthermore, the Appendix A.3 contains a complete list of the relevant orthologs and respective *E. coli* HT115(DE3) RNAi clones for their regulation.

1.7.5 Alzheimer's Disease Models of *Caenorhabditis elegans*

Due to the positive properties for research (Chapter 1.7), *C. elegans* has also been established as a model for AD. Wild-type nematode possess orthologs to major AD-associated genes in humans, such as protein with tau-like repeats (*ptl-1*[7]) and amyloid precursor-like (*apl-1*) [202]. Furthermore, genes involved in APP processing, like SUPpressor (*sup-17*) and *adm-4*, as orthologs of human *ADAM10* as well as *ADAM17*, and orthologs for all subunits of the γ-secretase complex, such as the PS homologous genes suppressor/enhancer of lin-12 (*sel-12*) and homolog of presenilin (*hop-1*), were identified [202–204] However, despite the

[6] The term reverse genetics refers to a research approach in which a specific gene is altered in order to study its function. In contrast, forward genetics seeks to find the genetic basis of a phenotype or trait.

[7] Nomenclature: Whereas human genes are written with all letters capitalized and italicized, typically followed by a number, *C. elegans* genes contain only lowercase letters and a hyphen preceding the number. In contrast, both human as well as *C. elegans* proteins are written with capitalized letters, followed by a number without or with a hyphen preceding the number, respectively.

similarities, *C. elegans* lacks an ortholog of β-secretase, which prevents the formation of Aβ in wild-type nematodes [202].

Consequently, several transgenic *C. elegans* strains expressing human Aβ were developed to investigate its proteotoxic properties and potential therapeutic agents for AD. One of the most widely used strains is CL2006. In this strain, the sequence of human $A\beta_{1-42}$ was introduced under the control of the unc-54 promoter. Accordingly, CL2006 expresses Aβ constitutively in body wall muscle cells, ultimately leading to progressive age-dependent paralysis of the nematodes [205]. McColl et al. (2009), however, demonstrated that CL2006 nematodes actually express an $A\beta_{3-42}$ fragment, which has a higher tendency to aggregate and appears to possess minor relevance in human AD pathogenesis [206]. The authors generated a new strain called GMC101 that is also the model used in this work, which carries a modified transgene to enable constitutive expression of $A\beta_{1-42}$ in body wall muscle cells, leading to progressive age-dependent paralysis following temperature upshift. GMC101 nematodes further carry a transgene that drives intestinal expression of GFP for the selection of transgenic nematodes [207]. Its corresponding control strain CL2122 consequently carries the same *gfp* transgene for selection while lacking the Aβ transgene.
Since AD pathogenesis is mostly affecting neurons, several transgenic strains with neuronal Aβ expression were generated. For instance, the modified Aβ sequence designed by McColl et al. was used for constitutive pan-neuronal expression of $A\beta_{1-42}$ in the transgenic strain GRU102, which also results in age-dependent motility defects [208]. Nevertheless, despite the potential closer modelling of human AD pathogenesis, neuronal *C. elegans* models pose methodological challenges. At first, neuronal phenotypes are often subtle and therefore challenging to quantify compared to muscular phenotypes. Moreover, neurons are generally refractory to RNAi. To overcome this limitation, the nematodes can be crossed with transgenic strains that express the dsRNA transporter systemic RNAi defective 1 (SID-1) in the respective neuronal cells [209]. While such a genetic crossing enhances sensitivity to RNAi, additional selection markers like genes encoding for fluorescent proteins are introduced, which may interfere with methods based on fluorescence. Another limitation is that the nervous system of *C. elegans* is naturally not comparable to the human brain [210, 211]. Due to these limitations, mostly transgenic *C. elegans* strains with Aβ expression in body wall muscle cells are used to model the cellular proteotoxicity of Aβ that is typically assessed by analysis of motility.

1.7.6 Proteostasis in *Caenorhabditis elegans*

Based on its central function in maintaining protein homeostasis, the proteostasis network (Chapter 1.2) is highly conserved in *C. elegans,* with the involved stress response pathways generally functioning similar to mammals.

As in mammals, the HSR is transcriptionally regulated by HSF-1, which induces the expression of cytosolic molecular chaperones [30, 212]. However, studies with GFP tagged HSF-1 showed that the transcription factor is primarily localized in the nucleus even under physiological conditions [213]. Following stress signals, HSF-1 redistributes into dynamic subnuclear structures that colocalize with markers of active transcription [213]. Moreover, a subset of HSR target genes seems to be regulated in concert with the FOXO (Chapter 1.3.2) ortholog abnormal dauer formation (DAF)-16 [214].

The induction of the UPR^{ER} in *C. elegans* is also dependent on orthologs of the three mammalian ER transmembrane stress sensors, termed IRE-1, PERK kinase homologue (PEK-1) and ATF-6 [215, 216]. The UPR^{ER} of the nematodes further seems to be dependent on a family of genes named activated in blocked UPR (*abu*), particularly when the classical pathways such as IRE-1 are impaired [217]. Moreover, in contrast to mammals, the nematodes express two orthologs of mammalian HSPA5 [GRP78; BIP] called HSP-3 and HSP-4 [215, 218]. Like the HSR, the UPR^{ER} may also be regulated in concert with DAF-16 [219].

Finally, the UPR^{mt} of *C. elegans* is even better explored than in mammals [43]. Accumulation of misfolded proteins in the mitochondrial matrix leads to their degradation by CLPP-1. Subsequently, the generated peptides are transported into the mitochondrial intermembrane space by the half transporter 1 (HAF-1), which impairs the import of the activating transcription factor associated with stress 1 (ATFS-1), an ortholog of mammalian ATF5 [220, 221]. This ultimately results in activation of ATFS-1 and defective proventriculus 1 (DVE-1) to induce the expression of proteins involved in the proteostasis network, such as mitochondrial molecular chaperones [222, 223].

1.7.7 Mitochondrial Homeostasis in *Caenorhabditis elegans*

Due to their essential role in a multitude of cellular processes, mitochondrial pathways including energy metabolism (Chapter 1.3.1) or mitochondrial quality control (Chapter 1.3.3) are also highly conserved.

The genome of the nematode *C. elegans* contains the genes *drp-1*, *fis-1* as well as *fis-2*, which encode for orthologs of the human fission proteins DRP1 and FIS1, respectively. In

addition, fuzzy onions (FZO-1) and EATing: abnormal pharyngeal pumping (EAT-3), could be identified as orthologs of the human fusion proteins MFN1, MFN2 as well as OPA1. [224]. *C. elegans* further contains the genes *pink-1* and Parkinson's disease related 1 (*pdr-1*), which encode orthologs of the central proteins of PINK1/Parkin-mediated mitophagy. Moreover, orthologs of genes involved in receptor-mediated mitophagy like DAF-16/FOXO controlled (*dct-1*), an ortholog of BNIP3, were found [225].

Two major transcription factors also involved in mitochondrial homeostasis of *C. elegans* are the FOXO ortholog DAF-16 and the ortholog of NRF2, termed skinhead 1 (SKN-1) [76, 226, 227]. Like in mammals, both are central for the induction of antioxidative defenses [76]. SKN-1 and DAF-16 are further involved in the induction of receptor-mediated mitophagy via DCT-1 [225, 228]. While the nematodes lack an ortholog of the NRF2 repressor KEAP1, the WD repeat protein 23 (WDR-23) seems to function similarly in regulating SKN-1 activity [226, 229]. In addition, no homologous sequence to *PGC1α* could be found for *C. elegans*, which substantiates the role of SKN-1 in mitochondrial biogenesis [225, 228]. Finally, as in mammals, mtDNA replication is also dependent on the *TFAM* ortholog high mobility group 5 (*hmg-5*) [230].

1.7.8 4-Phenylbutyric Acid Metabolism and Possible Molecular Targets in *Caenorhabditis elegans*

As described in Chapter 1.5, the potential protective mechanisms of 4-PBA on Aβ proteotoxicity depend on its FAO and inhibition of class I and class IIb HDAC. FAO generally functions like in mammals (Chapter 1.3.1). The *C. elegans* genome, however, contains four genes encoding for short-chain specific ACDH, namely *acdh-1, -2, -3* and *-4* [201]. In terms of class I and class IIb HDAC (Chapter 1.5.2), the nematodes lack an ortholog of *HDAC8*. Nevertheless, they contain the *HDAC1* ortholog *hda-3*, the *HDAC2* ortholog *hda-1*, the *HDAC3* ortholog *hda-2*, the *HDAC6* ortholog *hda-6* and the *HDAC10* ortholog *hda-10* [201, 231].

1.7.9 Caprylic Acid Metabolism and Possible Molecular Targets in *Caenorhabditis elegans*

Similar to 4-PBA, the FAO of CA could exhibit a protective effect on Aβ proteotoxicity (Chapter 1.6). In this regard, *C. elegans* has two genes encoding for medium-chain specific ACDH, termed *acdh-8* and *acdh-10* [201]. Moreover, CA is a precursor of ALA, an important cellular antioxidant and coenzyme in energy metabolism (Chapter 1.6.1), which can also be generated *de novo* in *C. elegans* nematodes by orthologous enzymes of the mammalian biogenesis pathway such as LIAS-1 [232]. CA could further result in biogenesis of ketone bodies, which may serve as an alternative energy fuel or as signaling molecules (Chapter 1.6.2). In contrast to mammals, *C. elegans* lacks a clear ortholog of BHB-DH. However, despite only around 40 % sequence identity, the short-chain dehydrogenase/reductase DRD-5 was found to exert inducible BHB-DH-activity following BHB incubation [231]. Although DRD-5 lacks basal BHB-DH activity [231], *C. elegans* was shown to contain ketone bodies [233], suggesting that other unknown enzymes may mediate *de novo* synthesis.

2 Aims of the Work

Alzheimer's disease (AD) is a neurodegenerative disorder and the most common form of dementia. The neurodegeneration results in progressive memory loss as well as psychological changes and can ultimately lead to an almost complete loss of cognitive abilities. With age being the main risk factor of sporadic AD and the advancing demographic change, the disease is a growing burden of modern society. Despite its great importance and intensive research, there is currently no cure for the disease, limiting therapy to symptomatic treatment. The pathogenesis is a complex process, in which the accumulation of proteotoxic amyloid β (Aβ) was identified as a central factor. Furthermore, mitochondrial dysfunction frequently already occurs at an early stage of the pathogenesis. These pathological features mutually aggravate each other in a vicious cycle that may eventually result in a disturbance of neurotransmission and neurodegeneration.

To maintain proteostasis and mitochondrial homeostasis, eukaryotes evolved interconnected quality control systems that involve specific stress response pathways. Since these systems are generally disturbed or overloaded in AD pathogenesis, it appears plausible to search for substances that stimulate them before they malfunction. Moreover, homeostasis could be maintained by alternative energy substrates circumventing the impaired glucose oxidation characteristic for AD or chemicals that directly reduce Aβ aggregation.

The aromatic short-chain fatty acid 4-phenylbutyric acid (4-PBA) and the medium-chain fatty acid caprylic acid (CA) are two substances that could contribute to maintain homeostasis through several mechanisms. First, both potentially serve as energy substrates via β-oxidation (fatty acid oxidation; FAO). 4-PBA may further act as a chemical chaperone or as an inducer of molecular chaperones through inhibition of histone deacetylases. In contrast, CA is a precursor for the biosynthesis of α-lipoic acid (ALA), a cellular antioxidant and coenzyme of enzymes involved in energy metabolism, as well as β-hydroxybutyric acid (BHB), which serves as another energy substrate and signaling molecule.

In the present work, the transgenic *Caenorhabditis elegans* strain GMC101, expressing human $A\beta_{1-42}$ in body wall muscle cells, was used to unravel the molecular effects of 4-PBA and CA on proteostasis and mitochondrial homeostasis. To this end, Aβ proteotoxicity was assessed using a phenotypic approach through computer-based analysis of motility. This approach was supplemented with the regulation of gene expression using RNA interference (RNAi) to identify relevant molecular pathways. Finally, further methods involving genetic crossing, fluorescence microscopy as well as biochemical assays were used to measure Aβ aggregation and parameters of mitochondrial homeostasis.

3 Methods

C. elegans and *E. coli* strains that were used in the present work, as well as further material including consumables, chemicals, reagents, kits, instruments and software, are listed in the Appendix A with additional relevant information. Furthermore, the compositions of the buffers, solutions and media used are described.

3.1 Cultivation Methods

To prevent contamination, all steps for the cultivation of *E. coli* and *C. elegans* were performed using aseptic techniques.

3.1.1 Continuous Cultivation of *Caenorhabditis elegans*

3.1.1.1 Cultivation of *Escherichia coli* OP50

E. coli OP50 (Table A.2) is a uracil auxotroph bacterial strain, which was used as the food source for the continuous cultivation of *C. elegans* on nematode growth medium (NGM) agar plates (Chapter 3.1.1.2) [182, 184]. Initially, a starter culture was obtained from the *Caenorhabditis* Genetics Center (CGC). From this culture, single colonies were isolated on 2x yeast extract tryptone (YT) agar plates (Table A.21) using the quadrant streak technique followed by overnight incubation at 37 °C.

Subsequently, 3 ml of 2xYT medium (Table A.20) was inoculated with a single colony of the streak plate in a cell culture tube and incubated for 19 h at 37 °C and 300 rpm in a shaking incubator. 800 µl of this overnight culture was mixed with 200 µl glycerol for long term storage at -80 °C, of which 50 µl was used to inoculate fresh overnight cultures at a given time.

The overnight culture was further used for subcultivation. Accordingly, 200 ml of 2xYT medium was inoculated with 500 µl of the overnight culture in an Erlenmeyer flask and incubated for 6 h at 37 °C and 300 rpm in a shaking incubator. This subculture was divided into four centrifuge tubes of 50 ml each and centrifuged at 5000 x g for 5 min. Finally, the supernatant was removed and the bacterial pellets were each resuspended with 5 ml of 2xYT medium. The overnight culture and subculture were stored at 4 °C and used for up to one week.

3.1.1.2 Continuous Cultivation of *Caenorhabditis elegans* on *Escherichia coli* OP50 seeded Nematode Growth Medium Agar Plates

For the continuous cultivation of *C. elegans*, 600 µl of the *E. coli* OP50 subculture (Chapter 3.1.1.1) was evenly distributed on individual NGM agar plates (Table A.19). Next, the plates were left open in the sterile bench until completely dry and stored at room temperature (i. e. 20 ± 3 °C) for up to one week. In regular intervals, *C. elegans* nematodes were moved from old to freshly seeded plates by chunking and transferring a piece of agar using a sterile scalpel. These *C. elegans* containing agar plates were maintained at 20 °C.

For long-term storage of *C. elegans*, plates containing freshly starved young larvae (L1 and L2 stage) were washed with freezing buffer A (Table A.10). Subsequently, an equal volume of freezing buffer B (Table A.11) containing 30% glycerol was added. Aliquots were placed into an isopropanol-filled freezing container to ensure a freezing rate of -1 °C/min and stored at -80 °C [234].

3.1.2 Experimental Setup

3.1.2.1 Cultivation of *Escherichia coli* HT115(DE3)

Due to their ability to regulate gene expression of *C. elegans*, *E. coli* HT115(DE3) (Appendix A.2) bacteria containing L4440-plasmids were used as the food source for all conducted experiments of this work.

Incubation of these bacteria with isopropyl-β-D-thiogalactopyranoside (IPTG) induces the expression of the T7 RNA polymerase through activation of the upstream genomic lac promoter. In turn, the T7 RNA polymerase drives the expression of an insert, which corresponds to the sequence of a specific GOI, flanked by opposing T7 RNA polymerase promoter sites in the L4440-plasmid. Based on the RNase III deficiency of the bacterial strain, the thus formed dsRNA is not subject to degradation and can be introduced into *C. elegans* by feeding. The dsRNA is liberated through digestion of the respective bacteria and distributed to distinct tissues, eventually leading to the biological process of RNAi that results in a GOI knockdown (Chapter 1.7.3). In addition, the bacteria exhibit resistance to tetracycline and ampicillin based on their genomic- and plasmid DNA, respectively, which is utilized for selection (Figure 3.1) [184, 235, 236].

For *C. elegans*, the two commercially available *E. coli* HT115(DE3) RNAi feeding libraries generated by the Ahringer- and Vidal laboratories cover around 90 % of the approximately

20000 predicted protein-coding genes through distinct inserts in the containing L4440-plasmids [193, 237–239]. The relevant orthologs for this work are described in Chapter 1.7. Furthermore, a comprehensive list of the respective *E. coli* HT115(DE3) RNAi clones used for their regulation is shown in Table A.3.

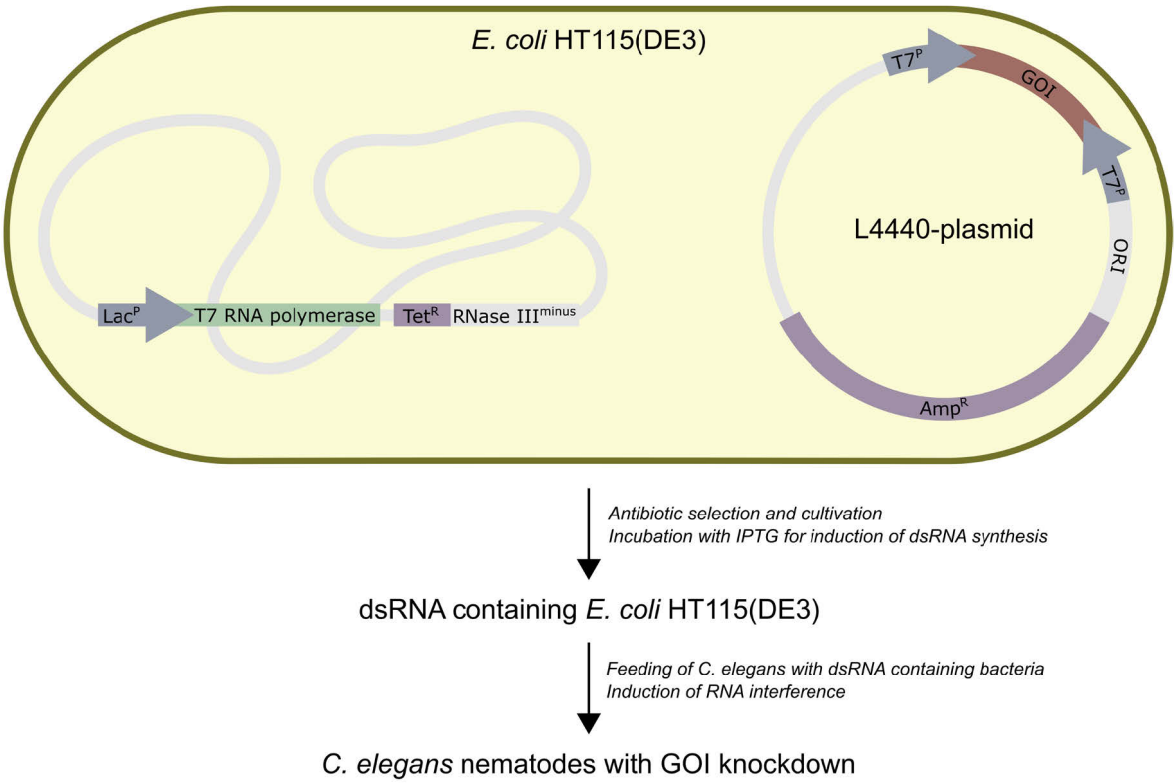

Figure 3.1 | Regulation of gene expression through RNAi by feeding *E. coli* HT115(DE3) RNAi clones
IPTG treatment of *E. coli* HT115(DE3) induces T7 RNA polymerase expression via upstream genomic lac promoter activation. T7 RNA polymerase binds to opposing $T7^P$ sites flanking the GOI sequence in the L4440-plasmid, resulting in expression of the respective dsRNA. After consumption and degradation of the bacteria, the dsRNA is incorporated by *C. elegans* and distributed to distinct tissues, leading to RNAi and finally to a GOI knockdown. Amp^R = ampicillin resistance, dsRNA = double-stranded RNA, GOI = gene of interest, IPTG = isopropyl-β-D-thiogalactopyranoside, Lac^P = lac promoter, ORI = origin of replication, RNAi = RNA interference, Tet^R = tetracycline resistance, $T7^P$ = T7 RNA polymerase promoter.

Initially, single colonies of the utilized RNAi clones and the corresponding vector control, characterized by the lack of an insert in the L4440-plasmid, were isolated on 2xYT agar plates containing selection antibiotics tetracycline (25 µg/ml) and ampicillin (100 µg/ml) (Table A.21) using the quadrant streak technique followed by overnight incubation at 37 °C. Subsequently, 2xYT medium (Table A.20) was supplemented with ampicillin (100 µg/ml), inoculated with a single colony of the streak plate in a cell culture tube or Erlenmeyer flask and incubated for 19 h at 37 °C and 300 rpm in a shaking incubator.

Since the RNAi feeding libraries were constructed on a large scale and may contain errors, the plasmids were extracted using the QIAprep Spin Miniprep Kit (Table A.6) according to the manufacturer's protocol and their inserts were sequenced by Microsynth Seqlab GmbH (Göttingen, DE) using standard M13 primers. Upon validation of the correct sequence via the Basic Local Alignment Search Tool (BLAST) of the National Center for Biotechnology Information (NCBI), 800 µl of the overnight culture was mixed with 200 µl glycerol for long term storage at -80 °C, which was used to streak fresh 2xYT agar plates containing selection antibiotics at a given time.

The overnight culture was also used for subcultivation and induction of dsRNA generation for individual experiments. Accordingly, 2xYT medium was supplemented with ampicillin (100 µg/ml) as well as isopropyl-β-D-thiogalactopyranoside (IPTG) (1 mM), inoculated with the overnight culture in a 1:11 dilution in an Erlenmeyer flask and incubated for 5 h at 37 °C and 300 rpm in a shaking incubator. This subculture was divided into 50 ml centrifuge tubes and centrifuged at 5000 x g for 5 min. Finally, the supernatant was removed and the bacterial pellets were resuspended with liquid NGM (Chapter 3.1.2.3, Table A.18). Whereas the streak plates were stored at 4 °C and used for up to 1 month, the overnight culture as well as the induced subculture were always freshly prepared for each experiment.

3.1.2.2 Age Synchronization of *Caenorhabditis elegans* by Hypochlorite Bleaching

To enable standardized experiments, age-synchronized populations of *C. elegans* nematodes were generated. First, agar plates containing large amounts of gravid hermaphrodites (Chapter 3.1.1.2) were washed with M9 buffer (Table A.8). The nematode suspension was subsequently collected in a 15 ml centrifuge tube using a glass Pasteur pipette (to prevent adhesion of nematodes to plastic) and filled up to 14 ml. Next, it was centrifuged at 500 x g for 2 min and the supernatant was aspirated to isolate the gravid hermaphrodites. After a second washing step with M9 buffer, the supernatant was aspirated to 3.5 ml. 1.5 ml of hypochlorite bleach solution (Table A.12) was added to lyse the gravid hermaphrodites and to extract their viable eggs. Accordingly, the centrifuge tube was shaken vigorously for approximately 6 minutes until a clear, slightly yellowish solution without visible nematode residues was formed. To stop the bleaching reaction and wash the eggs, the centrifuge tube was filled three times to 14 ml with M9 buffer, centrifuged at 4500 x g for 2 min and the supernatant was aspirated to approximately 1 ml. After a last refill with M9 buffer to 10 ml, 10 µl of

cholesterol solution (5 mg/ml) (Table A.7) was added due to the cholesterol-auxotrophy of *C. elegans* [184]. The suspension of viable eggs was incubated overnight at 20 °C in an overhead shaker at 25 rpm for larval hatching.

On the following day, the freshly hatched larvae were washed twice with 14 ml M9 buffer, centrifuged at 1500 x g for 2 min and the supernatant was aspirated to approximately 1 ml. Finally, the suspension was adjusted to a larval concentration of 10-15 larvae per 10 µl using a stereo microscope.

3.1.2.3 Cultivation of *Caenorhabditis elegans* in Liquid Nematode Growth Medium Supplemented with *Escherichia coli* HT115(DE3)

For all experiments, age-synchronized larvae were grown in liquid NGM (Table A.18) supplemented with *E. coli* HT115(DE3) bacteria (Chapter 3.1.2.1, Appendix A.2) as the food source. First, 100 µl of larvae suspension containing 100-150 larvae was seeded into each well of a 24-well plate. To achieve *ad libitum* feeding [240], the induced *E. coli* HT115(DE3) bacterial pellets were resuspended in freshly prepared liquid NGM to an optical density at 600 nm (OD_{600}) of 5, corresponding to approximately 4 x 10^9 bacteria/ml, and a volume of 440 µl NGM/bacteria suspension was added to each well. The well plate was placed in a cardboard box filled with a moistened paper towel to increase humidity and thus to minimize evaporation. Finally, the larvae were incubated for 44 h at 20 °C and 125 rpm until reaching the L4 stage.

Following the incubation, the media was exchanged to substitute live with heat-inactivated bacteria[8] to exclude bacterial metabolism of the applied substances of interest (e. g. 4-PBA, CA, etc.) (Table A.14), potentially resulting in higher bioavailability and the prevention of confounding metabolites [241]. To this end, the induced *E. coli* HT115(DE3) bacterial pellets were resuspended in 0.5 ml freshly prepared liquid NGM and placed in a water bath at 65 °C for 30 min. These inactivated bacteria were again diluted with liquid NGM to an OD_{600} of 5. Moreover, the L4 larvae were collected in a 15 ml centrifuge tube and washed 4 times with M9 buffer/Tween®20 (0.1% v/v) (Table A.9), centrifuged at 500 x g for 90 sec and the supernatant was aspirated to 0.5 ml. Subsequently, the centrifuge tube was filled twice with M9 buffer and the larvae were allowed to gravity settle for around 25 min to enable excretion of residual live bacteria in the intestine. The supernatant was aspirated to a volume

[8] Since bacteria appear to contain heat-labile nutrients for larval development of *C. elegans* (e. g. vitamin B2) [282], the nematodes could not be raised from the L1 stage with heat-inactivated bacteria.

corresponding to the number of wells used multiplied by 100 µl, enabling the redistribution of 100 µl larvae solution and 440 µl NGM/heat-inactivated bacteria suspension per fresh well. Depending on the experiment, 60 µl working solution of the respective substance of interest (Table A.14) was added, which contained a ten-fold enriched concentration compared to the final concentration in each well. Control nematodes were treated with identical volumes of solvent only. Finally, the nematodes were incubated for additional 3 to 4 day at 25 °C and 125 rpm until analysis.

On the day of analysis, the nematodes were collected in 15 ml centrifuge tubes and filtered[9] thrice through a 40 µm pluriStrainer® with M9 buffer to separate the age-synchronous adult nematodes from progeny and bacteria. After a final washing step with M9 buffer and centrifugation at 500 x g for 90 sec, the adult nematodes were used for their respective downstream applications.

3.2 Genetic Crossing of *Caenorhabditis elegans* strains

To enable genetic crossing of Aβ expressing GMC101 (*dvIs100 [unc-54p::A-beta-1-42::unc-54 3'-UTR; mtl-2p::GFP]*) nematodes with the fluorescent reporter strains IR2539 (*unc-119(ed3); Ex[myo-3p::TOMM-20::Rosella; unc-119(+)]*) and SJ4103 (*zcIs14 [myo3p::GFP(mit)*]) (Appendix A.1), males were generated by promoting X chromosome nondisjunction in germ cells undergoing meiosis through heat shocking L4 stage hermaphrodites for 5 h at 30 °C and subsequent propagation at 20 °C [242]. Next, a single GMC101 L4 stage hermaphrodite was mated with five IR2539 or SJ4103 males on a 35 mm NGM agar plate containing a 100 µl spot of *E. coli* OP50 bacteria as the food source. From the resulting F1 progeny that was consequently heterozygous for both transgenic constructs, single L4 stage hermaphrodites were isolated on individual NGM agar plates and allowed to self-fertilize. This step was repeated with L4 stage hermaphrodites of the following F2 progeny, which had a chance of homozygosity for both transgenic constructs [243]. Finally, the F3 progeny was screened for complete penetrance of the fluorescent marker transgenes[10] using an epifluorescence microscope, evidencing homozygosity and thus a successful genetic crossing.

[9] In contrast to sterilization of *C. elegans* via genetic approaches such as temperature sensitive mutants or 5-fluoro-2'-deoxyuridine (FUDR) incubation, filtering has been demonstrated to be a simple and effective mechanical method to maintain age-synchronization without affecting health markers [283, 284].

[10] I. e. intestinal GFP expression of the strain GMC101 along with Rosella biosensor or GFP expression in the mitochondria of body wall muscle cells of the strains IR2539 or SJ4103, respectively.

3.3 Computer-Based Analysis of Motility

Computer-based analysis of motility was used as a high-throughput method to assess the health of *C. elegans* and more specifically as a measure for Aβ proteotoxicity in GMC101 nematodes (Chapter 1.7.5, Appendix A.1). For each experimental group, 100 to 250 nematodes[11] were raised until day 7 and prepared for analysis as described in Chapter 3.1.2, with the supernatant being aspirated to 4.5 ml. Afterwards, the nematodes were mixed on an orbital shaker at 100 rpm for 1 min to stimulate their motility. Immediately after shaking, the nematodes were transferred to an unseeded 9.2 cm 2% agarose plate and staged for video recording with an imaging platform consisting of a 6 megapixel (MP) monochrome camera, a 16 mm fixed focal length (FL) objective and a diffuse LED illumination source, which was cleaned for each experimental group. After 90 sec, a 1 min video recording at 8-bit, 20 frames per sec (FPS) and M-JPEG compression with a quality of 95 was initiated using the FlyCapture®2 Software (Table A.23). Between the recordings of different experimental groups, the agarose plate was rinsed twice with M9 buffer to discard the imaged nematodes. Finally, nematode motility was analyzed using a modified version[12] of a custom software written in Python called the wide-field nematode tracking platform (WF-NTP) (Table A.23) [244]. For segmentation of nematodes, Gaussian adaptive thresholding was performed for each video frame. Next, the binary images were improved through post-processing via opening and closing operations. All remaining particles of similar size to nematodes were subsequently labeled. Afterwards, additional exclusion criteria that involve the maximum moved distance of particles between frames, the eccentricity of particles (termed worm-like in the code) and the minimum number of tracked frames were applied to further exclude background noise and contaminations (such as lint or small air bubbles). The remaining labeled particles were identified as individual nematodes and their positions were stored for each frame. Another important feature was the memory function, which allowed continuous tracking of individual nematodes without assignment of a new particle number after they crossed paths. Table 3.1 lists the used WF-NTP settings for all experiments.

[11] Since computer-based analysis of motility potentially enables the measurement of thousands of nematodes, a power analysis was performed to determine the optimal sample size. This calculation was based on initial experiments to unravel the average standard deviation and the measurement error of technical replicates for the parameter average speed. Accordingly, between 100 and 250 nematodes (depending on the downstream statistical analysis and thus on the experimental setup) were determined to be necessary to detect group differences larger than 15%, which were considered biologically relevant.

[12] The originally published code was modified to ensure compatibility with newer versions of Python, to preset analysis parameters and to implement the maximum speed as an additional motility measure.

Table 3.1 | Standard WF-NTP settings

Parameter	Setting
Video	
Start frame	0
Use frame	1200
FPS	20
Pixel to mm factor	0.029
Darkfield	Off
Locating	
Method	Keep dead
Z use images	N/A
Z pad/ dilate dead	N/A
Threshold	7
Opening	1
Closing	2
Skeletonize	Off
Prune size	N/A
Full prune	N/A
Filtering	
Minimum size (pixel)	60
Maximum size (pixel)	200
Worm-like (0-1)	0.91
Forming trajectories	
Maximum move distance (pixel)	10
Minimum length (frames)	151
Memory (frames)	200
Bends and velocity	
Bend threshold	2.8
Minimum bends	0.5
Frames to estimate velocity	150
Dead worm statistics	
Maximum bend per minute	5
Maximum velocity (mm/s)	1
Output	
Output frames	1
Font size	10

The software generates an output file that includes several parameters of motility. The eccentricity of each tracked nematode (i. e. a measure of the ratio of the major and minor ellipse axes) is an estimate of the respective body bends. Moreover, the average speed and the maximum speed are calculated based on the distance that the central point of individual nematodes travelled between frames. Finally, the distance travelled per body bend is derived from the first two parameters. The software further provides example images of the segmentation process based on the first video frame, which was used for quality control of video analysis.

3.4 Biochemical Methods

3.4.1 Quantification of Adenosine Triphosphate Levels in Nematode Homogenate via Luciferase Reaction

For the determination of ATP levels, nematode homogenates of Aβ expressing GMC101 nematodes (Chapter 1.7.5, Appendix A.1) were generated. To obtain sufficient quantities of ATP and protein, 1200 to 1800 nematodes were raised for each experimental group until day 7 and prepared for analysis as described in Chapter 3.1.2, using M9 buffer adjusted to pH 7.8[13]. Supernatants were aspirated and the nematodes were transferred into micro reaction tubes in a volume of 400 µl using low retention pipette tips moistened with M9 buffer/Tween®20 (0.1% v/v) (Table A.9) (to prevent adhesion of nematodes to plastic). Afterwards, the nematodes were flash-frozen in liquid nitrogen and subsequently lyzed by boiling in a water bath at 100 °C for 15 min. The lysates were centrifuged at 15.000 x g for 10 min at 4 °C and 250 µl of the supernatants were collected.

ATP levels in the nematode homogenates were determined using the ATP Bioluminescence-Assay-Kit CLS II (Table A.6), which is based on the ATP-dependent light emitting luciferase-catalyzed oxidation of luciferin. The luciferase reagent was prepared by dissolving the lyophilized powder in 10 ml ddH_2O and subsequent incubation for 5 min at 4 °C. Moreover, the lyophilized ATP standard was dissolved in M9 buffer (pH 7.8) to a concentration of 16.5 mM and used to generate a standard curve ranging from 1 nM to 10 µM.

The assay was set up in a white flat-bottom 96-well microplate with triplicates for each ATP standard concentration and sample. Per well, 50 µl ATP standard or sample were mixed with 50 µl luciferase reagent. Luminescence was measured in a Fluoroskan™ FL microplate

[13] pH 7.8 is the pH optimum of the luciferase reaction specified for the used ATP Bioluminescence-Assay-Kit CLS II.

fluorometer and luminometer (Table A.22) with an integration time of 1 s using the manufacturer's SkanIt 6 software (Table A.23). The remaining nematode homogenates were used to determine total protein concentrations (Chapter 3.4.2), which served as a measure of nematode count to normalize the ATP values of the samples.
Analysis of the measurements was performed using Microsoft Excel 2021 and GraphPad Prism 8.0.1 (Table A.23). In brief, after blanking all measures, the values of the ATP standards (concentration and luminescence) were log transformed to interpolate a linear standard curve. Finally, the logarithmic transformation of the interpolated nematode sample values was reverted and the ATP concentrations were normalized to the respective total protein concentration.

3.4.2 Quantification of Total Protein Concentration in Nematode Homogenate by Bicinchoninic Acid Assay

To normalize ATP values of the samples, the nematode homogenates were further used to determine total protein concentrations. To this end, the detergent-compatible two-component Pierce™ BCA Protein Assay Kit (Table A.6) was utilized, which is based on the reduction of Cu^{2+} to Cu^{1+} by proteins in an alkaline medium and the selective colorimetric detection of Cu^{1+} through chelation by bicinchoninic acid (BCA).
Following supplier instructions, the BCA working solution was produced by mixing reagents A and B in a ratio of 50:1 (v/v). Moreover, a bovine serum albumin (BSA) standard curve ranging from 25 µg/ml to 1500 µg/ml was generated using M9 buffer (pH 7.8) as the diluent. The assay was set up in a clear flat-bottom 96-well microplate with triplicates for each BSA standard concentration and sample. Per well, 25 µl BSA standard or sample were mixed with 200 µl BCA working solution. Absorption at 562 nm was measured in a Teca Sunrise™ microplate reader (Table A.22) using the manufacturer's Magellan software. Analysis of the measurements was performed using Microsoft Excel 2021 and GraphPad Prism 8.0.1 (Table A.23). In brief, after blanking all measures, the corrected values of the BSA standards were used to interpolate a second order polynomial (quadratic) standard curve. Finally, the interpolated protein concentrations of the samples were utilized as a measure of nematode count for normalization.

3.5 Epifluorescence Microscopy

For experiments based on epifluorescence microscopy, all working steps following the media exchange (Chapter 3.1.2.3) were performed under dimmed lighting conditions.

3.5.1 Quantification of Amyloid-β Aggregation with the Fluorescent Probe NIAD-4

Aβ aggregation was quantified using the fluorescent probe {[50-(p-hydroxyphenyl)-2,20-bithienyl-5-yl]-methylidene}-propanedinitrile (NIAD-4), which was developed as an *in vivo* marker that rapidly crosses the BBB and shows substantial enhancement of fluorescence with an emission maximum at 625 nm upon binding to amyloid fibrils[14] [245, 246].

Aβ expressing GMC101 and CL2122 control nematodes (Chapter 1.7.5, Appendix A.1) were raised until day 7 as described in Chapter 3.1.2. NIAD-4 working solution (Table A.15) was added in a 1:10 dilution to a final concentration of 1 µM (0.1% DMSO). After 4 h incubation at 25 °C and 125 rpm, the nematodes were collected in 15 ml centrifuge tubes, filtered and transferred to NGM agar plates seeded with 600 µl heat-inactivated bacteria (Chapter 3.1.1.2 & 3.1.2.3) for 20 h at 25 °C to remove residues of the fluorescent probe.

On the next day, the nematodes were again collected in 15 ml centrifuge tubes and washed thrice with M9 buffer. The supernatants were aspirated to 100 µl and the nematodes were anesthetized by addition of 11 µl sodium azide[15] (500 mM) (Table A.7). Following a short incubation, 30 µl of nematode suspensions were transferred onto labeled microscope slides and capped with high-precision cover slips.

The dye was visualized using an EVOS™ M5000 epifluorescence microscope equipped with an EVOS™ LED Light Cube RFP (excitation of 531 ± 40 nm, emission of 593 ± 40 nm), and a 10x magnification super-apochromatic coverslip-corrected dry objective (0.4 NA) (Table A.22). Nematodes with defects, such as internal hatching, a burst cuticle or excessive dye residue, as well as nematodes with overlapping signals due to close proximity were excluded. Ultimately, 16-bit RFP- and bright-field images of at least 20 nematodes per group were photographed using identical illumination parameters.

[14] However, NIAD-4 does not bind to Aβ oligomers, which are evidenced as the most toxic aggregation state in AD pathogenesis.

[15] Sodium azide (NaN_3) inhibits complex IV of the ETC and the ATP synthase [285].

The quantification of fluorescence intensity was done using ImageJ/Fiji (Table A.23). To this end, a custom user-guided macro was developed (Figure 3.2, https://github.com/StefanBaumanns/C.-elegans-ImageJ-Fiji-macros). In brief, segmentation of the head region of nematodes[16] was performed based on the recorded bright-field images through manual selection of the head until the end of the pharynx terminal bulb and subsequent automatic image processing. For pre-processing, a gaussian weighted median filter followed by an erosion operation and contrast enhancement via histogram stretching was utilized to enhance the outline of the nematodes. Next, thresholding was done using Huang's method and signals outside the initial selection were excluded. During post-processing, the resulting binary images were adjusted by multiple iterations of closing operations and filling holes of foreground elements. Finally, the extracted regions of interest (ROIs) were used to measure the mean red fluorescence intensity of individual GMC101 nematodes, after subtraction of the mean non-specific fluorescence of CL2122 nematodes that lack stainable Aβ.

[16] The analysis of fluorescence intensity was limited to the head region for every epifluorescence microscopy-based method due to several factors. First, *C. elegans* nematodes naturally exhibit relatively strong blue, green and red autofluorescence in the intestine depending on age and stress condition [286]. The Aβ expressing strain GMC101 further constitutively expresses an intestinal GFP selection marker (Chapter 1.7.5, Appendix A.1) that interferes with other green emitting fluorophores and potentially shows bleed-through to distinct fluorescent channels. Moreover, residues of fluorescent probes particularly accumulate in the intestine. Finally, the head region contains an enriched amount of body wall muscle cells and neurons relative to the rest of the body [187, 189].

A
GMC101 [unc-54p::Aβ-1-42::unc-54 3'-UTR + mtl-2p::GFP]
+
Incubation with red light emitting fluorescent probe
Epifluorescence microscopy
Bright-field
RFP-channel
Image analysis
Mean fluorescent probe fluorescence
B
① Subtraction of the background signal
② User selection of the head
③ Pre-processing
④ Feature extraction
⑤ Post-processing
⑥ Creation of a ROI outlining the head
⑦ User control of the final ROI
⑧ Transfer of the final ROI and signal quantification

Figure 3.2 | User-guided automated analysis of fluorescence intensity
(A) Aβ expressing GMC101 nematodes were incubated with red light emitting fluorescent probes (NIAD-4, TMRE, MTR CM-H_2Xros). Following the incubation, bright-field as well as RFP images were taken with an epifluorescence microscope at 10x magnification. Image analysis was performed using a custom user-guided ImageJ/Fiji macro to quantify the mean fluorescent probe fluorescence in the head region of the nematodes. (B) Segmentation of the head region of nematodes was done based on the recorded bright-field images through manual selection of the head until the end of the pharynx terminal bulb and subsequent automatic image processing. The extracted regions of interest were used to measure the mean NIAD-4 fluorescence of individual GMC101 nematodes, after subtraction of the mean non-specific fluorescence of CL2122 nematodes that lack stainable Aβ. For experiments with the fluorescent probes TMRE (Chapter 3.5.2) and MTR CM-H_2Xros (Chapter 3.5.3), the actual mean background fluorescence was used for subtraction. Furthermore, a modified version of this macro was used to quantify mitophagy in a genetic crossing of GMC101 with IR2539 nematodes, which express the dual colour-emission Rosella biosensor in mitochondria of body wall muscle cells (Chapter 3.5.5). In this case, additionally GFP images were taken and the manual selection of the head was limited to the beginning of the pharynx terminal bulb. For subtraction, the mean non-specific signal of nematodes that lost the transgene encoding the Rosella biosensor was used. Scale bar is 50 µm. Aβ = amyloid-β, GFP = green fluorescent protein, RFP = red fluorescent protein, ROI = region of interest.

3.5.2 Quantification of Mitochondrial Membrane Potential with the Fluorescent Probe Tetramethylrhodamine Ethyl Ester

The MMP was quantified using the cationic fluorescent probe tetramethylrhodamine ethyl ester (TMRE), which accumulates in mitochondria depending on their polarization and shows an emission maximum at 574 nm. Utilization of low concentrations of TMRE allows for measurements in the so-called non-quenching mode, in which depolarized (less negative) mitochondria will accumulate less cationic fluorescent probe and thus exhibit lower fluorescence [247].

Aβ expressing GMC101 nematodes (Chapter 1.7.5, Appendix A.1) were raised until day 6 as described in Chapter 3.1.2. TMRE working solution (Table A.17) was added in a 1:10 dilution to a final concentration of 50 nM (0.05% DMSO). After 20 h incubation at 25 °C and 125 rpm, the nematodes were collected in 15 ml centrifuge tubes, filtered and transferred to NGM agar plates seeded with 600 µl heat-inactivated bacteria (Chapter 3.1.1.2 & 3.1.2.3) for 2 h at 25 °C to remove residues of the fluorescent probe. Subsequently, the nematodes were again collected in 15 ml a centrifuge tubes and washed thrice with M9 buffer. The supernatant was aspirated to 50 µl and the nematodes were anesthetized by addition of 200 µl

levamisole[17] (20 mM) (Table A.7). Following a short incubation, 30 µl of nematode suspensions were transferred onto labeled microscope slides and capped with high-precision cover slips.

The imaging and analysis were performed as described for the quantification of Aβ aggregation in Chapter 3.5.1, with the modification that the actual mean signal of the background was used for correction.

3.5.3 Quantification of Mitochondrial Reactive Oxygen Species Levels with the Fluorescent Probe MitoTracker Red CM-H_2Xros

Mitochondrial ROS levels were quantified using the cationic fluorescent probe MitoTracker® Red (MTR) CM-H_2Xros, which accumulates in polarized[18] mitochondria and forms a fluorescent conjugate with thiol groups of mitochondrial proteins and peptides upon oxidation that exhibits an emission maximum at 599 nm [248, 249].

Aβ expressing GMC101 nematodes (Chapter 1.7.5, Appendix A.1) were raised until day 6 as described in Chapter 3.1.2. MTR CM-H_2Xros working solution (Table A.16) was added in a 1:10 dilution to a final concentration of 1 µM (0.1% DMSO). After 20 h incubation at 25 °C and 125 rpm, the nematodes were collected in 15 ml centrifuge tubes and filtered (Chapter 3.1.2.3). The supernatants were aspirated to 50 µl and the nematodes were anesthetized by addition of 200 µl levamisole (20 mM) (Table A.7). Following a short incubation, 30 µl of nematode suspensions were transferred onto labeled microscope slides and capped with high-precision cover slips. The imaging and analysis were performed as described for the quantification of Aβ aggregation in Chapter 3.5.1, with the modification that the actual mean signal of the background was used for correction.

[17] Levamisole is an agonist of ionotropic L-acetylcholine receptors at the *C. elegans* neuromuscular junction [287] that causes paralysis through overexcitation. It was used for all experiments involving mitochondria due to potential confounding effect of sodium azide on mitochondrial homeostasis.

[18] Since its accumulation in mitochondria is dependent on the MMP, the fluorescence of MTR CM-H_2Xros is only specific for mitochondrial ROS levels if the MMP is stable.

3.5.4 Measurement of Mitochondrial Morphology with a Mitochondrial Targeted Green Fluorescent Protein Marker

Mitochondrial morphology was quantified using a genetic crossing of Aβ expressing GMC101 with SJ4103 nematodes (Chapter 3.2, Appendix A.1), which express GFP in mitochondria of body wall muscle cells [250].

GMC101xSJ4103 hybrid nematodes were raised until day 6 as described in Chapter 3.1.2. They were collected in 15 ml centrifuge tubes and filtered (Chapter 3.1.2.3). Subsequently, the supernatants were aspirated to 50 µl and the nematodes were anesthetized by addition of 200 µl levamisole (20 mM) (Table A.7). Following a short incubation, the supernatant was aspirated to 100 µl and mixed with 100 µl iodixanol solution (60% w/v)/ OptiPrep™ [19] (Table A.5) to raise the refractive index of the medium to 1.38[20] in order to obtain images with lower spherical aberrations [251]. Furthermore, 5 µl 30 µm polystyrene micro particles (Table A.4) were added to slightly rotate the nematodes through nudging of the coverslip for better visualization of the body wall muscle cells. 30 µl of nematode suspensions were transferred onto labeled microscope slides and capped with high-precision cover slips. The GFP in mitochondria of body wall muscle cells was visualized using an EVOS™ M5000 epifluorescence microscope equipped with an EVOS™ LED Light Cube GFP (excitation of 482 ± 25 nm, emission of 524 ± 24 nm) and a 40x magnification super-apochromatic coverslip-corrected silicone oil immersion objective (1.25 NA) (Table A.22). Nematodes with defects, such as internal hatching or a burst cuticle, as well as nematodes with overlapping signals due to close proximity were excluded. Z-stacks of individual body wall muscle cells in the upper quadrants (Chapter 1.7.1.4) were taken with 300 nm spacing according to the Nyquist rate. For each experimental group at least 30 body wall muscle cells in total of at least 12 nematodes were photographed.

The Z-stacks were deconvolved[21] using Huygens Essential software version 20.04 (Table A.23). Further analysis was done using ImageJ/Fiji (Table A.23) with a custom user-guided macro (Figure 3.3, https://github.com/StefanBaumanns/C.-elegans-ImageJ-Fiji-macros). At

[19] This chemical was found be compatible with imaging of live specimen without any adverse effects [251].

[20] The adjusted refractive index thus better fitted the properties of *C. elegans* nematodes [288] and the silicone immersion oil.

[21] Deconvolution is a mathematical operation used, among other applications, for image restoration, in which it refers to the process of reversing the optical distortion that takes place in an optical system. Generally, this correction is based on the theoretically or experimentally determined point spread function (PSF) that describes the response of an optical imaging system to a point source of light.

first, maximum intensity projections (MIPs)[22] were created and single body wall muscle cells were outlined by manual selection. For pre-processing, two iterations of bilateral filtering were followed by background subtraction using the rolling ball algorithm. Furthermore, an unsharp mask was used to enhance the edges of mitochondria. Signals outside the initial selection were excluded and the contrast was enhanced via histogram stretching. Local thresholding was done using Phansalkar's algorithm. During post-processing, the resulting binary images were adjusted by filling holes of foreground elements and adjustable watershed. Finally, mitochondria were segmented as individual objects and multiple parameters with relevance for mitochondrial dynamics were collected.

In brief, the mitochondrial coverage is based on the area of a muscle cell covered by mitochondria and serves as a measure of mitochondrial mass and biogenesis. Additionally, the count of mitochondria normalized to the size of the corresponding muscle cell as well as the size of individual mitochondria directly indicate shifts towards mitochondrial fission (i. e. smaller more numerous mitochondria) or fusion (i. e. larger and fewer mitochondria), respectively. In contrast to mitochondrial fission that promotes the generation of less elongated mitochondria, fusion is associated with the formation of branched mitochondrial networks, which can be characterized by different shape descriptors. The aspect ratio is defined as the ratio of the major and minor axis of an ellipse fit to an object. With the minimum value of 1 for a perfect circle, higher values indicate elongated objects (e. g. mitochondria). Finally, the form factor (perimeter^2/(4π*area)) is the inverse of circularity and also shows a minimum value of 1 for a perfect circle. As it is based on an object's perimeter, higher values indicate more complex or more branched objects [252].

[22] Thus, the macro analyzes mitochondrial morphology in 2D, which is feasible due to lack of superposition of mitochondria in body muscle cells of *C. elegans*.

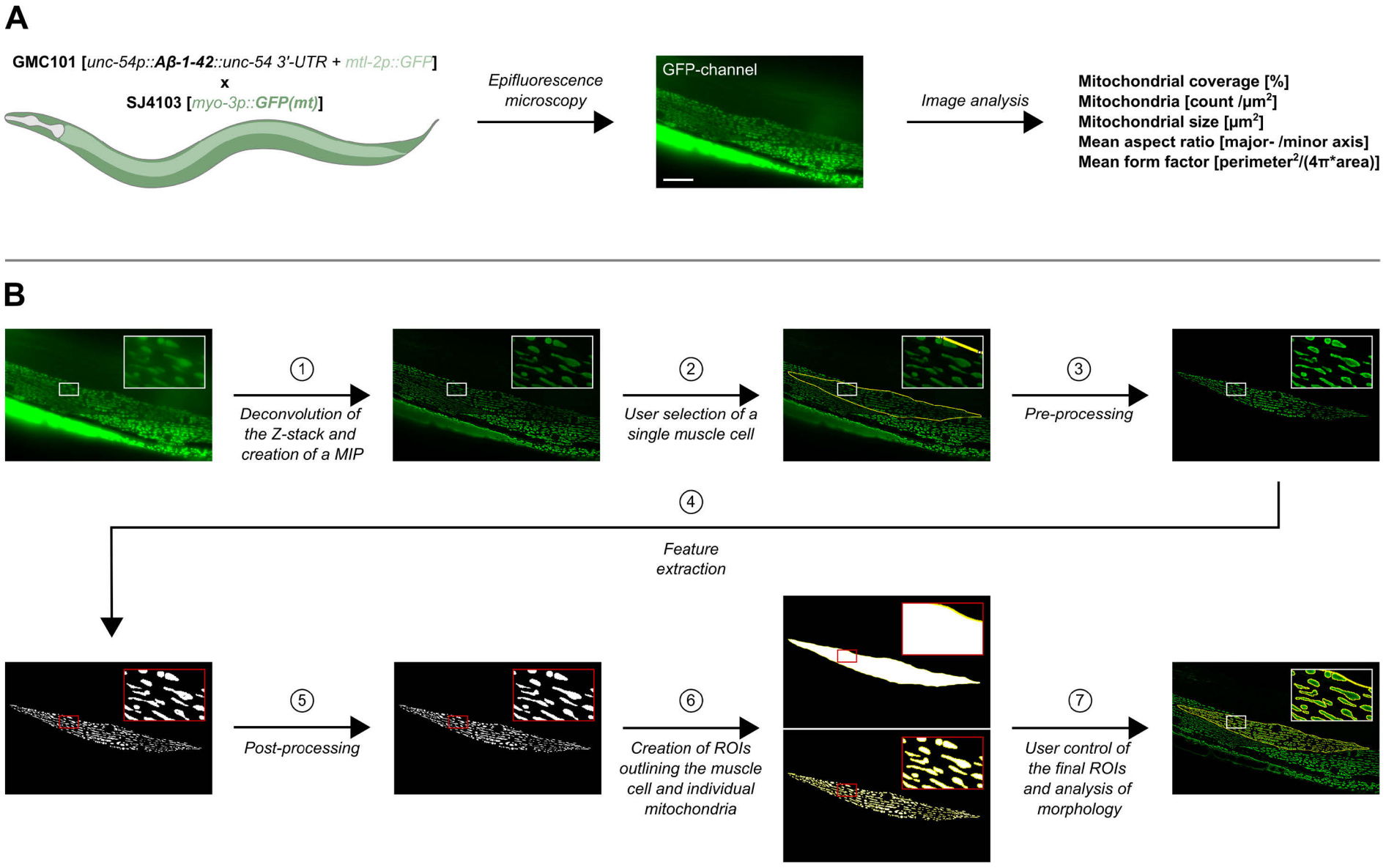
A
GMC101 [unc-54p::Aβ-1-42::unc-54 3'-UTR + mtl-2p::GFP]
x
SJ4103 [myo-3p::GFP(mt)]
Epifluorescence microscopy
GFP-channel
Image analysis
Mitochondrial coverage [%]
Mitochondria [count /µm²]
Mitochondrial size [µm²]
Mean aspect ratio [major- /minor axis]
Mean form factor [perimeter²/(4π*area)]
B
1
Deconvolution of the Z-stack and creation of a MIP
2
User selection of a single muscle cell
3
Pre-processing
4
Feature extraction
5
Post-processing
6
Creation of ROIs outlining the muscle cell and individual mitochondria
7
User control of the final ROIs and analysis of morphology

Figure 3.3 | User-guided automated analysis of mitochondrial morphology

(A) Z-stack GFP images of Aβ expressing GMC101 nematodes crossed with SJ4103 nematodes, which express GFP in mitochondria of body wall muscle cells, were taken with an epifluorescence microscope at 40x magnification. Image analysis was performed using a custom user-guided ImageJ/Fiji macro to measure multiple parameters with relevance for mitochondrial dynamics. (B) The images were deconvolved and MIPs were created. Segmentation of mitochondria was achieved through manual selection of individual body wall muscle cells and automatic image processing. Scale bar is 25 µm. Aβ = amyloid-β, GFP = green fluorescent protein, MIP = maximum intensity projection, ROI = region of interest.

3.5.5 Measurement of Mitophagy with a Mitochondrial Targeted Rosella Biosensor

Mitophagy was quantified using a genetic crossing of Aβ expressing GMC101 with IR2539 nematodes (Chapter 3.2, Appendix A.1), which express the dual colour-emission Rosella biosensor in mitochondria of body wall muscle cells. The biosensor combines a pH-insensitive DsRed with a pH-sensitive green fluorescent protein (GFP) variant [253, 254]. A reduced pH due to lysosomal degradation of mitochondria leads to denaturation of the GFP variant, consequently resulting in a higher DsRed/GFP fluorescence ratio as a measure of mitophagy induction [254]. GMC101xIR2539 hybrid nematodes were raised until day 6 as described in Chapter 3.1.2. They were collected in 15 ml centrifuge tubes and filtered (Chapter 3.1.2.3). Subsequently, the supernatants were aspirated to 50 µl and the nematodes were anesthetized by addition of 200 µl levamisole (20 mM) (Table A.7). Following a short incubation, 30 µl of nematode suspensions were transferred onto labeled microscope slides and capped with high-precision cover slips.

The Rosella biosensor was visualized using an EVOS™ M5000 epifluorescence microscope equipped with an EVOS™ LED Light Cube RFP (excitation of 531 ± 40 nm, emission of 593 ± 40 nm), an EVOS™ LED Light Cube GFP (excitation of 482 ± 25 nm, emission of 524 ± 24 nm) and a 10x magnification super-apochromatic coverslip-corrected dry objective (0.4 NA) (Table A.22). Nematodes with defects, such as internal hatching, a burst cuticle or excessive off-target fluorescence[23], as well as nematodes with overlapping signals due to close proximity were excluded. Ultimately, 16-bit RFP-, GFP- and bright-field images of at least 30 nematodes per group were photographed using identical illumination parameters.

[23] Due to the weak expression of the Rosella biosensor, nematodes with strong autofluorescence or high expression of the intestinal GFP selection marker from the GMC101 genetic background were excluded from the analysis to prevent faulty quantification of mitophagy.

The quantification of fluorescence intensity was done using ImageJ/Fiji (Table A.23). To this end, a custom user-guided macro was developed (a modified version of the macro described in Figure 3.2, https://github.com/StefanBaumanns/C.-elegans-ImageJ-Fiji-macros). In brief, segmentation of the head region of nematodes was performed based on the recorded bright-field images through manual selection of the head until the beginning[24] of the pharynx terminal bulb and subsequent automatic image processing. For pre-processing, a gaussian weighted median filter followed by an erosion operation and contrast enhancement via histogram stretching was utilized to enhance the outline of the nematodes. Next, thresholding was done using Huang's method and signals outside the initial selection were excluded. During post-processing, the resulting binary images were adjusted by multiple iterations of closing operations and filling holes of foreground elements. Finally, the extracted ROIs were used to measure the mean red and green fluorescence intensity of individual GMC101xIR2539 nematodes, after subtracting the mean non-specific fluorescence intensity of nematodes lacking Rosella biosensor expression, characterized by a dumpy phenotype[25].

3.6 Measurement of Oxygen Consumption

Oxygen consumption of *C. elegans* was quantified using an Oxygraph-2k Clark-type electrode (Table A.22), which measures generation of a current based on an electron flow between a silver anode and a platinum cathode that is directly proportional to the oxygen partial pressure in the samples.

To obtain a sufficient signal, approximately 1000 Aβ expressing GMC101 nematodes (Chapter 1.7.5, Appendix A.1) were raised for each experimental group until day 7 and prepared for analysis as described in Chapter 3.1.2. The supernatant was completely aspirated and the nematodes were immersed in 4 ml MiR05 mitochondrial respiration medium (Table A.6). After a centrifugation step at 1200 x g for 2 min and repeated complete aspiration of the supernatant, 2.4 ml MiR05 was added. The nematode suspension was immediately transferred to a measuring chamber of the Oxygraph-2k and sealed by a plug. Measurements of

[24] In contrast to the other methods described before (chapter 3.5.1 - 3.5.3), the head was only selected until the beginning of the pharynx terminal bulb to avoid faulty quantification due to stray light of the bright intestinal off-target fluorescence in relation to the fluorescence of the Rosella biosensor.

[25] The genetic background of IR2539 nematodes is based on a *unc-119* mutant that is rescued by the transgenic construct. Since the transgenic construct was not chromosomally integrated, some of the nematodes lose their transgene over generations and exhibit a dumpy phenotype of substantially reduced body length based on the *unc-119* mutation.

15 minutes at 20 °C per experimental group as well as data analysis were performed using the supplied DatLab software version 7.4.0.4 (Table A.23). After each measurement, the chamber and plug were cleaned with 70% ethanol and ddH_2O. Finally, the number of measured nematodes was extrapolated through evaluation of six 50 µl aliquots of the nematode suspension for each experimental group to normalize the oxygen consumption.

3.7 Statistics

All experiments were conducted at least 3 times and statistically analyzed with GraphPad Prism version 8.0.1 (Table A.23). Outliers were removed using the ROUT method with the chance of false-positive detection limited to 1% [255]. Further statistical analysis was performed with either Student's t-test or one-way ANOVA followed by Sidak's post-hoc test. In cases of heteroscedasticity determined by Brown-Forsythe's and Bartlett's test, Welch's t-test or Welch's ANOVA followed by Tamhane's T2 ($n < 50$) or Games-Howell's ($n > 50$) post-hoc test was used. For experiments without regulation of gene expression, all groups were compared to the respective control. Group comparisons for RNAi experiments were performed between both groups of the vector control, the vector control without treatment vs. the RNAi group without treatment, and both RNAi groups. A p-value < 0.05 was considered as statistically significant.

For computer-based analysis of motility (Chapter 3.3) and epifluorescence microscopy-based methods (Chapter 3.5), only one representative result is shown. Unless otherwise stated, data are presented as the means ± SEM normalized to the mean of the respective control group. The graphical illustration was done using GraphPad Prism version 8.0.1 and Inkscape version 1.2.1 (Table A.23).

4 Results

The pathogenesis of AD is characterized by Aβ proteotoxicity and mitochondrial dysfunction, which reinforce each other in a vicious cycle. First, computer-based analysis of motility was used to investigate the effect of Aβ proteotoxicity on the phenotype of Aβ expressing GMC101 nematodes. Afterwards, the effects of the aromatic SCFA 4-PBA and the MCFA CA on motility were investigated. RNAi experiments were conducted to identify genes involved in proteostasis and mitochondrial homeostasis relevant to the effects of 4-PBA and CA. Finally, the motility assessment was further supplemented with methods based on genetic crossing, fluorescence microscopy and biochemical assays.

4.1 Effects of Human Amyloid-β on the Motility of *C. elegans* Nematodes

To establish the groundwork for upcoming experiments investigating the molecular effects of 4-PBA and CA on Aβ proteotoxicity, the Aβ expressing transgenic *C. elegans* strain GMC101 was phenotypically characterized compared to its corresponding control strain CL2122 (Figure 4.1). Computer-based analysis of motility revealed that the average speed of GMC101 was reduced by 0.17 mm/s, corresponding to a 79% decrease ($p < 0.0001$). Aβ proteotoxicity further impaired the maximum speed by 0.11 mm/s, which is equivalent to a 32% reduction ($p < 0.0001$). Surprisingly, GMC101 nematodes performed 8 more body bends per minute compared to its control strain (12%; $p = 0.0073$). The travelled distance per body bend of GMC101 nematodes, however, was decreased by 0.12 mm (52%; $p < 0,0001$), indicating that GMC101 nematodes either exert lower force per body bend or move less coordinated. Due to its sensitivity and higher measurement accuracy compared to the other parameters, the average speed was chosen as the relevant metric of Aβ proteotoxicity in all subsequent experiments.

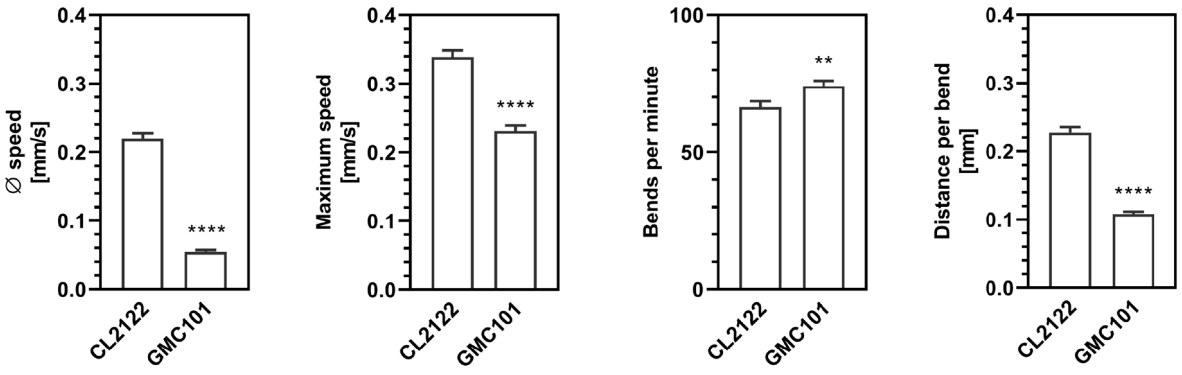

Figure 4.1 | Aβ proteotoxicity impairs the motility of *C. elegans* GMC101 nematodes

The average as well as maximum speed, the body bends per minute and the travelled distance per body bend of 7-day old nematodes of the Aβ expressing strain GMC101 and of its corresponding control strain CL2122 were compared using computer-based analysis of motility. Bar plots represent the mean ± SEM. Welch's t-test was performed. ** $p < 0.01$; **** $p < 0.0001$ versus CL2122 nematodes.

4.2 Effects of 4-Phenylbutyric Acid on Proteostasis and Mitochondrial Homeostasis in *C. elegans* GMC101 Nematodes

4.2.1 Effects of 4-Phenylbutyric Acid on Amyloid-β Proteotoxicity and Aggregation

4-PBA is an aromatic SCFA that may attenuate Aβ proteotoxicity through several mechanism, such as induction of molecular chaperones by inhibition of HDAC, acting as a chemical chaperone or providing energy via FAO (Chapter 1.5). First, it was tested whether incubation with 4-PBA affects the motility as a surrogate parameter for the health of Aβ expressing GMC101 nematodes. Figure 4.2A shows that 4-PBA improved the motility of GMC101 nematodes dose-dependently. The largest effect was achieved by incubation with 10 mM 4-PBA, leading to a 102% increase of the average speed ($p < 0.0001$), whereas the average speed of CL2122 control nematodes was reduced by 24% ($p = 0.0003$; Figure 4.2B), indicating a specific protective effect on Aβ proteotoxicity in GMC101 nematodes. Based on these results, a concentration of 10 mM 4-PBA was selected for further experiments with GMC101 nematodes.

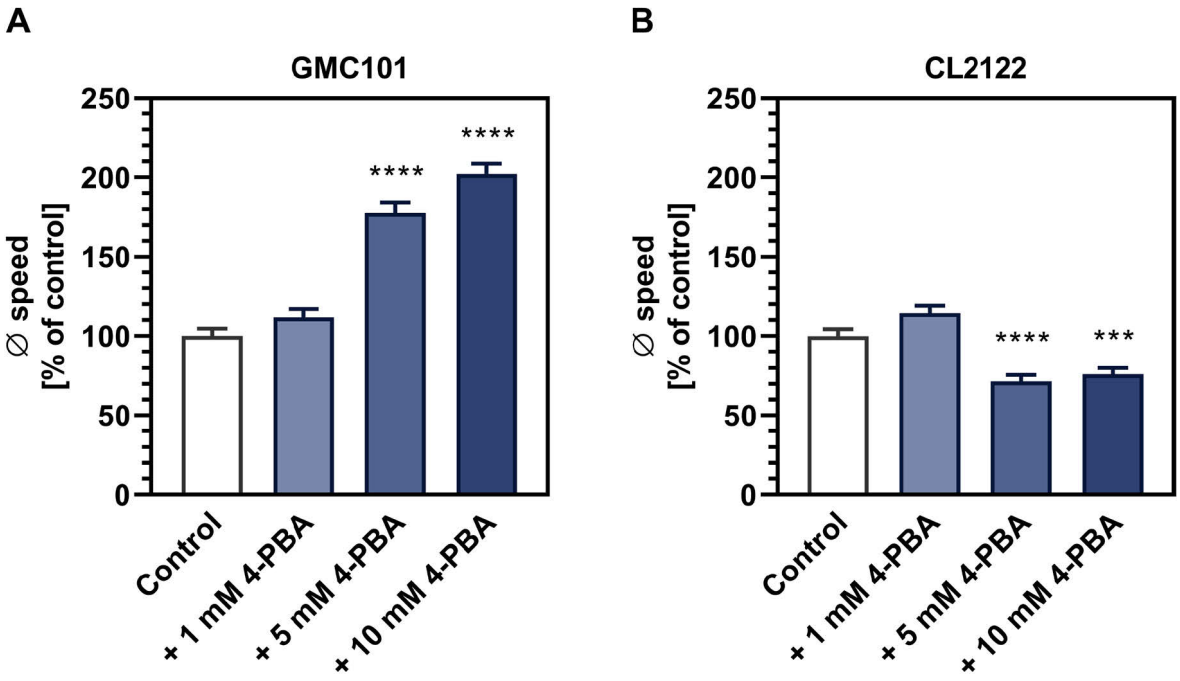

Figure 4.2 | 4-PBA dose-dependently attenuates Aβ proteotoxicity

Nematodes of the Aβ expressing strain GMC101 and of its corresponding control strain CL2122 were treated with liquid NGM (solvent control) or different concentrations of 4-PBA from the L4 stage (day 3). Finally, the average speed of 7-day-old nematodes was measured. All measurements were normalized to the mean of the control. Bar plots represent the normalized mean ± SEM. Welch's ANOVA with Games-Howell's post-hoc test was performed. *** $p < 0.001$; **** $p < 0.0001$ versus the control.

Since 4-PBA has been suggested to act as a chemical chaperone or inducer of molecular chaperones and the reduction of Aβ proteotoxicity is likely coupled to its aggregation, the latter was subsequently measured using the Aβ specific fluorescent probe NIAD-4. Figure 4.3 shows that incubation with 10 mM 4-PBA reduced the mean fluorescence of NIAD-4 by 68%, evidencing a decrease of Aβ aggregation in GMC101 nematodes ($p < 0.0001$).

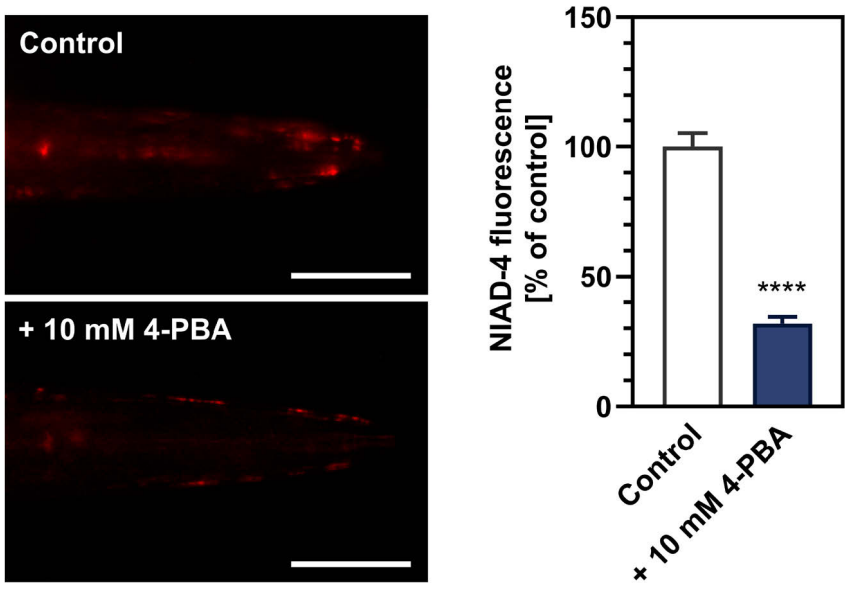

Figure 4.3 | 4-PBA reduces Aβ aggregation

Aβ expressing GMC101 nematodes were treated with liquid NGM (solvent control) or 10 mM 4-PBA from the L4 stage (day 3). At day 7, the nematodes were stained for 4 h with 1 µM of the Aβ specific fluorescent probe NIAD-4 (0.1% DMSO), followed by a 20 h period to remove fluorescent probe residues. Finally, the average NIAD-4 fluorescence of the nematodes was measured in the head region using epifluorescence microscopy and subsequent analysis in ImageJ/Fiji. The left panel displays representative fluorescence images. Scale bar is 50 µm. The right panel shows the quantification of the average fluorescence intensity. All measurements were normalized to the mean of the control. Bar plots represent the normalized mean ± SEM. Unpaired t-test was performed. **** $p < 0.0001$ versus the control.

4.2.2 Role of the Proteostasis Network for the Protective Effect of 4-Phenylbutyric Acid

Based on the findings that 4-PBA reduces Aβ proteotoxicity as well as aggregation and the proposed link of HDAC inhibition to activation of the proteostasis network (Chapter 1.5.2), the role of the proteostasis network for the protective effect of 4-PBA was further investigated. To this end, major transcription factors of the compartment specific stress response pathways (Chapter 1.2.2-1.2.4) were regulated using RNAi. First, knockdown of *hsf-1*, an ortholog of human *HSF1* that is essential for the HSR, reduced the average speed of GMC101 nematodes by 35% ($p < 0.0001$) and abolished the motility increase by 4-PBA incubation (Figure 4.4A). In contrast, the protective effect of 4-PBA was independent of *atf-6* and *atfs-1*, encoding for major transcription factors involved in the UPR^{ER} and UPR^{mt}, respectively (Figure 4.4B & C).

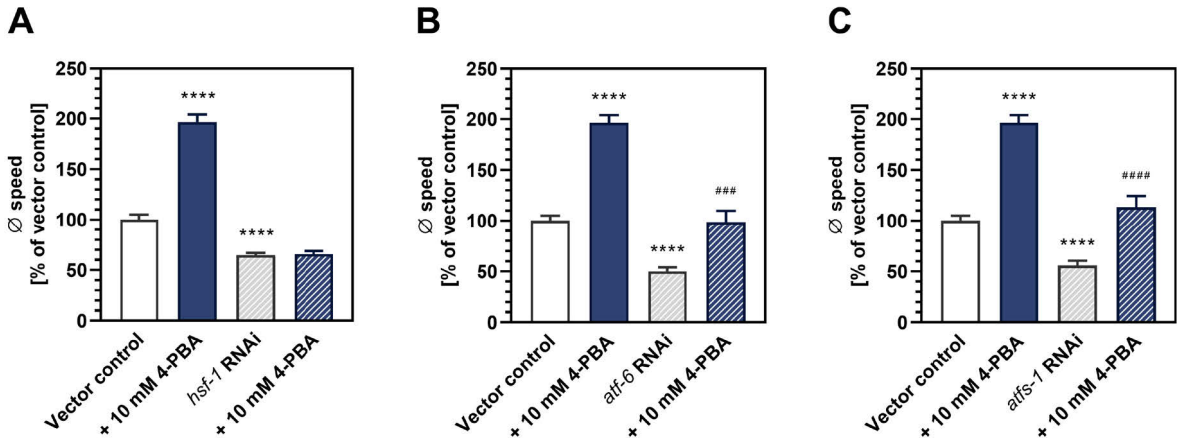

Figure 4.4 | Knockdown of *hsf-1*, the major transcription factor of the HSR, abolishes the motility increase by 4-PBA incubation

(A) Aβ expressing GMC101 nematodes were subjected to the *E. coli* HT115 vector control or *hsf-1* RNAi from the L4 stage (day 3). Moreover, nematodes were subjected to *E. coli* HT115 vector control (B) *atf-6* RNAi or (C) *atfs-1* RNAi from the L1 stage (day 1). All nematodes were treated with liquid NGM (solvent control) or 10 mM 4-PBA from the L4 stage. Finally, the average speed of 7-day-old nematodes was measured. All measurements were normalized to the mean of the vector control. Bar plots represent normalized mean ± SEM. Welch's ANOVA with Games-Howell post-hoc test was performed. **** $p < 0.0001$ versus vector control. #### $p < 0.0001$ versus RNAi.

Next, Figure 4.5 shows that the Aβ aggregation decreasing effect of 4-PBA was also abolished by *hsf-1* RNAi. Consequently, this evidence suggests that the effect of 4-PBA on Aβ proteotoxicity and aggregation depends on the HSR and may induce the expression of molecular chaperones rather than acting as a chemical chaperone.

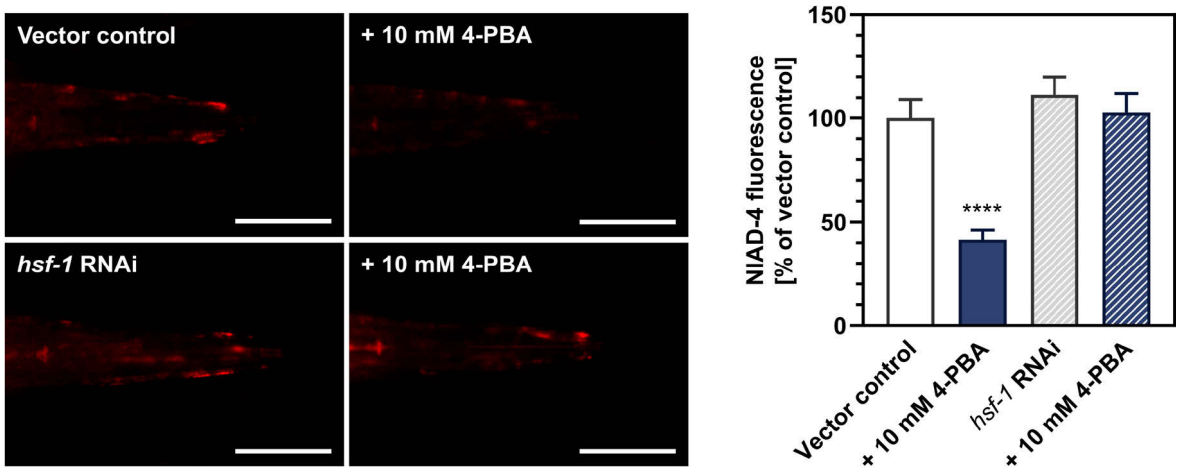

Figure 4.5 | Knockdown of *hsf-1* abolishes the Aβ aggregation decreasing effect of 4-PBA

Aβ expressing GMC101 nematodes were subjected to the *E. coli* HT115 vector control or *hsf-1* RNAi and treated with liquid NGM (solvent control) or 10 mM 4-PBA from the L4 stage (day 3). At day 7, the nematodes were stained for 4 h with 1 µM of the Aβ specific fluorescent probe NIAD-4 (0.1% DMSO), followed by a 20 h period to remove fluorescent probe residues. Finally, the average NIAD-4 fluorescence of the nematodes was measured in the head region using epifluorescence microscopy and subsequent analysis in ImageJ/Fiji. The left panel displays representative fluorescence images. Scale bar is 50 µm. The right panel shows the quantification of the average fluorescence intensity. All measurements were normalized to the mean of the solvent control. Bar plots represent the normalized mean ± SEM. One-way ANOVA with Sidak's post-hoc test was performed. **** $p < 0.0001$ versus the vector control.

To investigate the potential link between activation of the HSR and class I as well as class IIa HDAC inhibition, the latter was modeled via knockdown using RNAi. Knockdown of *hda-1*, encoding an ortholog for human HDAC2, increased the average speed of GMC101 nematodes by 109% ($p < 0.0001$; Figure 4.6A), whereas RNAi against the other respective *C. elegans* HDAC orthologs resulted in an impaired motility (data not shown). In analogy to the motility enhancing properties of 4-PBA, this protective effect of *hda-1* RNAi was also abolished by simultaneous knockdown of *hsf-1*, thus suggesting that 4-PBA and *hda-1* RNAi act through the same molecular mechanism of HSF-1 activation. This was further evidenced by a lacking additive effect of both interventions combined (Figure 4.6B).

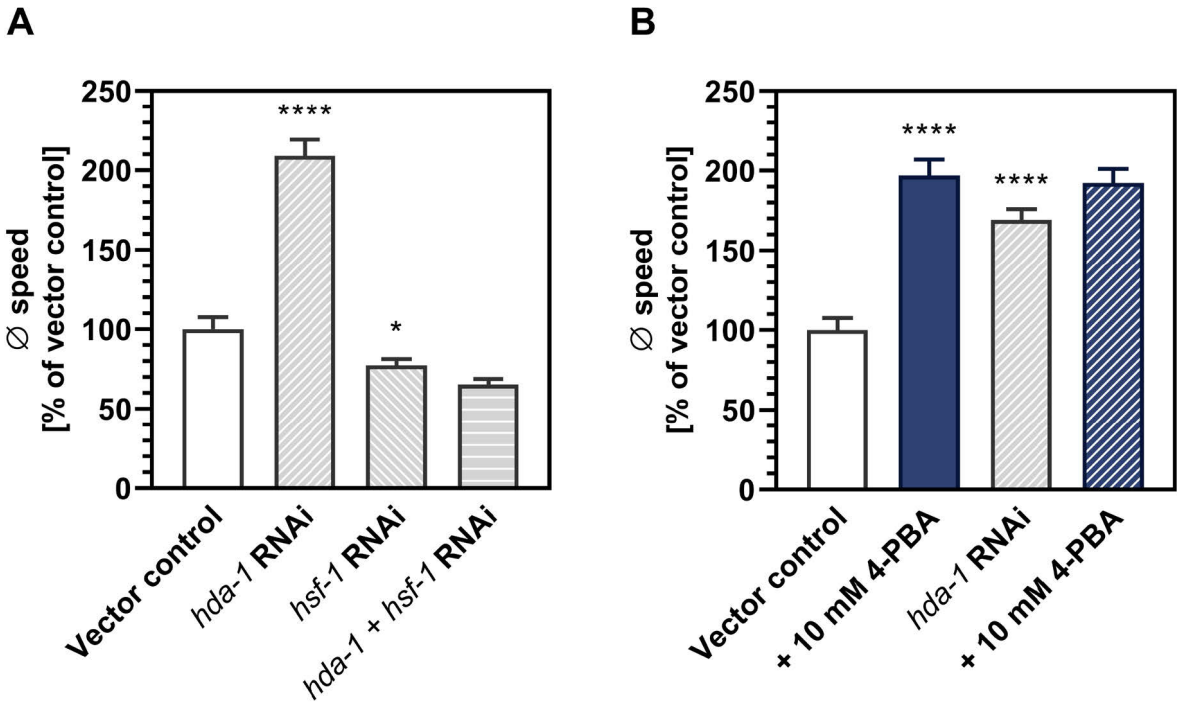

Figure 4.6 | Knockdown of the HDAC2 ortholog *hda-1* also increases motility in dependence on *hsf-1* and lacks an additive effect with 4-PBA incubation

(A) Aβ expressing GMC101 nematodes were subjected to the *E. coli* HT115 vector control, 50% *hda-1* RNAi, 50% *hsf-1* RNAi or an equal mixture of both RNAi from the L4 stage (day 3). (B) Nematodes were subjected to the *E. coli* HT115 vector control or 50% *hda-1* RNAi and treated with liquid NGM (solvent control) or 10 mM 4-PBA from the L4 stage (day 3). Finally, the average speed of 7-day-old nematodes was measured. All measurements were normalized to the mean of the vector control. Bar plots represent normalized mean ± SEM. Welch's ANOVA with Games-Howell post-hoc test was performed. * $p < 0.05$; **** $p < 0.0001$ versus vector control.

4.2.3 Contribution of Energy Metabolism and Mitochondrial Quality Control to the Protective Effect of 4-Phenylbutyric Acid

As described in Chapter 1.4, Aβ proteotoxicity and mitochondrial dysfunction mutually aggravate each other in a vicious cycle. Consequently, it was tested whether the attenuation of Aβ proteotoxicity by 4-PBA was associated with improved mitochondrial function. Figure 4.7A shows that incubation of GMC101 nematodes with 4-PBA increased the ATP levels by 74% ($p = 0.0162$). Moreover, improvement of mitochondrial function was reflected by an enhanced MMP, indicated by 423% greater average TMRE fluorescence ($p < 0.0001$; Figure 4.7B).

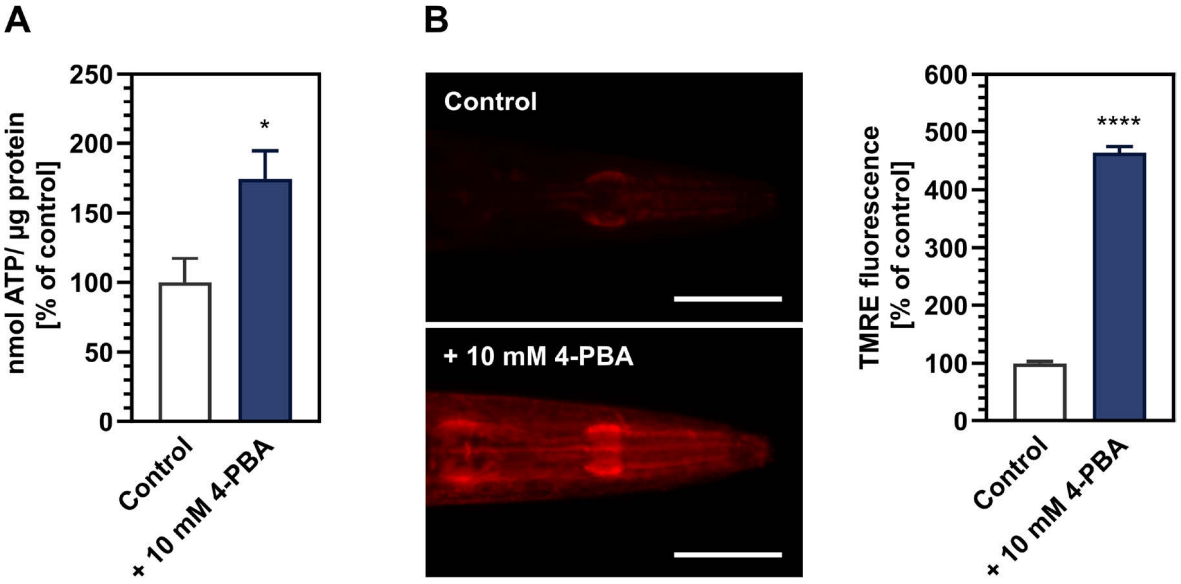

Figure 4.7 | 4-PBA improves mitochondrial function

Aβ expressing GMC101 nematodes were treated with liquid NGM (solvent control) or 10 mM 4-PBA from the L4 stage (day 3). (A) At day 7, nematode homogenates were generated and ATP levels were quantified using a bioluminescence-assay in relation to protein concentrations. (B) At day 6, the nematodes were stained for 24 h with 50 nM of the MMP sensitive fluorescent probe TMRE (0.05% DMSO), followed by a 2 h period to remove fluorescent probe residues. Finally, the average TMRE fluorescence of the nematodes was measured in the head region using epifluorescence microscopy and subsequent analysis in ImageJ/Fiji. The left panel displays representative fluorescence images. Scale bar is 50 µm. The right panel shows the quantification of the average fluorescence intensity. All measurements were normalized to the mean of the control. Bar plots represent the normalized mean ± SEM. Unpaired t-test was performed. * $p < 0.05$; **** $p < 0.0001$ versus the control.

Nevertheless, additional mechanisms could also account for the improvement of mitochondrial function following 4-PBA incubation. Since 4-PBA is partly metabolized to PAA via FAO, it was plausible to conclude that this may promote ATP synthesis and motility. Despite being statistically significant, knockdown of *acdh-2*, an ortholog of human short-chain *ACDH*, reduced the motility increasing effect of 4-PBA (Figure 4.8A). This reduced effect of 4-PBA on motility was evidence by quantification of the effect size parameter Cohen's d[26], which decreased from 1.31 to 0.45 by knockdown of *acdh-2*. The same outcome was observed using RNAi against the other three short-chain *ACDH* orthologs of *C. elegans*, namely *acdh-1*, *acdh-3* and *acdh-4* (data not shown). Accordingly, the remaining motility increase by 4-PBA incubation under RNAi versus *acdh-2* could also be explained by the occurrence of these *acdh* gene variants. Moreover, knockdown of *nuo-3*, encoding an

[26] Cohen's *d* is a measure of effect size and thus independent of sample size, which is derived from the mean difference between two groups divided by their SD.

ortholog of complex I of the ETC, receiving reduction equivalents from NADH + H^+, and *mev-1*, encoding an ortholog of $FADH_2$ accepting complex II of the ETC, abolished the motility increasing effect of 4-PBA (Figure 4.8B & C), further demonstrating its dependency on energy generation by FAO.

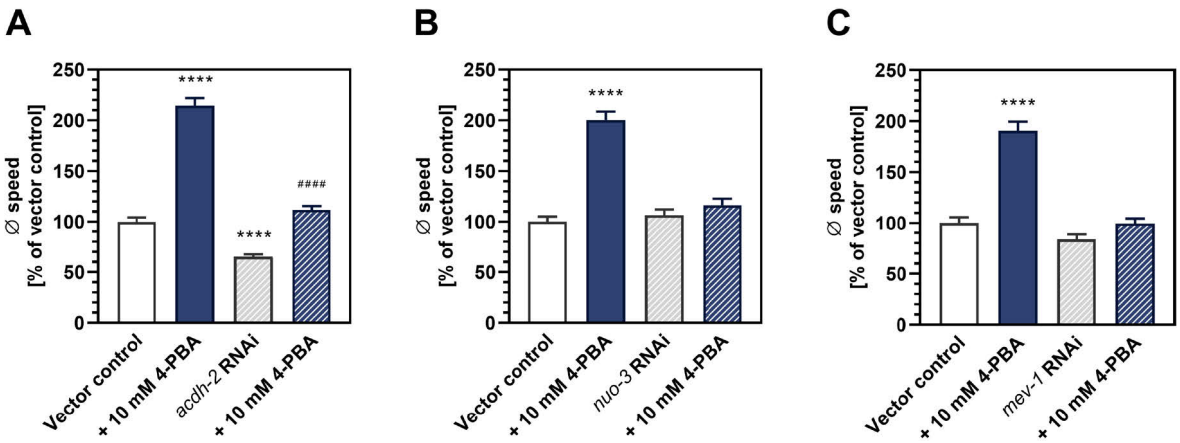

Figure 4.8 | Knockdown of genes involved in FAO or complex I and II of the ETC decreases the protective effect of 4-PBA

Aβ expressing GMC101 nematodes were subjected to the *E. coli* HT115 vector control, (A) *acdh-2* RNAi, (B) *nuo-3* RNAi or (C) *mev-1* RNAi from the L1 stage (day 1) and treated with liquid NGM (solvent control) or 10 mM 4-PBA from the L4 stage (day 3). Finally, the average speed of 7-day-old nematodes was measured. All measurements were normalized to the mean of the vector control. Bar plots represent normalized mean ± SEM. Welch's ANOVA with Games-Howell post-hoc test was performed. **** $p < 0.0001$ versus the vector control. #### $p < 0.0001$ versus RNAi.

Also consistent with the importance of energy supply via FAO, direct incubation with PAA, the metabolite of 4-PBA oxidation, resulted in a significantly reduced effect on motility compared to its precursor ($p < 0.0001$; Figure 4.9).

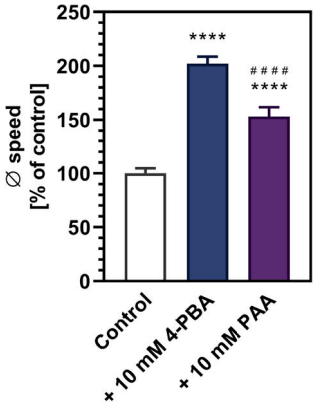

Figure 4.9 | PAA shows a lower motility increasing effect than its precursor 4-PBA

Aβ expressing GMC101 nematodes were treated with liquid NGM (solvent control), 10 mM 4-PBA or 10 mM PAA from the L4 stage (day 3). Finally, the average speed of 7-day-old nematodes was measured. All measurements were normalized to the mean of the control. Bar plots represent the normalized mean ± SEM. Welch's ANOVA with Games-Howell's post-hoc test was performed. **** $p < 0.0001$ versus the control. #### $p < 0.0001$ versus 10 mM 4-PBA.

Another mechanism that may account for the improvement of mitochondrial function by 4-PBA incubation is the activation of mitochondrial quality control. Similar to *acdh-2*, knockdown of *drp-1*, encoding an ortholog of the mitochondrial fission protein DRP1, reduced the protective effect of 4-PBA (Figure 4.10A), evidenced by a decrease in Cohen's *d* from 1.53 to 0.46. Furthermore, whereas knockdown of *dct-1*, encoding an ortholog of the OMM mitophagy receptor BNIP3, abolished the motility increasing effect of 4-PBA, it was unaffected by RNAi against *pink-1*, which encodes the essential ortholog of PINK1/Parkin-mediated mitophagy (Figure 4.10B & C). Accordingly, these data indicate that 4-PBA may promote mitochondrial fission and receptor-mediated mitophagy.

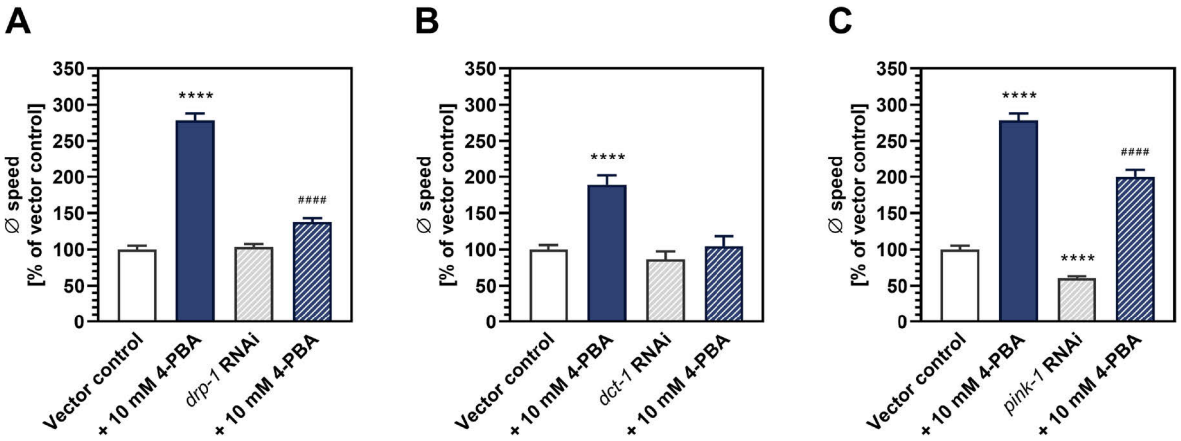

Figure 4.10 | Knockdown of genes involved in mitochondrial fission and receptor-mediated mitophagy reduces the motility increase by 4-PBA incubation

Aβ expressing GMC101 nematodes were subjected to the *E. coli* HT115 vector control, (A) *drp-1* RNAi, (B) *dct-1* RNAi or (C) *pink-1* RNAi from the L1 stage (day 1) and treated with liquid NGM (solvent control) or 10 mM 4-PBA from the L4 stage (day 3). Finally, the average speed of 7-day-old nematodes was measured. All measurements were normalized to the mean of the vector control. Bar plots represent normalized mean ± SEM. Welch's ANOVA with Games-Howell's post-hoc test was performed. **** $p < 0.0001$ versus the vector control. #### $p < 0.0001$ versus RNAi.

To validate the induction of mitochondrial fission, mitochondrial morphology was directly assessed using a genetic crossing of GMC101 with SJ4103 nematodes, expressing GFP in mitochondria of body wall muscle cells. Figure 4.11 demonstrates that 4-PBA incubation results in smaller but more numerous mitochondria ($p < 0.0001$), confirming the induction of mitochondrial fission.

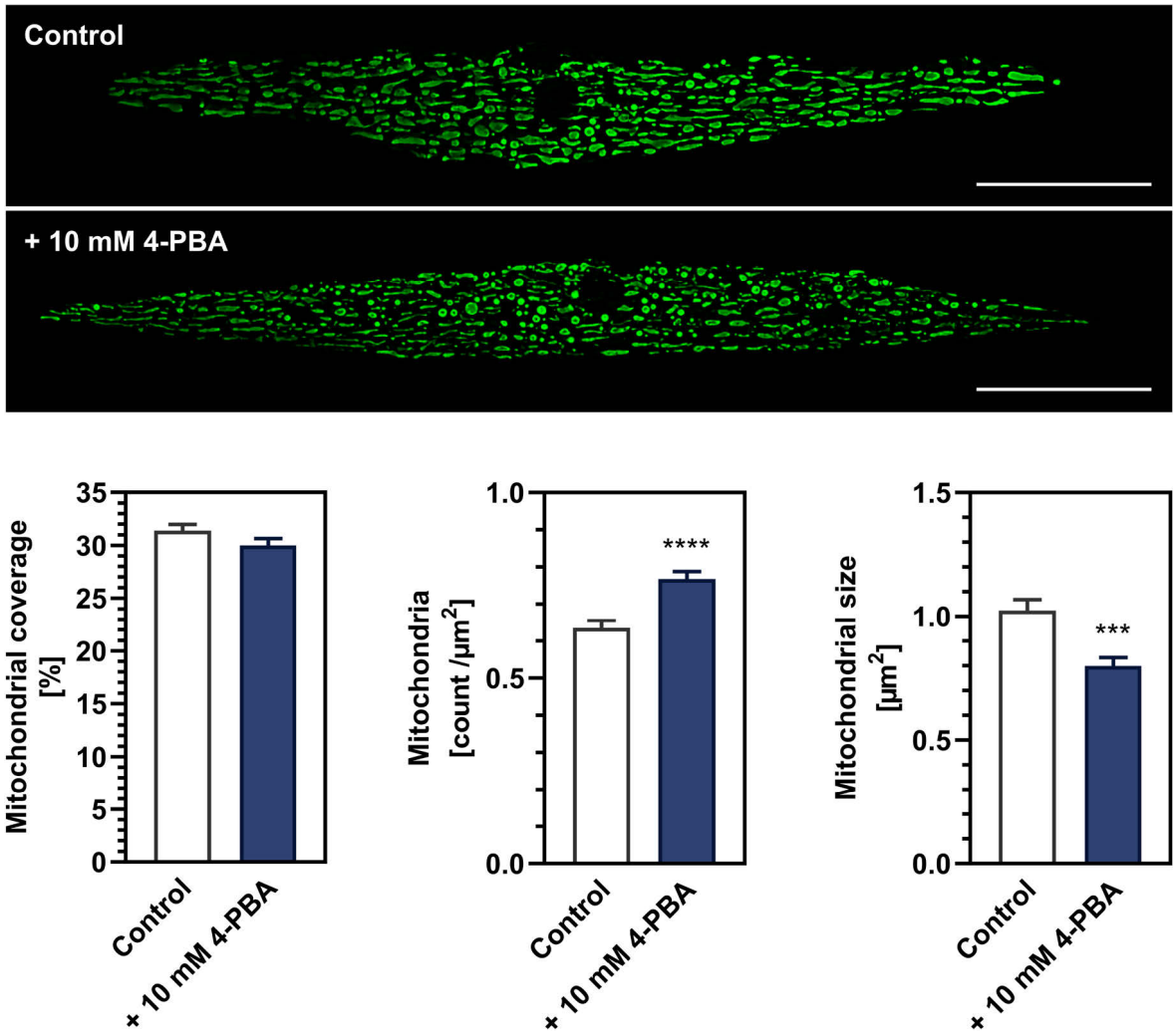

Figure 4.11 | 4-PBA promotes mitochondrial fission

Aβ expressing GMC101 nematodes were crossed with SJ4103 nematodes, which express GFP in mitochondria of body wall muscle cells. The nematodes were treated with liquid NGM (solvent control) or 10 mM 4-PBA from the L4 stage (day 3). At day 7, the morphology of mitochondria in individual body wall muscle cells was measured using epifluorescence microscopy, deconvolution and subsequent analysis in ImageJ/Fiji. The upper panel displays representative fluorescence images. Scale bar is 25 µm. The lower panel shows the quantification of mitochondrial morphology. Bar plots represent the mean ± SEM. Unpaired t-test was performed. *** $p < 0.001$; **** $p < 0.0001$ versus the control.

Finally, 4-PBA increased mitophagy, evidenced by a 22% greater DsRed/GFP fluorescence ratio in GMC101 crossed with IR2539 nematodes that express the Rosella biosensor in mitochondria of body wall muscle cells ($p = 0.0489$; Figure 4.12). Since incubation with 4-PBA concurrently did not decrease mitochondrial coverage (Figure 4.11), it is further indicated that mitochondrial biogenesis was induced.

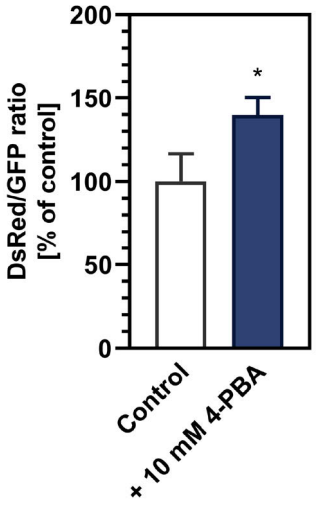

Figure 4.12 | 4-PBA induces mitophagy

Aβ expressing GMC101 nematodes were crossed with IR2539 nematodes, which express the Rosella biosensor in mitochondria of body wall muscle cells. The nematodes were treated with liquid NGM (solvent control) or 10 mM 4-PBA from the L4 stage (day 3). At day 6, the average DsRed and GFP fluorescence of the nematodes was measured in the head region using epifluorescence microscopy and subsequent analysis in ImageJ/Fiji. A higher DsRed/GFP ratio indicates induction of mitophagy due to quenching of the pH-sensitive GFP fluorescence in acidic lysosomes. All measurements were normalized to the mean of the control. Bar plots represent the normalized mean ± SEM. Unpaired t-test was performed. * $p < 0.05$ versus the control.

In summary, the presented data suggest that 4-PBA improves mitochondrial function through different mechanisms that involve restoration of proteostasis, energy supply via FAO and the mitochondrial quality control.

4.3 Effects of Caprylic Acid on Proteostasis and Mitochondrial Homeostasis in *C. elegans* GMC101 Nematodes

4.3.1 Effects of Caprylic Acid on Amyloid-β Proteotoxicity and Aggregation

CA is a MCFA that could potentially attenuate Aβ proteotoxicity through several mechanism, such as biogenesis of ALA and BHB or providing energy via FAO (Chapter 1.6). First, it was tested whether CA positively affects the motility as a surrogate parameter for the health of Aβ expressing GMC101 nematodes. Figure 4.13A shows that CA indeed improved the motility of GMC101 nematodes dose-dependently. The largest effect was achieved by incubation with 7.5 mM CA, leading to a 56% increase of the average speed ($p < 0.0001$), whereas the average speed of CL2122 control nematodes was only raised by 17% ($p = 0.0027$; Figure 4.13B), indicating a specific protective effect on Aβ proteotoxicity in GMC101 nematodes. Based on these results, a concentration of 7.5 mM CA was selected for further experiments with GMC101 nematodes.

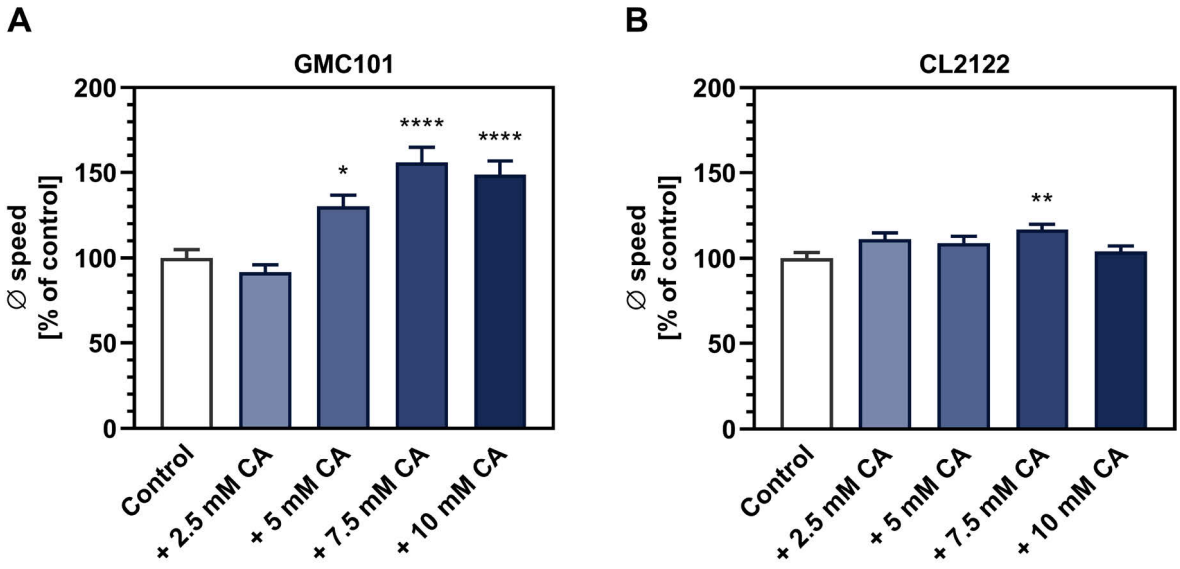

Figure 4.13 | CA dose-dependently attenuates Aβ proteotoxicity

Nematodes of the Aβ expressing strain GMC101 and of its corresponding control strain CL2122 were treated with M9 buffer (solvent control) or different concentrations of CA from the L4 stage (day 3). Finally, the average speed of 7-day-old nematodes was measured. All measurements were normalized to the mean of the control. Bar plots represent the normalized mean ± SEM. Welch's ANOVA with Games-Howell's post-hoc test was performed. * $p < 0.05$; ** $p < 0.01$; **** $p < 0.0001$ versus the control.

Since the reduction of Aβ proteotoxicity is likely coupled to its aggregation, the latter was subsequently measured using the Aβ specific fluorescent probe NIAD-4. Figure 4.14 shows that incubation with 7.5 mM CA reduced the mean fluorescence of NIAD-4 by 39%, evidencing a decrease of Aβ aggregation ($p < 0.0001$).

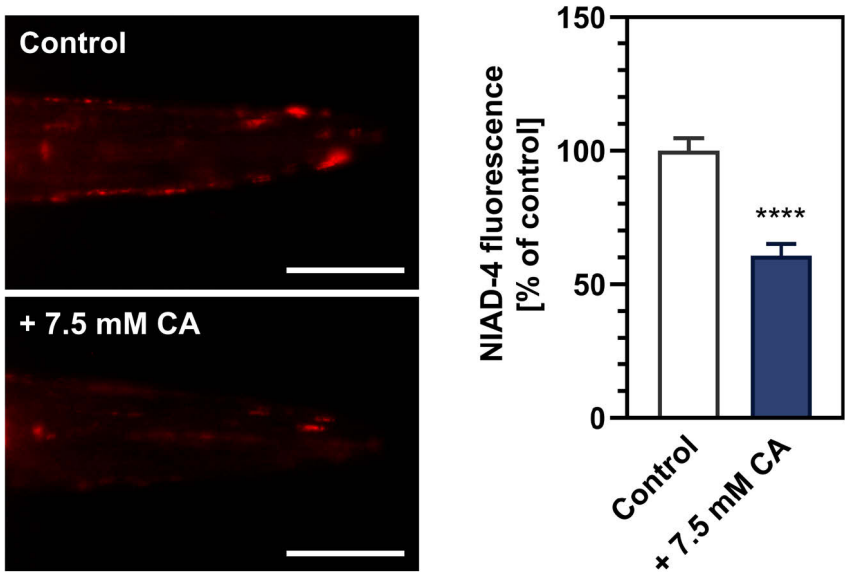

Figure 4.14 | CA reduces Aβ aggregation

Aβ expressing GMC101 nematodes were treated with M9 buffer (solvent control) or 7.5 mM CA from the L4 stage (day 3). At day 7, the nematodes were stained for 4 h with 1 µM of the Aβ specific fluorescent probe NIAD-4 (0.1% DMSO), followed by a 20 h period to remove fluorescent probe residues. Finally, the average NIAD-4 fluorescence of the nematodes was measured in the head region using epifluorescence microscopy and subsequent analysis in ImageJ/Fiji. The left panel displays representative fluorescence images. Scale bar is 50 µm. The right panel shows the quantification of the average fluorescence intensity. All measurements were normalized to the mean of the control. Bar plots represent the normalized mean ± SEM. Unpaired t-test was performed. **** $p < 0.0001$ versus the control.

4.3.2 Role of β-Hydroxybutyric Acid and α-Lipoic Acid Biosynthesis for the Protective Effect of Caprylic Acid

To identify the molecular mechanisms underlying the motility increasing and therefore protective effect of CA on Aβ proteotoxicity, knockdown of genes encoding key enzymes for BHB or ALA biosynthesis was accomplished using RNAi. Figure 4.15 shows that knockdown of either *drd-5*, encoding an ortholog of BHB-DH, or *lias-1*, encoding an ortholog of LIAS, did not prevent the motility increasing effect of CA, thus demonstrating that neither a key enzyme for BHB biosynthesis nor a key enzyme for ALA biosynthesis is necessary for the protective effect of CA.

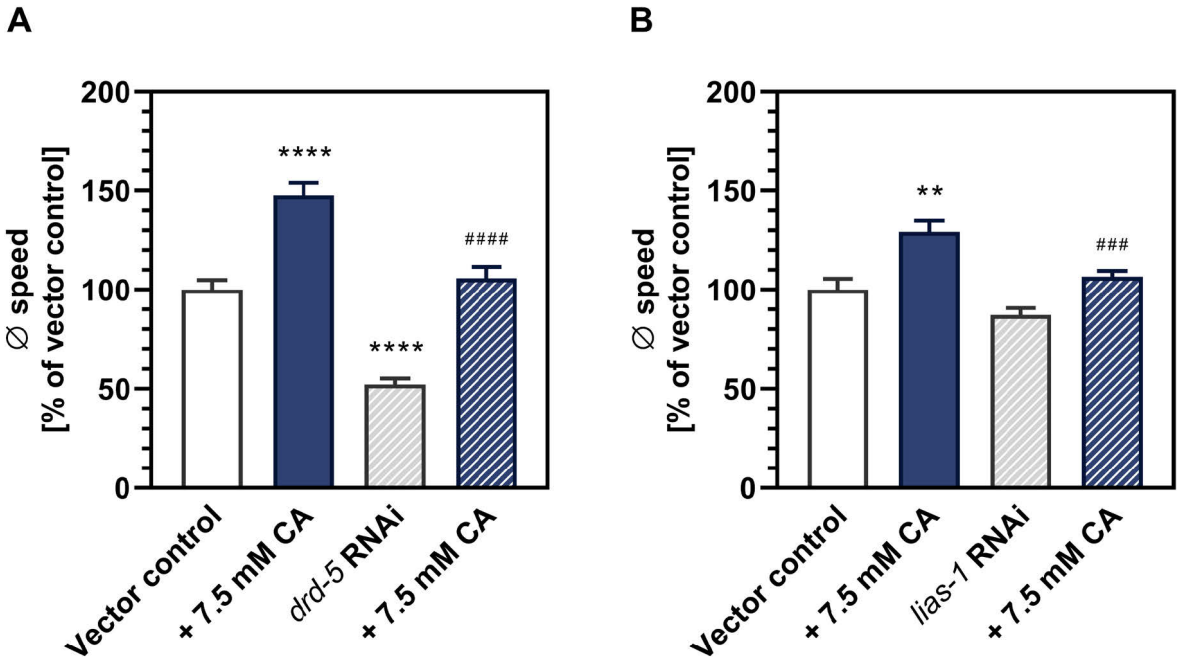

Figure 4.15 | Knockdown of genes involved in BHB and ALA synthesis does not mitigate the motility increase by CA incubation

Aβ expressing GMC101 nematodes were subjected to the *E. coli* HT115 vector control, (A) *drd-5* RNAi or (B) *lias-1* RNAi from the L1 stage (day 1) and treated with M9 buffer (solvent control) or 7.5 mM CA from the L4 stage (day 3). Finally, the average speed of 7-day-old nematodes was measured. All measurements were normalized to the mean of the vector control. Bar plots represent normalized mean ± SEM. Welch's ANOVA with Games-Howell's post-hoc test was performed. ** $p < 0.01$; **** $p < 0.0001$ versus vector control. ### $p < 0.001$; #### $p < 0.0001$ versus RNAi.

Since DRD-5 has only around 40% protein sequence identity to human BHB-DH and no other homolog with basal BHB-DH activity could be identified [231], an additional approach to investigate the role of BHB biosynthesis was performed. Accordingly, it was tested whether direct incubation with (*R*)-BHB could replicate the motility increasing effect of CA. Figure 4.16A shows that 20 mM (*R*)-BHB raised the average speed of GMC101 nematodes by 36% ($p < 0.001$), whereas all lower concentrations were ineffective. Nevertheless, assuming similar bioavailability, biosynthesis of 20 mM (*R*)-BHB could not be achieved by incubation with 7.5 mM CA, even upon complete conversion. Next, the same approach was used to further study the role of ALA biosynthesis. Although 100 µM (*R*)-ALA increased the average speed of GMC101 nematodes by 17% ($p = 0.0577$), all tested concentrations failed to significantly improve the motility (Figure 4.16B). Together, these results further support the conclusion that the protective effect of CA is independent of BHB and ALA biosynthesis.

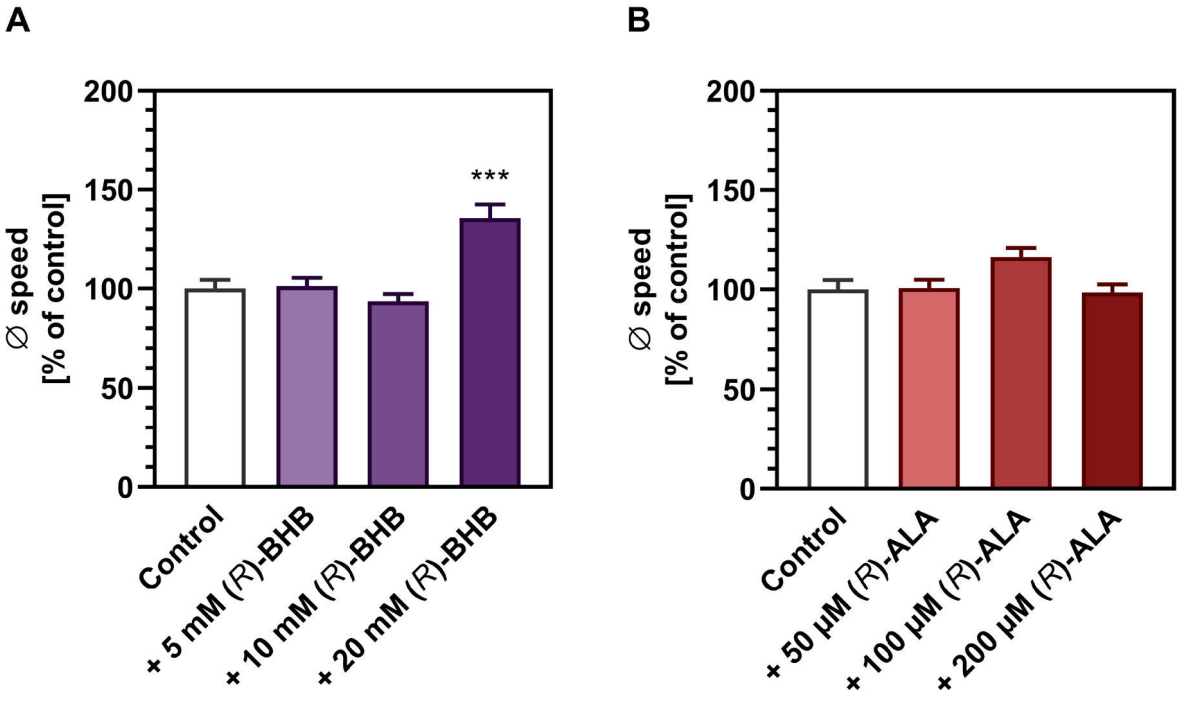

Figure 4.16 | Effects (*R*)-BHB and (*R*)-ALA on Aβ proteotoxicity

Aβ expressing GMC101 nematodes were treated with M9 buffer (solvent control) or different concentrations of (A) (*R*)-BHB or (B) (*R*)-ALA from the L4 stage (day 3). Finally, the average speed of 7-day-old nematodes was measured. All measurements were normalized to the mean of the control. Bar plots represent the normalized mean ± SEM. Welch's ANOVA with Games-Howell's post-hoc test was performed. *** $p < 0.001$ versus the control.

4.3.3 Importance of Energy Metabolism for the Protective Effect of Caprylic Acid

To test the role of energy supply for the motility increase by CA incubation in GMC101, *acdh-10*, encoding an ortholog of human medium-chain ACDH, a key enzyme of FAO, *nuo-3*, encoding an ortholog of complex I of the ETC, receiving reduction equivalents from NADH + H^+, and *mev-1*, encoding an ortholog of $FADH_2$ accepting complex II of the ETC, were downregulated using RNAi. Figure 4.17 shows each knockdown abolished the motility increasing effect of CA, demonstrating its dependency on energy generation by FAO.

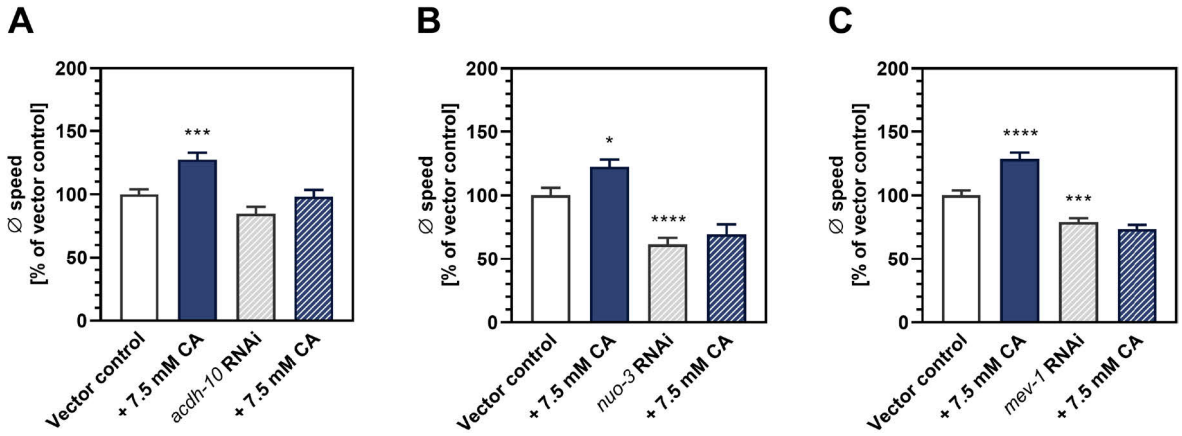

Figure 4.17 | Knockdown of genes involved in FAO or complex I and II of the ETC abolishes the motility increase by CA incubation

Aβ expressing GMC101 nematodes were subjected to the *E. coli* HT115 vector control, (A) *acdh-10* RNAi, (B) *nuo-3* RNAi or (C) *mev-1* RNAi from the L1 stage (day 1) and treated with M9 buffer (solvent control) or 7.5 mM CA from the L4 stage (day 3). Finally, the average speed of 7-day-old nematodes was measured. All measurements were normalized to the mean of the vector control. Bar plots represent normalized mean ± SEM. Welch's ANOVA with Games-Howell's post-hoc test was performed. * $p < 0.05$; ** $p < 0.01$; *** $p < 0.001$; **** $p < 0.0001$ versus the vector control.

In accordance with the necessity of a functional FAO and delivery of reduction equivalents to the ETC as a requirement to enable the motility increasing effect of CA in GMC101 nematodes, ATP levels were raised by 40% following CA incubation ($p = 0.0075$; Figure 4.18A). The increased delivery of reduction equivalents to the ETC in the presence of CA was further reflected by an enhanced MMP, indicated by 89% greater average TMRE fluorescence ($p < 0.0001$; Figure 4.18B).

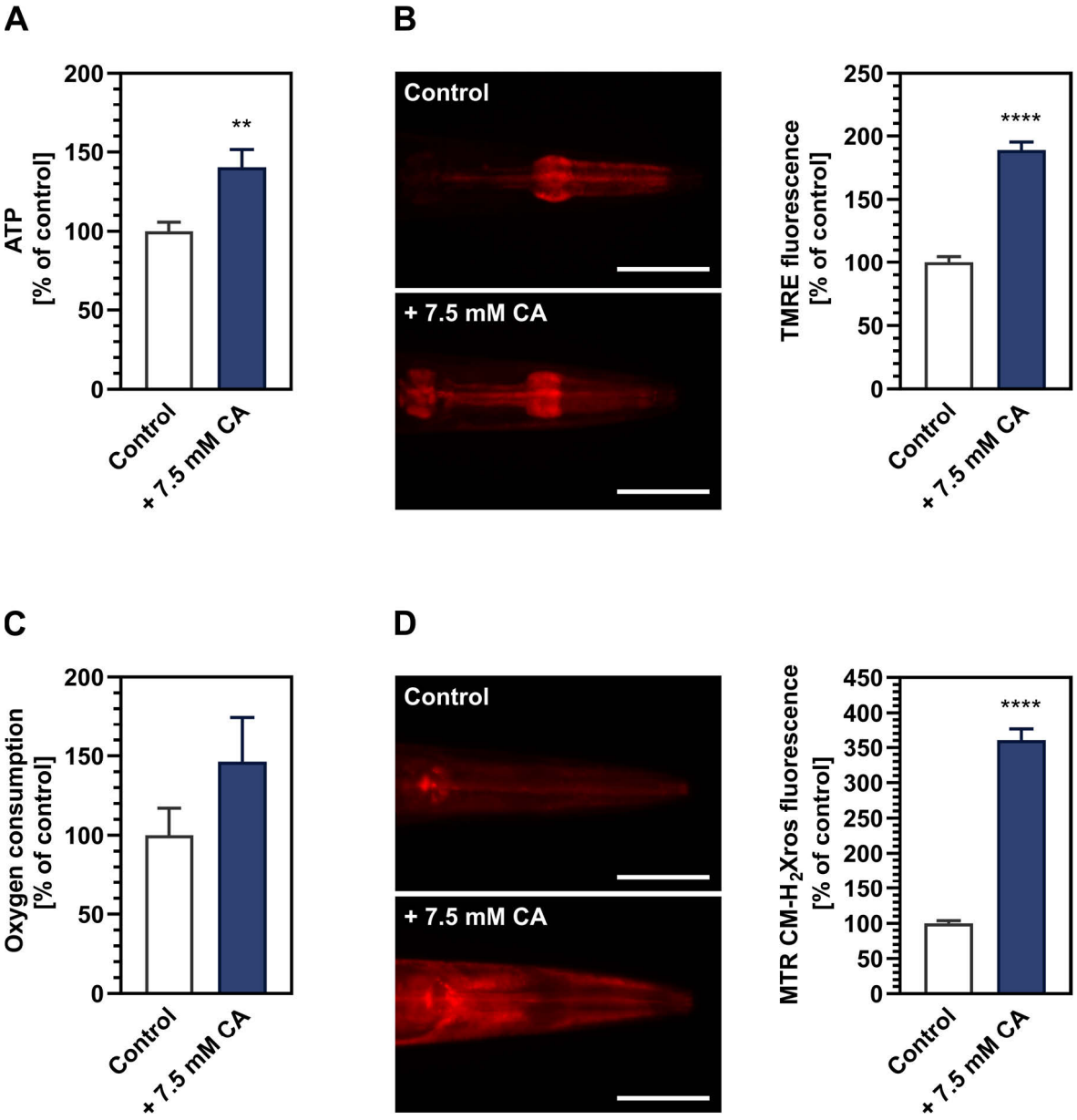

Figure 4.18 | CA enhances mitochondrial energy gain

Aβ expressing GMC101 nematodes were treated with M9 buffer (solvent control) or 7.5 mM CA from the L4 stage (day 3). (A) At day 7, nematode homogenates were generated and ATP levels were quantified using a bioluminescence-assay in relation to protein concentrations. (B) At day 6, the nematodes were stained for 24 h with 50 nM of the MMP sensitive fluorescent probe TMRE (0.05% DMSO), followed by a 2 h period to remove fluorescent probe residues. Finally, the average TMRE fluorescence of the nematodes was measured in the head region using epifluorescence microscopy and subsequent analysis in ImageJ/Fiji. The left panel displays representative fluorescence images. Scale bar is 50 µm. The right panel shows the quantification of the average fluorescence intensity. (C) At day 7, oxygen consumption of the nematodes was measured using a Clark-type electrode. (D) At day 6, the nematodes were stained for 24 h with 1 µM of the ROS sensitive fluorescent probe MTR CM-H_2Xros (0.1% DMSO). Finally, the average MTR CM-H_2Xros fluorescence of the nematodes was measured in the head region using epifluorescence microscopy and subsequent analysis in ImageJ/Fiji. All measurements were normalized to the mean of the control. Bar plots represent the normalized mean ± SEM. Unpaired t-test was performed. ** $p < 0.01$; **** $p < 0.0001$ versus the control.

4.3.4 Contribution of Hormesis to the Protective Effect of Caprylic Acid

Since the increased ROS levels observed under CA exposure (Figure 4.18) could potentially act in opposing ways, either by causing oxidative damage or inducing a beneficial hormetic adaptation, their contribution to the protective effect of CA on GMC101 nematodes was investigated using several approaches. First, *daf-16* and *skn-1*, encoding for orthologs of the major stress response transcription factors FOXO and NRF2, were downregulated using RNAi. While CA maintained its motility increasing effect following knockdown of *daf-16*, the protective effect was abolished using RNAi versus *skn-1* (Figure 4.19), indicating a potential hormetic effect through activation of the transcription factor.

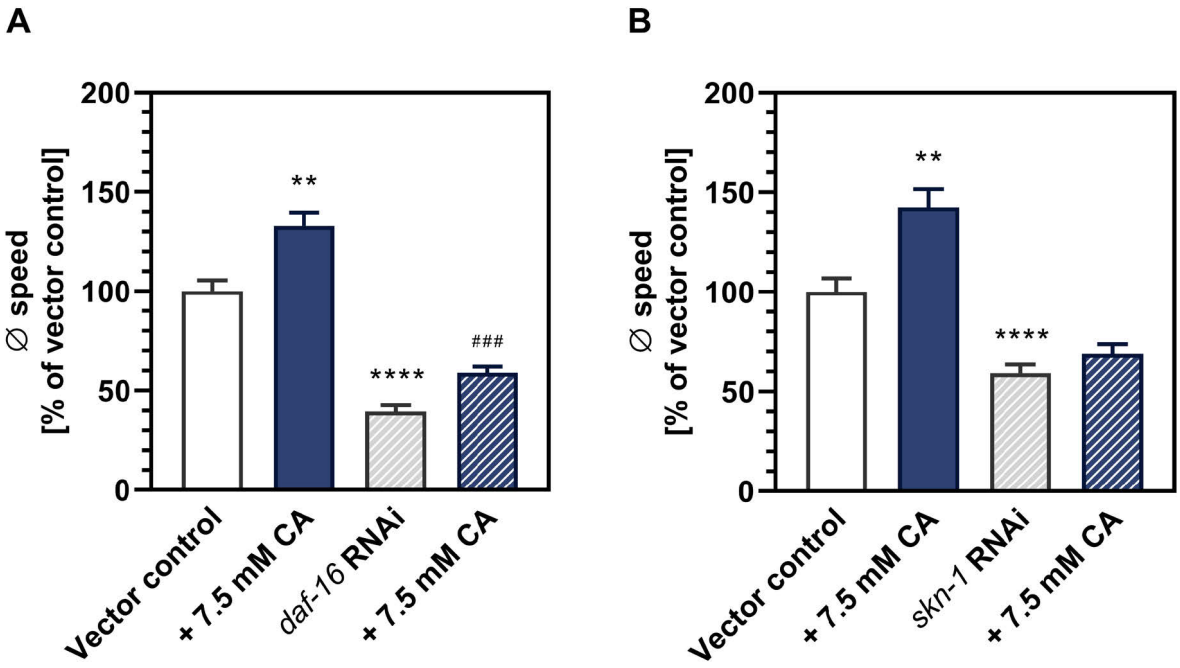

Figure 4.19 | Knockdown of genes involved in the transcriptional control of stress response reduces the protective effect of CA

Aβ expressing GMC101 nematodes were subjected to the *E. coli* HT115 vector control, (A) *daf-16* RNAi or (B) *skn-1* RNAi from the L1 stage (day 1) and treated with M9 buffer (solvent control) or 7.5 mM CA from the L4 stage (day 3). Finally, the average speed of 7-day-old nematodes was measured. All measurements were normalized to the mean of the vector control. Bar plots represent normalized mean ± SEM. Welch's ANOVA with Games-Howell's post-hoc test was performed. ** $p < 0.01$; **** $p < 0.0001$ versus the vector control. ### $p < 0.001$ versus RNAi.

In order to further examine the role of SKN-1 for the effects of CA, the importance of SKN-1 target genes associated with mitochondrial quality control [225], which could also be connected to the demonstrated improvement of mitochondrial function, was investigated using

RNAi. Figure 4.20 shows that the motility increasing effect of CA was independent of *drp-1*, encoding an ortholog of the mitochondrial fission protein DRP1, *dct-1*, encoding an ortholog of the OMM mitophagy receptor BNIP3, and *pink-1*, encoding the essential ortholog of PINK1/Parkin-mediated mitophagy.

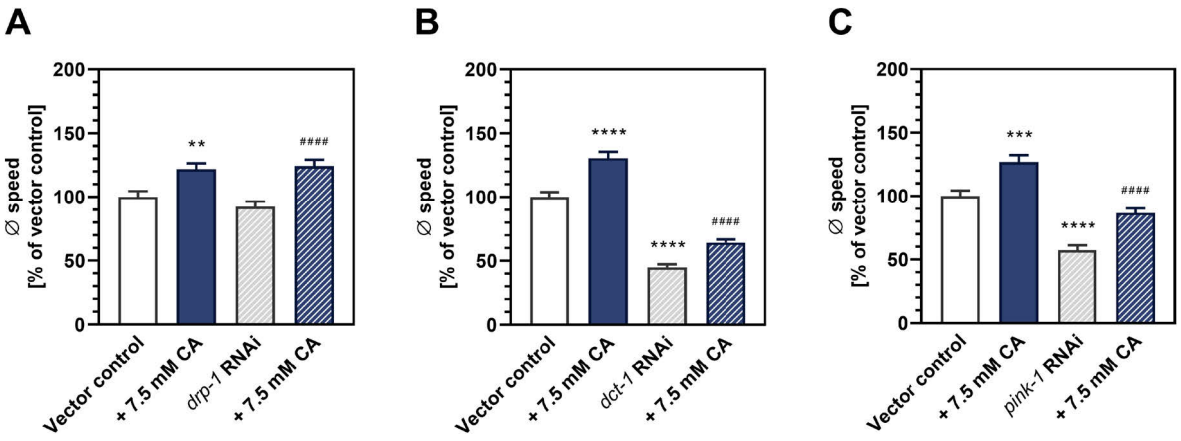

Figure 4.20 | Knockdown of genes involved in mitochondrial fission and mitophagy does not affect the motility increase by CA incubation

Aβ expressing GMC101 nematodes were subjected to the *E. coli* HT115 vector control, (A) *drp-1* RNAi, (B) *dct-1* RNAi or (C) *pink-1* RNAi from the L1 stage (day 1) and treated with M9 buffer (solvent control) or 7.5 mM CA from the L4 stage (day 3). Finally, the average speed of 7-day-old nematodes was measured. All measurements were normalized to the mean of the vector control. Bar plots represent normalized mean ± SEM. Welch's ANOVA with Games-Howell's post-hoc test was performed. ** $p < 0.01$; *** $p < 0.001$; **** $p < 0.0001$ versus the vector control. ### $p < 0.001$ versus RNAi.

Moreover, the absent effect of CA on mitochondria quality control was directly assessed using genetic crosses of GMC101 with fluorescent reporter strains. Figure 4.21 shows that mitochondrial mass and mitochondrial dynamics were unchanged following CA incubation in GMC101 crossed with SJ4103 nematodes, expressing GFP in mitochondria of body wall muscle cells. Finally, CA did not affect mitophagy, evidenced by an unaltered DsRed/GFP fluorescence ratio in GMC101 crossed with IR2539 nematodes that express the Rosella biosensor in mitochondria of body wall muscle cells (Figure 4.22).

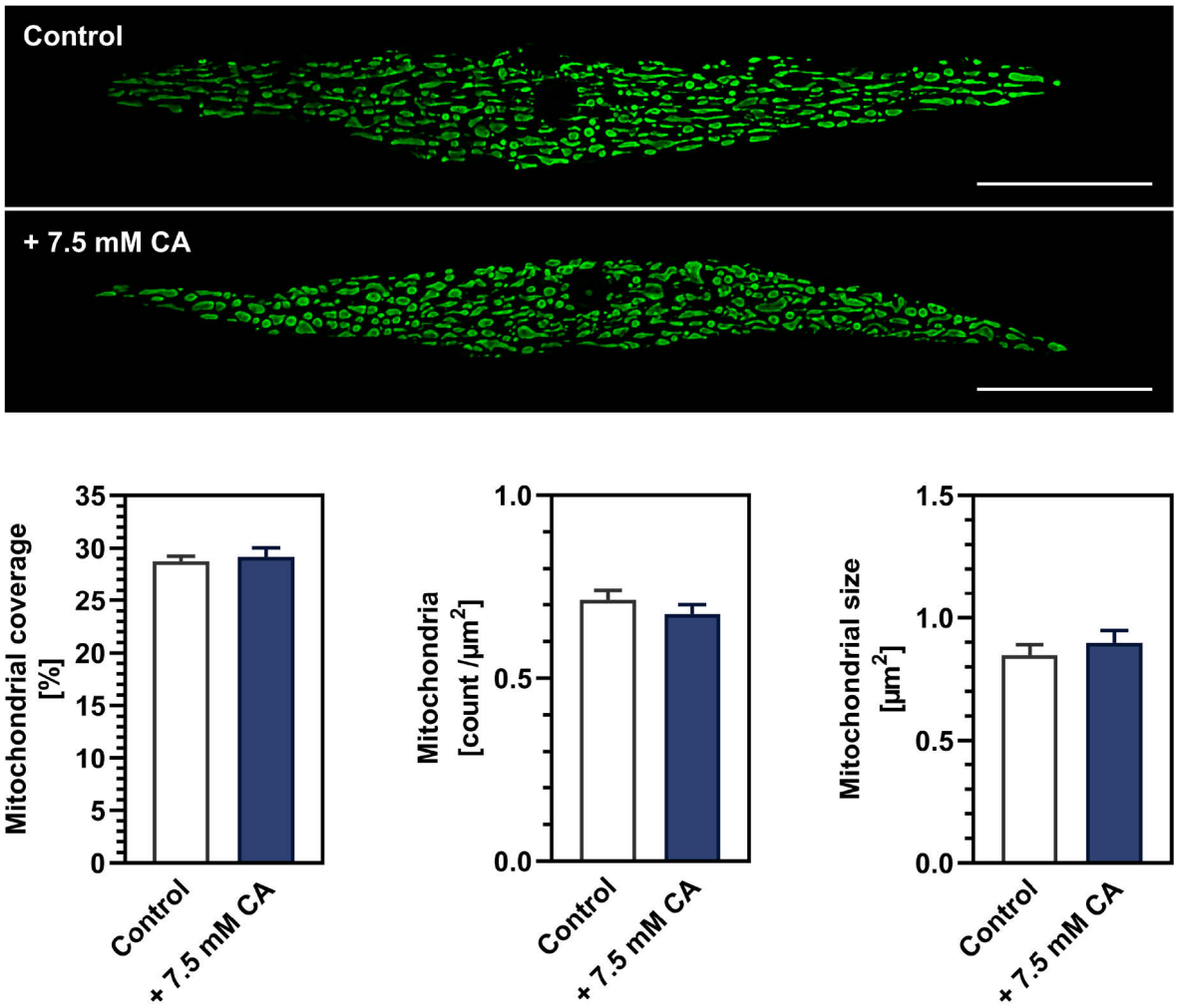

Figure 4.21 | CA has no influence on mitochondrial mass or mitochondrial dynamics

Aβ expressing GMC101 nematodes were crossed with SJ4103 nematodes, which express GFP in mitochondria of body wall muscle cells. The nematodes were treated with M9 buffer (solvent control) or 7.5 mM CA from the L4 stage (day 3). At day 7, the morphology of mitochondria in individual body wall muscle cells was measured using epifluorescence microscopy, deconvolution and subsequent analysis in ImageJ/Fiji. The upper panel displays representative fluorescence images. Scale bar is 25 µm. The lower panel shows the quantification of mitochondrial morphology. Bar plots represent the mean ± SEM. Unpaired t-test was performed.

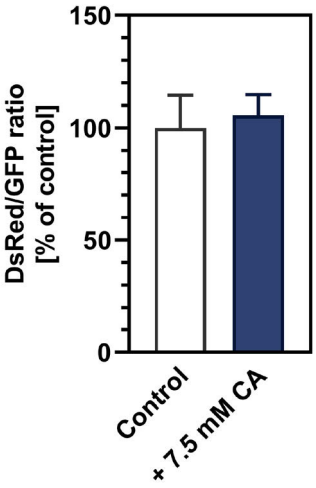

Figure 4.22 | CA does not affect mitophagy

Aβ expressing GMC101 nematodes were crossed with IR2539 nematodes, which express the Rosella biosensor in mitochondria of body wall muscle cells. The nematodes were treated with M9 buffer (solvent control) or 7.5 mM CA from the L4 stage (day 3). At day 6, the average DsRed and GFP fluorescence of the nematodes was measured in the head region using epifluorescence microscopy and subsequent analysis in ImageJ/Fiji. A higher DsRed/GFP ratio indicates induction of mitophagy due to quenching of the pH-sensitive GFP fluorescence in acidic lysosomes. All measurements were normalized to the mean of the control. Bar plots represent the normalized mean ± SEM. Unpaired t-test was performed.

Since the investigated SKN-1 target genes were surprisingly dispensable for the protective effect of CA, it was tested whether reduction of ROS levels using the water-soluble antioxidant ascorbic acid (AA) could mitigate the motility increase by CA incubation. Although AA reduced the elevated ROS level under CA incubation, evidenced by an 162% decrease in average MTR CM-H_2Xros fluorescence (Figure 4.23A), the motility increasing effect of CA was unaffected (Figure 4.23B), suggesting independence from hormesis. However, considering that ROS levels were not reduced to the baseline of the control under concurrent incubation with CA and AA, a hormetic effect of CA could ultimately not be completely excluded.

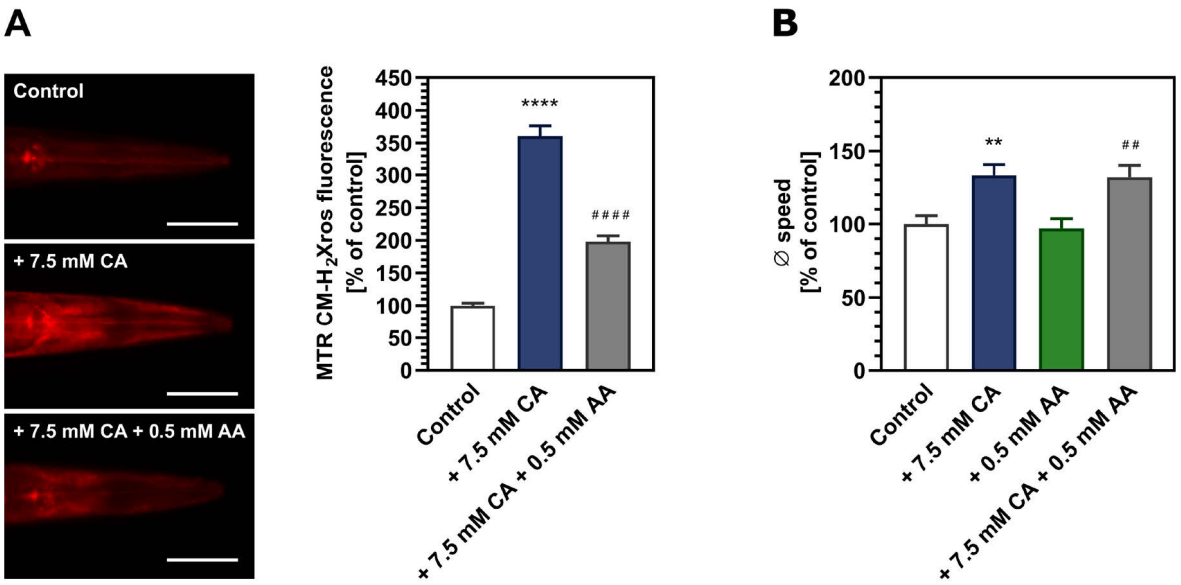

Figure 4.23 | AA reduces ROS levels without affecting the motility increase by CA incubation

Aβ expressing GMC101 nematodes were treated with M9 buffer (solvent control), 7.5 mM CA, 0.5 mM AA or a combination of CA and AA from the L4 stage (day 3). (A) At day 6, the nematodes were stained for 24 h with 1 µM of the ROS sensitive fluorescent probe MTR CM-H2Xros (0.1% DMSO). Finally, the average MTR CM-H2Xros fluorescence of the nematodes was measured in the head region using epifluorescence microscopy and subsequent analysis in ImageJ/Fiji. The left panel displays representative fluorescence images. Scale bar is 50 µm. The right panel shows the quantification of the average fluorescence intensity. Welch's ANOVA with Tamhane's T2 post-hoc test was performed. **** $p < 0.0001$ versus the control. #### $p < 0.0001$ versus CA. (B) The average speed of 7-day-old nematodes was measured. Welch's ANOVA with Games-Howell's post-hoc test was performed. ** $p < 0.01$ versus the control. ## $p < 0.01$ versus AA. All measurements were normalized to the mean of the control. Bar plots represent the normalized mean ± SEM.

5 Discussion

AD is a neurodegenerative disorder and the most common form of dementia. With age being the main risk factor of sporadic AD, the disease is a growing burden of modern society. The pathogenesis of AD is a complex irreversible process characterized by a long preclinical phase, in which accumulation of proteotoxic Aβ aggregates and mitochondrial dysfunction were identified as major features that mutually aggravate one another in a vicious cycle, eventually leading to progressive disturbance of neurotransmission and neurodegeneration [1, 133, 135].

To maintain proteostasis and mitochondrial homeostasis, eukaryotes evolved interconnected quality control systems that involve specific stress response pathways and degradation systems. Since these systems are generally disturbed or overloaded in AD pathogenesis, it appears plausible to search for substances that conserve or activate them before they malfunction. Moreover, homeostasis could be maintained through other approaches, such as alternative energy substrates circumventing the steps specific for impaired glucose oxidation [72, 133] or chemicals that directly reduce Aβ aggregation [140].

The aromatic SCFA 4-PBA and the MCFA CA are two substances that could act through several pathways to promote homeostasis. Both potentially serve as energy substrates via FAO. 4-PBA may further act as a chemical chaperone or as an inducer of molecular chaperones through inhibition of HDACs. In contrast, CA is a precursor for the biosynthesis of ALA, a cellular antioxidant and coenzyme of enzymes involved in energy metabolism, and BHB, which serves as another energy substrate and signaling molecule [133, 176, 181, 256].

The nematode *Caenorhabditis elegans* is a widely used research model for the investigation of metabolism, aging and age-associated diseases due to beneficial properties, such as accessibility for phenotypic characterization, transparency and simple genetic manipulation. In the course of this work, the molecular effects of 4-PBA and CA on proteostasis and mitochondrial homeostasis were investigated in a *C. elegans* model of Aβ proteotoxicity, i. e. the transgenic Aβ expressing strain GMC101. Computer-based analysis of motility was used as a measure of Aβ proteotoxicity. This approach was supplemented with the regulation of gene expression using RNAi and further methods involving genetic crossing, fluorescence microscopy as well as biochemical assays to measure Aβ aggregation and parameters of mitochondrial homeostasis.

5.1 4-Phenylbutyric Acid Attenuates Amyloid-β Aggregation and Proteotoxicity

In the present work, computer-based analysis of motility revealed that 4-PBA dose-dependently attenuates Aβ proteotoxicity in Aβ expressing GMC101 nematodes, reaching its highest effect at a concentration of 10 mM. Furthermore, 4-PBA was found to reduce the aggregation of Aβ. These results are in line with *in vitro* evidence, demonstrating reduced aggregation of proteins involved in distinct diseases and increased viability of cells, such as SH-SY5Y cells overexpressing the Pael receptor, or trisomic fibroblasts and neurons, following 4-PBA incubation in the millimolar range [141–143]. Moreover, 4-PBA was shown to decrease Aβ aggregation and improve cognitive function in animal models of AD [145–147].

Surprisingly, incubation with 4-PBA decreased the motility of CL2122 nematodes, the corresponding wild-type of GMC101. Since physiologically occurring misfolded proteins or protein aggregates may exert an hormetic effect, it might be speculated that incubation with 4-PBA suppressed such adaptive mechanism through its mitigating action on misfolding and aggregation that is discussed below.

5.1.1 The Protective Effect of 4-Phenylbutyric Acid Depends on Activation of the Proteostasis Network by Inhibition of Histone Deacetylases

Mechanistically, 4-PBA was found to exert weak inhibition of class I and class IIb HDAC *in vitro* and *in vivo* [142, 148, 166, 168, 169]. Despite the complex nature of research on HDACs, evidence suggests that their inhibition may activate the compartment specific stress response pathways of the proteostasis network (Chapter 1.5.2) [153, 161–163], which could attenuate the accumulation of proteotoxic Aβ aggregates.

Accordingly, the importance of major proteostasis transcription factors for the motility increase by 4-PBA incubation was investigated using RNAi. First, the protective effect of 4-PBA on Aβ proteotoxicity was demonstrated to be independent of *atf-6* and *atfs-1*, encoding for transcription factors of the UPR^{ER} and UPR^{mt}, respectively. In contrast, knockdown of *hsf-1*, encoding an ortholog of the major HSR transcription factor, abolished the 4-PBA-dependent motility increase and reduction of Aβ aggregation, consequently suggesting activation of HSF-1 as a mechanism of action. Consistent with results from another study, *hsf-1*

knockdown impaired the motility of Aβ expressing nematodes [257]. However, Aβ aggregation was surprisingly unaffected by *hsf-1* RNAi, as assessed using the fluorescent probe NIAD-4. Whereas this is in line with experiments from authors that used the same *C. elegans* model and method to examine the role of *hsf-1* for the aggregation reducing effect of carnosine and kynurenic acid [258], it appears to contradict the important function of HSF-1 in maintaining proteostasis. A simple explanation for this phenomenon is based on the properties of NIAD-4, whose fluorescence is particularly dependent on Aβ fibrils [245]. Thus, other aggregation states of Aβ, such as oligomers, could have accumulated as a consequence of *hsf-1* RNAi without being detected. Although further methods to measure Aβ aggregation *in vivo* are limited, the accumulation of other aggregation states could be assessed via western blot or immunostaining using specific Aβ antibodies. Moreover, HSF-1 also participates in the transcription of genes that are not involved proteostasis [61], providing another possible explanation for the relatively greater effect on motility compared to Aβ aggregation.

Despite its dependency on HSF-1, knockdown of genes encoding for individual cytosolic chaperones, such as cytosolic HSPAs [HSP70s] and HSPCs [HSP90s], did not inhibit the motility increase by 4-PBA incubation (data not shown). Since HSF-1 upregulates the expression of a large number of chaperones [212], it is reasonable to assume that the protective effect of 4-PBA is mediated by the totality of regulated genes. In fact, upregulation of specific individual chaperones may even exert neurotoxicity through disaggregation of relatively inert high molecular weight aggregates into oligomers or oligomer stabilization. It consequently appears that the interaction of different chaperones with various co-chaperones confers their protective potential [259]. While 4-PBA was already shown to increase the expression of diverse molecular chaperones like cytosolic HSPAs [HSP70s] and HSPCs [HSP90s] *in vitro* [166], additional quantitative polymerase chain reaction (qPCR) experiments could further demonstrate the enhanced transcriptional activity of HSF-1 postulated herein.

Next, HDAC inhibition was modelled using RNAi against HDAC orthologs of *C. elegans*. Whereas RNAi against *hda-2*, *hda-3* and *hda-6* lacked a protective effect, knockdown of *hda-1*, an ortholog of HDAC2, showed a comparable motility increase to 4-PBA incubation. The motility increasing effect was also suppressed by concurrent RNAi against *hsf-1*, ultimately suggesting that 4-PBA and inhibition of HDA-1 act through the same mechanism. Although this specific mechanistic link is not described in the literature, HSF-1 activation thus appears to be mediated by inhibition of the HDAC2 ortholog HDA-1, which was further evidenced by a lacking additive effect of both interventions combined.

In summary, the essential role of HSF-1, the major transcription factor of the HSR, for the reduction of Aβ proteotoxicity and aggregation by 4-PBA incubation suggests that 4-PBA acts as an inducer of molecular chaperones rather than as a chemical chaperone. Since the proteostasis network is subject to a functional decline during aging and AD pathogenesis, 4-PBA consequently may aid to restore protein homeostasis. Indeed, drugs that aim to reduce the aggregation of toxic protein aggregates through modulation of molecular chaperone expression are proposed as a viable therapeutic strategy in neurodegenerative disorders [25].

5.1.2 4-Phenylbutyric Acid Improves Mitochondrial Function by Supplying Energy via β-Oxidation and Activation of Mitochondrial Quality Control

Next, it was tested whether the attenuation of Aβ proteotoxicity by 4-PBA was associated with improved mitochondrial function. Indeed, it was shown for the first time that incubation with 4-PBA increased ATP levels and the MMP. Although reduction of Aβ aggregation is a plausible mechanism for improvement of mitochondrial function, additional pathways that directly impact mitochondrial homeostasis were examined.

As a FA, 4-PBA may serve as an energy source through generation of acetyl-CoA via FAO and subsequent metabolization in the TCA cycle. In contrast to glycolysis, which exclusively yields NADH + H^+, FAO generates equal amounts of $NADH^+ + H^+$ and $FADH_2$. Since impaired enzymatic activities of the ETC complex I and the PDH have been shown in aging and AD pathogenesis [72, 125, 132, 133], generation of more $FADH_2$, which delivers reduction equivalents to complex II, and circumvention of the PDH via FAO may result in a higher efficiency of energy production compared to glucose metabolism. Consistent with the hypothesis that alternative substrates circumventing the steps specific for glucose oxidation could be a potential therapeutic strategy in AD, RNAi against genes involved in FAO, and complex I as well as complex II of the ETC, demonstrated that the motility increase by 4-PBA incubation was dependent on energy metabolism. It is, however, important to note that the regulation of FAO through knockdown of *acdh-2*, encoding for an ortholog of human short-chain ACDH, only partially abolished the protective effect of 4-PBA as compared to RNAi against complex I and complex II subunits. Whereas this could suggest that energy gain by FAO is only of minor importance, *C. elegans* contains three additional short-chain ACDH orthologs that presumable compensated the *acdh-2* knockdown to some extent. Indeed, the same outcome was observed using RNAi against the other orthologs, namely

acdh-1, *acdh-3* and *acdh-4*, suggesting that their importance for FAO of SCFA is similar. Moreover, knockdown of the complex I and complex II is inevitably accompanied by accumulation of reduction equivalents, which may further inhibit pathways of energy metabolism upstream of the ETC, including the TCA cycle and FAO. The results obtained from inhibition of complex I and complex II consequently do not rule out a prominent role of FAO for the protective effect of 4-PBA on Aβ proteotoxicity. Complementary, direct incubation with PAA, the resulting metabolite of 4-PBA oxidation, led to a decreased effect on motility compared to its precursor, further demonstrating the importance of energy supply via FAO. Although FAO to PAA also occurs in humans to enable ammonia scavenging by 4-PBA [136, 137], the translation of the presented findings to AD pathology is obscure, due to the lack of studies investigating FAO of aromatic SCFAs in the human brain. However, it is reasonable to assume that FAO of aromatic SCFAs displays overlap to MCFA oxidation, which is discussed in detail in Chapter 5.2.2.

Finally, knockdown of genes involved in mitochondrial fission and receptor-mediated mitophagy resulted in a decreased protective effect of 4-PBA. This was further evidenced using genetic crossings of Aβ expressing GMC101 nematodes with transgenic reporter strains, revealing a reduction of mitochondrial size and eventually increased mitophagy. Indeed, induction of mitophagy has been suggested as a promising strategy in AD therapy that was already found to prevent cognitive impairment in mouse models of AD [129, 130, 260]. Since the increase of mitophagy demonstrated in this work was not accompanied by a decrease of mitochondrial coverage, it is further indicated that mitochondrial biogenesis was induced. This conclusion is supported by results from Brose et al. (2012), demonstrating increased mitochondrial mass associated with elevated expression of PGC1α, a major transcription factor of mitochondrial biogenesis, in human fibroblasts [166].

As a prerequisite for its use in AD, 4-PBA has been shown to readily cross the BBB [138]. However, a direct transfer of the dose used in AD mouse models, in which 200 mg/kg body weight was found to be of therapeutic benefit, would translate into a high effective dose of about 15 g per day for patients [136]. Since this roughly corresponds to the maximum tolerated dose in patients with amyotrophic lateral sclerosis and Huntington's disease [261, 262], generation of derivatives with lower side effects or higher potency could be of great importance [263]. Moreover, side effects could potentially be reduced through intravenous application of 4-PBA, which may further also result in higher brain uptake due to a reduced first-pass-effect.

5.2 Caprylic Acid Attenuates Amyloid-β Aggregation and Proteotoxicity

In this work, CA was shown to dose-dependently increase the motility of Aβ expressing GMC101 nematodes, reaching its highest effect in a concentration of 7.5 mM. Since the motility increase was substantially lower in the corresponding control strain CL2122, CA most likely exerts a specific effect on Aβ proteotoxicity. Consistent with this postulate, it was further demonstrated that CA reduces the aggregation of Aβ. While research on the molecular effects of CA in AD models is limited, one study found that CA decreased the Aβ-induced decline in cell viability of cortical neuronal cultures from rats [264]. Furthermore, several studies showed improvements in cognitive function following treatment with 30-50 g/d of the MCT tricaprylin in patients with mild cognitive impairment and AD [178–180].

5.2.1 The Protective Effect of Caprylic Acid is Independent of β-Hydroxybutyric Acid and α-Lipoic Acid Biosynthesis

The authors of the aforementioned studies suggested that the improvement in cognitive function is based on a ketogenic effect of CA, providing an alternative energy source for the brain that circumvents impaired glucose metabolism associated with AD [178–180]. Indeed, even a single dosage of tricaprylin was found to result in plasma ketone concentrations of around 0.8 mM [265]. It was further shown that MCT treatment enhanced total brain energy metabolism by increasing ketone supply without affecting brain glucose utilization [178–180]. In the present work, however, blocking biosynthesis of the ketone body BHB by RNAi versus *drd-5*, an ortholog encoding human BHB-DH, did not prevent the motility increase by CA incubation in GMC101 nematodes. Due to only around 40% protein sequence identity of DRD-5 to human BHB-DH and the lack of other orthologs with basal BHB-DH activity [231], an additional approach to investigate the role of BHB for the protective effect of CA was performed. In this approach, GMC101 nematodes were directly incubated with different concentrations of (*R*)-BHB, of which 20 mM (*R*)-BHB led to an increase of motility. This is in line with another study that showed a reduction of Aβ-induced paralysis in the Aβ expressing strain CL4176 following (*R*)-BHB incubation [231]. Nevertheless, since one molecule CA can only generate up to four molecules acetyl-CoA through three cycles of FAO, which in turn may constitute two molecules acetoacetate, a maximum concentration of

15 mM BHB could be achieved by incubation with 7.5 mM CA, provided that a similar bioavailability is assumed. The protective effect of CA on Aβ proteotoxicity shown in this work must therefore be considered as independent of BHB biosynthesis. Furthermore, it can be speculated that CA lacks a notable ketogenic effect in the nematodes.

Next, the role of ALA biosynthesis, a cellular antioxidant and coenzyme of 2-oxoacid (α-ketoacid) dehydrogenases involved in energy metabolism such as the PDH, was investigated. Since knockdown of an ortholog encoding for LIAS did not affect the motility increase following CA incubation, the biosynthesis of ALA was also suggested to be dispensable for the protective effect in GMC101 nematodes. Again, in an alternative approach, GMC101 nematodes were directly incubated with different concentrations of (*R*)-ALA, all of which failed to significantly improve the motility. Incubation with comparable ALA concentrations also did not affect Aβ-induced paralysis in Aβ expressing CL4176 nematodes [266]. However, ALA reduced hippocampal-dependent memory deficits of Tg2576 mice, an AD model that overexpresses a mutant form of APP [267]. Nevertheless, the improvement of memory was not associated with a reduction of Aβ levels. Although the molecular mechanisms of ALA were not further explored by Quinn et al. (2007), it is possible that ALA specifically acted on neuronal function in the mouse model, thus providing an explanation for the lacking effect in *C. elegans* AD models with muscular Aβ expression.

5.2.2 Caprylic Acid Acts by Supplying Energy via β-Oxidation

As an MCFA, CA can serve to supply energy through generation of acetyl-CoA via FAO and subsequent metabolization in the TCA cycle, which consequently circumvents impaired enzymatic activities of the ETC complex I and the PDH that have been shown in aging and AD pathogenesis [72, 125, 132, 133]. Similar to the results of 4-PBA incubation, the protective effect of CA in Aβ expressing GMC101 nematodes was abolished under knockdown of genes involved in FAO and complex I as well as complex II of the ETC. Furthermore, ATP levels, oxygen consumption and the MMP were increased as a result of CA incubation in GMC101 nematodes.

An essential point that needs to be addressed in translating the results from nematodes to humans concerns the availability of CA in the human brain and the ability of neurons for its oxidation. First, studies showed that MCFAs could pass the BBB and may reach brain

concentrations of up to 0.25 mM in mice, which were more than 50% of those in plasma [173–175]. Once inside the brain, cellular uptake and mitochondrial import of MCFAs, unlike LCFAs, is not limited by fatty acid transport proteins, fatty acid binding proteins or carnitine [170, 171]. Nevertheless, the oxidation of FAs in neurons and their contribution to energy supply is a highly discussed topic.

At first, it was shown that the brain of rats has a limited FAO capacity due to low enzymatic activities [268]. It has to be taken into account, however, that the measured low activities for FAO were related to the oxidation of palmitoylcarnitine, a carnitine-esterified LCFA. In contrast, MCFA oxidation may not be limited due to the existence of chain length specific enzymes [67]. In accordance with this, the activity of octanoyl-CoA dehydrogenase was shown to be considerably higher compared to that of palmitoyl-CoA dehydrogenase at all developmental stages and in all brain regions of rats, in cultured neuronal cell lines and also in the human brain [269]. Furthermore, FAO of CA was shown in SH-SY5Y cells, a human derived cell line of neuroblastoma [270]. Interestingly, the absolute oxidation rate of 250 µM ^{13}C-labeled CA even reached about 25% of 3 mM ^{13}C-labeled glucose, indicating that CA could potentially provide a substantial amount of energy. The FAO of CA in the brain was also evidenced by results of Haynes et al. (2020). They found that CA was predominately oxidized in hypothalamic-derived N29/4 neurons and the hypothalamus of mice after administration directly into the CSF via the lateral ventricle, into the right carotid artery or into the intestine. In contrast, LCFAs showed limited hypothalamic uptake after administration into the right carotid artery or intestine and were predominately stored following direct application into the CSF [175], further demonstrating the importance of chain length for FAO in the brain. Another study by Ebert et al. (2003) found that FAO of ^{13}C-labeled CA in rat brain following injection into the jugular vein contributed 20% to total brain oxidative energy production. Metabolite labeling patterns indicated compartmentalized oxidation of CA primarily in astrocytes [271], interacting cells of neurons that also appear to be involved in AD pathogenesis [272, 273]. Although the role of astrocytes in AD pathogenesis is poorly understood, FAO of CA in astrocytes may indirectly promote energy metabolism of neurons. Astrocytes primarily metabolize glucose via anaerobic glycolysis to lactate, which in turn serves as an energy supply for neurons especially during synaptic activity. This indicates that FAO could be the major source of energy in astrocytes and increased oxidation of MCFAs may lead to a saving of glucose for direct or indirect utilization in neurons [274]. Furthermore, it was shown that CA can promote ketogenesis in astrocytes, providing an alternative energy source for neurons [275]. Finally, based on findings that simultaneous

application of palmitoylcarnitine and additional substrates like pyruvate or succinate markedly increased FAO in isolated brain mitochondria of rats, it was suggested that substrate mixtures, better representing the scenario *in vivo*, may promote FAO in the brain [274].
The presented evidence indicates that MCFAs, especially CA, can serve as energy supply in the human brain following oral ingestion. However, future research needs to explore the quantitative contribution of MCFA oxidation to total brain energy production in health and disease.

5.2.3 Radical Oxygen Species Induced by Caprylic Acid Lack an Hormetic Effect

Although the oxidation of FAs produces a considerable amount of ATP, the oxygen demand relative to the generated energy is increased compared to glucose utilization due to a lower $NADH + H^+/FADH_2$ ratio. This potentially results in a higher risk of hypoxia and the production of ROS [276, 277]. Indeed, incubation with CA increased the ROS levels of GMC101 nematodes concurrently to ATP levels, oxygen consumption and the MMP.

Since CA incubation demonstrated overall protective properties, a potential hormetic effect of the elevated ROS levels was investigated using RNAi against *daf-16* and *skn-1*, encoding for orthologs of the major stress response transcription factors FOXO and NRF2 (Chapter 1.3.2). Whereas CA maintained its protective effect following knockdown of *daf-16*, the motility increase by CA incubation was abolished using RNAi versus *skn-1*, indicating indeed an hormetic effect of CA through SKN-1 activation.
Thus, the potential hormetic effect of CA through activation of SKN-1 was further examined. While the activation of SKN-1 could have been investigated using qPCR, a simple increase of target gene expression does not necessarily translate into a relevant effect on Aβ proteotoxicity. Based on the improvement of mitochondrial function by CA incubation and the importance of SKN-1 target genes, such as *dct-1* and *pink-1*, for mitochondrial quality control [225], the role of these genes for the motility increase by CA incubation was tested using RNAi. Surprisingly, the protective effect of CA was independent of these SKN-1 target genes and CA did not affect mitochondrial mass, mitochondrial dynamics or mitophagy. To further examine a potential hormetic effect with a different approach, it was tested whether reduction of ROS levels using the water-soluble antioxidant AA could mitigate the motility increase by CA incubation. Although AA reduced the elevated ROS level under CA

incubation, the motility increasing effect of CA was unaffected, suggesting independence from hormesis.

This may ultimately indicate that the protective effect of CA requires a certain basal SKN-1 expression (i. e. not reduced by knockdown) to compensate the elevated ROS generation arising as a byproduct of increased energy metabolism. Nevertheless, as AA failed to lower the elevated ROS levels to their baseline, a hormetic effect of CA could eventually not be completely ruled out. Consequently, SKN-1 target genes distinct from the set investigated in this work may be more relevant for the SKN-1-dependent motility increase by CA incubation. Accordingly, SKN-1 is involved in a variety of other cellular stress defenses, such as the proteostasis network [278, 279], which could also unravel a mechanistic link to the reduced Aβ aggregation observed following CA incubation that needs further investigation.

5.3 4-Phenylbutyric Acid and Caprylic Acid Act through Common and Distinct Molecular Mechanisms

In summary, this work demonstrates for the first time that 4-PBA as well as CA attenuate Aβ proteotoxicity in an AD model of the nematode *C. elegans* and adds insight of their molecular mechanisms to the overall limited body of evidence. They share the improvement of mitochondrial function and reduction of Aβ aggregation as common targets. Moreover, both substances serve as energy fuel via FAO, consequently circumventing the steps specific for glucose oxidation that are impaired in AD. 4-PBA further activates the proteostasis network and the mitochondrial quality control, explaining its increased protective effect relative to CA, as evidenced by approximately twofold greater stimulation of motility in Aβ expressing GMC101 nematodes. Since both substances are bioavailable following oral uptake, exhibit a high safety level and readily pass the BBB, they may be suitable for long term administration as preventive or therapeutic agents for AD.

6 Summary

Alzheimer's disease (AD) is a neurodegenerative disorder and the most common form of dementia. The neurodegeneration results in progressive memory loss as well as psychological changes and can ultimately lead to an almost complete loss of cognitive abilities. With age being the main risk factor of sporadic AD and the advancing demographic change, the disease is a growing burden of modern society. Despite its great importance and intensive research, there is currently no cure for the disease, limiting therapy to symptomatic treatment. The pathogenesis of AD is a complex irreversible process characterized by a long preclinical phase, in which accumulation of proteotoxic amyloid-β (Aβ) aggregates and mitochondrial dysfunction were identified as major features that mutually aggravate one another in a vicious cycle, eventually leading to progressive disturbance of neurotransmission and neurodegeneration.

In the present work, the molecular effects of the aromatic short-chain fatty acid 4-phenylbutyric acid (4-PBA) and the medium-chain fatty acid caprylic acid (CA) on proteostasis and mitochondrial homeostasis were investigated using the transgenic *Caenorhabditis elegans* strain GMC101, expressing human $A\beta_{1-42}$ in body wall muscle cells. Computer-based analysis of motility revealed that Aβ proteotoxicity particularly impaired the average speed of GMC101 compared to its corresponding control strain CL2122. 4-PBA and CA both increased the motility of GMC101 nematodes dose-dependently and selectively. Their selective effect on Aβ proteotoxicity was further reflected by a reduction of Aβ aggregation, as assessed using the Aβ-specific fluorescent probe NIAD-4.

Given that 4-PBA, as a weak inhibitor of class I and IIb histone deacetylases (HDACs), may activate protein quality control through several mechanisms, the importance of major proteostasis transcription factors was investigated using RNA interference (RNAi). Knockdown of *hsf-1*, an ortholog essential for the cytosolic heat shock response, abolished the reduction of Aβ aggregation and proteotoxicity by 4-PBA incubation. Since knockdown of *hda-1*, an ortholog of *HDAC2*, also increased motility in a *hsf-1*-dependent manner, and application of 4-PBA under *hda-1* RNAi showed no additive effect, it can be assumed that 4-PBA activates HSF-1 via inhibition of HDA-1.
Next, it was tested whether the attenuation of Aβ proteotoxicity by 4-PBA was associated with improved mitochondrial function. Accordingly, incubation with 4-PBA increased adenosine triphosphate (ATP) levels, measured via luciferase assay, and the mitochondrial

membrane potential (MMP), quantified using the fluorescent probe TMRE. Using RNAi against genes involved in β-oxidation (fatty acid oxidation; FAO), and complex I as well as complex II of the electron transport chain (ETC), the motility increasing effect of 4-PBA was demonstrated to be dependent on its oxidation to phenylacetic acid (PAA) and thus on its properties as an energy source. Finally, knockdown of genes involved in mitochondrial fission and receptor-mediated mitophagy resulted in a decreased protective effect of 4-PBA. This was further evidenced using genetic crossings of Aβ expressing GMC101 nematodes with transgenic fluorescent reporter strains, confirming increased mitochondrial fission and eventually induction of mitophagy.

CA is a precursor for the biosynthesis of α-lipoic acid (ALA), a cellular antioxidant and coenzyme involved in energy metabolism, as well as the ketone body β-hydroxybutyric acid (BHB), which may serve as an alternative energy substrate and signaling molecule. The motility increase by CA incubation, however, was found to be independent of ALA and BHB biosynthesis. As in the case of 4-PBA, RNAi against genes involved in FAO, and complex I as well as complex II of the ETC abolished the motility increasing effect of CA. In accordance with the necessity of a functional FAO and delivery of reduction equivalents to the ETC as a requirement to enable the motility increasing effect of CA in GMC101 nematodes, ATP levels, oxygen consumption and the MMP were also elevated as a consequence of CA incubation.

In conclusion, both 4-PBA as well as CA attenuate Aβ proteotoxicity in an AD model of the nematode *C. elegans*. They share the reduction of Aβ aggregation and improvement of mitochondrial function as common targets. Moreover, both substances serve as energy fuel via FAO, thus circumventing the steps specific for glucose oxidation that are impaired in AD. 4-PBA further activates the proteostasis network and the mitochondrial quality control, explaining its overall increased protective effect relative to CA.

7 Graphical Abstract

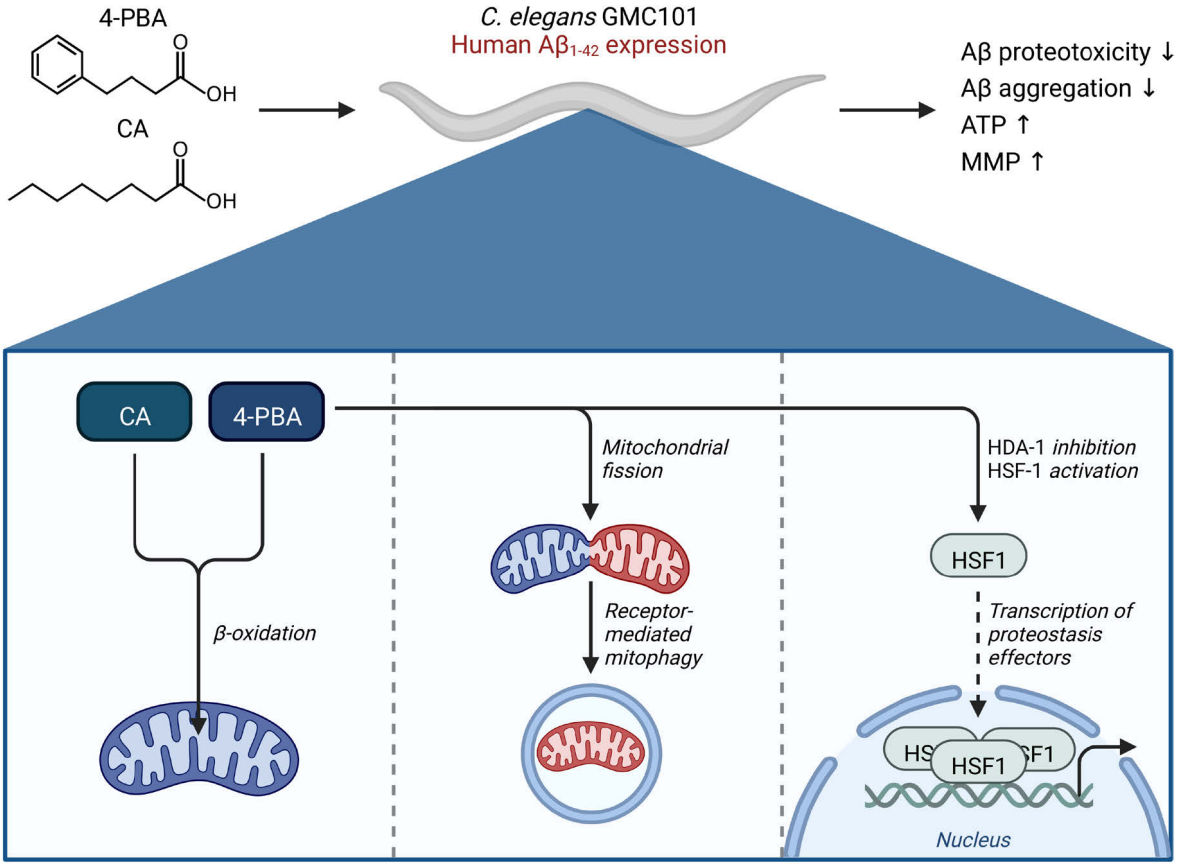

8 Zusammenfassung

Morbus Alzheimer ist eine neurodegenerative Erkrankung und die häufigste Form der Demenz. Die Neurodegeneration resultiert in einem progressiven Gedächtnisverlust sowie in psychologischen Veränderungen und kann schließlich zu einer fast vollständigen Beeinträchtigung der kognitiven Fähigkeiten führen. Aufgrund des Alters als Hauptrisikofaktor der sporadischen Form der Alzheimer-Krankheit und des fortschreitenden demografischen Wandels ist die Erkrankung eine zunehmende Belastung für die moderne Gesellschaft. Trotz ihrer außerordentlichen Bedeutung und intensiver Forschung ist die derzeitige Therapie auf eine rein symptomatische Behandlung beschränkt. Die Pathogenese der Erkrankung ist ein komplexer, durch eine lange präklinische Phase gekennzeichneter, irreversibler Prozess. Dabei wurden die Akkumulation von proteotoxischen Amyloid-β (Aβ) Aggregaten und die mitochondriale Dysfunktion als sich gegenseitig verstärkende zentrale Merkmale identifiziert, welche letztendlich in einer progressiven Störung der Neurotransmission und Neurodegeneration resultieren.

In der vorliegenden Arbeit wurden die molekularen Effekte der aromatischen kurzkettigen Fettsäure 4-Phenylbuttersäure (*4-phenylbutyric acid*; 4-PBA) und der mittelkettigen Fettsäure Caprylsäure (*caprylic acid*; CA) auf die Proteostase und die mitochondriale Homöostase anhand des transgenen *Caenorhabditis elegans* Stamms GMC101, der humanes $A\beta_{1-42}$ in Körperwandmuskelzellen exprimiert, untersucht. Mittels computergestützter Analyse der Motilität wurde festgestellt, dass die durchschnittliche Geschwindigkeit von GMC101 durch die Proteotoxizität von Aβ im Vergleich zum korrespondierenden Kontrollstamm CL2122 erheblich reduziert ist. Sowohl 4-PBA als auch CA konnten dosisabhängig und selektiv die Motilität von GMC101-Nematoden erhöhen. Ihr selektiver protektiver Effekt auf die Proteotoxizität von Aβ wurde zudem durch eine Reduzierung der Aβ-Aggregation unter Verwendung des Aβ-spezifischen Fluoreszenzfarbstoffs NIAD-4 bestätigt.
Da 4-PBA als schwacher Inhibitor von Histon-Deacetylasen (HDACs) der Klassen I und IIb über verschiedene Mechanismen potenziell die Protein-Qualitätskontrolle aktiviert, wurde zunächst die Bedeutung der wichtigsten Proteostase-Transkriptionsfaktoren mittels RNA-Interferenz (RNAi) untersucht. Durch den *knockdown* von *hsf-1*, einem Ortholog mit essentieller Funktion in der cytosolischen *heat shock response*, wurde die 4-PBA-abhängige Verringerung der Aβ-Aggregation und Proteotoxizität unterdrückt. Da der *knockdown* von *hda-1*, einem Ortholog von *HDAC2*, die Motilität ebenfalls in Abhängigkeit von *hsf-1* steigerte und die Applikation von 4-PBA unter *hda-1* RNAi keine additive Wirkung aufwies,

ist davon auszugehen, dass 4-PBA HSF-1 über die Inhibition von HDA-1 aktiviert. Zusätzlich zur Aktivierung der Protein-Qualitätskontrolle steigerte 4-PBA die mitochondriale Funktion. Dies zeigte sich sowohl im Hinblick auf den mittels Luciferase-Assay gemessenen Adenosintriphosphat (ATP)-Spiegel als auch auf das unter Verwendung des Fluoreszenzfarbstoffes TMRE quantifizierte mitochondriale Membranpotenzial (MMP). Durch die Nutzung von RNAi gegen Gene, die an der β-Oxidation (*fatty acid oxidation*; FAO) und an Komplex I sowie Komplex II der Elektronentransportkette (*electron transport chain*; ETC) beteiligt sind, konnte nachgewiesen werden, dass die motilitätssteigernde Wirkung von 4-PBA von seiner Oxidation zu Phenylessigsäure (*phenylacetic acid*; PAA) und damit von seinen Eigenschaften als Energiequelle abhängig ist. Weiterhin führte die Regulation von Genen mit zentraler Funktion bei der mitochondrialen Fission und der rezeptorvermittelten Mitophagie zu einer verringerten protektiven Wirkung von 4-PBA. Dies wurde ferner durch genetische Kreuzungen von Aβ-exprimierenden GMC101-Nematoden mit transgenen fluoreszierenden Reporterstämmen untersucht, wodurch eine erhöhte mitochondriale Fission und schließlich eine Induktion der Mitophagie bestätigt werden konnten.
CA ist eine Vorstufe für die Biosynthese von α-Liponsäure (*α-lipoic acid*; ALA), einem zellulären Antioxidans und Coenzym mit wichtiger Funktion im Energiestoffwechsel, sowie des Ketonkörpers β-Hydroxybuttersäure (BHB), welcher als alternatives Energiesubstrat und Signalmolekül dienen kann. Es wurde gezeigt, dass CA unabhängig von der Biosynthese beider Metabolite protektiv wirkt. Wie im Fall von 4-PBA wurde die motilitätssteigernde Wirkung der CA durch RNAi gegen Gene, die an FAO und Komplex I sowie Komplex II des ETC beteiligt sind, aufgehoben. In Übereinstimmung mit der Notwendigkeit einer funktionsfähigen FAO und der Bereitstellung von Reduktionsäquivalenten für die ETC als Voraussetzung der motilitätssteigernden Wirkung der CA waren der ATP-Spiegel, der Sauerstoffverbrauch und das MMP ebenfalls als Folge der CA-Inkubation erhöht.

Zusammenfassend lässt sich feststellen, dass sowohl 4-PBA als auch CA die Aβ-Proteotoxizität in einem Alzheimer-Modell des Fadenwurms *C. elegans* abschwächen. Beide Substanzen wirken über die Verringerung der Aβ-Aggregation sowie die Verbesserung der mitochondrialen Funktion. Zudem dienen sie als Substrate der FAO, wodurch Energie unabhängig der bei Morbus Alzheimer üblicherweise beeinträchtigten Glukoseoxidation gewonnen werden kann. 4-PBA aktiviert darüber hinaus das Proteostase-Netzwerk und die mitochondriale Qualitätskontrolle, was die im Vergleich zu CA insgesamt beobachtete erhöhte protektive Wirkung erklärt.

9 References

[1] Querfurth, H. W.; LaFerla, F. M. (2010). Alzheimer's Disease, *The New England Journal of Medicine*, Vol. 362, No. 4, 329–344. doi:10.1056/NEJMra040223

[2] Prince, M.; Wimo, A.; Guerchet, M.; Ali, G.-C.; Wu, Y.-T.; Prina, M. (2015). World Alzheimer Report 2015 - The Global Impact of Dementia - An Analysis of Prevalence, Incidence, Cost and Trends. *Alzheimer's Disease International*

[3] Oboudiyat, C.; Glazer, H.; Seifan, A.; Greer, C.; Isaacson, R. S. (2013). Alzheimer's disease, *Seminars in Neurology*, Vol. 33, No. 4, 313–329. doi:10.1055/s-0033-1359319

[4] Lane, C. A.; Hardy, J.; Schott, J. M. (2018). Alzheimer's disease, *European Journal of Neurology*, Vol. 25, No. 1, 59–70. doi:10.1111/ene.13439

[5] Scheltens, P.; Blennow, K.; Breteler, M. M. B.; de Strooper, B.; Frisoni, G. B.; Salloway, S.; van der Flier, W. M. (2016). Alzheimer's disease, *The Lancet*, Vol. 388, No. 10043, 505–517. doi:10.1016/S0140-6736(15)01124-1

[6] LaFerla, F. M.; Oddo, S. (2005). Alzheimer's disease: Aβ, tau and synaptic dysfunction, *Trends in Molecular Medicine*, Vol. 11, No. 4, 170–176. doi:10.1016/j.molmed.2005.02.009

[7] Prince, M.; Albanese, E.; Guerchet, M.; Prina, M. (2014). World Alzheimer Report 2014 - Dementia and Risk Reduction - An Analysis of Protective and Modifiable Factors. *Alzheimer's Disease International*

[8] Anand, R.; Gill, K. D.; Mahdi, A. A. (2014). Therapeutics of Alzheimer's disease: Past, present and future, *Neuropharmacology*, Vol. 76, 27–50. doi:10.1016/j.neuropharm.2013.07.004

[9] van der Kant, R.; Goldstein, L. S. B. (2015). Cellular Functions of the Amyloid Precursor Protein from Development to Dementia, *Developmental Cell*, Vol. 32, No. 4, 502–515. doi:10.1016/j.devcel.2015.01.022

[10] Müller, U. C.; Deller, T.; Korte, M. (2017). Not just amyloid: Physiological functions of the amyloid precursor protein family, *Nature Reviews Neuroscience*, Vol. 18, No. 5, 281–298. doi:10.1038/nrn.2017.29

[11] LaFerla, F. M.; Green, K. N.; Oddo, S. (2007). Intracellular amyloid-β in Alzheimer's disease, *Nature Reviews Neuroscience*, Vol. 8, No. 7, 499–509. doi:10.1038/nrn2168

[12] Olsson, F.; Schmidt, S.; Althoff, V.; Munter, L. M.; Jin, S.; Rosqvist, S.; Lendahl, U.; Multhaup, G.; Lundkvist, J. (2014). Characterization of intermediate steps in amyloid beta (Aβ) production under near-native conditions, *Journal of Biological Chemistry*, Vol. 289, No. 3, 1540–1550. doi:10.1074/jbc.M113.498246

[13] Wang, H.; Megill, A.; He, K.; Kirkwood, A.; Lee, H. K. (2012). Consequences of inhibiting amyloid precursor protein processing enzymes on synaptic function and plasticity, *Neural Plasticity*, Vol. 2012. doi:10.1155/2012/272374

[14] Mclean, C. A.; Cherny, R. A.; Fraser, F. W.; Hons, B.; Fuller, S. J.; Smith, M. J.; Beyreuther, K.; Bush, A. I.; Masters, C. L. (1999). Soluble Pool of Aβ Amyloid as a Determinant of Severity of Neurodegeneration in Alzheimer's Disease, *Annals of Neurology*, Vol. 46, 860–866. doi:10.1002/1531-8249(199912)46:6<860::aid-ana8>3.0.co;2-m

[15] Jarrett, J. T.; Berger, E. P.; Lansbury, P. T. (1993). The Carboxy Terminus of the Amyloid Protein Is Critical for the Seeding of Amyloid Formation: Implications for the Pathogenesis of Alzheimer's Disease?, *Biochemistry*, Vol. 32, No. 18. doi:10.1021/bi00069a001

[16] Kayed, R.; Lasagna-Reeves, C. A. (2013). Molecular Mechanisms of Amyloid Oligomers Toxicity, *Journal of Alzheimer's Disease*, Vol. 33, 67–78. doi:10.3233/JAD-2012-129001

[17] Kandimalla, K. K.; Scott, O. G.; Fulzele, S.; Davidson, M. W.; Poduslo, J. F. (2009). Mechanism of Neuronal versus endothelial cell uptake of Alzheimer's disease amyloid β protein, *PLoS ONE*, Vol. 4, No. 2. doi:10.1371/journal.pone.0004627

[18] McLaurin, J.; Lai, A. Y. (2011). Mechanisms of amyloid-beta peptide uptake by neurons: The role of lipid rafts and lipid raft-associated proteins, *International Journal of Alzheimer's Disease*. doi:10.4061/2011/548380

[19] Strazielle, N.; Ghersi-Egea, J.-F.; Ghiso, J.; Dehouck, M.-P.; Frangione, B.; Patlak, C.; Fenstermacher, J.; Gorevic, P. (2000). In Vitro Evidence That-Amyloid Peptide 1-40 Diffuses Across the Blood-Brain Barrier and Affects Its Permeability, *Journal of Neuropathology and Experimental Neurology*, Vol. 59, No. 1

[20] Hartl, F. U.; Bracher, A.; Hayer-Hartl, M. (2011). Molecular chaperones in protein folding and proteostasis, *Nature*, Vol. 475, No. 7356, 324–332. doi:10.1038/nature10317

[21] Dunker, A. K.; Silman, I.; Uversky, V. N.; Sussman, J. L. (2008). Function and structure of inherently disordered proteins, *Current Opinion in Structural Biology*, Vol. 18, No. 6, 756–764. doi:10.1016/j.sbi.2008.10.002

[22] Hipp, M. S.; Kasturi, P.; Hartl, F. U. (2019). The proteostasis network and its decline in ageing, *Nature Reviews Molecular Cell Biology*, Vol. 20, No. 7, 421–435. doi:10.1038/s41580-019-0101-y

[23] Bose, S.; Cho, J. (2017). Targeting chaperones, heat shock factor-1, and unfolded protein response: Promising therapeutic approaches for neurodegenerative disorders, *Ageing Research Reviews*, Vol. 35, 155–175. doi:10.1016/j.arr.2016.09.004

[24] Hageman, J.; Vos, M. J.; van Waarde, M. A. W. H.; Kampinga, H. H. (2007). Comparison of intra-organellar chaperone capacity for dealing with stress-induced protein unfolding, *Journal of Biological Chemistry*, Vol. 282, No. 47, 34334–34345. doi:10.1074/jbc.M703876200

[25] Kampinga, H. H.; Bergink, S. (2016). Heat shock proteins as potential targets for protective strategies in neurodegeneration, *The Lancet Neurology*, Vol. 15, No. 7, 748–759. doi:10.1016/S1474-4422(16)00099-5

[26] Kampinga, H. H.; Hageman, J.; Vos, M. J.; Kubota, H.; Tanguay, R. M.; Bruford, E. A.; Cheetham, M. E.; Chen, B.; Hightower, L. E. (2009, January). Guidelines for the nomenclature of the human heat shock proteins, *Cell Stress and Chaperones*, 105–111. doi:10.1007/s12192-008-0068-7

[27] Johnson, B. D.; Schumacher, R. J.; Ross, E. D.; Toft, D. O. (1998). Hop modulates hsp70/hsp90 interactions in protein folding, *Journal of Biological Chemistry*, Vol. 273, No. 6, 3679–3686. doi:10.1074/jbc.273.6.3679

[28] Kettern, N.; Dreiseidler, M.; Tawo, R.; Höhfeld, J. (2010). Chaperone-assisted degradation: Multiple paths to destruction, *Biological Chemistry*, Vol. 391, No. 5, 481–489. doi:10.1515/BC.2010.058

[29] Arndt, V.; Rogon, C.; Höhfeld, J. (2007). To be, or not to be - Molecular chaperones in protein degradation, *Cellular and Molecular Life Sciences*, Vol. 64, Nos. 19–20, 2525–2541. doi:10.1007/s00018-007-7188-6

[30] Taylor, R. C.; Berendzen, K. M.; Dillin, A. (2014). Systemic stress signalling: Understanding the cell non-autonomous control of proteostasis, *Nature Reviews Molecular Cell Biology*, Vol. 15, No. 3, 211–217. doi:10.1038/nrm3752

[31] Anckar, J.; Sistonen, L. (2011). Regulation of HSF1 function in the heat stress response: Implications in aging and disease, *Annual Review of Biochemistry*, Vol. 80, 1089–1115. doi:10.1146/annurev-biochem-060809-095203

[32] Masser, A. E.; Ciccarelli, M.; Andréasson, C. (2020). Hsf1 on a leash – controlling the heat shock response by chaperone titration, *Experimental Cell Research*, Vol. 396, No. 1. doi:10.1016/j.yexcr.2020.112246

[33] Pernet, L.; Faure, V.; Gilquin, B.; Dufour-Guérin, S.; Khochbin, S.; Vourc'H, C. (2014). HDAC6-ubiquitin interaction controls the duration of HSF1 activation after heat shock, *Molecular Biology of the Cell*, Vol. 25, No. 25, 4187–4194. doi:10.1091/mbc.E14-06-1032

[34] Gomez-Pastor, R.; Burchfiel, E. T.; Thiele, D. J. (2018). Regulation of heat shock transcription factors and their roles in physiology and disease, *Nature Reviews Molecular Cell Biology*, Vol. 19, No. 1, 4–19. doi:10.1038/nrm.2017.73

[35] Boyault, C.; Zhang, Y.; Fritah, S.; Caron, C.; Gilquin, B.; So, H. K.; Garrido, C.; Yao, T. P.; Vourc'h, C.; Matthias, P.; Khochbin, S. (2007). HDAC6 controls major cell response pathways to cytotoxic accumulation of protein aggregates, *Genes and Development*, Vol. 21, No. 17, 2172–2181. doi:10.1101/gad.436407

[36] Åkerfelt, M.; Morimoto, R. I.; Sistonen, L. (2010). Heat shock factors: Integrators of cell stress, development and lifespan, *Nature Reviews Molecular Cell Biology*, Vol. 11, No. 8, 545–555. doi:10.1038/nrm2938

[37] Hetz, C.; Chevet, E.; Oakes, S. A. (2015). Proteostasis control by the unfolded protein response, *Nature Cell Biology*, Vol. 17, No. 7, 829–838. doi:10.1038/ncb3184

[38] Hetz, C.; Zhang, K.; Kaufman, R. J. (2020). Mechanisms, regulation and functions of the unfolded protein response, *Nature Reviews Molecular Cell Biology*, Vol. 21, No. 8, 421–438. doi:10.1038/s41580-020-0250-z

[39] Bertolotti, A.; Zhang, Y.; Hendershot, L. M.; Harding, H. P.; Ron, D. (2000). Dynamic interaction of BiP and ER stress transducers in the unfolded-protein response, *Nature Cell Biology*, Vol. 2, 326–332. doi:10.1038/35014014

[40] Shen, J.; Chen, X.; Hendershot, L.; Prywes, R. (2002). ER Stress Regulation of ATF6 Localization by Dissociation of BiP/GRP78 Binding and Unmasking of Golgi Localization Signals, *Developmental Cell*, Vol. 3, 99–111. doi:10.1016/s1534-5807(02)00203-4

[41] Wu, J.; Kaufman, R. J. (2006). From acute ER stress to physiological roles of the unfolded protein response, *Cell Death and Differentiation*, Vol. 13, No. 3, 374–384. doi:10.1038/sj.cdd.4401840

[42] Nishitoh, H. (2012). CHOP is a multifunctional transcription factor in the ER stress response, *Journal of Biochemistry*, Vol. 151, No. 3, 217–219. doi:10.1093/jb/mvr143

[43] Shpilka, T.; Haynes, C. M. (2018). The mitochondrial UPR: Mechanisms, physiological functions and implications in ageing, *Nature Reviews Molecular Cell Biology*, Vol. 19, No. 2, 109–120. doi:10.1038/nrm.2017.110

[44] Zhu, L.; Zhou, Q.; He, L.; Chen, L. (2021). Mitochondrial unfolded protein response: An emerging pathway in human diseases, *Free Radical Biology and Medicine*, Vol. 163, 125–134. doi:10.1016/j.freeradbiomed.2020.12.013

[45] Fiorese, C. J.; Schulz, A. M.; Lin, Y. F.; Rosin, N.; Pellegrino, M. W.; Haynes, C. M. (2016). The Transcription Factor ATF5 Mediates a Mammalian Mitochondrial UPR, *Current Biology*, Vol. 26, No. 15, 2037–2043. doi:10.1016/j.cub.2016.06.002

[46] Teske, B. F.; Fusakio, M. E.; Zhou, D.; Shan, J.; McClintick, J. N.; Kilberg, M. S.; Wek, R. C. (2013). CHOP induces activating transcription factor 5 (ATF5) to trigger apoptosis in response to perturbations in protein homeostasis, *Molecular Biology of the Cell*, Vol. 24, No. 15, 2477–2490. doi:10.1091/mbc.E13-01-0067

[47] Quirós, P. M.; Prado, M. A.; Zamboni, N.; D'Amico, D.; Williams, R. W.; Finley, D.; Gygi, S. P.; Auwerx, J. (2017). Multi-omics analysis identifies ATF4 as a key regulator of the mitochondrial stress response in mammals, *Journal of Cell Biology*, Vol. 216, No. 7, 2027–2045. doi:10.1083/jcb.201702058

[48] Ng, M. Y. W.; Wai, T.; Simonsen, A. (2021). Quality control of the mitochondrion, *Developmental Cell*, Vol. 56, No. 7, 881–905. doi:10.1016/j.devcel.2021.02.009

[49] Vilchez, D.; Saez, I.; Dillin, A. (2014). The role of protein clearance mechanisms in organismal ageing and age-related diseases, *Nature Communications*, Vol. 5, No. 1, 1–13. doi:10.1038/ncomms6659

[50] Ravikumar, B.; Futter, M.; Jahreiss, L.; Korolchuk, V. I.; Lichtenberg, M.; Luo, S.; Massey, D. C. O.; Menzies, F. M.; Narayanan, U.; Renna, M.; Jimenez-Sanchez, M.; Sarkar, S.; Underwood, B.; Winslow,

A.; Rubinsztein, D. C. (2009). Mammalian macroautophagy at a glance, *Journal of Cell Science*, Vol. 122, No. 11, 1707–1711. doi:10.1242/jcs.031773

[51] Parzych, K. R.; Klionsky, D. J. (2014). An overview of autophagy: Morphology, mechanism, and regulation, *Antioxidants and Redox Signaling*, Vol. 20, No. 3, 460–473. doi:10.1089/ars.2013.5371

[52] Dikic, I.; Elazar, Z. (2018). Mechanism and medical implications of mammalian autophagy, *Nature Reviews Molecular Cell Biology*, Vol. 19, No. 6, 349–364. doi:10.1038/s41580-018-0003-4

[53] Jin, M.; Liu, X.; Klionsky, D. J. (2013). SnapShot: Selective autophagy., *Cell*, Vol. 152, Nos. 1–2. doi:10.1016/j.cell.2013.01.004

[54] Li, W. W.; Li, J.; Bao, J. K. (2012). Microautophagy: Lesser-known self-eating, *Cellular and Molecular Life Sciences*, Vol. 69, No. 7, 1125–1136. doi:10.1007/s00018-011-0865-5

[55] Sahu, R.; Kaushik, S.; Clement, C. C.; Cannizzo, E. S.; Scharf, B.; Follenzi, A.; Potolicchio, I.; Nieves, E.; Cuervo, A. M.; Santambrogio, L. (2011). Microautophagy of Cytosolic Proteins by Late Endosomes, *Developmental Cell*, Vol. 20, No. 1, 131–139. doi:10.1016/j.devcel.2010.12.003

[56] Pakos-Zebrucka, K.; Koryga, I.; Mnich, K.; Ljujic, M.; Samali, A.; Gorman, A. M. (2016). The integrated stress response, *EMBO Reports*, Vol. 17, No. 10, 1374–1395. doi:10.15252/embr.201642195

[57] Boos, F.; Krämer, L.; Groh, C.; Jung, F.; Haberkant, P.; Stein, F.; Wollweber, F.; Gackstatter, A.; Zöller, E.; van der Laan, M.; Savitski, M. M.; Benes, V.; Herrmann, J. M. (2019). Mitochondrial protein-induced stress triggers a global adaptive transcriptional programme, *Nature Cell Biology*, Vol. 21, No. 4, 442–451. doi:10.1038/s41556-019-0294-5

[58] Katiyar, A.; Fujimoto, M.; Tan, K.; Kurashima, A.; Srivastava, P.; Okada, M.; Takii, R.; Nakai, A. (2020). HSF1 is required for induction of mitochondrial chaperones during the mitochondrial unfolded protein response, *FEBS Open Bio*, Vol. 10, No. 6, 1135–1148. doi:10.1002/2211-5463.12863

[59] Song, J.; Herrmann, J. M.; Becker, T. (2020). Quality control of the mitochondrial proteome, *Nature Reviews Molecular Cell Biology*, Vol. 22, No. January, 5–7. doi:10.1038/s41580-020-00300-2

[60] Tan, K.; Fujimoto, M.; Takii, R.; Takaki, E.; Hayashida, N.; Nakai, A. (2015). Mitochondrial SSBP1 protects cells from proteotoxic stresses by potentiating stress-induced HSF1 transcriptional activity, *Nature Communications*, Vol. 6. doi:10.1038/ncomms7580

[61] Barna, J.; Csermely, P.; Vellai, T. (2018). Roles of heat shock factor 1 beyond the heat shock response, *Cellular and Molecular Life Sciences*, Vol. 75, No. 16, 2897–2916. doi:10.1007/s00018-018-2836-6

[62] Galluzzi, L.; Yamazaki, T.; Kroemer, G. (2018). Linking cellular stress responses to systemic homeostasis, *Nature Reviews Molecular Cell Biology*, Vol. 19, No. 11, 731–745. doi:10.1038/s41580-018-0068-0

[63] Baker, M. J.; Tatsuta, T.; Langer, T. (2011). Quality control of mitochondrial proteostasis, *Cold Spring Harbor Perspectives in Biology*, Vol. 3, No. 7, 1–19. doi:10.1101/cshperspect.a007559

[64] Newmeyer, D. D.; Ferguson-Miller, S. (2003). Mitochondria: Releasing Power for Life and Unleashing the Machineries of Death, *Cell*, Vol. 112, 481–490. doi:10.1016/s0092-8674(03)00116-8

[65] Tait, S. W. G.; Green, D. R. (2012). Mitochondria and cell signalling, *Journal of Cell Science*, Vol. 125, No. 4, 807–815. doi:10.1242/jcs.099234

[66] Alexeyev, M. F.; Ledoux, S. P.; Wilson, G. L. (2004). Mitochondrial DNA and aging, *Clinical Science*, Vol. 107, 355–364. doi:10.1042/CS20040148

[67] Houten, S. M.; Wanders, R. J. A. (2010). A general introduction to the biochemistry of mitochondrial fatty acid β-oxidation, *Journal of Inherited Metabolic Disease*, Vol. 33, No. 5, 469–477. doi:10.1007/s10545-010-9061-2

[68] Hayamizu, K. (2017). Amino Acids and Energy Metabolism: An Overview, *Sustained Energy for Enhanced Human Functions and Activity*, Elsevier Inc., 339–349. doi:10.1016/B978-0-12-805413-0.00021-1

[69] Angelova, P. R.; Abramov, A. Y. (2016). Functional role of mitochondrial reactive oxygen species in physiology, *Free Radical Biology and Medicine*, Vol. 100, 81–85. doi:10.1016/j.freeradbiomed.2016.06.005

[70] Owen, O. E.; Kalhan, S. C.; Hanson, R. W. (2002). The key role of anaplerosis and cataplerosis for citric acid cycle function, *Journal of Biological Chemistry*, Vol. 277, No. 34, 30409–30412. doi:10.1074/jbc.R200006200

[71] Andreyev, A. Y.; Kushnareva, Y. E.; Murphy, A. N.; Starkov, A. A. (2015). Mitochondrial ROS metabolism: 10 Years later, *Biochemistry (Moscow)*, Vol. 80, No. 5, 517–531. doi:10.1134/S0006297915050028

[72] Müller, W. E.; Eckert, A.; Kurz, C.; Eckert, G. P.; Leuner, K. (2010). Mitochondrial dysfunction: Common final pathway in brain aging and Alzheimer's disease-therapeutic aspects, *Molecular Neurobiology*, Vol. 41, Nos. 2–3, 159–171. doi:10.1007/s12035-010-8141-5

[73] Kensler, T. W.; Wakabayashi, N.; Biswal, S. (2007). Cell survival responses to environmental stresses via the Keap1-Nrf2-ARE pathway, *Annual Review of Pharmacology and Toxicology*, Vol. 47, 89–116. doi:10.1146/annurev.pharmtox.46.120604.141046

[74] Joshi, G.; Johnson, J. A. (2012). The Nrf2-ARE pathway: a valuable therapeutic target for the treatment of neurodegenerative diseases, *Recent Patents on CNS Drug Discovery*, Vol. 7, No. 3, 218–229. doi:10.2174/157488912803252023

[75] Eijkelenboom, A.; Burgering, B. M. T. (2013). FOXOs: Signalling integrators for homeostasis maintenance, *Nature Reviews Molecular Cell Biology*, Vol. 14, No. 2, 83–97. doi:10.1038/nrm3507

[76] Krafczyk, N.; Klotz, L. O. (2022). FOXO transcription factors in antioxidant defense, *IUBMB Life*, Vol. 74, No. 1, 53–61. doi:10.1002/iub.2542

[77] Palikaras, K.; Tavernarakis, N. (2014). Mitochondrial homeostasis: The interplay between mitophagy and mitochondrial biogenesis, *Experimental Gerontology*, Vol. 56, 182–188. doi:10.1016/j.exger.2014.01.021

[78] Cai, Q.; Tammineni, P. (2016). Alterations in Mitochondrial Quality Control in Alzheimer's Disease, *Frontiers in Cellular Neuroscience*, Vol. 10, No. February, 1–17. doi:10.3389/fncel.2016.00024

[79] Kim, D. I.; Lee, K. H.; Oh, J. Y.; Kim, J. S.; Han, H. J. (2017). Relationship Between β-Amyloid and Mitochondrial Dynamics, *Cellular and Molecular Neurobiology*, Vol. 37, No. 6, 955–968. doi:10.1007/s10571-016-0434-4

[80] Zimmermann, M.; Reichert, A. S. (2017). How to get rid of mitochondria: Crosstalk and regulation of multiple mitophagy pathways, *Biological Chemistry*, Vol. 399, No. 1, 29–45. doi:10.1515/hsz-2017-0206

[81] Twig, G.; Shirihai, O. S. (2011). The interplay between mitochondrial dynamics and mitophagy, *Antioxidants and Redox Signaling*, Vol. 14, No. 10, 1939–1951. doi:10.1089/ars.2010.3779

[82] Xian, H.; Liou, Y. C. (2020). Functions of outer mitochondrial membrane proteins: mediating the crosstalk between mitochondrial dynamics and mitophagy, *Cell Death and Differentiation*. doi:10.1038/s41418-020-00657-z

[83] Chen, G.; Han, Z.; Feng, D.; Chen, Y.; Chen, L.; Wu, H.; Huang, L.; Zhou, C.; Cai, X.; Fu, C.; Duan, L.; Wang, X.; Liu, L.; Liu, X.; Shen, Y.; Zhu, Y.; Chen, Q. (2014). A regulatory signaling loop comprising the PGAM5 phosphatase and CK2 controls receptor-mediated mitophagy, *Molecular Cell*, Vol. 54, No. 3, 362–377. doi:10.1016/j.molcel.2014.02.034

[84] Bhujabal, Z.; Birgisdottir, Å. B.; Sjøttem, E.; Brenne, H. B.; Øvervatn, A.; Habisov, S.; Kirkin, V.; Lamark, T.; Johansen, T. (2017). FKBP8 recruits LC3A to mediate Parkin-independent mitophagy, *EMBO Reports*, Vol. 18, No. 6, 947–961. doi:10.15252/embr.201643147

[85] Wei, Y.; Chiang, W.-C.; Sumpter, R. Jr.; Mishra, P.; Levine, B. (2017). Prohibitin 2 Is an Inner Mitochondrial Membrane Mitophagy Receptor, *Cell*, Vol. 168, Nos. 1–2, 224–238. doi:10.1016/j.cell.2016.11.0

[86] Chu, C. T.; Ji, J.; Dagda, R. K.; Jiang, J. F.; Tyurina, Y. Y.; Kapralov, A. A.; Tyurin, V. A.; Yanamala, N.; Shrivastava, I. H.; Mohammadyani, D.; Qiang Wang, K. Z.; Zhu, J.; Klein-Seetharaman, J.; Balasubramanian, K.; Amoscato, A. A.; Borisenko, G.; Huang, Z.; Gusdon, A. M.; Cheikhi, A.; Steer, E. K.; Wang, R.; Baty, C.; Watkins, S.; Bahar, I.; Bayir, H.; Kagan, V. E. (2013). Cardiolipin externalization to the outer mitochondrial membrane acts as an elimination signal for mitophagy in neuronal cells, *Nature Cell Biology*, Vol. 15, No. 10, 1197–1205. doi:10.1038/ncb2837

[87] Sentelle, R. D.; Senkal, C. E.; Jiang, W.; Ponnusamy, S.; Gencer, S.; Panneer Selvam, S.; Ramshesh, V. K.; Peterson, Y. K.; Lemasters, J. J.; Szulc, Z. M.; Bielawski, J.; Ogretmen, B. (2012). Ceramide targets autophagosomes to mitochondria and induces lethal mitophagy, *Nature Chemical Biology*, Vol. 8, No. 10, 831–838. doi:10.1038/nchembio.1059

[88] Shiba-Fukushima, K.; Arano, T.; Matsumoto, G.; Inoshita, T.; Yoshida, S.; Ishihama, Y.; Ryu, K. Y.; Nukina, N.; Hattori, N.; Imai, Y. (2014). Phosphorylation of Mitochondrial Polyubiquitin by PINK1 Promotes Parkin Mitochondrial Tethering, *PLoS Genetics*, Vol. 10, No. 12. doi:10.1371/journal.pgen.1004861

[89] Lazarou, M.; Sliter, D. A.; Kane, L. A.; Sarraf, S. A.; Wang, C.; Burman, J. L.; Sideris, D. P.; Fogel, A. I.; Youle, R. J. (2015). The ubiquitin kinase PINK1 recruits autophagy receptors to induce mitophagy, *Nature*, Vol. 524, No. 7565, 309–314. doi:10.1038/nature14893

[90] Martinez-Vicente, M. (2017). Neuronal Mitophagy in Neurodegenerative Diseases, *Frontiers in Molecular Neuroscience*, Vol. 10, 64. doi:10.3389/fnmol.2017.00064

[91] Szargel, R.; Shani, V.; Elghani, F. A.; Mekies, L. N.; Liani, E.; Rott, R.; Engelender, S. (2016). The PINK1, synphilin-1 and SIAH-1 complex constitutes a novel mitophagy pathway, *Human Molecular Genetics*, Vol. 25, No. 16, 3476–3490. doi:10.1093/hmg/ddw189

[92] Montava-Garriga, L.; Ganley, I. G. (2019). Outstanding Questions in Mitophagy: What we Do and Do Not Know, *Journal of Molecular Biology*. doi:10.1016/j.jmb.2019.06.032

[93] Durcan, T. M.; Tang, M. Y.; Pérusse, J. R.; Dashti, E. A.; Aguileta, M. A.; McLelland, G.; Gros, P.; Shaler, T. A.; Faubert, D.; Coulombe, B.; Fon, E. A. (2014). USP 8 regulates mitophagy by removing K 6-linked ubiquitin conjugates from parkin, *The EMBO Journal*, Vol. 33, No. 21, 2473–2491. doi:10.15252/embj.201489729

[94] Wang, Y.; Serricchio, M.; Jauregui, M.; Shanbhag, R.; Stoltz, T.; di Paolo, C. T.; Kim, P. K.; Angus McQuibban, G. (2015). Deubiquitinating enzymes regulate PARK2-mediated mitophagy, *Autophagy*, Vol. 11, No. 4, 595–606. doi:10.1080/15548627.2015.1034408

[95] Cornelissen, T.; Haddad, D.; Wauters, F.; van Humbeeck, C.; Mandemakers, W.; Koentjoro, B.; Sue, C.; Gevaert, K.; de Strooper, B.; Verstreken, P.; Vandenberghe, W. (2014). The deubiquitinase USP15 antagonizes Parkin-mediated mitochondrial ubiquitination and mitophagy, *Human Molecular Genetics*, Vol. 23, No. 19, 5227–5242. doi:10.1093/hmg/ddu244

[96] Heo, J. M.; Ordureau, A.; Paulo, J. A.; Rinehart, J.; Harper, J. W. (2015). The PINK1-PARKIN Mitochondrial Ubiquitylation Pathway Drives a Program of OPTN/NDP52 Recruitment and TBK1 Activation to Promote Mitophagy, *Molecular Cell*, Vol. 60, No. 1, 7–20. doi:10.1016/j.molcel.2015.08.016

[97] Esteban-Martínez, L.; Sierra-Filardi, E.; McGreal, R. S.; Salazar-Roa, M.; Mariño, G.; Seco, E.; Durand, S.; Enot, D.; Graña, O.; Malumbres, M.; Cvekl, A.; Cuervo, A. M.; Kroemer, G.; Boya, P. (2017). Programmed mitophagy is essential for the glycolytic switch during cell differentiation, *The EMBO Journal*, Vol. 36, No. 12, 1688–1706. doi:10.15252/embj.201695916

[98] Wei, H.; Liu, L.; Chen, Q. (2015). Selective removal of mitochondria via mitophagy: Distinct pathways for different mitochondrial stresses, *Biochimica et Biophysica Acta - Molecular Cell Research*, Vol. 1853, No. 10, 2784–2790. doi:10.1016/j.bbamcr.2015.03.013

[99] Schweers, R. L.; Zhang, J.; Randall, M. S.; Loyd, M. R.; Li, W.; Dorsey, F. C.; Kundu, M.; Opferman, J. T.; Cleveland, J. L.; Miller, J. L.; Ney, P. A. (2007). NIX is required for programmed mitochondrial clearance during reticulocyte maturation, *Proceedings of the National Academy of Sciences*, Vol. 104, No. 49, 19500–19505. doi:10.1073/pnas.0708818104

[100] Lee, Y.; Lee, H.-Y.; Hanna, R. A.; Gustafsson, Å. B. (2011). Mitochondrial autophagy by Bnip3 involves Drp1-mediated mitochondrial fission and recruitment of Parkin in cardiac myocytes, *Am J Physiol Heart Circ Physiol*, Vol. 301, 1924–1931. doi:10.1152/ajpheart.00368.2011

[101] Lu, R. C.; Tan, M. S.; Wang, H.; Xie, A. M.; Yu, J. T.; Tan, L. (2014). Heat shock protein 70 in alzheimer's disease, *BioMed Research International*, Vol. 2014. doi:10.1155/2014/435203

[102] Zhang, T.; Xue, L.; Li, L.; Tang, C.; Wan, Z.; Wang, R.; Tan, J.; Tan, Y.; Han, H.; Tian, R.; Billiar, T. R.; Tao, W. A.; Zhang, Z. (2016). BNIP3 protein suppresses PINK1 kinase proteolytic cleavage to promote mitophagy, *Journal of Biological Chemistry*, Vol. 291, No. 41, 21616–21629. doi:10.1074/jbc.M116.733410

[103] Graef, M. (2016). A dividing matter: Drp1/Dnm1-independent mitophagy, *Journal of Cell Biology*, Vol. 215, No. 5, 599–601. doi:10.1083/jcb.201611079

[104] Tanaka, A.; Cleland, M. M.; Xu, S.; Narendra, D. P.; Suen, D. F.; Karbowski, M.; Youle, R. J. (2010). Proteasome and p97 mediate mitophagy and degradation of mitofusins induced by Parkin, *Journal of Cell Biology*, Vol. 191, No. 7, 1367–1380. doi:10.1083/jcb.201007013

[105] Gegg, M. E.; Cooper, J. M.; Chau, K. Y.; Rojo, M.; Schapira, A. H. v; Taanman, J. W. (2010). Mitofusin 1 and mitofusin 2 are ubiquitinated in a PINK1/parkin-dependent manner upon induction of mitophagy, *Human Molecular Genetics*, Vol. 19, No. 24, 4861–4870. doi:10.1093/hmg/ddq419

[106] Yamashita, S. I.; Jin, X.; Furukawa, K.; Hamasaki, M.; Nezu, A.; Otera, H.; Saigusa, T.; Yoshimori, T.; Sakai, Y.; Mihara, K.; Kanki, T. (2016). Mitochondrial division occurs concurrently with autophagosome formation but independently of Drp1 during mitophagy, *Journal of Cell Biology*, Vol. 215, No. 5, 649–665. doi:10.1083/jcb.201605093

[107] Xian, H.; Yang, Q.; Xiao, L.; Shen, H. M.; Liou, Y. C. (2019). STX17 dynamically regulated by Fis1 induces mitophagy via hierarchical macroautophagic mechanism, *Nature Communications*, Vol. 10, No. 1. doi:10.1038/s41467-019-10096-1

[108] Wang, X.; Winter, D.; Ashrafi, G.; Schlehe, J.; Wong, Y. L.; Selkoe, D.; Rice, S.; Steen, J.; Lavoie, M. J.; Schwarz, T. L. (2011). PINK1 and Parkin target miro for phosphorylation and degradation to arrest mitochondrial motility, *Cell*, Vol. 147, No. 4, 893–906. doi:10.1016/j.cell.2011.10.018

[109] Ploumi, C.; Daskalaki, I.; Tavernarakis, N. (2017). Mitochondrial biogenesis and clearance: a balancing act, *FEBS Journal*, Vol. 284, No. 2, 183–195. doi:10.1111/febs.13820

[110] Wu, Z.; Puigserver, P.; Andersson, U.; Zhang, C.; Adelmant, G.; Mootha, V.; Troy, A.; Cinti, S.; Lowell, B.; Scarpulla, R. C.; Spiegelman, B. M. (1999). Mechanisms Controlling Mitochondrial Biogenesis and Respiration through the Thermogenic Coactivator PGC-1, *Cell*, Vol. 98, 115–124. doi:10.1016/S0092-8674(00)80611-X

[111] Virbasius, J. v; Scarpulla, R. C. (1994). Activation of the human mitochondrial transcription factor A gene by nuclear respiratory factors: A potential regulatory link between nuclear and mitochondrial gene expression in organelle biogenesis, *Proceedings of the National Academy of Sciences of the United States of America*, Vol. 91, 1309–1313. doi:10.1073/pnas.91.4.1309

[112] Hou, Y.; Dan, X.; Babbar, M.; Wei, Y.; Hasselbalch, S. G.; Croteau, D. L.; Bohr, V. A. (2019). Ageing as a risk factor for neurodegenerative disease, *Nature Reviews Neurology*. doi:10.1038/s41582-019-0244-7

[113] Mink, J. W.; Blumenschine, R. J.; Adams, D. B.; Ratio, D. B. A. (1981). Ratio of central nervous system to body metabolism in vertebrates: its constancy and functional basis, *American Journal of Physiology-*

Regulatory, Integrative and Comparative Physiology, Vol. 241, No. 3, 203–212. doi:10.1152/ajpregu.1981.241.3.R203

[114] Harris, J. J.; Jolivet, R.; Attwell, D. (2012). Synaptic Energy Use and Supply, *Neuron*, Vol. 75, No. 5, 762–777. doi:10.1016/j.neuron.2012.08.019

[115] Attwell, D.; Laughlin, S. B. (2001). An Energy Budget for Signaling in the Grey Matter of the Brain, *Journal of Cerebral Blood Flow and Metabolism*, Vol. 21, 1133–1145. doi:10.1097/00004647-200110000-00001

[116] Wang, X.; Wang, W.; Li, L.; Perry, G.; Lee, H.; Zhu, X. (2014). Oxidative Stress and Mitochondrial Dysfunction in Alzheimer's Disease, *Biochimica et Biophysica Acta*, Vol. 1842, No. 8, 1240–1247. doi:10.1016/j.bbadis.2013.10.015

[117] Guo, L.; Tian, J.; Du, H. (2017). Mitochondrial Dysfunction and Synaptic Transmission Failure in Alzheimer's Disease, *Journal of Alzheimer's Disease*, Vol. 57, No. 4, 1071–1086. doi:10.3233/JAD-160702

[118] Metaxakis, A.; Ploumi, C.; Tavernarakis, N. (2018). Autophagy in Age-Associated Neurodegeneration, *Cells*, Vol. 7, No. 5, 37. doi:10.3390/cells7050037

[119] Sheng, Z. H. (2014). Mitochondrial trafficking and anchoring in neurons: New insight and implications, *Journal of Cell Biology*, Vol. 204, No. 7, 1087–1098. doi:10.1083/jcb.201312123

[120] Kato, D.; Takahashi, Y.; Iwata, H.; Hatakawa, Y.; Lee, S. H.; Oe, T. (2022). Comparative studies for amyloid beta degradation: "Neprilysin vs insulysin", "monomeric vs aggregate", and "whole Aβ40 vs its peptide fragments", *Biochemistry and Biophysics Reports*, Vol. 30. doi:10.1016/j.bbrep.2022.101268

[121] Saido, T.; Leissring, M. A. (2012). Proteolytic degradation of amyloid β-protein, *Cold Spring Harbor Perspectives in Medicine*, Vol. 2, No. 6. doi:10.1101/cshperspect.a006379

[122] Zhang, W.; Xu, C.; Sun, J.; Shen, H. M.; Wang, J.; Yang, C. (2022). Impairment of the autophagy–lysosomal pathway in Alzheimer's diseases: Pathogenic mechanisms and therapeutic potential, *Acta Pharmaceutica Sinica B*, Vol. 12, No. 3, 1019–1040. doi:10.1016/j.apsb.2022.01.008

[123] Ji, X. R.; Cheng, K. C.; Chen, Y. R.; Lin, T. Y.; Cheung, C. H. A.; Wu, C. L.; Chiang, H. C. (2018). Dysfunction of different cellular degradation pathways contributes to specific β-amyloid42-induced pathologies, *FASEB Journal*, Vol. 32, No. 3, 1375–1387. doi:10.1096/fj.201700199RR

[124] Levine, B.; Kroemer, G. (2008). Autophagy in the Pathogenesis of Disease, *Cell*, Vol. 132, No. 1, 27–42. doi:10.1016/j.cell.2007.12.018

[125] Pagani, L.; Eckert, A. (2011). Amyloid-Beta Interaction with Mitochondria, *International Journal of Alzheimer's Disease*, Vol. 2011. doi:10.4061/2011/925050

[126] Pinho, C. M.; Teixeira, P. F.; Glaser, E. (2014). Mitochondrial import and degradation of amyloid-β peptide, *Biochimica et Biophysica Acta - Bioenergetics*, Vol. 1837, No. 7, 1069–1074. doi:10.1016/j.bbabio.2014.02.007

[127] Chen, J. X.; Yan, S. S. (2010). Role of Mitochondrial Amyloid-β in Alzheimer's Disease, *Journal of Alzheimer's Disease*, Vol. 20, 569–578. doi:10.3233/JAD-2010-100357

[128] Murakami, Y.; Ohsawa, I.; Kasahara, T.; Ohta, S. (2009). Cytoprotective role of mitochondrial amyloid β peptide-binding alcohol dehydrogenase against a cytotoxic aldehyde, *Neurobiology of Aging*, Vol. 30, No. 2, 325–329. doi:10.1016/j.neurobiolaging.2007.07.002

[129] Fang, E. F.; Hou, Y.; Palikaras, K.; Adriaanse, B. A.; Kerr, J. S.; Yang, B.; Lautrup, S.; Hasan-Olive, M. M.; Caponio, D.; Dan, X.; Rocktäschel, P.; Croteau, D. L.; Akbari, M.; Greig, N. H.; Fladby, T.; Nilsen, H.; Cader, M. Z.; Mattson, M. P.; Tavernarakis, N.; Bohr, V. A. (2019). Mitophagy inhibits amyloid-β and tau pathology and reverses cognitive deficits in models of Alzheimer's disease, *Nature Neuroscience*, Vol. 22, No. 3, 401–412. doi:10.1038/s41593-018-0332-9

[130] Lou, G.; Palikaras, K.; Lautrup, S.; Scheibye-Knudsen, M.; Tavernarakis, N.; Fang, E. F. (2020). Mitophagy and Neuroprotection, *Trends in Molecular Medicine*, Vol. 26, No. 1, 8–20. doi:10.1016/j.molmed.2019.07.002

[131] Gibson, G. E.; Shi, Q. (2010). A Mitocentric View of Alzheimer's Disease Suggests Multi- Faceted Treatments, *Journal of Alzheimer's Disease*, Vol. 20, No. 0 2, 591–607. doi:10.3233/JAD-2010-100336

[132] Cunnane, S. C.; Courchesne-Loyer, A.; Vandenberghe, C.; St-Pierre, V.; Fortier, M.; Hennebelle, M.; Croteau, E.; Bocti, C.; Fulop, T.; Castellano, C.-A. (2016). Can Ketones Help Rescue Brain Fuel Supply in Later Life? Implications for Cognitive Health during Aging and the Treatment of Alzheimer's Disease., *Frontiers in Molecular Neuroscience*, Vol. 9, 53. doi:10.3389/fnmol.2016.00053

[133] Cunnane, S. C.; Trushina, E.; Morland, C.; Prigione, A.; Casadesus, G.; Andrews, Z. B.; Beal, M. F.; Bergersen, L. H.; Brinton, R. D.; de la Monte, S.; Eckert, A.; Harvey, J.; Jeggo, R.; Jhamandas, J. H.; Kann, O.; la Cour, C. M.; Martin, W. F.; Mithieux, G.; Moreira, P. I.; Murphy, M. P.; Nave, K. A.; Nuriel, T.; Oliet, S. H. R.; Saudou, F.; Mattson, M. P.; Swerdlow, R. H.; Millan, M. J. (2020). Brain energy rescue: an emerging therapeutic concept for neurodegenerative disorders of ageing, *Nature Reviews Drug Discovery*, Vol. 19, No. 9, 609–633. doi:10.1038/s41573-020-0072-x

[134] Alikhani, N.; Ankarcrona, M.; Glaser, E. (2009). Mitochondria and Alzheimer's disease: Amyloid-β peptide uptake and degradation by the presequence protease, hPreP, *Journal of Bioenergetics and Biomembranes*, Vol. 41, No. 5, 447–451. doi:10.1007/s10863-009-9244-4

[135] Swerdlow, R. H. (2018). Mitochondria and Mitochondrial Cascades in Alzheimer's Disease, *Journal of Alzheimer's Disease*, Vol. 62, No. 3, 1403–1416. doi:10.3233/JAD-170585

[136] Cuadrado-Tejedor, M.; Garcia-Osta, A.; Ricobaraza, A.; Oyarzabal, J.; Franco, R. (2011). Defining the Mechanism of Action of 4-Phenylbutyrate to Develop a Small-Molecule-Based Therapy for Alzheimers Disease, *Current Medicinal Chemistry*, Vol. 18, No. 36, 5545–5553. doi:10.2174/092986711798347315

[137] Kolb, P. S.; Ayaub, E. A.; Zhou, W.; Yum, V.; Dickhout, J. G.; Ask, K. (2015). The therapeutic effects of 4-phenylbutyric acid in maintaining proteostasis, *International Journal of Biochemistry and Cell Biology*, Vol. 61, 45–52. doi:10.1016/j.biocel.2015.01.015

[138] Berg, S.; Serabe, B.; Aleksic, A.; Bomgaars, L.; McGuffey, L.; Dauser, R.; Durfee, J.; Nuchtern, J.; Blaney, S. (2001). Pharmacokinetics and cerebrospinal fluid penetration of phenylacetate and phenylbutyrate in the nonhuman primate, *Cancer Chemotherapy and Pharmacology*, Vol. 47, No. 5, 385–390. doi:10.1007/s002800000256

[139] Papp, E.; Csermely, · P. (2006). *Chemical Chaperones: Mechanisms of Action and Potential Use*, (K. Starke & M. Gaestel, Eds.)*HEP* (Vol. 172). doi:10.1007/3-540-29717-0_16

[140] Cortez, L.; Sim, V. (2014). The therapeutic potential of chemical chaperones in protein folding diseases, *Prion*, Vol. 8, No. 2, 197–202. doi:10.4161/pri.28938

[141] Hirata, K.; Nambara, T.; Kawatani, K.; Nawa, N.; Yoshimatsu, H.; Kusakabe, H.; Banno, K.; Nishimura, K.; Ohtaka, M.; Nakanishi, M.; Taniguchi, H.; Arahori, H.; Wada, K.; Ozono, K.; Kitabatake, Y. (2020). 4-Phenylbutyrate ameliorates apoptotic neural cell death in Down syndrome by reducing protein aggregates, *Scientific Reports*, Vol. 10, No. 1. doi:10.1038/s41598-020-70362-x

[142] Kubota, K.; Niinuma, Y.; Kaneko, M.; Okuma, Y.; Sugai, M.; Omura, T.; Uesugi, M.; Uehara, T.; Hosoi, T.; Nomura, Y. (2006). Suppressive effects of 4-phenylbutyrate on the aggregation of Pael receptors and endoplasmic reticulum stress, *Journal of Neurochemistry*, Vol. 97, No. 5, 1259–1268. doi:10.1111/j.1471-4159.2006.03782.x

[143] Guiberson, N. G. L.; Pineda, A.; Abramov, D.; Kharel, P.; Carnazza, K. E.; Wragg, R. T.; Dittman, J. S.; Burré, J. (2018). Mechanism-based rescue of Munc18-1 dysfunction in varied encephalopathies by chemical chaperones, *Nature Communications*, Vol. 9, No. 1. doi:10.1038/s41467-018-06507-4

[144] Inden, M.; Kitamura, Y.; Takeuchi, H.; Yanagida, T.; Takata, K.; Kobayashi, Y.; Taniguchi, T.; Yoshimoto, K.; Kaneko, M.; Okuma, Y.; Taira, T.; Ariga, H.; Shimohama, S. (2007). Neurodegeneration of mouse nigrostriatal dopaminergic system induced by repeated oral administration of rotenone is prevented by 4-phenylbutyrate, a chemical chaperone, *Journal of Neurochemistry*, Vol. 101, No. 6, 1491–1504. doi:10.1111/j.1471-4159.2006.04440.x

[145] Wiley, J. C.; Pettan-Brewer, C.; Ladiges, W. C. (2011). Phenylbutyric acid reduces amyloid plaques and rescues cognitive behavior in AD transgenic mice, *Aging Cell*, Vol. 10, No. 3, 418–428. doi:10.1111/j.1474-9726.2011.00680.x

[146] Ricobaraza, A.; Cuadrado-Tejedor, M.; Garcia-Osta, A. (2011). Long-term Phenylbutyrate administration prevents memory deficits in Tg2576 mice by decreasing Aβ, *Frontiers in Bioscience*, Vol. 3, No. 4, 1375–1385. doi:10.2741/e340

[147] Ricobaraza, A.; Cuadrado-Tejedor, M.; Marco, S.; Pérez-Otaño, I.; García-Osta, A. (2010). Phenylbutyrate rescues dendritic spine loss associated with memory deficits in a mouse model of Alzheimer disease, *Hippocampus*, Vol. 22, No. 5, 1040–1050. doi:10.1002/hipo.20883

[148] Mimori, S.; Ohtaka, H.; Koshikawa, Y.; Kawada, K.; Kaneko, M.; Okuma, Y.; Nomura, Y.; Murakami, Y.; Hamana, H. (2013). 4-Phenylbutyric acid protects against neuronal cell death by primarily acting as a chemical chaperone rather than histone deacetylase inhibitor, *Bioorganic and Medicinal Chemistry Letters*, Vol. 23, No. 21, 6015–6018. doi:10.1016/j.bmcl.2013.08.001

[149] de Almeida, S. F.; Picarote, G.; Fleming, J. v; Carmo-Fonseca, M.; Azevedo, J. E.; de Sousa, M. (2007). Chemical chaperones reduce endoplasmic reticulum stress and prevent mutant HFE aggregate formation, *Journal of Biological Chemistry*, Vol. 282, No. 38, 27905–27912. doi:10.1074/jbc.M702672200

[150] Liang, T.; Xue, F.; Hang, W.; Wen, B.; Zhang, Q.; Chen, J.; Liu, X.; Chen, J.; Tian, Q. (2019). Neuron-Specific Apolipoprotein E4 (1-272) Fragment Induces Tau Hyperphosphorylation and Axonopathy via Triggering Endoplasmic Reticulum Stress, *Journal of Alzheimer's Disease*, Vol. 71, No. 2, 597–611. doi:10.3233/JAD-190419

[151] Bhardwaj, A.; Bhardwaj, R.; Dhawan, D. K.; Kaur, T. (2019). Exploring the Effect of Endoplasmic Reticulum Stress Inhibition by 4-Phenylbutyric Acid on AMPA-Induced Hippocampal Excitotoxicity in Rat Brain, *Neurotoxicity Research*, Vol. 35, No. 1, 83–91. doi:10.1007/s12640-018-9932-0

[152] Kulka, L. A. M.; Fangmann, P. V.; Panfilova, D.; Olzscha, H. (2020). Impact of HDAC Inhibitors on Protein Quality Control Systems: Consequences for Precision Medicine in Malignant Disease, *Frontiers in Cell and Developmental Biology*, Vol. 8. doi:10.3389/fcell.2020.00425

[153] Rao, R.; Fiskus, W.; Ganguly, S.; Kambhampati, S.; Bhalla, K. N. (2012). HDAC Inhibitors and Chaperone Function, *Advances in Cancer Research*, Vol. 116, 239–262. doi:10.1016/B978-0-12-394387-3.00007-0

[154] Yang, S. shuang; Zhang, R.; Wang, G.; Zhang, Y. fang. (2017). The development prospection of HDAC inhibitors as a potential therapeutic direction in Alzheimer's disease, *Translational Neurodegeneration*, Vol. 6, No. 1. doi:10.1186/s40035-017-0089-1

[155] Peleg, S.; Feller, C.; Ladurner, A. G.; Imhof, A. (2016). The Metabolic Impact on Histone Acetylation and Transcription in Ageing, *Trends in Biochemical Sciences*, Vol. 41, No. 8, 700–711. doi:10.1016/j.tibs.2016.05.008

[156] Feser, J.; Tyler, J. (2011). Chromatin structure as a mediator of aging, *FEBS Letters*, Vol. 585, No. 13, 2041–2048. doi:10.1016/j.febslet.2010.11.016

[157] Shukla, S.; Tekwani, B. L. (2020). Histone Deacetylases Inhibitors in Neurodegenerative Diseases, Neuroprotection and Neuronal Differentiation, *Frontiers in Pharmacology*, Vol. 11. doi:10.3389/fphar.2020.00537

[158] McIntyre, R. L.; Daniels, E. G.; Molenaars, M.; Houtkooper, R. H.; Janssens, G. E. (2019). From molecular promise to preclinical results: HDAC inhibitors in the race for healthy aging drugs, *EMBO Molecular Medicine*, Vol. 11, No. 9. doi:10.15252/emmm.201809854

[159] Gupta, R.; Ambasta, R. K.; Kumar, P. (2020). Pharmacological intervention of histone deacetylase enzymes in the neurodegenerative disorders, *Life Sciences*, Vol. 243. doi:10.1016/j.lfs.2020.117278

[160] Baumeister, P.; Dong, D.; Fu, Y.; Lee, A. S. (2009). Transcriptional induction of GRP78/BiP by histone deacetylase inhibitors and resistance to histone deacetylase inhibitor-induced apoptosis, *Molecular Cancer Therapeutics*, Vol. 8, No. 5, 1086–1094. doi:10.1158/1535-7163.MCT-08-1166

[161] Zelin, E.; Freeman, B. C. (2015). Lysine deacetylases regulate the heat shock response including the age-associated impairment of HSF1, *Journal of Molecular Biology*, Vol. 427, No. 7, 1644–1654. doi:10.1016/j.jmb.2015.02.010

[162] Bali, P.; Pranpat, M.; Bradner, J.; Balasis, M.; Fiskus, W.; Guo, F.; Rocha, K.; Kumaraswamy, S.; Boyapalle, S.; Atadja, P.; Seto, E.; Bhalla, K. (2005). Inhibition of histone deacetylase 6 acetylates and disrupts the chaperone function of heat shock protein 90: A novel basis for antileukemia activity of histone deacetylase inhibitors, *Journal of Biological Chemistry*, Vol. 280, No. 29, 26729–26734. doi:10.1074/jbc.C500186200

[163] Kahali, S.; Sarcar, B.; Prabhu, A.; Seto, E.; Chinnaiyan, P. (2012). Class I histone deacetylases localize to the endoplasmic reticulum and modulate the unfolded protein response, *The FASEB Journal*, Vol. 26, No. 6, 2437–2445. doi:10.1096/fj.11-193706

[164] Gómez, A. v; Córdova, G.; Munita, R.; Parada, G. E.; Barrios, Á. P.; Cancino, G. I.; Álvarez, A. R.; Andrés, M. E. (2015). Characterizing HSF1 binding and post-translational modifications of hsp70 promoter in cultured cortical neurons: Implications in the heat-shock response, *PLoS ONE*, Vol. 10, No. 6. doi:10.1371/journal.pone.0129329

[165] Ren, M.; Leng, Y.; Jeong, M. R.; Leeds, P. R.; Chuang, D. M. (2004). Valproic acid reduces brain damage induced by transient focal cerebral ischemia in rats: Potential roles of histone deacetylase inhibition and heat shock protein induction, *Journal of Neurochemistry*, Vol. 89, No. 6, 1358–1367. doi:10.1111/j.1471-4159.2004.02406.x

[166] Brose, R. D.; Shin, G.; Mcguinness, M. C.; Schneidereith, T.; Purvis, S.; Dong, G. X.; Keefer, J.; Spencer, F.; Smith, K. D. (2012). Activation of the stress proteome as a mechanism for small molecule therapeutics, *Human Molecular Genetics*, Vol. 21, No. 19, 4237–4252. doi:10.1093/hmg/dds247

[167] Simões-Pires, C.; Zwick, V.; Nurisso, A.; Schenker, E.; Carrupt, P. A.; Cuendet, M. (2013). HDAC6 as a target for neurodegenerative diseases: What makes it different from the other HDACs?, *Molecular Neurodegeneration*, Vol. 8, No. 1. doi:10.1186/1750-1326-8-7

[168] Fass, D. M.; Shah, R.; Ghosh, B.; Hennig, K.; Norton, S.; Zhao, W. N.; Reis, S. A.; Klein, P. S.; Mazitschek, R.; Maglathlin, R. L.; Lewis, T. A.; Haggarty, S. J. (2011). Short-chain HDAC inhibitors differentially affect vertebrate development and neuronal chromatin, *ACS Medicinal Chemistry Letters*, Vol. 2, No. 1, 39–42. doi:10.1021/ml1001954

[169] Ricobaraza, A.; Cuadrado-Tejedor, M.; Pérez-Mediavilla, A.; Frechilla, D.; del Río, J.; García-Osta, A. (2009). Phenylbutyrate ameliorates cognitive deficit and reduces tau pathology in an alzheimer's disease mouse model, *Neuropsychopharmacology*, Vol. 34, No. 7, 1721–1732. doi:10.1038/npp.2008.229

[170] Marten, B.; Pfeuffer, M.; Schrezenmeir, J. (2006). Medium-chain triglycerides, *International Dairy Journal*, Vol. 16, No. 11, 1374–1382. doi:10.1016/j.idairyj.2006.06.015

[171] Bach, A. C.; Babayan, V. K. (1982). Medium-chain triglycerides: an update, *American Journal of Clinical Nutrition*, Vol. 36, 950–962. doi:10.1093/ajcn/36.5.950

[172] Augustin, K.; Khabbush, A.; Williams, S.; Eaton, S.; Orford, M.; Heales, S. J. R.; Walker, M. C.; Williams, R. S. B. (2018). Mechanisms of action for the medium-chain triglyceride ketogenic diet in neurological and metabolic disorders, *The Lancet Neurology*, Vol. 17, No. 1, 84–93. doi:10.1016/S1474-4422(17)30408-8

[173] Spector, R. (1988). Fatty Acid Transport Through the Blood-Brain Barrier, *Journal of Neurochemistry*, Vol. 50, No. 2, 639–643. doi:10.1111/j.1471-4159.1988.tb02958.x

[174] Wlaź, P.; Socała, K.; Nieoczym, D.; Łuszczki, J. J.; Arnowska, I.; Arnowski, T.; Czuczwar, S. J.; Gasior, M. (2012). Anticonvulsant profile of caprylic acid, a main constituent of the medium-chain triglyceride (MCT) ketogenic diet, in mice, *Neuropharmacology*, Vol. 62, No. 4, 1882–1889. doi:10.1016/j.neuropharm.2011.12.015

[175] Haynes, V. R.; Michael, N. J.; van den Top, M.; Zhao, F. Y.; Brown, R. D.; de Souza, D.; Dodd, G. T.; Spanswick, D.; Watt, M. J. (2020). A Neural basis for Octanoic acid regulation of energy balance, *Molecular Metabolism*, Vol. 34, No. January, 54–71. doi:10.1016/j.molmet.2020.01.002

[176] Mayr, J. A.; Feichtinger, R. G.; Tort, F.; Ribes, A.; Sperl, W. (2014). Lipoic acid biosynthesis defects, *Journal of Inherited Metabolic Disease*, Vol. 37, No. 4, 553–563. doi:10.1007/s10545-014-9705-8

[177] Włodarek, D. (2019). Role of ketogenic diets in neurodegenerative diseases (Alzheimer's disease and parkinson's disease), *Nutrients*, Vol. 11, No. 1. doi:10.3390/nu11010169

[178] Croteau, E.; Castellano, C. A.; Richard, M. A.; Fortier, M.; Nugent, S.; Lepage, M.; Duchesne, S.; Whittingstall, K.; Turcotte, É. E.; Bocti, C.; Fülöp, T.; Cunnane, S. C. (2018). Ketogenic Medium Chain Triglycerides Increase Brain Energy Metabolism in Alzheimer's Disease, *Journal of Alzheimer's Disease*, Vol. 64, No. 2, 551–561. doi:10.3233/JAD-180202

[179] Fortier, M.; Castellano, C. A.; Croteau, E.; Langlois, F.; Bocti, C.; St-Pierre, V.; Vandenberghe, C.; Bernier, M.; Roy, M.; Descoteaux, M.; Whittingstall, K.; Lepage, M.; Turcotte, É. E.; Fulop, T.; Cunnane, S. C. (2019). A ketogenic drink improves brain energy and some measures of cognition in mild cognitive impairment, *Alzheimer's and Dementia*, Vol. 15, No. 5, 625–634. doi:10.1016/j.jalz.2018.12.017

[180] Ota, M.; Matsuo, J.; Ishida, I.; Takano, H.; Yokoi, Y.; Hori, H.; Yoshida, S.; Ashida, K.; Nakamura, K.; Takahashi, T.; Kunugi, H. (2019). Effects of a medium-chain triglyceride-based ketogenic formula on cognitive function in patients with mild-to-moderate Alzheimer's disease, *Neuroscience Letters*, Vol. 690, No. October 2018, 232–236. doi:10.1016/j.neulet.2018.10.048

[181] Achanta, L. B.; Rae, C. D. (2017). β-Hydroxybutyrate in the Brain: One Molecule, Multiple Mechanisms, *Neurochemical Research*, Vol. 42, No. 1, 35–49. doi:10.1007/s11064-016-2099-2

[182] Brenner, S. (1974). The Genetics of *Caenorhabditis elegans*, *Genetics*, Vol. 77, 71–94. doi:10.1111/j.1749-6632.1999.tb07894.x

[183] Altun, Z. F.; Hall, D. H. (2009). Introduction, *WormAtlas*. doi:10.3908/wormatlas.1.1

[184] Corsi, A. K. (2006). A Biochemist's Guide to *C. elegans*, *Analytical Biochemistry*, Vol. 1, No. 359, 1–17. doi:10.1016/j.dcn.2011.01.002

[185] Culetto, E.; Sattelle, D. B. (2000). A role for *Caenorhabditis elegans* in understanding the function and interactions of human disease genes, *Human Molecular Genetics*, Vol. 9, No. 6, 869–877

[186] Corsi, A. K.; Wightman, B.; Chalfie, M. (2015). A transparent window into biology: A primer on *Caenorhabditis elegans*, *Genetics*, Vol. 200, No. 2, 387–407. doi:10.1534/genetics.115.176099

[187] Altun, Z. F.; Hall, D. H. (2011). Nervous system, general description, *WormAtlas*. doi:10.3908/wormatlas.1.18

[188] Richmond, J. (2007). Synaptic function, *WormBook: The Online Review of C. elegans Biology*. doi:10.1895/wormbook.1.69.1

[189] Altun, Z. F.; Hall, D. H. (2009). Muscle system, somatic muscle, *WormAtlas*. doi:10.3908/wormatlas.1.7

[190] Altun, Z. F.; Hall, D. H. (2009). Alimentary system, intestine, *WormAtlas*. doi:10.3908/wormatlas.1.4

[191] Lints, R.; Hall, D. H. (2009). Reproductive system, *WormAtlas*. doi:10.3908/wormatlas.1.21

[192] Dykxhoorn, D. M.; Novina, C. D.; Sharp, P. A. (2003). Killing the messenger: Short RNAs that silence gene expression, *Nature Reviews Molecular Cell Biology*, Vol. 4, No. 6, 457–467. doi:10.1038/nrm1129

[193] Conte Jr., D.; MacNeil, L. T.; Walhout, A. J. M.; Mello, C. C. (2015). RNA Interference in *Caenorhabditis elegans*, *Current Protocols in Molecular Biology*, Vol. 109. doi:10.1002/0471142727.mb2603s109

[194] Grishok, A. (2005). RNAi mechanisms in *Caenorhabditis elegans*, *FEBS Letters*, Vol. 579, No. 26, 5932–5939. doi:10.1016/j.febslet.2005.08.001

[195] Shaye, D. D.; Greenwald, I. (2011). OrthoList: a compendium of *C. elegans* genes with human orthologs, *PloS One*, Vol. 6, No. 5, e20085. doi:10.1371/journal.pone.0020085

[196] Kim, W.; Underwood, R. S.; Greenwald, I.; Shaye, D. D. (2018). Ortholist 2: A new comparative genomic analysis of human and *Caenorhabditis elegans* genes, *Genetics*, Vol. 210, No. 2, 445–461. doi:10.1534/genetics.118.301307

[197] Schwarz, E. M. (2005). Genomic classification of protein-coding gene families., *WormBook: The Online Review of C. elegans Biology*. doi:10.1895/wormbook.1.29.1

[198] Spencer, W. C.; Zeller, G.; Watson, J. D.; Henz, S. R.; Watkins, K. L.; McWhirter, R. D.; Petersen, S.; Sreedharan, V. T.; Widmer, C.; Jo, J.; Reinke, V.; Petrella, L.; Strome, S.; von Stetina, S. E.; Katz, M.; Shaham, S.; Rätsch, G.; Miller, D. M. (2011). A spatial and temporal map of *C. elegans* gene expression, *Genome Research*, Vol. 21, No. 2, 325–341. doi:10.1101/gr.114595.110

[199] Srinivasan, S.; Sadegh, L.; Elle, I. C.; Christensen, A. G. L.; Faergeman, N. J.; Ashrafi, K. (2008). Serotonin Regulates *C. elegans Fat* and Feeding through Independent Molecular Mechanisms, *Cell Metabolism*, Vol. 7, No. 6, 533–544. doi:10.1016/j.cmet.2008.04.012

[200] Kaletsky, R.; Yao, V.; Williams, A.; Runnels, A. M.; Tadych, A.; Zhou, S.; Troyanskaya, O. G.; Murphy, C. T. (2018). Transcriptome analysis of adult *Caenorhabditis elegans* cells reveals tissue-specific gene and isoform expression, *PLoS Genetics*, Vol. 14, No. 8. doi:10.1371/journal.pgen.1007559

[201] Davis, P.; Zarowiecki, M.; Arnaboldi, V.; Becerra, A.; Cain, S.; Chan, J.; Chen, W. J.; Cho, J.; da Veiga Beltrame, E.; Diamantakis, S.; Gao, S.; Grigoriadis, D.; Grove, C. A.; Harris, T. W.; Kishore, R.; Le, T.; Lee, R. Y. N.; Luypaert, M.; Müller, H. M.; Nakamura, C.; Nuin, P.; Paulini, M.; Quinton-Tulloch, M.; Raciti, D.; Rodgers, F. H.; Russell, M.; Schindelman, G.; Singh, A.; Stickland, T.; van Auken, K.; Wang, Q.; Williams, G.; Wright, A. J.; Yook, K.; Berriman, M.; Howe, K. L.; Schedl, T.; Stein, L.; Sternberg, P. W. (2022). WormBase in 2022 - data, processes, and tools for analyzing *Caenorhabditis elegans*, *Genetics*, Vol. 220, No. 4. doi:10.1093/genetics/iyac003

[202] Saraceno, C.; Musardo, S.; Marcello, E.; Pelucchi, S.; di Luca, M. (2013). Modeling Alzheimer's disease: From past to future, *Frontiers in Pharmacology*, Vol. 4 JUN. doi:10.3389/fphar.2013.00077

[203] Smialowska, A.; Baumeister, R. (2006). Presenilin function in *Caenorhabditis elegans*, *Neurodegenerative Diseases*, Vol. 3, Nos. 4–5, 227–232. doi:10.1159/000095260

[204] Dimitriadi, M.; Hart, A. C. (2010). Neurodegenerative disorders: Insights from the nematode *Caenorhabditis elegans*, *Neurobiology of Disease*, Vol. 40, No. 1, 4–11. doi:10.1016/j.nbd.2010.05.012

[205] Link, C. D. (1995). Expression of human β-amyloid peptide in transgenic *Caenorhabditis elegans*, *Neurobiology*, Vol. 92, 9368–9372. doi:10.1073/pnas.92.20.9368

[206] McColl, G.; Roberts, B. R.; Gunn, A. P.; Perez, K. A.; Tew, D. J.; Masters, C. L.; Barnham, K. J.; Cherny, R. A.; Bush, A. I. (2009). The *Caenorhabditis elegans* A beta 1-42 model of Alzheimer disease predominantly expresses A beta 3-42, *The Journal of Biological Chemistry*, Vol. 284, No. 34, 22697–702. doi:10.1074/jbc.C109.028514

[207] McColl, G.; Roberts, B. R.; Pukala, T. L.; Kenche, V. B.; Roberts, C. M.; Link, C. D.; Ryan, T. M.; Masters, C. L.; Barnham, K. J.; Bush, A. I.; Cherny, R. A. (2012). Utility of an improved model of amyloid-beta (Aβ1-42) toxicity in *Caenorhabditis elegans* for drug screening for Alzheimer's disease, *Molecular Neurodegeneration*, Vol. 7, No. 57. doi:10.1186/1750-1326-7-57

[208] Fong, S.; Teo, E.; Ng, L. F.; Chen, C. B.; Lakshmanan, L. N.; Tsoi, S. Y.; Moore, P. K.; Inoue, T.; Halliwell, B.; Gruber, J. (2016). Energy crisis precedes global metabolic failure in a novel *Caenorhabditis elegans* Alzheimer Disease model, *Scientific Reports*, Vol. 6, No. September, 1–9. doi:10.1038/srep33781

[209] Caldwell, K. A.; Willicott, C. W.; Caldwell, G. A. (2020). Modeling neurodegeneration in *Caenorhabditis elegans*, *Disease Models and Mechanisms*, Vol. 13, No. 10. doi:10.1242/dmm.046110

[210] van Pelt, K. M.; Truttmann, M. C. (2020). *Caenorhabditis elegans* as a model system for studying aging-associated neurodegenerative diseases, *Translational Medicine of Aging*, Vol. 4, 60–72. doi:10.1016/j.tma.2020.05.001

[211] Wolozin, B.; Gabel, C.; Ferree, A.; Guillily, M.; Ebata, A. (2011). Watching worms whither: Modeling neurodegeneration in *C. elegans*, *Progress in Molecular Biology and Translational Science*, Vol. 100, 499–514. doi:10.1016/B978-0-12-384878-9.00015-7

[212] Brunquell, J.; Morris, S.; Lu, Y.; Cheng, F.; Westerheide, S. D. (2016). The genome-wide role of HSF-1 in the regulation of gene expression in *Caenorhabditis elegans*, *BMC Genomics*, Vol. 17, No. 1. doi:10.1186/s12864-016-2837-5

[213] Morton, E. A.; Lamitina, T. (2013). *C. elegans* HSF-1 is an essential nuclear protein that formsstress granule-like structures following heat shock, *Aging Cell*, Vol. 12, No. 1, 112–120. doi:10.1111/acel.12024

[214] Hsu, A.-L.; Murphy, C. T.; Kenyon, C. (2003). Regulation of Aging and Age-Related Disease by DAF-16 and Heat-Shock Factor, *Science*, Vol. 300, No. 5622, 1242–1245. doi:10.1126/science.1083701

[215] Shen, X.; Ellis, R. E.; Lee, K.; Liu, C.-Y.; Yang, K.; Solomon, A.; Yoshida, H.; Morimoto, R.; Kurnit, D. M.; Mori, K.; Kaufman, R. J. (2001). Complementary Signaling Pathways Regulate the Unfolded Protein Response and Are Required for *C. elegans* Development to the cytoplasm and nucleus, *Cell*, Vol. 107, 893–903. doi:10.1016/s0092-8674(01)00612-2

[216] Richardson, C. E.; Kinkel, S.; Kim, D. H. (2011). Physiological IRE-1-XBP-1 and PEK-1 signaling in *Caenorhabditis elegans* larval development and immunity, *PLoS Genetics*, Vol. 7, No. 11. doi:10.1371/journal.pgen.1002391

[217] Urano, F.; Calfon, M.; Yoneda, T.; Yun, C.; Kiraly, M.; Clark, S. G.; Ron, D. (2002). A survival pathway for *Caenorhabditis elegans* with a blocked unfolded protein response, *Journal of Cell Biology*, Vol. 158, No. 4, 639–646. doi:10.1083/jcb.200203086

[218] Komoike, Y.; Matsuoka, M. (2016). Endoplasmic reticulum stress-mediated neuronal apoptosis by acrylamide exposure, *Toxicology and Applied Pharmacology*, Vol. 310, 68–77. doi:10.1016/j.taap.2016.09.005

[219] Henis-Korenblit, S.; Zhang, P.; Hansen, M.; McCormick, M.; Lee, S. J.; Cary, M.; Kenyon, C. (2010). Insulin/IGF-1 signaling mutants reprogram ER stress response regulators to promote longevity, *Proceedings of the National Academy of Sciences of the United States of America*, Vol. 107, No. 21, 9730–9735. doi:10.1073/pnas.1002575107

[220] Haynes, C. M.; Petrova, K.; Benedetti, C.; Yang, Y.; Ron, D. (2007). ClpP Mediates Activation of a Mitochondrial Unfolded Protein Response in *C. elegans*, *Developmental Cell*, Vol. 13, No. 4, 467–480. doi:10.1016/j.devcel.2007.07.016

[221] Haynes, C. M.; Yang, Y.; Blais, S. P.; Neubert, T. A.; Ron, D. (2010). The Matrix Peptide Exporter HAF-1 Signals a Mitochondrial UPR by Activating the Transcription Factor ZC376.7 in *C. elegans*, *Molecular Cell*, Vol. 37, No. 4, 529–540. doi:10.1016/j.molcel.2010.01.015

[222] Nargund, A. M.; Pellegrino, M. W.; Fiorese, C. J.; Baker, B. M.; Haynes, C. M. (2012). Mitochondrial import efficiency of ATFS-1 regulates mitochondrial UPR activation, *Science*, Vol. 337, No. 6094, 587–590. doi:10.1126/science.1223560

[223] Pellegrino, M. W.; Nargund, A. M.; Haynes, C. M. (2013). Signaling the mitochondrial unfolded protein response, *Biochimica et Biophysica Acta - Molecular Cell Research*, Vol. 1833, No. 2, 410–416. doi:10.1016/j.bbamcr.2012.02.019

[224] Westermann, B. (2010). Mitochondrial dynamics in model organisms: What yeasts, worms and flies have taught us about fusion and fission of mitochondria, *Seminars in Cell and Developmental Biology*, Vol. 21, No. 6, 542–549. doi:10.1016/j.semcdb.2009.12.003

[225] Palikaras, K.; Lionaki, E.; Tavernarakis, N. (2015). Coordination of mitophagy and mitochondrial biogenesis during ageing in *C. elegans*, *Nature*, Vol. 521, No. 7553, 525–528. doi:10.1038/nature14300

[226] Blackwell, T. K.; Steinbaugh, M. J.; Hourihan, J. M.; Ewald, C. Y.; Isik, M. (2015). SKN-1/Nrf, stress responses, and aging in *Caenorhabditis elegans*, *Free Radical Biology and Medicine*, Vol. 88, 290–301. doi:10.1016/j.freeradbiomed.2015.06.008

[227] Murphy, C. T. (2006). The search for DAF-16/FOXO transcriptional targets: Approaches and discoveries, *Experimental Gerontology*, Vol. 41, No. 10, 910–921. doi:10.1016/j.exger.2006.06.040

[228] Palikaras, K.; Lionaki, E.; Tavernarakis, N. (2015). Balancing mitochondrial biogenesis and mitophagy to maintain energy metabolism homeostasis, *Cell Death and Differentiation*, Vol. 22, No. 9, 1399–1401. doi:10.1038/cdd.2015.86

[229] Choe, K. P.; Przybysz, A. J.; Strange, K. (2009). The WD40 Repeat Protein WDR-23 Functions with the CUL4/DDB1 Ubiquitin Ligase To Regulate Nuclear Abundance and Activity of SKN-1 in *Caenorhabditis elegans*, *Molecular and Cellular Biology*, Vol. 29, No. 10, 2704–2715. doi:10.1128/mcb.01811-08

[230] Sumitani, M.; Kasashima, K.; Matsugi, J.; Endo, H. (2011). Biochemical properties of *Caenorhabditis elegans* HMG-5, a regulator of mitochondrial DNA, *Journal of Biochemistry*, Vol. 149, No. 5, 581–589. doi:10.1093/jb/mvr008

[231] Edwards, C.; Canfield, J.; Copes, N.; Rehan, M.; Lipps, D.; Bradshaw, P. C. (2014). D-beta-hydroxybutyrate extends lifespan in *C. elegans*, *Aging*, Vol. 6, No. 8, 621–644. doi:10.18632/aging.100683

[232] Lavatelli, A.; de Mendoza, D.; Mansilla, M. C. (2020). Defining *Caenorhabditis elegans* as a model system to investigate lipoic acid metabolism, *Journal of Biological Chemistry*, Vol. 295, No. 44, 14973–14986. doi:10.1074/jbc.RA120.013760

[233] Sugawa, H.; Yachi, A.; Fujimoto, Y.; Nagai, R. (2021). Accumulation of *Nε* -(carboxyethyl) lysine in *Caenorhabditis elegans* is correlated with the formation of ketone body, *The Journal of Biochemistry*, Vol. 170, No. 5, 587–592. doi:10.1093/jb/mvab079

[234] Stiernagle, T. (2006). Maintenance of *C. elegans*, *WormBook: The Online Review of C. elegans Biology*. doi:10.1895/wormbook.1.101.1

[235] Kamath, R. S.; Fraser, A. G.; Dong, Y.; Poulin, G.; Durbin, R.; Gotta, M.; Kanapink, A.; le Bot, N.; Moreno, S.; Sohrmann, M.; Welchman, D. P.; Zipperlen, P.; Ahringer, J. (2003). Systematic functional analysis of the *Caenorhabditis elegans* genome using RNAi, *Nature*, Vol. 421, No. 6920, 231–237. doi:10.1038/nature01278

[236] Timmons, L.; Court, D. L.; Fire, A. (2001). Ingestion of bacterially expressed dsRNAs can produce specific and potent genetic interference in *Caenorhabditis elegans*, *Gene*, Vol. 263, 103–112. doi:10.1016/s0378-1119(00)00579-5

[237] Lehner, B.; Tischler, J.; Fraser, A. G. (2006). RNAi screens in *Caenorhabditis elegans* in a 96-well liquid format and their application to the systematic identification of genetic interactions, *Nature Protocols*, Vol. 1, No. 3, 1617–1620. doi:10.1038/nprot.2006.245

[238] Fraser, A. G.; Kamath, R. S.; Zipperlen, P.; Martinez-Campos, M.; Sohrmann, M.; Ahringer, J. (2000). Functional genomic analysis of *C. elegans* chromosome I by systematic RNA interference, *Nature*, Vol. 408, No. 6810, 325–330. doi:10.1038/35042517

[239] Rual, J. F.; Ceron, J.; Koreth, J.; Hao, T.; Nicot, A. S.; Hirozane-Kishikawa, T.; Vandenhaute, J.; Orkin, S. H.; Hill, D. E.; van den Heuvel, S.; Vidal, M. (2004). Toward improving *Caenorhabditis elegans* phenome mapping with an ORFeome-based RNAi library, *Genome Research*, Vol. 14, No. 10 B, 2162–2168. doi:10.1101/gr.2505604

[240] Gruber, J.; Ng, L. F.; Poovathingal, S. K.; Halliwell, B. (2009). Deceptively simple but simply deceptive – *Caenorhabditis elegans* lifespan studies: Considerations for aging and antioxidant effects, *FEBS Letters*, Vol. 583, No. 21, 3377–3387. doi:10.1016/J.FEBSLET.2009.09.051

[241] Zheng, S. Q.; Ding, A. J.; Li, G. P.; Wu, G. S.; Luo, H. R. (2013). Drug Absorption Efficiency in *Caenorhbditis elegans* Delivered by Different Methods, *PLoS ONE*, Vol. 8, No. 2, 1–9. doi:10.1371/journal.pone.0056877

[242] Fay, D. S. (2013). Classical genetic methods, *WormBook: The Online Review of C. elegans Biology*. doi:doi/10.1895/wormbook.1.165.1

[243] Anderson, J. L.; Morran, L. T.; Phillips, P. C. (2010). Outcrossing and the maintenance of males within *C. elegans* populations, *Journal of Heredity*, Vol. 101, No. SUPPL. 1, 62–74. doi:10.1093/jhered/esq003

[244] Perni, M.; Challa, P. K.; Kirkegaard, J. B.; Limbocker, R.; Koopman, M.; Hardenberg, M. C.; Sormanni, P.; Müller, T.; Saar, K. L.; Roode, L. W. Y.; Habchi, J.; Vecchi, G.; Fernando, N.; Casford, S.; Nollen, E. A. A.; Vendruscolo, M.; Dobson, C. M.; Knowles, T. P. J. (2018). Massively parallel *C. elegans* tracking provides multi-dimensional fingerprints for phenotypic discovery, *Journal of Neuroscience Methods*, Vol. 306, 57–67. doi:10.1016/j.jneumeth.2018.02.005

[245] Peccati, F.; Hernando, J.; Blancafort, L.; Solans-Monfort, X.; Sodupe, M. (2015). Disaggregation-induced fluorescence enhancement of NIAD-4 for the optical imaging of amyloid-β fibrils, *Physical Chemistry Chemical Physics*, Vol. 17, No. 30, 19718–19725. doi:10.1039/c5cp02728d

[246] Nesterov, E. E.; Skoch, J.; Hyman, B. T.; Klunk, W. E.; Bacskai, B. J.; Swager, T. M. (2005). In vivo optical imaging of amyloid aggregates in brain: Design of fluorescent markers, *Angewandte Chemie - International Edition*, Vol. 44, No. 34, 5452–5456. doi:10.1002/anie.200500845

[247] Perry, S. W.; Norman, J. P.; Barbieri, J.; Brown, E. B.; Gelbard, H. A. (2011). Mitochondrial membrane potential probes and the proton gradient: A practical usage guide, *BioTechniques*, Vol. 50, No. 2, 98–115. doi:10.2144/000113610

[248] Liao, P. C.; Franco-Iborra, S.; Yang, Y.; Pon, L. A. (2020). Live cell imaging of mitochondrial redox state in mammalian cells and yeast, *Methods in Cell Biology*, Vol. 155, 295–319. doi:10.1016/bs.mcb.2019.11.008

[249] Can, K.; Kügler, S.; Müller, M. (2017). Live Imaging of Mitochondrial ROS Production and Dynamic Redox Balance in Neurons, S. Strack; Y. M. Usachev (Eds.), *Techniques to Investigate Mitochondrial Function in Neurons* (Vol. 123), Springer, 1–27. doi:10.1007/978-1-4939-6890-9

[250] Benedetti, C.; Haynes, C. M.; Yang, Y.; Harding, H. P.; Ron, D. (2006). Ubiquitin-like protein 5 positively regulates chaperone gene expression in the mitochondrial unfolded protein response, *Genetics*, Vol. 174, No. 1, 229–239. doi:10.1534/genetics.106.061580

[251] Boothe, T.; Hilbert, L.; Heide, M.; Berninger, L.; Huttner, W. B.; Zaburdaev, V.; Vastenhouw, N. L.; Myers, E. W.; Drechsel, D. N.; Rink, J. C. (2017). A tunable refractive index matching medium for live imaging cells, tissues and model organisms, *ELife*, Vol. 6, 1–15. doi:10.7554/eLife.27240

[252] Merrill, R. A.; Flippo, K. H.; Strack, S. (2017). Measuring Mitochondrial Shape with ImageJ, S. Strack; Y. M. Usachev (Eds.), *Techniques to Investigate Mitochondrial Function in Neurons*, Springer, 31–48. doi:10.1007/978-1-4939-6890-9

[253] Rosado, C. J.; Mijaljica, D.; Hatzinisiriou, I.; Prescott, M.; Devenish, R. J. (2008). Rosella: A fluorescent pH-biosensor for reporting vacuolar turnover of cytosol and organelles in yeast, *Autophagy*, Vol. 4, No. 2, 205–213. doi:10.4161/auto.5331

[254] Palikaras, K.; Tavernarakis, N. (2017). *In vivo* Mitophagy Monitoring in *Caenorhabditis elegans* to Determine Mitochondrial Homeostasis, *Bio-Protocol*, Vol. 7, No. 7, 1–10. doi:10.21769/bioprotoc.2215

[255] Motulsky, H. J.; Brown, R. E. (2006). Detecting outliers when fitting data with nonlinear regression - A new method based on robust nonlinear regression and the false discovery rate, *BMC Bioinformatics*, Vol. 7, 1–20. doi:10.1186/1471-2105-7-123

[256] Newman, J. C.; Verdin, E. (2017). β-Hydroxybutyrate: A Signaling Metabolite, *Annual Review of Nutrition*, Vol. 37, No. 1, 51–76. doi:10.1146/annurev-nutr-071816-064916

[257] Cohen, E.; Bieschke, J.; Perciavalle, R. M.; Kelly, J. W.; Dillin, A. (2006). Opposing activities protect against age-onset proteotoxicity, *Science*, Vol. 313, No. 5793, 1604–1610. doi:10.1126/science.1124646

[258] Joshi, P.; Perni, M.; Limbocker, R.; Mannini, B.; Casford, S.; Chia, S.; Habchi, J.; Labbadia, J.; Dobson, C. M.; Vendruscolo, M. (2021). Two human metabolites rescue a *C. elegans* model of Alzheimer's disease via a cytosolic unfolded protein response, *Communications Biology*, Vol. 4, No. 1, 1–14. doi:10.1038/s42003-021-02218-7

[259] Tittelmeier, J.; Nachman, E.; Nussbaum-Krammer, C. (2020). Molecular Chaperones: A Double-Edged Sword in Neurodegenerative Diseases, *Frontiers in Aging Neuroscience*, Vol. 12. doi:10.3389/fnagi.2020.581374

[260] Palikaras, K.; Lionaki, E.; Tavernarakis, N. (2018). Mechanisms of mitophagy in cellular homeostasis, physiology and pathology, *Nature Cell Biology*, Vol. 20, No. 9, 1013–1022. doi:10.1038/s41556-018-0176-2

[261] Hogarth, P.; Lovrecic, L.; Krainc, D. (2007). Sodium phenylbutyrate in Huntington's disease: A dose-finding study, *Movement Disorders*, Vol. 22, No. 13, 1962–1964. doi:10.1002/mds.21632

[262] Cudkowicz, M. E.; Andres, P. L.; Macdonald, S. A.; Bedlack, R. S.; Choudry, R.; Brown, R. H.; Zhang, H.; Schoenfeld, D. A.; Shefner, J.; Matson, S.; Matson, W. R.; Ferrante, R. J. (2009). Phase 2 study of sodium phenylbutyrate in ALS, *Amyotrophic Lateral Sclerosis*, Vol. 10, No. 2, 99–106. doi:10.1080/17482960802320487

[263] Azoulay-Ginsburg, S.; Trobiani, L.; Setini, A.; Favaloro, F. L.; Giorda, E.; Jacob, A.; Hauschner, H.; Levy, L.; Cestra, G.; de Jaco, A.; Gruzman, A. (2020). A Lipophilic 4-Phenylbutyric Acid Derivative That Prevents Aggregation and Retention of Misfolded Proteins, *Chemistry European Journal*, Vol. 26, No. 8, 1834–1845. doi:10.1002/chem.201904292

[264] Nafar, F.; Clarke, J. P.; Mearow, K. M. (2017). Coconut oil protects cortical neurons from amyloid beta toxicity by enhancing signaling of cell survival pathways, *Neurochemistry International*, Vol. 105, 64–79. doi:10.1016/j.neuint.2017.01.008

[265] St-Pierre, V.; Vandenberghe, C.; Lowry, C.-M.; Fortier, M.; Castellano, C.-A.; Wagner, R.; Cunnane, S. C. (2019). Plasma Ketone and Medium Chain Fatty Acid Response in Humans Consuming Different Medium Chain Triglycerides During a Metabolic Study Day, *Frontiers in Nutrition*, Vol. 6, No. April, 1–8. doi:10.3389/fnut.2019.00046

[266] Brown, M. K.; Evans, J. L.; Luo, Y. (2006). Beneficial effects of natural antioxidants EGCG and α-lipoic acid on life span and age-dependent behavioral declines in *Caenorhabditis elegans*, *Pharmacology Biochemistry and Behavior*, Vol. 85, No. 3, 620–628. doi:10.1016/j.pbb.2006.10.017

[267] Quinn, J. F.; Bussiere, J. R.; Hammond, R. S.; Montine, T. J.; Henson, E.; Jones, R. E.; Stackman, R. W. (2007). Chronic dietary α-lipoic acid reduces deficits in hippocampal memory of aged Tg2576 mice, *Neurobiology of Aging*, Vol. 28, No. 2, 213–225. doi:10.1016/j.neurobiolaging.2005.12.014

[268] Yang, S. Y.; He, X. Y.; Schulz, H. (1987). Fatty acid oxidation in rat brain is limited by the low activity of 3-ketoacyl-coenzyme A thiolase., *The Journal of Biological Chemistry*, Vol. 262, No. 27, 13027–13032. doi:10.1016/s0021-9258(18)45161-7

[269] Reichmann, H.; Maltese, W. A.; DeVivo, D. C. (1988). Enzymes of Fatty Acid β-Oxidation in Developing Brain, *Journal of Neurochemistry*, Vol. 51, No. 2, 339–344. doi:10.1111/j.1471-4159.1988.tb01044.x

[270] Khabbush, A.; Orford, M.; Tsai, Y. C.; Rutherford, T.; O'Donnell, M.; Eaton, S.; Heales, S. J. R. (2017). Neuronal decanoic acid oxidation is markedly lower than that of octanoic acid: A mechanistic insight

into the medium-chain triglyceride ketogenic diet, *Epilepsia*, Vol. 58, No. 8, 1423–1429. doi:10.1111/epi.13833

[271] Ebert, D.; Haller, R. G.; Walton, M. E. (2003). Energy contribution of octanoate to intact rat brain metabolism measured by 13C nuclear magnetic resonance spectroscopy, *Journal of Neuroscience*, Vol. 23, No. 13, 5928–5935. doi:10.1523/jneurosci.23-13-05928.2003

[272] Arranz, A. M.; de Strooper, B. (2019). The role of astroglia in Alzheimer's disease: pathophysiology and clinical implications, *The Lancet Neurology*, Vol. 18, No. 4, 406–414. doi:10.1016/S1474-4422(18)30490-3

[273] Nanclares, C.; Baraibar, A. M.; Araque, A.; Kofuji, P. (2021). Dysregulation of astrocyte–neuronal communication in Alzheimer's disease, *International Journal of Molecular Sciences*, Vol. 22, No. 15. doi:10.3390/ijms22157887

[274] Panov, A.; Orynbayeva, Z.; Vavilin, V.; Lyakhovich, V. (2014). Fatty acids in energy metabolism of the central nervous system, *BioMed Research International*, Vol. 2014. doi:10.1155/2014/472459

[275] Thevenet, J.; de Marchi, U.; Domingo, J. S.; Christinat, N.; Bultot, L.; Lefebvre, G.; Sakamoto, K.; Descombes, P.; Masoodi, M.; Wiederkehr, A. (2016). Medium-chain fatty acids inhibit mitochondrial metabolism in astrocytes promoting astrocyte-neuron lactate and ketone body shuttle systems, *FASEB Journal*, Vol. 30, No. 5, 1913–1926. doi:10.1096/fj.201500182

[276] Tracey, T. J.; Steyn, F. J.; Wolvetang, E. J.; Ngo, S. T. (2018). Neuronal lipid metabolism: Multiple pathways driving functional outcomes in health and disease, *Frontiers in Molecular Neuroscience*, Vol. 11, No. January, 1–25. doi:10.3389/fnmol.2018.00010

[277] Schönfeld, P.; Wojtczak, L. (2021). How the brain fights fatty acids' toxicity, *Neurochemistry International*, Vol. 148. doi:10.1016/j.neuint.2021.105050

[278] Li, X.; Matilainen, O.; Jin, C.; Glover-Cutter, K. M.; Holmberg, C. I.; Blackwell, T. K. (2011). Specific SKN-1/NrF stress responses to perturbations in translation elongation and proteasome activity, *PLoS Genetics*, Vol. 7, No. 6. doi:10.1371/journal.pgen.1002119

[279] Glover-Cutter, K. M.; Lin, S.; Blackwell, T. K. (2013). Integration of the Unfolded Protein and Oxidative Stress Responses through SKN-1/Nrf, *PLoS Genetics*, Vol. 9, No. 9. doi:10.1371/journal.pgen.1003701

[280] Fay, D. S.; Fluet, A.; Johnson, C. J.; Link, C. D. (1998). *In vivo* aggregation of β-amyloid peptide variants, *J. Neurochem*, Vol. 71, 1616–1625. doi:10.1046/j.1471-4159.1998.71041616.x

[281] Takiff, H. E.; Chen, S.-M.; Courtt, D. L.; Morri-Son, P. T.; Lovett, S. T.; Gilson, L.; Kolodner, R. D. (1989). Genetic Analysis of the rnc Operon of *Escherichia coli*, *Journal of Bacteriology*, Vol. 171, No. 5, 2581–2590. doi:10.1128/jb.171.5.2581-2590.1989

[282] Qi, B.; Kniazeva, M.; Han, M. (2017). A vitamin-B2-sensing mechanism that regulates gut protease activity to impact animal's food behavior and growth, *ELife*, Vol. 6, 1–19. doi:10.7554/eLife.26243

[283] Hunter, S.; Maulik, M.; Scerbak, C.; Vayndorf, E.; Taylor, B. E. (2018). *Caenorhabditis* Sieve: A Low-tech Instrument and Methodology for Sorting Small Multicellular Organisms, *Journal of Visualized Experiments*, No. 137, 1–12. doi:10.3791/58014

[284] Dilberger, B.; Baumanns, S.; Spieth, S. T.; Wenzel, U.; Eckert, G. P. (2020). Infertility induced by auxin in PX627 *Caenorhabditis elegans* does not affect mitochondrial functions and aging parameters, *Aging*, Vol. 12, 1–17. doi:10.18632/aging.103413

[285] Massie, M. R.; Lapoczka, E. M.; Boggs, K. D.; Stine, K. E.; White, G. E. (2003). Exposure to the metabolic inhibitor sodium azide induces stress protein expression and thermotolerance in the nematode *Caenorhabditis elegans*, *Brief Communication Cell Stress & Chaperones*, Vol. 8, No. 1, 1–7. doi:10.1379/1466-1268(2003)8<1:ettmis>2.0.co;2

[286] Pincus, Z.; Mazer, T. C.; Slack, F. J. (2016). Autofluorescence as a measure of senescence in *C. elegans*: Look to red, not blue or green, *Aging*, Vol. 8, No. 5, 889–898. doi:10.18632/aging.100936

[287] Chaya, T.; Patel, S.; Smith, E. M.; Lam, A.; Miller, E.; Clupper, M.; Kervin, K.; Tanis, J. E. (2021). A *C. elegans* genome-wide RNAi screen for altered levamisole sensitivity identifies genes required for muscle function, *G3: Genes, Genomes, Genetics*, Vol. 11, No. 4. doi:10.1093/g3journal/jkab047

[288] Choi, W.; Fang-Yen, C.; Badizadegan, K.; Oh, S.; Lue, N.; Dasari, R. R.; Feld, M. S. (2007). Tomographic phase microscopy, *Nature Methods*, Vol. 4, No. 9, 717–719. doi:10.1038/nmeth1078

A Appendix: Material

A.1 *Caenorhabditis elegans* Strains

Table A.1 lists the utilized *C. elegans* strains with information on their genotype and reference. CL2122, GMC101 and SJ4103 stocks were purchased from the *Caenorhabditis* Genetics Center (CGC), University of Minnesota, Minneapolis, USA. IR2539 was obtained from Nektarios Tavernarakis, Institute of Molecular Biology and Biotechnology (IMBB), Foundation for Research and Technology-Hellas (FORTH), Heraklion, Crete, GR. Moreover, genetic crossings of GMC101 with IR2539 and SJ4103 were generated in the present work. A more detailed description of the utilized strains is given below.

Table A.1 | List of *C. elegans* strains

Strain	Genotype	Reference
CL2122	*dvIs15 [unc-54p(vector); mtl-2p::GFP]*	[280]
GMC101	*dvIs100 [unc-54p::A-beta-1-42::unc-54 3'-UTR; mtl-2p::GFP]*	[207]
GMC101xIR2539	*dvIs100 [unc-54p::A-beta-1-42::unc-54 3'-UTR; mtl-2p::GFP]; unc-119(ed3); Ex[myo-3p::TOMM-20::Rosella; unc-119(+)]*	[207]
GMC101xSJ4103	*dvIs100 [unc-54p::A-beta-1-42::unc-54 3'-UTR; mtl-2p::GFP]; zcIs14 [myo-3p::GFP(mit)]*	[207, 250]
IR2539	*unc-119(ed3); Ex[myo-3p::TOMM-20::Rosella; unc-119(+)]*	[254]*
SJ4103	*zcIs14 [myo-3p::GFP(mit)]*	[250]
* IR2539 was created to replace the transgenic strain IR1631 described in the referenced journal article, which was found to exhibit health deficiencies due to proteotoxicity of high transgene expression.		

CL2122

The transgenic strain CL2122 (*dvIs15 [unc-54p(vector); mtl-2p::GFP]*) is the corresponding control strain to GMC101. Since it only contains the *unc-54* promoter vector, CL2122 lacks Aβ expression. Moreover, the nematodes express the same selection marker as GMC101 to control for any potential effects of the intestinal GFP. Transgenesis was performed through microinjection of the transgenic construct into the gonads, followed by stable chromosomal integration via γ-irradiation. Finally, the generated strain was outcrossed 3 times with wild-type nematodes [280].

GMC101

The transgenic strain GMC101 (*dvIs100 [unc-54p::A-beta-1-42::unc-54 3'-UTR; mtl-2p::GFP]*) expresses human $A\beta_{1-42}$ under control of the body wall muscle *unc-54* promoter that leads to age-dependent motility deficits and eventually paralysis following temperature upshift to 25 °C in the L4 or young adult stage. GMC101 further expresses GFP in the intestine as a selection marker. Transgenesis was performed through microinjection of the transgenic construct into the gonads, followed by stable chromosomal integration via γ-irradiation. Finally, the generated strain was outcrossed 4 times with wild-type nematodes [207].

IR2539

The transgenic strain IR2539 (*unc-119(ed3); Ex[myo-3p::TOMM-20::Rosella; unc-119(+)]*) expresses the Rosella biosensor as a fusion protein with the mitochondrial TOMM-20 under control of the body wall muscle *myo-3* promoter. The biosensor combines a pH-insensitive DsRed with a pH-sensitive green fluorescent protein (GFP) variant [253, 254]. A reduced pH due to lysosomal degradation of mitochondria leads to denaturation of the GFP variant, consequently resulting in a higher DsRed/GFP fluorescence ratio as a measure of mitophagy induction [254]. The genetic background of IR2539 nematodes is based on an *unc-119* loss-of-function mutation that is rescued by the transgenic construct, which was introduced into the nematodes using biolistic bombardment. Since the transgenic construct was not chromosomally integrated, some of the nematodes lose their transgene and exhibit a dumpy phenotype of substantially reduced body length based on the *unc-119* mutation.

To investigate mitophagy in the context of Aβ proteotoxicity, the strain IR2539 was crossed with GMC101 to generate GMC101xIR2539 nematodes (*dvIs100 [unc-54p::A-beta-1-42::unc-54 3'-UTR; mtl-2p::GFP]; unc-119(ed3); Ex[myo-3p::TOMM-20::Rosella; unc-119(+)]*) (Chapter 3.2).

SJ4103

The transgenic strain SJ4103 (*zcIs14 [myo-3p::GFP(mit)]*) expresses GFP with a mitochondrial import sequence under control of the body wall muscle *myo-3* promoter that allows for visualization of mitochondrial morphology. Transgenesis was performed through microinjection of the transgenic construct into the gonads, followed by stable chromosomal integration. Finally, the generated strain was outcrossed 3 times with wild-type nematodes [250].

To investigate mitochondrial dynamics in the context of Aβ proteotoxicity, the strain SJ4103 was crossed with GMC101 to generate GMC101xSJ4103 nematodes (*dvIs100 [unc-54p::A-beta-1-42::unc-54 3'-UTR; mtl-2p::GFP]; zcIs14 [myo-3p::GFP(mit)]*) (Chapter 3.2).

A.2 *Escherichia coli* Strains

Table A.2 lists the utilized *E. coli* strains with details on their genotype and reference. Original *E. coli* cultures were obtained from the CGC.

Table A.2 | List of *E. coli* strains

Strain	Genotype	Reference
E. coli OP50	*ura-*	[182]
E. coli HT115(DE3)	*F-; mcrA; mcrB; IN(rrnD-rrnE)1; lambda-; rnc14::Tn10(DE3 lysogen: lavUV5p-T7 polymerase)*	[236, 281]
The utilized *E. coli* HT115(DE3) RNAi clones (Appendix A.3) additionally carry an L4440-plasmid that confers resistance to ampicillin and contains an insert, corresponding to the sequence of a GOI, flanked by opposing T7 RNA polymerase promoter sites.		

A.3 *Escherichia coli* HT115(DE3) RNA Interference Clones

Table A.3 lists the utilized *E. coli* HT115(DE3) RNAi clones that are named according to the targeted *C. elegans* gene. They were obtained from the Ahringer and Vidal libraries (Chapter 3.1.2.1) [235, 238, 239]. RNAi clones of the Ahringer library were provided by Günter Lochnit, Institute of Biochemistry, Gießen, DE. The Vidal library was purchased from Horizon Discovery Ltd., Cambridge, UK.

Table A.3 | List of *E. coli* HT115(DE3) RNAi clones

***C. elegans* gene**	**Sequence name**	**Human gene**	**Function**	**Library**
acdh-2	C17C3.12	*ACADSB*	FAO of SCFA	Vidal
acdh-10	T08G2.3	*ACADM*	FAO of MCFA	Vidal
atf-6	F45E6.2	*ATF6*	UPR^{ER}	Vidal
atfs-1	ZC376.7	*ATF5*	UPR^{mt}	Vidal
daf-16	R13H8.1	*FOXO*	Stress response	Vidal
dct-1	C14F5.1	*BNIP3*	Receptor-mediated mitophagy	Vidal
drd-5	F55E10.6	*HSD17B6; SDR9C7*	BHB synthesis, oxidoreductase	Ahringer

drp-1	T12E12.4	*DRP1*	Mitochondrial fission	Vidal
hda-1	C53A5.3	*HDAC2*	Histone deacetylase	Vidal
hsf-1	Y53C10A.12	*HSF1*	HSR	Ahringer
lias-1	M01F1.3	*LIAS*	ALA synthesis	Ahringer
mev-1	T07C4.7	*SDHC*	ETC complex II subunit	Vidal
nuo-3	Y57G11C.12	N/A	ETC complex I subunit	Vidal
pink-1	EEED8.9	*PINK1*	PINK1/Parkin-mediated mitophagy	Vidal
pdr-1	K08E3.7	*PARK2*	PINK1/Parkin-mediated mitophagy	Vidal
skn-1	T19E7.2	*NRF1; NRF2*	Stress response	Vidal

With the exception of *hsf-1* and *hda-1* that were fed from the L4 stage, all other RNAi clones were fed from the L1 stage. Moreover, *hsf-1* and *hda-1* were used in a 50% dilution with the vector control or with each other for the experiment in Figure 4.6.

A.4 Consumables

Table A.4 lists the used consumables with their respective manufacturer.

Table A.4 | List of consumables

Consumable	**Manufacturer**
Aluminum foil	Carl Roth GmbH & Co. KG (Karlsruhe, DE)
Autoclave bags	Sarstedt AG & Co. KG (Nürnbrecht, DE)
Beakers	Schott AG (Mainz, DE)
Cardboard cryoboxes (136 mm x 136 mm x 130 mm)	Carl Roth GmbH & Co. KG (Karlsruhe, DE)
Cell culture tube (14 ml)	Greiner Bio-One GmbH (Frickenhausen, DE)
Centrifuge tubes (15 ml, 50 ml)	Sarstedt AG & Co. KG (Nürnbrecht, DE)
Disposable cuvettes (1.5 ml)	Brand GmbH & Co. KG (Wertheim, DE)
Disposable nitrile examination gloves, powder-free	Unigloves® (Troisdorf, DE)
Distritips® for Distriman® (125 µl, 1250 µl, 12500 µl)	Gilson S.A.S. (Villiers-le-Bel, FR)
Erlenmeyer flasks (50 ml, 100 ml, 500 ml)	Schott AG (Mainz, DE)
Folded towels, 2-ply	Carl Roth GmbH & Co. KG (Karlsruhe, DE)

Funnel (Ø 50 mm)	Carl Roth GmbH & Co. KG (Karlsruhe, DE)
Graduated cylinders (50 ml, 250 ml)	Hirschmann Laborgeräte GmbH & Co. KG (Eberstadt, DE)
High Precision Cover Glasses, 1.5H (24 mm x 50 mm)	Carl Roth GmbH & Co. KG (Karlsruhe, DE)
Inoculation loop, reusable	Carl Roth GmbH & Co. KG (Karlsruhe, DE)
Kimtech Science paper towels	Hakle-Kimberly Deutschland GmbH (Koblenz, DE)
Laboratory bottles with screw cap (50 ml, 100 ml, 250 ml, 500 ml, 1000 ml)	Schott AG (Mainz, DE)
Lab coat	Bierbaum-Proenen GmbH & Co. KG (Cologne, DE)
Micro reaction tube, clear (1.5 ml, 2 ml)	Sarstedt AG & Co. KG (Nürnbrecht, DE)
Micro reaction tube, brown (2 ml)	Sarstedt AG & Co. KG (Nürnbrecht, DE)
Microtiter plates, flat-bottom, clear (24-well, 96-well)	Greiner Bio-One GmbH (Frickenhausen, DE)
Microtiter plates, flat-bottom, white (96-well)	Greiner Bio-One GmbH (Frickenhausen, DE)
Microscope slides, ground 90 °, frosted edge	Carl Roth GmbH & Co. KG (Karlsruhe, DE)
Parafilm® M	Bemis Company Inc. (Neenah, USA)
Pasteur pipettes, glass, without cotton plug	Carl Roth GmbH & Co. KG (Karlsruhe, DE)
Petri dishes round (35 mm x 10 mm, 92 mm x 16 mm)	Sarstedt AG & Co. KG (Nürnbrecht, DE)
Pipette filter tips (10 µl, 200 µl, 1000 µl)	Sarstedt AG & Co. KG (Nürnbrecht, DE)
Pipette tips (10 µl, 200 µl, 1000 µl)	Sarstedt AG & Co. KG (Nürnbrecht, DE)
Pipette tips low retention (10 µl, 200 µl, 1000 µl)	Sarstedt AG & Co. KG (Nürnbrecht, DE)
PluriStrainer® (40 µm)	PluriSelect Life Science (Leipzig, DE)
Serological pipettes (2 ml, 5 ml, 10 ml, 25 ml, 50 ml)	Sarstedt AG & Co. KG (Nürnbrecht, DE)
Silicone immersion oil	Olympus Europa SE & Co. KG (Hamburg, DE)
Spatula, L-shape	VWR International GmbH (Darmstadt, DE)
Stainless steel scalpel	B. Braun SE (Melsungen, DE)
Toothpick (80 mm)	Hermann Metz GmbH & Co. KG (Quickborn, DE)

Whatman® lens cleaning tissue, Grade 105	Whatman International Ltd. (Maidstone, UK)
Weighing spatula	Carl Roth GmbH & Co. KG (Karlsruhe, DE)

A.5 Chemicals and Reagents

Table A.5 lists the used chemicals and reagents with their respective supplier and order number.

Table A.5 | List of chemicals and reagents

Product	Supplier	Order number
Agar Agar SERVA Kobe I	SERVA Electrophoresis GmbH (Heidelberg, DE)	11392.03
Agarose	SERVA Electrophoresis GmbH (Heidelberg, DE)	T846.2
Ampicillin sodium salt	Carl Roth GmbH & Co. KG (Karlsruhe, DE)	K029.1
Calcium chloride dihydrate ($CaCl_2 \times 2\ H_2O$)	Carl Roth GmbH & Co. KG (Karlsruhe, DE)	5239.2
Caprylic acid (CA)/ Octanoic acid	Merck KGaA (Darmstadt, DE)	C2875
Carbenicillin disodium salt	Merck KGaA (Darmstadt, DE)	C1389
Cholesterol	Merck KGaA (Darmstadt, DE)	C8667
Dimethyl sulfoxide (C_2H_6OS) (DMSO)	Merck KGaA (Darmstadt, DE)	276855
Disodium hydrogen phosphate (Na_2HPO_4)	Carl Roth GmbH & Co. KG (Karlsruhe, DE)	P030.1
Ethanol (> 99.5%)	Carl Roth GmbH & Co. KG (Karlsruhe, DE)	5054.3
Ethanol, denatured (70%)	Carl Roth GmbH & Co. KG (Karlsruhe, DE)	T913.3
Glycerin	Carl Roth GmbH & Co. KG (Karlsruhe, DE)	3783.1
Iodixanol solution (60% w/v)/ OptiPrep™	Merck KGaA (Darmstadt, DE)	D1556
Isopropanol (2-Propanol, 99.8%)	Carl Roth GmbH & Co. KG (Karlsruhe, DE)	6752.3
Isopropyl-β-D-thiogalactopyranoside (IPTG)	Carl Roth GmbH & Co. KG (Karlsruhe, DE)	2316.4

L-ascorbic acid (AA)	Merck KGaA (Darmstadt, DE)	A92902
Levamisole hydrochloride	Merck KGaA (Darmstadt, DE)	L0380000
Magnesium sulfate heptahydrate ($MgSO_4 \times 7\ H_2O$)	Carl Roth GmbH & Co. KG (Karlsruhe, DE)	P027.2
Micro particles based on polystyrene (30 µm)	Merck KGaA (Darmstadt, DE)	84135
MitoTracker™ Red (MTR) CM-H_2Xros	Thermo Fisher Scientific Inc. (Waltham, USA)	M7513
Mucocit® T	Merz Dental GmbH (Lütjenburg, DE)	6992
{[50-(p-hydroxyphenyl)-2,20-bithienyl-5-yl]-methylidene}-propanedinitrile (NIAD-4)	Cayman Chemical (Ann Arbor, USA)	18520
Nystatin suspension	Merck KGaA (Darmstadt, DE)	N1638
Peptone from casein	Merck KGaA (Darmstadt, DE)	1.11931
Phenylacetic acid (PAA)	Merck KGaA (Darmstadt, DE)	108723
Potassium dihydrogen phosphate (KH_2PO_4)	Carl Roth GmbH & Co. KG (Karlsruhe, DE)	3904.1
Rea-pur®	Hirschmann Laborgeräte GmbH & Co. KG (Eberstadt, DE)	9710105
(*R*)-α-Lipoic Acid ((*R*)-ALA)	Cayman Chemical (Ann Arbor, USA)	27299
(*R*)-3-hydroxybutyric acid ((*R*)-BHB)	Merck KGaA (Darmstadt, DE)	54920
Sodium azide (NaN_3)	Merck KGaA (Darmstadt, DE)	S2002
Sodium chloride (NaCl)	Carl Roth GmbH & Co. KG (Karlsruhe, DE)	3957.1
Sodium hypochlorite (NaClO in H_2O; 12% Cl)	Carl Roth GmbH & Co. KG (Karlsruhe, DE)	9062.3
Tetracycline hydrochloride	Merck KGaA (Darmstadt, DE)	T7660
Tetramethylrhodamine ethylester perchlorat (TMRE)	Merck KGaA (Darmstadt, DE)	87917
Tween®20	Carl Roth GmbH & Co. KG (Karlsruhe, DE)	9127.2
2x yeast extract tryptone (YT) medium	Carl Roth GmbH & Co. KG (Karlsruhe, DE)	X966.2
4-phenylbutyric acid	Merck KGaA (Darmstadt, DE)	P21005

A.6 Kits

Table A.6 lists the used kits with their respective supplier and order number.

Table A.6 | List of kits

Product	Supplier	Order number
ATP Bioluminescence Assay Kit CLS II	Merck KGaA (Darmstadt, DE)	11699695001
MiR05-Kit	Oroboros Instruments GmbH (Innsbruck, AT)	60101-01
Pierce™ BCA Protein Assay Kit	Thermo Fisher Scientific Inc. (Waltham, USA)	23225
QIAprep Spin Miniprep Kit	Qiagen N.V. (Hilden, NL)	27104

A.7 Buffers and Solutions

Table A.7 lists the used stock solutions with their respective concentration, solvent and storage temperature.

Table A.7 | List of stock solutions

Stock solution	Concentration	Solvent	Storage temperature
(*R*)-ALA	50 mM, 100 mM, 200 mM	Ethanol	-20 °C
Ampicillin	100 mg/ml	50 % Ethanol	-20 °C
$CaCl_2$	0.1 M	ddH_2O	4 °C
Carbenicillin	25 mg/ml	50 % Ethanol	-20 °C
Cholesterol	5 mg/ml	Ethanol	-20 °C
IPTG	1 M	50 % Ethanol	-20 °C
KH_2PO_4	1 M	ddH_2O	4 °C
$MgSO_4$	1 M	ddH_2O	4 °C
Levamisole	20 mM	M9 buffer	4 °C
MTR CM-H_2Xros*	1 mM	DMSO	-20 °C
NaN_3	500 mM	ddH_2O	4 °C
NaOH	5 M	ddH_2O	20 °C
NIAD-4*	1 mM	DMSO	-20 °C
Tetracycline	25 mg/ml	50 % Ethanol	-20 °C
TMRE*	100 µM	DMSO	-20 °C

*The preparation was performed under dimmed lighting conditions. Components were pipetted into brown micro reaction tubes, mixed and divided into single-use aliquots.

General buffers and solutions for *C. elegans* cultivation and experimental setup

Table A.8 - Table A.13 list the recipes for the buffers and solutions used for *C. elegans* cultivation and experimental setup.

Table A.8 | M9 buffer

Substance	Quantity for 500 ml total volume
KH_2PO_4	1.5 g
Na_2HPO_4	3 g
NaCl	2.5 g
ddH_2O	ad 500 ml
$MgSO_4$ (1 M)	0.5 ml

The components, except for $MgSO_4$ (1 M), were dissolved using a magnetic stirrer and the buffer was subsequently autoclaved at 121 °C for 15 min. After cooling to 55 °C, $MgSO_4$ (1 M) was added under sterile conditions. Storage was at room temperature.

Table A.9 | M9 buffer/Tween®20 (0.1%)

Substance	Quantity for 500 ml total volume
M9 buffer	500 ml
Tween®20	0.5 ml

Tween®20 was pipetted into M9 buffer under sterile conditions and mixed. Storage was at room temperature.

Table A.10 | Freezing buffer A

Substance	Quantity for 500 ml total volume
KH_2PO_4	6.8 g
K_2HPO_4	8.7 g
NaCl	2.9 g
ddH_2O	ad 500 ml

The components were dissolved using a magnetic stirrer, the pH was adjusted to 5.95 and the buffer was subsequently autoclaved at 121 °C for 15 min. Storage was at 4 °C.

Table A.11 | Freezing buffer B

Substance	Quantity for 500 ml total volume
Freezing buffer A	700 ml
Glycerol	300 ml

Glycerol was pipetted into freezing buffer A under sterile conditions and mixed. Storage was at 4 °C.

Table A.12 | Bleaching solution

Substance	Quantity for 1.8 ml total volume
ddH_2O	0.6 ml
NaClO (12% Cl)	0.6 ml
NaOH (5 M)	0.6 ml

The bleaching solution was freshly prepared for each experiment.

Table A.13 | NaCl-peptone solution

Substance	Quantity for 500 ml total volume
Peptone from casein	1.25 g
NaCl	1.5 g
ddH_2O	ad 500 ml

The components were dissolved using a magnetic stirrer and the solution was subsequently autoclaved at 121 °C for 15 min. Storage was at room temperature.

Working solutions of the substances of interest

Table A.14 lists the working solutions of the substances of interest. Each working solution was prepared immediately before use. With the exception of 4-PBA that was directly dissolved in the liquid NGM used to resuspend *E. coli* HT115(DE3) bacteria (Chapter 3.1.2), working solutions contained ten-fold enriched concentrations compared to the final concentration in each well. For each experiment a matching solvent control was included.

4-PBA working solutions were homogenized using an ultrasonic bath. The odd concentrations were based on the dilution that occurred by adding the volume of M9 buffer/larvae suspension to each well (Chapter 3.1.2.3).

CA working solutions were always prepared in the same volumes using the same consumables to minimize the error due to accumulation of the lipophilic CA on the plastic surface. Accordingly, the appropriate volume of M9 buffer required to achieve the desired CA

concentration in a total volume of 2 ml was first pipetted into 2 ml micro reaction vessels. The corresponding volume of CA was then added using low retention pipette tips. The solution was homogenized using an ultrasonic bath. Finally, low retention tips were also used to add the CA working solutions to the experimental setup (Chapter 3.1.2.3).
(*R*)-ALA working solutions were prepared through 1:100 dilution of the respective stock solution (Table A.7).

Table A.14 | Working solutions of the substances of interest

Substance	Concentration	Solvent
AA	5 mM	M9 buffer
CA	25 mM, 50 mM, 75 mM, 100 mM	M9 buffer
(*R*)-ALA	0.5 mM, 1 mM, 2 mM	M9 buffer/ 1% Ethanol
(*R*)-BHB	5 mM, 10 mM, 15 mM, 20 mM	M9 buffer
PAA	10 mM, 50 mM, 100 mM	M9 buffer
4-PBA	1.2 mM, 6.1 mM, 12.3 mM	NGM

Working solutions of fluorescent probes

Table A.15 - Table A.17 list the recipes for the working solutions of the fluorescent probes. The preparation was performed under dimmed lighting conditions immediately before use.

Table A.15 | NIAD-4 working solution (10 µM in 1% DMSO)

Substance	Quantity for 2 ml total volume
M9 buffer	1980 µl
NIAD-4 stock solution (1 mM in 100% DMSO)	20 µl

Table A.16 | MTR CM-H_2Xros working solution (10 µM in 1% DMSO)

Substance	Quantity for 2 ml total volume
M9 buffer	1980 µl
MTR CM-H_2Xros stock solution (1 mM in 100% DMSO)	20 µl

Table A.17 | TMRE working solution (500 nM in 0.5% DMSO)

Substance	Quantity for 2 ml total volume
M9 buffer	1990 µl
TMRE stock solution (100 µM in 100% DMSO)	10 µl

A.8 Media

Table A.18 - Table A.21 list the recipes for the media used for *E. coli* as well as *C. elegans* cultivation and experimental setup.

Table A.18 | NGM

Substance	Quantity for 10 ml total volume
$CaCl_2$ (0,1 M)	10 µl
Carbenicillin (25 mg/ml)	10 µl
Cholesterol (5 mg/ml)	10 µl
IPTG (1 M)	10 µl
KH_2PO_4 (1 M)	250 µl
$MgSO_4$ (1 M)	10 µl
NaCl-Peptone	9.7 ml

For each experiment, the necessary amount of NGM was freshly prepared under sterile conditions. Due to its higher stability, the ampicillin analogue carbenicillin was used.

Table A.19 | NGM agar

Substance	Quantity for 1 l total volume
Agar	12 g
NaCl-Peptone	770 ml
$CaCl_2$ (0,1 M)	800 µl
Carbenicillin (25 mg/ml)	800 µl
Cholesterol (5 mg/ml)	800 µl
KH_2PO_4 (1 M)	20 ml
$MgSO_4$ (1 M)	800 µl
Nystatin-Suspension (10.000 U)	10 ml

The agar was dissolved in NaCl-Peptone and the solution was subsequently autoclaved at 121 °C for 15 minutes. Upon cooling to 55 °C, the remaining substances were then added under sterile conditions. Using a plate pouring machine, 92 mm Petri dishes were each filled with 9 ml of the medium. After curing, storage was at room temperature.

Table A.20 | 2xYT medium

Substance	Quantity for 1 l total volume
2xYT medium, powder	31 g
ddH_2O	ad 1 l

The components were dissolved using a magnetic stirrer and the medium was subsequently autoclaved at 121 °C for 15 minutes. Storage was at room temperature.

Table A.21 | 2xYT medium agar

Substance	Quantity for 1 l total volume
2xYT medium, powder	31 g
Agar	15 g
ddH_2O	ad 1 l

The components were dissolved using a magnetic stirrer and the medium was subsequently autoclaved at 121 °C for 15 minutes. For cultivation of *E. coli* HT115(DE3), the medium was supplemented with 1 µl of ampicillin (100 mg/ml) and tetracycline (25 mg/ml) upon cooling to 55 °C. Using a plate pouring machine, 92 mm Petri dishes were each filled with 9 ml of the medium. After curing, storage was at 4 °C.

A.9 Instruments

Table A.22 lists the used instruments with their respective supplier.

Table A.22 | List of instruments

Instrument	Supplier
Analytical balance	Kern & Sohn GmbH (Balingen, DE)
Autoclave DX-45	Systec GmbH (Wettenberg, DE)
Benchtop centrifuge Universal 320	Hettich GmbH & Co. KG (Tuttlingen, DE)
Benchtop centrifuge 5430R	Eppendorf SE (Hamburg, DE)
Benchtop refrigerated centrifuge Universal 320R	Hettich GmbH & Co. KG (Tuttlingen, DE)
Bunsen burner FIREBOY eco, with butane cartridge	Integra Bioscience GmbH (Biebertal, DE)
Camera Grasshopper 3 GS3-U3-60QS6M-C, monochrome, 6 megapixel, USB 3.0	FLIR® Integrated Imaging Solutions, Inc, (Richmond, CA)
Clark-type electrode Oxygraph-2k	Oroboros Instruments GmbH (Innsbruck, AT)
Cold light source KL200	Schott AG (Mainz, DE)

Cryo 1 °C freezing container Nalgene® Mr. Frosty®	Thermo Fisher Scientific Inc. (Waltham, USA)
Epifluorescence microscope EVOS™ M5000	Thermo Fisher Scientific Inc. (Waltham, USA)
EVOS™ Light Cube, GFP	Thermo Fisher Scientific Inc. (Waltham, USA)
EVOS™ Light Cube, RFP	Thermo Fisher Scientific Inc. (Waltham, USA)
Freezer (-20 °C)	Liebherr Hausgeräte Ochsenhausen GmbH (Ochsenhausen, DE)
Fume hood	Prutscher Laboratory Systems GmbH (Neudörfl, AT)
Hazardous material cabinet FWF 90	Düberthal Sicherheitstechnik GmbH & Co.KG (Karlsstein, DE)
Incubator 1000	Heidolph Instruments GmbH & Co. KG (Schwabach, DE)
LED light AI Side-Fired Backlight, white (8" x 8")	Edmund Optics GmbH (Mainz, DE)
Magnetic stirrer, up to 20 l, analog	neoLab Laborbedarf-Vertriebs GmbH (Heidelberg, DE)
Microbiological safety cabinet HS 12/2	Heraeus Holding GmbH (Hanau, DE)
Microliter centrifuge mikro 120	Hettich GmbH & Co. KG (Tuttlingen, DE)
Microplate fluorometer and luminometer Fluoroskan™ FL	Thermo Fisher Scientific Inc. (Waltham, USA)
Microplate reader Sunrise™	Tecan Trading AG (Männedorf, CH)
Microvolume spectrophotometer and fluorometer DS-11	DeNovix Inc. (Wilmington, USA)
Objective AMEP4753, 10x, dry, 0.4 numerical aperture (NA), super-apochromat, coverslip-corrected	Thermo Fisher Scientific Inc. (Waltham, USA)
Objective UPLSAPO40XS, 40x, silicone oil immersion, 1.25 NA, super-apochromat, coverslip-corrected	Olympus Europa SE & Co. KG (Hamburg, DE)
Objective, 16 mm fixed focal length (FL), 10 megapixel	Edmund Optics GmbH (Mainz, DE)
Overhead shaker Intelli-Mixer	neoLab Migge GmbH (Heidelberg, DE)
Petri dish filler MEDIAJET	Integra Bioscience GmbH (Biebertal, DE)
pH meter	Schott Instruments (Mainz, DE)
Photometer BioPhotometer plus	Eppendorf SE (Hamburg, DE)
Pipettes (2 µl, 10 µl, 20 µl, 100 µl, 200 µl, 1000 µl)	Gilson International B.V. (Bad Camberg, DE)
Pipette controller Pipetus®	Hirschmann Laborgeräte GmbH & Co. KG (Eberstadt, DE)

Refrigerator	Liebherr-Hausgeräte Ochsenhausen GmbH (Ochsenhausen, DE)
Repetitive pipette Distriman®	Gilson International B.V. (Bad Camberg, DE)
Shaker Unimax 2010	Heidolph Instruments GmbH & Co. KG (Schwabach, DE)
Stereomicroscope BMS 141 Bino Zoom	Breukhoven Microscope Systems (Capelle aan den Ijssel, NL)
Sterilizer UT20	Heraeus Holding GmbH (Hanau, DE)
Stopwatch	Oregon Scientific (Rhede, DE)
Suction system Vacusafe™ Comfort	Integra Bioscience GmbH (Biebertal, DE)
Suction system Vacusip	Integra Bioscience GmbH (Biebertal, DE)
Thermoshaker Biometra TS1	Analytik Jena GmbH (Jena, DE)
Thermostat cabinet Lovibond	Tintometer GmbH (Dortmund, DE)
Ultra-low temperature freezer (-80 °C)	Thermo Fisher Scientific Inc. (Waltham, USA)
Ultrasonic water bath Sonorex Super	Bandelin electronic GmbH & Co. KG (Berlin, DE)
Vortex shaker Phoenix	Phoenix instrument GmbH (Garbsen, DE)
Vortex shaker Reax top	Heidolph Instruments GmbH & Co. KG (Schwabach, DE)
Water bath Aqualine AL5	LAUDA GmbH & Co. KG (Lauda-Königshofen, DE)
Water treatment system Synergy	Merck Millipore (Schwalbach, DE)
Workstation, Intel® Core™ i7-5960X 3.00 GHz processor, Nvidia Quadro RTX6000, 64GB RAM	Bechtle GmbH & Co. KG (Darmstadt, DE)

A.10 Software

Table A.23 lists the used software and its respective supplier.

Table A.23 | List of software

Software	Supplier
DatLab 7.4.0.4.	Oroboros Instruments GmbH (Innsbruck, AT)
FlyCapture®2 Software Development Kit	FLIR Integrated Imaging Solutions, Inc. (Richmond, CA)
GraphPad Prism 8.0.1	Graph Pad Software Inc. (La Jolla, USA)

Huygens Essential 20.04	Scientific Volume Imaging B. V. (Hilversum, NL)
ImageJ/ Fiji is just ImageJ (Fiji) 1.53q	ImageJ, National Institutes of Health (Bethesda, USA)
Inkscape 1.2.1	GitLab Inc. (San Francisco, USA)
Magellan™ 7.3	Tecan Trading AG (Männedorf, CH)
Microsoft Office 2021	Microsoft Office Germany (Unterschleißheim, DE)
SkanIt 6	Thermo Fisher Scientific Inc. (Waltham, USA)
Wide field-of-view nematode tracking platform (WF-NTP)*	Centre for Misfolding Diseases, Department of Chemistry, University of Cambrige (Cambridge, UK)
*The originally published code was modified to ensure compatibility with newer versions of Python, to preset analysis parameters and to implement the maximum speed as an additional motility measure.	

Danksagung

An dieser Stelle möchte ich mich gerne herzlich bei allen bedanken, die mich in den letzten vier Jahren während der Promotion unterstützt haben.
Ein besonderer Dank gilt Prof. Dr. Uwe Wenzel für die Ermöglichung dieser Promotion durch die Bereitstellung des interessanten Themas sowie der notwendigen Ressourcen und für das entgegengebrachte Vertrauen. Zudem haben seine konstruktiven Ideen und hilfreichen Ratschläge maßgeblich zum Gelingen dieser Arbeit beigetragen.

Weiterhin möchte ich mich bei Prof. Dr. Gunter P. Eckert für die freundliche Übernahme der Zweitkorrektur und die stets angenehme Zusammenarbeit mit seiner Arbeitsgruppe bedanken. Dabei danke ich insbesondere meinen ehemaligen Doktorandenkollegen Dr. Benjamin Dilberger, Bernhard Hellmann und Fabian Schmitt für den gemeinsamen Erfahrungsaustausch und die gegenseitige Unterstützung im Labor.

Ein herzliches Dankeschön gilt auch Dr. Daniel Beis, der mich jederzeit durch sein fundiertes Wissen unterstützt hat. Die vielen Gespräche waren nicht nur fachlich, sondern auch menschlich immer wieder eine Bereicherung.

Ich möchte mich ebenfalls bei meinen geschätzten Kolleginnen Therese Kubetzki-Bauer, Angelika Balzer, Carmen Haas, Sabine Lang und Elli Berger für die stetige Hilfsbereitschaft und das angenehme Arbeitsklima bedanken.

Darüber hinaus bedanke ich mich bei den vielen Studierenden - Julia Stötzel, Carina Fischer, Dorothee Hensgens, Marlisa Quiskamp, Anika Halberstadt, Laura Miesbauer, Jonas Baake, Leonie Grebe, Eva Roloff, Anne Ringelmann, Lena Schreiber, Theresa Brecht, Wiebke Diederich, Julia Wolf, Marleen Wagner, Christopher Spahn und Felix Mühlemeyer - für ihr Engagement im Labor während ihrer Abschlussarbeiten und teilweise darüber hinaus als HiWis. Vor allem danke ich den letzten beiden genannten, welche mich beinahe über die gesamte Promotion begleitet haben, für ihren bedingungslosen Einsatz und die schöne gemeinsame Zeit.

Abschließend gilt ein besonderer Dank meiner Lebensgefährtin Linda Wigger, die alle Höhen und Tiefen dieser Promotion sowie privat miterlebt hat und mir stets den nötigen Rückhalt gab.

Publication List

[1] **Baumanns, S.**; Schmitt, F.; Spahn, C.; Ringelmann; A. E.; Beis, D. M.; Eckert, G. P.; Wenzel, U. (2023) Caprylic acid attenuates amyloid-β proteotoxicity by supplying energy via β-oxidation in an Alzheimer's disease model of the nematode *Caenorhabditis elegans*. *Nutritional Neuroscience*. Epub ahead of print. doi: 10.1080/1028415X.2023.2180870

[2] **Baumanns, S.**; Beis, D. M.; Wenzel, U. (2022) RNA-interference in the nematode *Caenorhabditis elegans* is effective using paraformaldehyde-inactivated *E. coli* HT115 bacteria as a food source. *BBA - Molecular Cell Research*, Vol. 1870, No. 1. doi: 10.1016/j.bbamcr.2022.119375

[3] Dilberger, B.; **Baumanns, S.**; Spieth, S. T.; Wenzel, U.; Eckert, G. P. (2020) Infertility induced by auxin in PX627 *Caenorhabditis elegans* does not affect mitochondrial functions and aging parameters. *Aging*, Vol. 12. 1-17. doi: 10.18632/aging.103413

[4] Leiteritz, A.; **Baumanns, S.**; Wenzel, U. (2020) Amyloid-beta (Aβ1–42)-induced paralysis in *Caenorhabditis elegans* is reduced through NHR-49/PPARalpha. *Neuroscience Letters*, Vol. 730, 135042. doi: 10.1016/j.neulet.2020.135042

[5] Dilberger, B.; **Baumanns, S.**; Schmitt, F.; Schmiedl, T.; Hardt, M.; Wenzel, U.; Eckert, G. P. (2019) Mitochondrial Oxidative Stress Impairs Energy Metabolism and Reduces Stress Resistance and Longevity of *C. elegans*. *Oxidative Medicine and Cellular Longevity*, Vol. 2019, doi: 10.1155/2019/6840540

[6] Leiteritz, A.; Schmiedel, T.; **Baumanns, S.**; Wenzel, U. (2019) Amyloid-beta induced paralysis is reduced by cholecalciferol through inhibition of the steroid-signaling pathway in an Alzheimer model of *Caenorhabditis elegans*. *Nutritional Neuroscience*. doi: 10.1080/1028415X.2019.1596371

Eidesstattliche Erklärung

Ich erkläre: Ich habe die vorgelegte Dissertation selbständig und ohne unerlaubte fremde Hilfe und nur mit den Hilfen angefertigt, die ich in der Dissertation angegeben habe.
Alle Textstellen, die wörtlich oder sinngemäß aus veröffentlichten Schriften entnommen sind, und alle Angaben, die auf mündlichen Auskünften beruhen, sind als solche kenntlich gemacht.
Bei den von mir durchgeführten und in der Dissertation erwähnten Untersuchungen habe ich die Grundätze guter wissenschaftlicher Praxis, wie sie in der „Satzung der Justus-Liebig-Universität Gießen zur Sicherung guter wissenschaftlicher Praxis“ niedergelegt sind, eingehalten.

Gießen, den 08.11.2022

Stefan Baumanns